Thin Film Perovskite Solar Cells: Fabrication via Spin Coating, Flash Evaporation and Chemical Vapor Deposition (CVD)

Claudiu, Mortan

(2020)

Thin Film Perovskite Solar Cells

Fabrication via Spin Coating, Flash Evaporation and Chemical Vapor Deposition (CVD)

Dünnschicht-Perowskitsolarzellen: Herstellung durch Rotationsbeschichtung, Blitzverdampfung und chemische Gasphasenabscheidung

Zur Erlangung des akademischen Grades Doktor-Ingenieur (Dr.-Ing.)
Genehmigte Dissertation von **Claudiu Mortan** aus Oradea

Tag der Einreichung: 20.10.2020, Tag der Prüfung: 23.11.2020
Darmstadt – D 17

1. Gutachten: Prof. Dr. Wolfram Jaegermann
2. Gutachten: Prof. Dr. Barbara Albert

TECHNISCHE UNIVERSITÄT DARMSTADT

Energy Science and Engineering
Surface Science Division
Materials Science Department

MATERIAL-WISSENSCHAFT

Surface Science

Graduate School of Energy Science and Engineering

“Thin Film Perovskite Solar Cells – Fabrication via Spin Coating, Flash Evaporation and Chemical Vapor Deposition (CVD)”

„Dünnschicht-Perowskitsolarzellen – Herstellung durch Rotationsbeschichtung, Blitzverdampfung und chemische Gasphasenabscheidung“

Genehmigte Dissertation von Claudiu Mortan aus Oradea

1. Gutachten: Prof Dr. Wolfram Jaegermann
2. Gutachten: Prof. Dr. Barbara Albert

Tag der Einreichung: 20.10.2020

Darmstadt 2020 – D 17

Bitte zitieren Sie dieses Dokument als:

URN: urn:nbn:de:tuda-tuprints-146189

URL: https://tuprints.ulb.tu-darmstadt.de/id/eprint/14618

Dieses Dokument wird bereitgestelt von tuprints,

E-Publishing-Service der TU Darmstadt

http://tuprints.ulb.tu-darmstadt.de

tuprints@ulb.tu-darmstadt.de

Declaration of Authorship

I hereby declare that the thesis submitted is my own unaided work. All direct or indirect sources used are acknowledged as references. This work has not yet been submitted to any examination authority in the same or similar form.

Darmstadt, 20.10.2020

_____

Claudiu Mortan

"I don't spend my time pontificating about high-concept things; I spend my time solving engineering and manufacturing problems."

Elon Musk – 2013

Abstract

In this work, thin film perovskite solar cells with different compositions have been manufactured with the help of the methods: spin coating, spray pyrolysis, etching, sputtering, chemical bath deposition, flash evaporation and chemical vapor deposition (CVD). The solar cells and their materials have been characterized electrically at the solar simulator setup, respectively through UV/Vis absorption spectroscopy, photoluminescence (PL), scanning electron microscopy (SEM), X-ray diffraction (XRD) and X-ray photoelectron spectroscopy (XPS). In a classical approach, which has been optimized within our Surface Science group, a two-step spin coating and chemical bath deposition method for producing the perovskite material methylammonium lead iodide (MAPI) was used in this work to manufacture Glass/FTO/c-TiO_2/m-TiO_2/MAPI/spiro-MeOTAD/Au solar cells, having a maximum power conversion efficiency (PCE) of 15,6 %, with a solar cell dimension of 32,5 mm^2 and a mini-module substrate dimension of 4 cm^2. In a next approach, a one-step spin coating and antisolvent method was used according to literature[1] to deposit a thin film of a triple cation, double anion lead perovskite: $(Cs_aMA_bFA_c)_1PbI_xBr_{3-x}$. This approach is used to compare the performance of solar cells made using our lab methods and the production of our own stack of materials Glass/FTO/c-TiO_2/m-TiO_2/$(Cs_aMA_bFA_c)_1PbI_xBr_{3-x}$/spiro-MeOTAD/Au with those in literature. While according to literature[1] the published perovskite recipe reached a maximum PCE of over 20% in the authors' labs, a maximum efficiency of 18,5 % could be obtained within this work. A further increase in efficiency is discussed with respect to our solar simulator measurement method. Furthermore, a flash evaporation setup has been built and employed in a novel solvent-free approach to produce films of the alternative perovskite material for solar cells, methylammonium tin iodide (MASI), which uses tin (Sn) instead of the widely used lead (Pb). These experiments show that the flash evaporation process can produce MASI films of a high chemical purity. Additionally, a new chemical vapor deposition (CVD) setup has been built and used to test a variety of precursor combinations for synthesizing methylammonium lead iodide (MAPI), formamidinium lead iodide (FAPI), or hydrogen lead iodide ($HPbI_3$). For producing MAPI perovskite films, methylamine gas (MA) and home-made hydrogen iodide (HI) gas were successfully used. For these reactions, the mechanism has been clarified using XPS and XRD. The best solar cell built using the up-scalable CVD setup shows an efficiency of 12,9 %.

Zusammenfassung

In dieser Arbeit wurden Dünnschichtsperowskitsolarzellen mit unterschiedlichen Zusammensetzungen mithilfe der folgenden Methoden hergestellt: Rotationsbeschichtung, Sprühpyrolyse, Ätzen, Sputtern, chemische Badabscheidung, Blitzverdampfung und chemische Gasphasenabscheidung (CVD). Die Solarzellen und ihre Materialien wurden am Solarsimulator elektrisch charakterisiert, bzw. mithilfe von UV/Vis-Absorptionsspektroskopie, Photolumineszenz (PL), Rasterelektronenmikroskopie (REM), Röntgenbeugung (XRD) und Röntgenphotoelektronenspektroskopie (XPS). In einem klassischen Ansatz, der innerhalb unserer Surface Science-Gruppe optimiert wurde, wurde in dieser Arbeit ein zweistufiges Rotationsbeschichtung- und chemisches Badabscheidungsverfahren zur Herstellung des Perowskitmaterials Methylammonium-Bleiiodid (MAPI) weiter optimiert, um Glas / FTO / c-TiO_2 / m-TiO_2 / MAPI / Spiro-MeOTAD / Au-Solarzellen mit einem maximalen Wirkungsgrad von 15,6% herzustellen, einer Solarzellenabmessung von 32,5 mm^2 und einer Minimodul Substratabmessung von 4 cm^2. In einem nächsten Ansatz wurde ein einstufiges Rotationsbeschichtung- und Antilösungsmittelverfahren gemäß Literatur[1] verwendet, um einen dünnen Film aus einem Dreifachkation-Doppelanion-Blei-Perowskit abzuscheiden: $(Cs_aMA_bFA_c)_1PbI_xBr_{3-x}$. Dieser Ansatz wurde verwendet um die Leistung der Solarzellen, die mit unseren Labormethoden hergestellt werden, unter Anwendung unseres eigenen Materialstapels: Glas / FTO / c-TiO_2 / m-TiO_2 / $(Cs_aMA_bFA_c)_1PbI_xBr_{3-x}$ / Spiro-MeOTAD / Au mit Ergebnissen aus der Literatur zu vergleichen. Während das veröffentlichte Rezept[1] eine maximale Solarzelleneffizienz von mehr als 20% im Labor der Autoren erreichte, konnte innerhalb dieser Arbeit eine Effizienz von 18,5% erreicht werden. Eine weitere Effizienzsteigerung wird in Bezug auf unsere Messmethode am Solarsimulator diskutiert. Darüber hinaus wurde ein Blitzverdampfungsgerät aufgebaut und in einem neuartigen lösungsmittelfreien Ansatz eingesetzt um Dünnschichtfilme aus dem alternativen Solarzellen-Perowskitmaterial Methylammonium-Zinniodid (MASI) herzustellen, bei dem Zinn (Sn) anstelle des weit verbreiteten Blei (Pb) verwendet wird. Diese Experimente zeigen, dass durch den Blitzverdampfungsprozess MASI-Filme mit hoher chemischer Reinheit erzeugt werden können. Des Weiteren wurde ein neuer Aufbau für chemische Gasphasenabscheidungen (CVD) entwickelt, mit dem verschiedene Eduktkombinationen für die Synthese von Methylammonium-Bleiiodid (MAPI), Formamidinium-Bleiiodid (FAPI) oder Wasserstoff-Bleiiodid ($HPbI_3$) getestet wurden. Zur Herstellung von MAPI-Perowskitfilmen wurden Methylamingas (MA) und selbst hergestelltes Iodwasserstoffgas (HI) erfolgreich verwendet. Für diese Reaktionen wurde der Mechanismus mithilfe von XPS und XRD geklärt. Die beste Solarzelle, die mit dem hochskalierbaren CVD-Aufbau hergestellt wurde, weist einen Wirkungsgrad von 12,9 % auf.

Table of Contents

1. Important abbreviations

AM	air mass
B.E.	binding energy
CBM	conduction band minimum
CVD	chemical vapor deposition
DMF	N,N-Dimethylformamide
DMSO	Dimethyl sulfoxide
EDS	energy-dispersive X-ray spectroscopy
E_F	Fermi energy
E_g	band gap energy
ETM	electron transport material
FAPI	formamidinium lead iodide
FTO	fluorine doped tin oxide
FF	fill factor
GBL	γ-butyrolactone
HOMO	highest occupied molecular orbital
HTM	hole transport material
I	current
I_{MPP}	current at maximum power point
ISC	short circuit current
ITO	indium tin oxide
IV	current-voltage
J	current density
J_{MPP}	current density at maximum power point
J_{SC}	short circuit current density
LUMO	lowest occupied molecular orbital
MA	methylamine
MAI	methylammonium iodide
MAPI	methylammonium lead iodide

MASI	methylammonium tin iodide
MPP	maximum power point
PCE	power conversion efficiency
PL	photoluminescence
PVD	physical vapor deposition
R_p	parallel resistance
R_s	series resistance
SC	semiconductor
SEM	scanning electron microscopy
Spiro-MeOTAD	N2,N2,N2',N2',N7,N7,N7',N7'-octakis(4-methoxyphenyl)-9,9'-spirobi[9H-fluorene]-2,2',7,7'-tetramine
TCO	transparent conductive oxide
UV/Vis	indicates ultraviolet/visible radiation spectroscopy
VBM	valence band maximum
V_{MPP}	voltage at maximum power point
V_{OC}	open circuit voltage
XPS	X-ray photoelectron spectroscopy
XRD	X-ray diffraction

2. Introduction

We live in a time of energy transition. Our use of fossil fuels over the last century enabled us to live in prosperity, but in a few decades, the age of fossil fuels will foreseeably dusk, with the coming age of the fourth industrial revolution, including an energy, as well as a technological revolution, i.e. the advancement of artificial intelligence. One side effect of burning fossil fuels to produce energy is the acceleration of global warming through the emission of the greenhouse gas CO_2. In the greenhouse effect, high energy electromagnetic radiation with short wavelengths coming from the sun is absorbed by Earth's surface. Earth then emits longer wavelength radiation as heat, that is trapped in the atmosphere by greenhouse gases like H_2O, CO_2, CH_4, etc. (see Figure 2.1). Examples of the effects of global warming are an increasing number of extreme weather events, like hurricanes, droughts, or bushfires, polar ice caps melting and sea level rise, due to which whole cities are endangered by flooding, or the extinction of ecosystems due to the rise of the average global temperature. The diagram in Figure 2.2, published by NASA, shows the fast carbon cycle and its movement between land, atmosphere, and the oceans. According to this figure, global human emissions of CO_2 accumulate to 9 gigatons per year (shown in red), but only 3 Gt can be taken back up by photosynthesis on land (plant biomass) and 2 Gt by photosynthesis in the oceans (mainly phytoplankton), leaving 4 Gt/a to accumulate in the atmosphere and to promote the greenhouse effect. For counteracting global warming, "The main task is the sustainable transition from fossil, non-renewable primary energy sources of today to renewable and clean energy resources of tomorrow." – Darmstadt Graduate School of Excellence Energy Science and Engineering.[2]

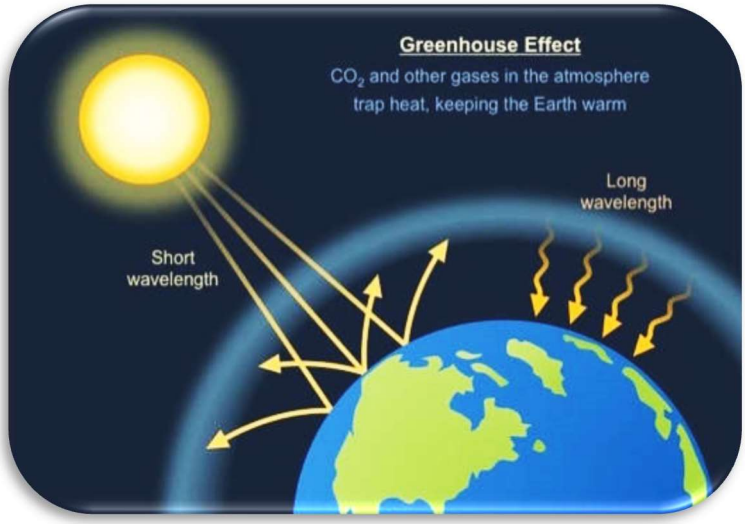

Figure 2.1 Simplified schematics of the greenhouse effect by Climate Central, **NASA**

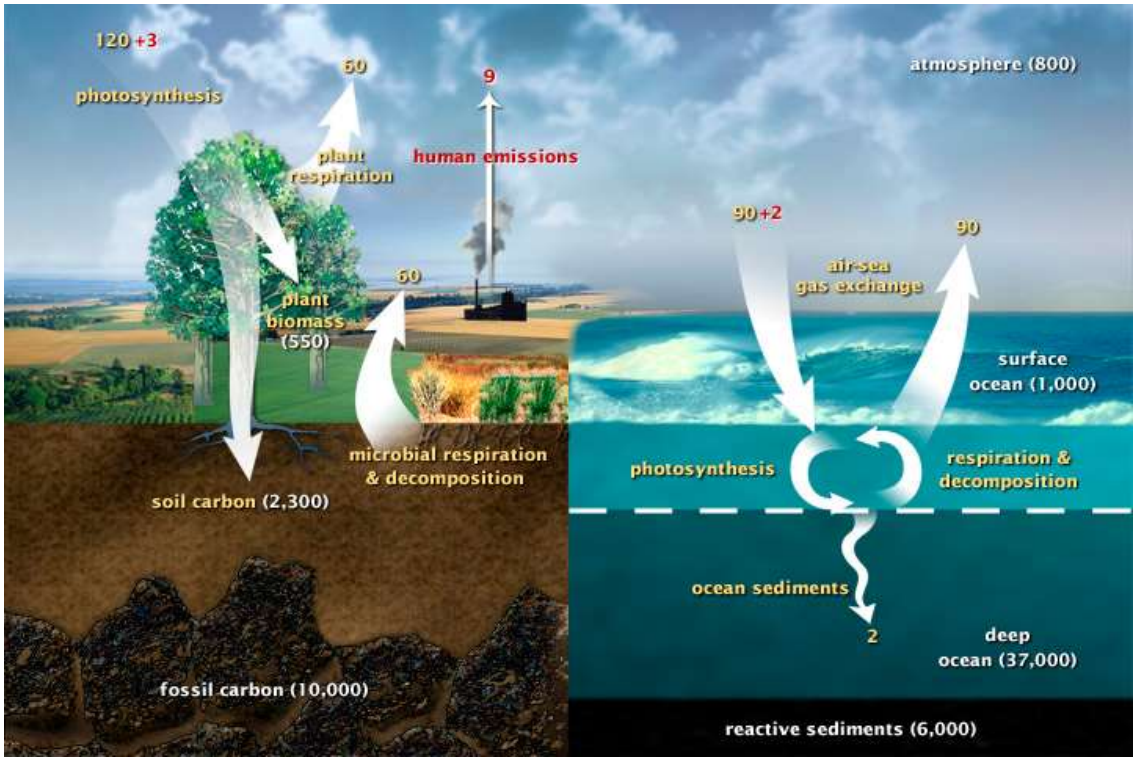

Figure 2.2 The fast carbon cycle. The units of all numbers are **gigatons of carbon per year (Gt/a)**. Diagram adapted by **NASA** from the U.S. DOE, Biological and Environmental Research Information System

There is virtually an infinite amount of resources and energy in the universe compared to the scale of our Earth. Ideally, we should promote and use these resources as economically, as en-

vironmentally friendly and as sustainably as possible. Figure 2.3, made by the German Aerospace Center (DLR: Deutsches Zentrum für Luft- und Raumfahrt), sums up the amount of resources and reserves of available sustainable energies on Earth, like solar, wind, biomass, geothermal energy, heat from the seas, energy from the waves and water power. “The natural availability of renewable energy (cubes at the back) is extraordinarily large. The potential energy yield in the form of electricity, heat and chemical energy carriers (front cubes) exceeds the present-day energy needs (grey cube) by a factor of six.” – DLR, 2004. Current and future challenges will be harvesting sustainable energies (e.g. using photovoltaic systems, wind turbines) and storing them (e.g. hydrogen, Li-ion batteries), by keeping in mind material criticality: supply risk, vulnerability to supply restriction and environmental implication.

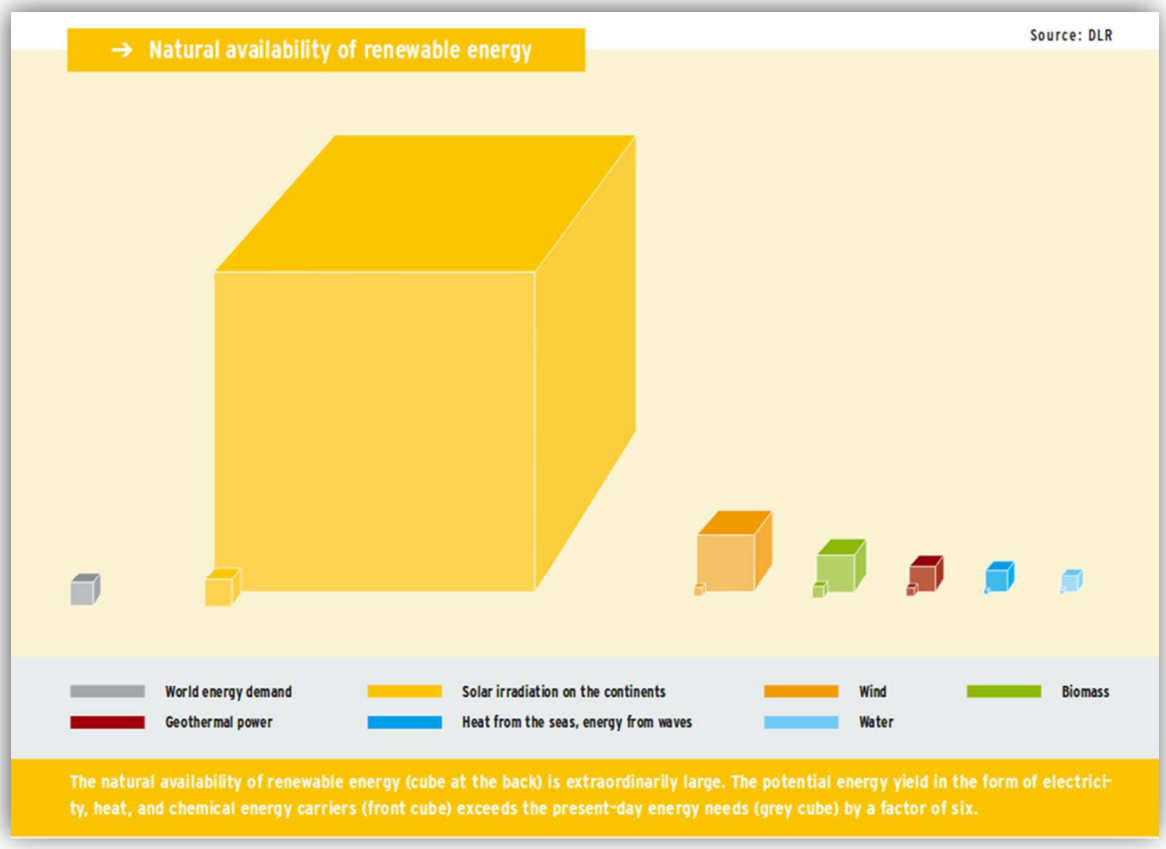

Figure 2.3 World energy demand along with resources and reserves of sustainable energies. Diagram made by the German Aerospace Center (**DLR**: Deutsches Zentrum für Luft- und Raumfahrt) in 2004

This work is a contribution in tackling climate change. The research performed in the course of 3,5 years for this PhD is about a new type of solar cell technology that uses a novel photoactive, semiconducting class of materials: Perovskites. Many thin film deposition techniques are used throughout the specialized literature in producing the layers needed for manufacturing perovskite solar cells on a laboratory scale, ranging from spin coating, [3, 4] to physical vapor deposition (PVD),[5, 6] slot die coating,[7, 8] chemical vapor deposition (CVD),[9, 10] printing[11, 12] and many more. This thesis discusses practical experiments mainly addressing the manufacturing of perovskite solar cells with the goal of attaining high power conversion efficiencies while using upscalable production methods.

The main part of this thesis, Chapter 4, which includes all experiments, is divided into four main subchapters. Chapter 4.1 involves producing solar cells from methylammonium lead iodide ($CH_3NH_3PbI_3$) by using the manufacturing techniques: spray pyrolysis, spin-coating, chemical bath deposition and sputtering, then subsequently measuring electrical characteristics of the produced solar cells, using a solar simulator setup. The methods and materials presented in this subchapter are used as references for fabricating solar cells by alternative methods and with alternative materials in the next three chapters. In Chapter 4.2, an alternative perovskite material ($(Cs_aRb_bMA_cFA_d)_1PbI_xBr_{3-x}$) is deposited by spin-coating, while keeping all other needed layers within the solar cell the same, as in the previous chapter. These solar cells with a different absorber layer are characterized electrically, by using the solar simulator setup. In Chapter 4.3 a new thin film deposition method is introduced and employed: the flash evaporation. A flash evaporation apparatus has been built-up specifically for the deposition of different perovskite materials (e.g. $CH_3NH_3PbI_3$, or $CH_3NH_3SnI_3$) and the formed perovskite films are characterized by SEM, EDS, photoluminescence, optical microscopy, XRD and XPS. Chapter 4.4 is the most complex part of this work and it involves a newly built chemical vapor deposition (CVD) setup that can use a number of precursors to manufacture different types of photoactive perovskite thin films. In this chapter, the perovskite films (e.g. $CH_3NH_3PbI_3$, or $CN_2H_5PbI_3$) are characterized by SEM, XRD, XPS, UV/vis spectroscopy, photoluminescence and optical microscopy, and the manufactured solar cells are electrically characterized using the solar simulator setup.

The goal of this work was not only to correlate the properties of different perovskite materials and perovskite solar cells to the different processing steps and deposition techniques used, but also to engineer new up-scalable fabrication methods and devices that would allow a convenient and affordable way of producing these types of solar cells.

3. Theoretical framework

3.1 Semiconductors

The age of silicon, or the information age is the historical period that we currently live in, which started with the digital revolution in the late 20th century. Silicon is by far the most used element in semiconductor devices. Material science has contributed to the development of the information age by inventions of electronic components like diodes, transistors (e.g. MOSFET, BJT, FET), capacitors and many more. A large number of electronic components rely on the phenomenon of semiconductivity. Semiconductors are used in consumer electronics like TVs, personal computers and smartphones, to name a few, or power electronics like rectifiers or inverters. They are also crucial components of energy conversion and storage systems like solar cells, rechargeable batteries, electrochemical water splitting devices and many more. Semiconductors are a material class with conductivity between conductors (e.g. metal) and insulators (e.g. glass). While conductors always allow electricity to flow through them, semiconductors have a band gap, a zone between the valence band and the conduction band, where there are no electronic states (see Figure 3.1). Semiconductors are defined by the energy of their band gap $E_g \leq 3.2$ eV, while insulators have a band gap larger than 3.2 eV. By radiation of photons on a semiconductor, with an energy equal or larger than its band gap, electrons can be excited from the valence band of the material (in organic semiconductors also referred to as HOMO: highest occupied molecular orbital), to its conduction band (in organic semiconductors also referred to as LUMO: lowest unoccupied molecular orbital) and the material is able to convert light into electrical energy: the origin of the photovoltaic effect used in solar cells.

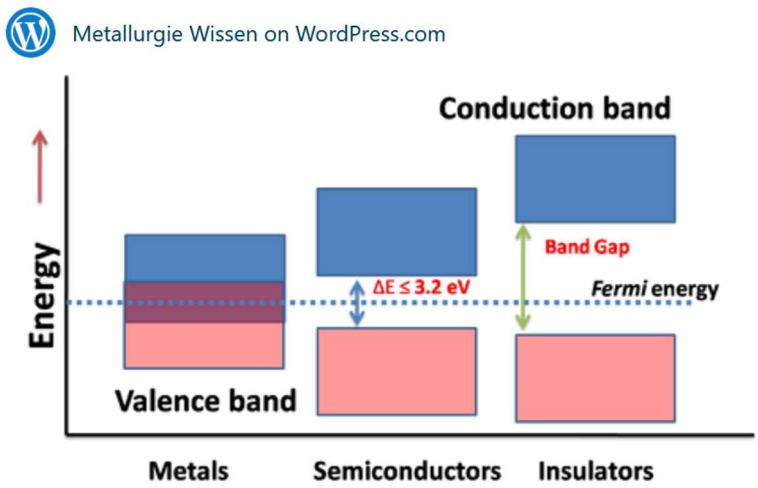

Figure 3.1 Schematics of the energy bands of metals, semiconductors and insulators

Diagram published by **Metallurgie Wissen** on WordPress

The light coming from the sun has a continuous spectrum of ultraviolet (UV) radiation (10 nm - 380 nm), visible light (380 nm - 700 nm) and infrared radiation (700 nm - 1 mm). Figure 3.2 shows different spectra of the sun. The grey curve is a simulated black body radiation according to Planck's law, at a temperature T = 5800 K, which is approximately the surface of the sun. This curve correlates well with the AM0 spectrum (AM = atmospheric mass), which is the spectrum of the sun in space, before entering Earth's atmosphere. The AM1,5G spectrum is defined as the spectrum of the sun whose light passes through a 1,5x air mass, i.e. at 41° angle above the horizon. The integral of this spectrum (area under the curve) gives a total irradiance of 1000 W / m^2, or 1 Sun, defined as a standard, mean value for comparing the efficiencies of solar cells. This spectrum is a good representation of the illumination on a photovoltaic array on a clear day without clouds near noon in the geographical mid latitudes.

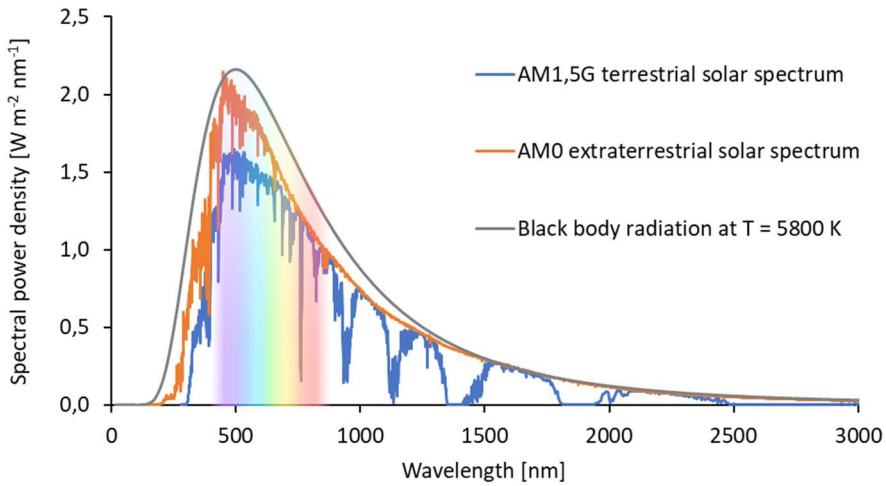

Figure 3.2 AM0, AM1,5G sun spectra; and spectrum of a black body at a temperature of 5800K (surface of the sun), derived from Planck's law. Sun spectrum data plotted from standards: ASTMG173 (AM1,5G) resp. ASTM E490 (AM0)

To excite electrons from the valence band to the conduction band of a light absorbing semiconducting material with a direct band gap, an absorbed photon must have enough energy for the electron to overcome the band gap. Photons with energies below the band gap E_g of the material will not be absorbed. In 1961 William Shockley and Hans-Joachim Queisser calculated the theoretical maximum efficiency of a pn-junction solar cell, in which the only loss mechanism is radiative recombination. They publishing the results in their paper entitled "Detailed Balance Limit of Efficiency of p-n Junction Solar Cells".[13] By using a black body radiation with a temperature of 6000 K they could calculate the efficiency of a pn-junction solar cell in respect to its band gap as shown in Figure 3.3. Their calculations reached a maximum efficiency of 30% for a 1.1 eV band gap material. More recent calculations for an AM1,5G spectrum reach a maximum theoretical efficiency of 33,7% for a 1,34 eV band gap semiconductor. [14]

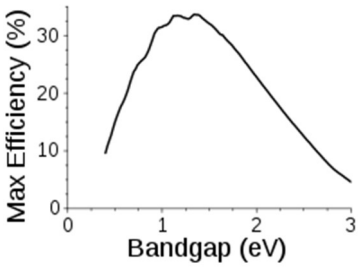

Figure 3.3 Shockley–Queisser limit for the efficiency of single junction p-n solar cells in respect to their band gap energy

Wikimedia, public domain

The solution to overcoming the Shockley-Queisser efficiency that is valid for single junction solar cells is by using multiple semiconductors stacked upon each other in a tandem configuration. With this approach, efficiencies of over 50% would be realizable. The current record for tandem solar cells measured under 1 Sun lies at 39,2 %, using six junctions III-V SCs (NREL J-6, see Figure 3.11) and the current efficiency record for a Si/Perovskite tandem solar cell is 29,1 % (HZB, see Figure 3.11).

Elemental semiconductors, as can be found in group IV of the periodic table of elements, like silicon (Si) or Germanium (Ge) are materials that have four valence electrons per atom. Their electrons form covalent bonds between neighboring atoms, forming a crystal lattice as illustrated in Figure 3.4. With the help of an energy applied to the material which can overcome its band gap (e.g. light: electromagnetic radiation), these electrons can be excited to higher energetic states, e.g. in the conduction band, leading to a change in the chemical potential of the electrons, which may be harvested for energy conversion. The addition of small amounts of certain impurities to the lattice of an intrinsic semiconductor is called doping and the material is then called an extrinsic semiconductor. An n-type elemental SC is obtained by adding an element belonging to group V of the periodic table to the intrinsic SC, e.g. phosphorous (P), or arsenic (As). Elements of group V have five valence electrons, but only four electrons can participate in making bonds with the material and the extra electron can easily be excited to the conduction band, aiding in conducting electricity. The dopants of the n-type SC are called donors, because they can donate electrons to the CB. A p-type SC is made by adding an element

belonging to group III of the periodic table to the intrinsic SC, e.g. boron (B), or gallium (Ga). Elements of group III have three valence electrons; thus, one electron is missing to forming full covalent bonds with group IV materials and a positively charged vacancy, or hole is available in the valence band. The positively charged hole can travel in the valence band the same way a negatively charged electron can travel in the conduction band of the doped material. The dopants of the p-type elemental SC are called acceptors because they can accept electrons from the valence band.

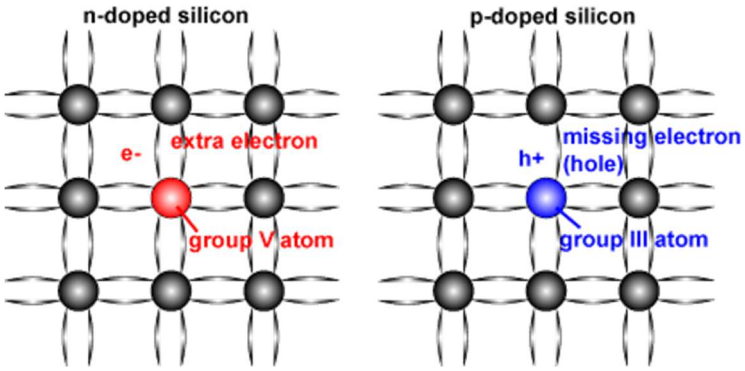

Figure 3.4 Schematic of a silicon crystal lattice doped with impurities to produce an n-type and a p-type semiconductor material

Diagram published by **PVEDUCATION**.org

Doping of semiconductors is an essential ingredient for the manufacturing of semiconductor devices, e.g. for solar cells, however the doping mechanism for perovskites may be much more complex than in the case of silicon. For example, Phung et al.[15] show that low doping levels enable the incorporation of the dopant within the perovskite lattice, whereas high doping concentrations induce surface segregation, thus in their case the low doping regime results in a more n-type material, while the high doping regime induces a less n-type doping character.

The position of the so-called Fermi Energy E_F is an important quantity to define the properties of semiconductors based on their doping levels, i.e. intrinsic, n-type or p-type. The Fermi energy level is defined as the energy level at which the probability of an electron occupation at 0 K is equal to 50% (all bands are either full or empty).[16] As illustrated by Figure 3.5, the

Fermi energy of an intrinsic SC lies in the middle of the band gap. For an n-type SC, E_F is closer to the conduction band of the material and for a p-type SC, closer to the valence band.

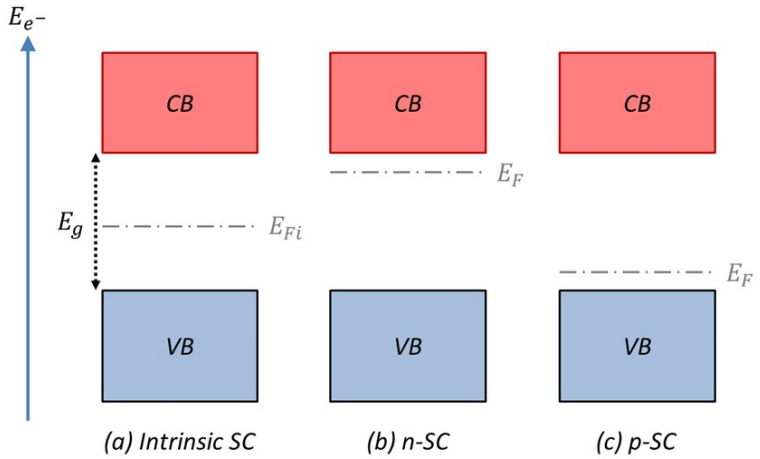

Figure 3.5 Illustrated scheme showing the Fermi level position within the band gap of a semiconductor for an (a) intrinsic, (b) n-type and (c) p-type semiconductor [17]

For intrinsic SCs at room temperature, thermally induced electron transitions from the VB to the CB are highly unlikely due to the much larger band gap than the *RT* thermal energy of 25 meV. When the temperature is above absolute zero, at thermal equilibrium, the electrons do not simply fill the lowest energy states first. In this case, the Fermi-Dirac statistics needs to be considered, which gives the probability distribution of an electron of energy E at temperature T as shown in Equation 3.1, whereas E is the electron energy, E_F, the Fermi Energy, k_B: Boltzmann's constant and T, the temperature. [18, 19] For absolute zero, and $E < E_F$, the Fermi-Dirac distribution $f_e(E)$ equals 1, while $f_e(E) = 0$ for $E > E_F$. Electrons will be thermally excited around E_F, and $f_e(E) < 1$ near $E_F (E < E_F)$ while $f_e(E) > 0$ at $E > E_F$. At $E = E_F$, $f_e(E) = 1/2$ regardless of the temperature. A typical plot for three different temperatures is illustrated in Figure 3.6.[3]

Equation 3.1 $$f_e(E) = \frac{1}{1+\exp\left(\frac{E-E_F}{k_B T}\right)}$$

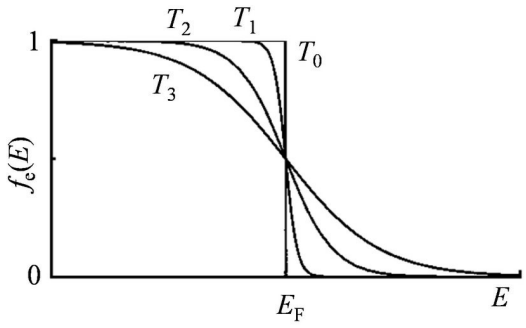

Figure 3.6 Fermi-Dirac distribution function at different temperatures: $T_3 > T_2 > T_1$ (and $T_0 = 0$ K). At the absolute zero temperature (T_0), the probability of an electron to have an energy below the Fermi energy E_F is equal to 1, while the probability to have higher energy is zero. [18]

The more general formulation of Fermi-Dirac statistics involves a chemical potential μ' instead of E_F. This chemical potential depends on the temperature and the applied potential. But in most cases of semiconductors, the difference between μ' and E_F is very small at the temperature that is usually considered. [3]

3.2 Solar Cells

In the photovoltaic effect, a voltage and a current are generated in a material upon illumination. This chemo-physical phenomenon was first discovered by Edmund Becquerel in 1839, who immersed two silver coated platinum electrodes in an acid solution. By exposing one electrode to sunlight, while keeping the other in shade, he could observe a flow of electricity.[20] In 1876, William G. Adams and his student Richard E. Day showed for the first time that electrical power is directly produced by illuminating the solid material selenium.[21] Seven years later, in 1883, the New Yorker Charles Fritz produced the first solar cell ever made, by coating selenium with a thin layer of gold. His solar cell exhibited a light-to-electricity conversion efficiency of 1 to 2 %.[22] After his discovery, Fritz contacted the famous German expert Werner von Siemens, who then reproduced and confirmed the functionality of the device.[23]

Today, 137 years later, solar cells are widely used on house roof tops, solar fields, satellites, pocket calculators, charging power banks, lawn mower robots, etc. We distinguish between three generations of solar cells. The first generation of solar cells are traditional silicon solar cells, which is the most widely used PV technology, known for its reliability and affordability given by its economy of scale. The second generation solar cells are also called thin-film solar cells. They use stacks of semiconducting materials only a few µm thick, in comparison to silicon solar cells that are in the range of several hundred µm. Mentionable materials are cadmium telluride (CdTe), or copper indium gallium diselenide (CIGS). Third generation solar cells are the newest generation of PVs and are often called emerging PV technologies. These may include organic photovoltaics (OPVs), dye sensitized solar cells (DSSCs), quantum dots, or perovskites, as defined by some fraction of the PV community. Originally, the 3rd generation concept was defined to describe solar cells with potential power conversion efficiencies beyond the Shockley-Queisser limit of single junction solar cells.

Light emission and absorption in a semiconductor are dependent on the detailed band structure of a semiconductor. Semiconductors can be divided into direct band gap semiconductors and indirect band gap semiconductors. Figure 3.7 illustrates the absorptions of photons in direct and indirect semiconductors. In direct SCs, image **a)**, the energy of the conduction band minimum E_{CBM} occurs at the same wavevector k (momentum $p = \hbar k$) as for the energy of the valence band maximum E_{VBM}. Direct band gap semiconductors have a strong absorption of light, characterized by their larger absorption coefficient. Indirect semiconductors have a smaller absorption coefficient, their E_{CBM} not occurring at the same wavevector k as their E_{VBM} (image **b)**).

The difference between direct band gap SCs and indirect band gap SCs can be further explained by the conservation of energy and momentum required for the electron-photon interaction. In the direct band gap SC, image **a)**, a photon is absorbed when an empty state is available in the CB, for which the energy and momentum is equal to that of an electron in the VB plus that of the incident photon. Photons have little momentum relative to their energy since

they have no mass and they travel at the speed of light. In this case, the electron makes a vertical transition in the *E-k* diagram.

An electron transition in an indirect band gap SC is illustrated in image **b)**. In this case, E_{CBM} and E_{VBM} are not aligned vertically, so an incident photon will not provide an electron with the correct energy and momentum corresponding to that of an empty state in the CB. Here, the absorption of a photon needs the energy and momentum of a phonon. Phonons are lattice vibrations with large momentums and lower energy and velocities than light (in the range of the speed of sound). Conservation of energy and momentum can occur if a photon and a phonon participate in the excitation of the electron. In Figure 3.7 **b)** the absorption of a phonon aids the absorption of a photon in the indirect band gap semiconductor.

Since in an indirect band gap SC the interaction of all three particles, i.e. electron, photon and phonon has to take place, the probability of a photon absorption is lower than in a direct band gap semiconductor, in which the absorption is much stronger.

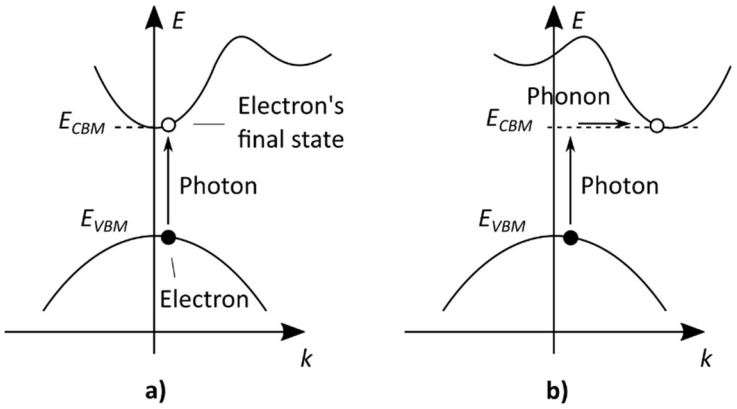

Figure 3.7 Direct vs. indirect band gap semiconductors: energy *E* vs. wave vector *k* diagram. **a)** Photon absorption in a direct bandgap semiconductor. **b)** Photon absorption in an indirect bandgap semiconductor by phonon absorption

Examples of direct band gap semiconductors are GaAs, CdTe, CIGS or CZTS and examples of indirect band gap semiconductors are silicon (Si), or Germanium (Ge), while there are other

materials like methylammonium lead iodide (perovskite, $CH_3NH_3PbI_3$), that have both a direct and an indirect band gap character,[24] which may provide specific advantage for their use in solar cells, like a strong absorption and long charge carrier lifetime. The weak indirect band gap character of perovskites like methylammonium lead iodide is a consequence of spin-orbit coupling resulting in Rashba-splitting.[25, 26]

One of the key principles in solid state electronics is the p-n junction. When a p-type and an n-type material are brought together, a space charge region forms at their contact as shown in Figure 3.8. From this effect a diode is formed, in which current flows only in one direction, i.e. when forward biased. In an unbiased p-n junction, charge accumulates in the space charge region at the interface of the materials and the diffusion current, given by different carrier concentration and their chemical potentials, is in exact balance with the drift current in opposite direction, given by the formed electrical field, which is confined in the space charge region. In this case the diode is in equilibrium. In a forward biased diode, a voltage with a negative pole at the n-type material and a positive pole at the p-type material is applied. Electrons from the bulk of the n-type material diffuse towards the holes of the p-n junction and the holes from the bulk of the p-type material diffuse towards the electrons of the p-n junction. At the junction, electrons and holes recombine, maintaining a continuous current flow. A reverse biased diode will block a current flow until reaching the so called breakdown voltage, in which the high electrical field formed will still allow a current flow.

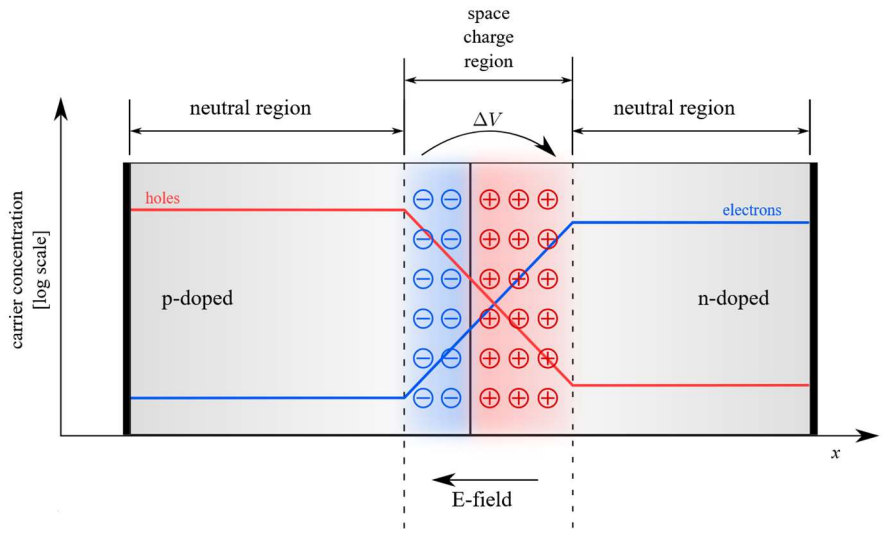

Figure 3.8 The equilibrium of a p-n junction

Creative Commons Attribution 3.0, Wikimedia, Credit: Adundovi

The Shockley diode equation or the diode law in Equation 3.2 gives the current-voltage characteristic of a diode with either a forward, or a reverse bias voltage. In this equation, *I(V)* is the diode current, I_0 is the reverse bias saturation current (or scale current), *q* is the absolute value of the electron charge, k_B is Boltzmann's constant and *T*, the temperature.

Equation 3.2 $$I(V) = I_0 \left(e^{\frac{qV}{k_B T}} - 1 \right)$$

A band diagram of a p-n junction device under open circuit condition is shown in Figure 3.9. When the two materials (n-type and p-type) are brought into contact, a band bending results at their interface, given by the different electro-chemical potentials of the electrons, which is caused by the electron transfer across the junction, with the formation of an electrical field. In the dark case, i.e. at thermodynamic equilibrium of the charge carriers, the Fermi levels of the materials are aligned. When the device is illuminated, electrons are excited from the valence band into the conduction band and a quasi-Fermi level splitting (or *imref*, Fermi spelled backwards) occurs. Charges accumulate at both sides of the device and an open circuit voltage V_{OC} can be measured.

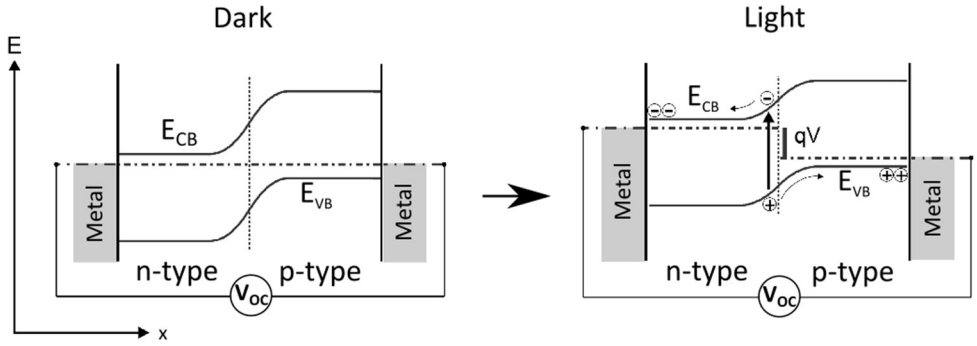

Figure 3.9 Band diagram of a p-n solar cell under open circuit condition in the dark and under illumination

When the terminals of an illuminated p-n solar cell are short circuited, Figure 3.10, charge carriers that are formed by the absorption of light in the p-n junction start flowing in opposite directions to each other and a short circuit current I_{SC} can be measured.

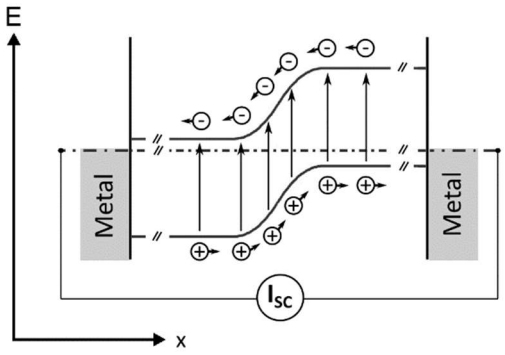

Figure 3.10 Band diagram of a p-n solar cell under short circuit condition under illumination

Macroscopically, the flow of electrons in a solar cell device results in a photocurrent I_{Ph} which by definition is subtracted from the total current in the diode equation (Equation 3.3), where *j* is defined as the current density, equal to the ratio of the current I and the area *A* of a solar cell, as shown in Equation 3.4.

Equation 3.3 $$j(V) = j_0 \left(e^{\frac{qV}{k_B T}} - 1 \right) - j_{Ph}$$

Equation 3.4 $$j(V) = \frac{I(V)}{A}$$

Currently, the best laboratory-scale single crystal silicon solar cell reaches a certified efficiency of 26,1 % (ISFH: Institute for Solar Energy Research in Hamelin) and the best multijunction, monolithic, 2-terminal, concentrator solar cell reaches an efficiency as high as 47,1 % (NREL: National Renewable Energy Laboratory). A chart of further best research cell efficiencies is provided by NREL, shown in Figure 3.11. On a commercial scale, according to Clean Energy Reviews: "Top 10 Solar Panels – Latest Technology 2020", Sunpower (USA), with manufacturing facilities in USA, Mexico, China and Philippines produces panels with a maximum efficiency of 22,6 % and a 25 year warranty, followed by LG (South Korea), that has manufacturing facilities in South Korea and USA, who produce panels with 21,7 % and a 25 year warranty. The warranty guarantees up to 80 % - 90 % of the initial efficiency, depending on exact model of the panel. According to the "Photovoltaics Report" prepared by Fraunhofer Institute for Solar Energy Systems (ISE) in 2020, the energy payback time of PV systems, which is the time that a panel needs to run for, to produce the energy used for its manufacturing, is between 1 year and 2,5 years, depending on the geographical location of its operation, i.e. southern Europe, resp. northern Europe. In comparison to silicon technologies, thin film PV systems have a lower energy payback time, e.g. CdTe with 0,6 years, resp. 1,1 years in southern, resp. northern Europe.[27]

Global grid-connected solar capacity reached 580,1 GW at the end of 2019, along with 3,4 GW of off-grid PV, according to the International Renewable Energy Agency (IEA), while the worldwide electricity consumption amounts to 25,7 mil. GWh / year. With a yearly global sunshine duration of 1200 h,[28] a solar capacity of 21400 GW would be needed to supply the whole world with electricity from PV devices, which is 37-fold of the current installed capacity.

Thin film solar cells would have a serious advantage compared to established silicon PV technologies by using cheap materials, as easy and inexpensive deposition technologies are developed to reach the same efficiency and stability as that known for silicon solar cells.

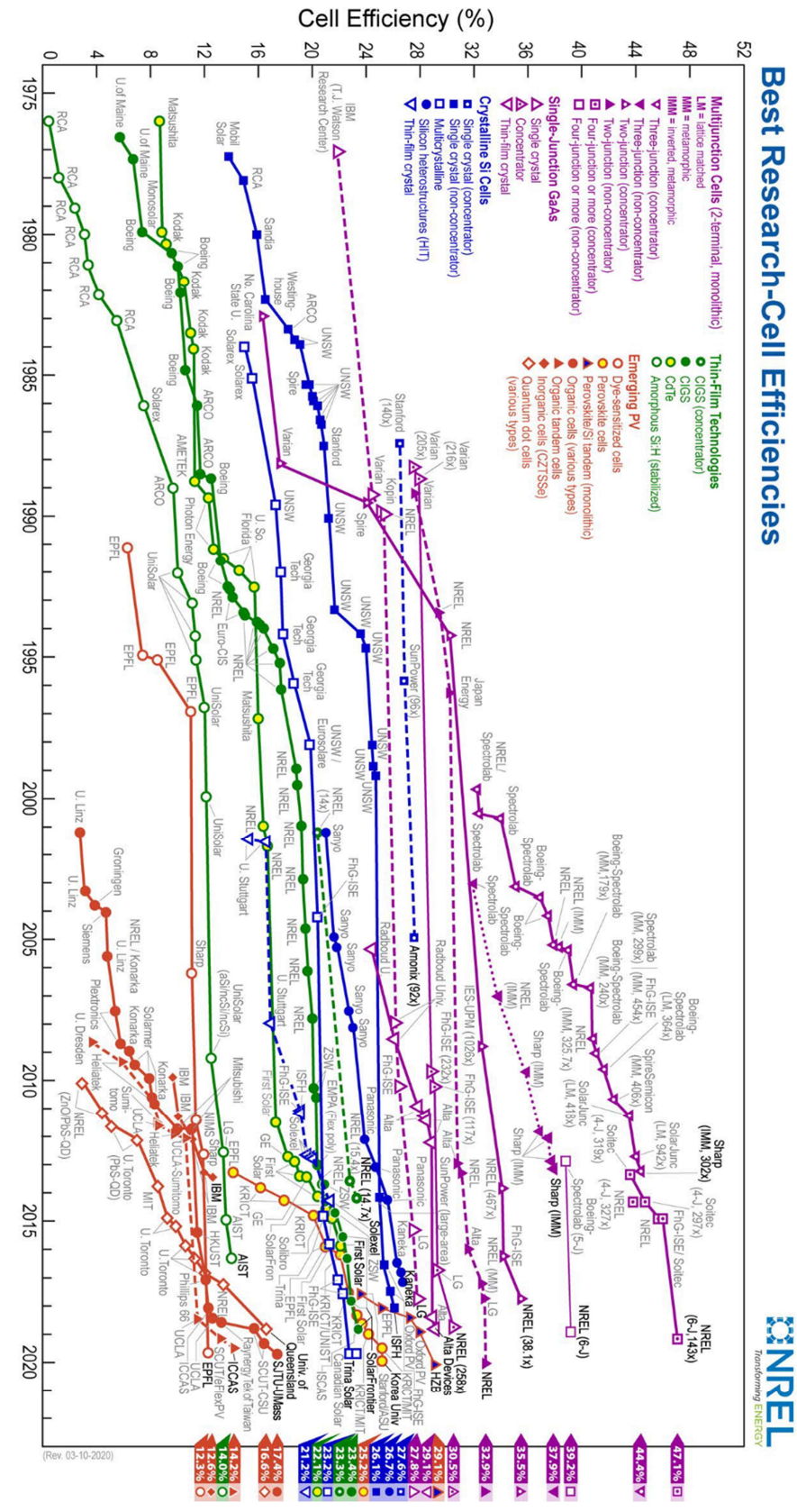

Figure 3.11 Best certified research solar cell efficiencies up to March 2020, provided by **NREL** (National Renewable Energy Laboratory)

3.2.1 Perovskite solar cells

The name Perovskite describes a class of materials with the chemical formula ABX_3 and a crystal structure as shown in Figure 3.12, that was initially derived from the mineral calcium titanate, $CaTiO_3$ (see Figure 3.12 a). This mineral was discovered in the Ural mountains in Russia by Gustav Rose in 1839 and it has been named in honor of the Russian mineralogist Count Lev Alekseevich Perovski.[29] In calcium titanate, the A site is a Ca^{2+} ion in the body center of a cubic lattice of the B site, which are Ti^{4+} ions, that are themselves surrounded by octahedra of O^{2-} ions in the X site.

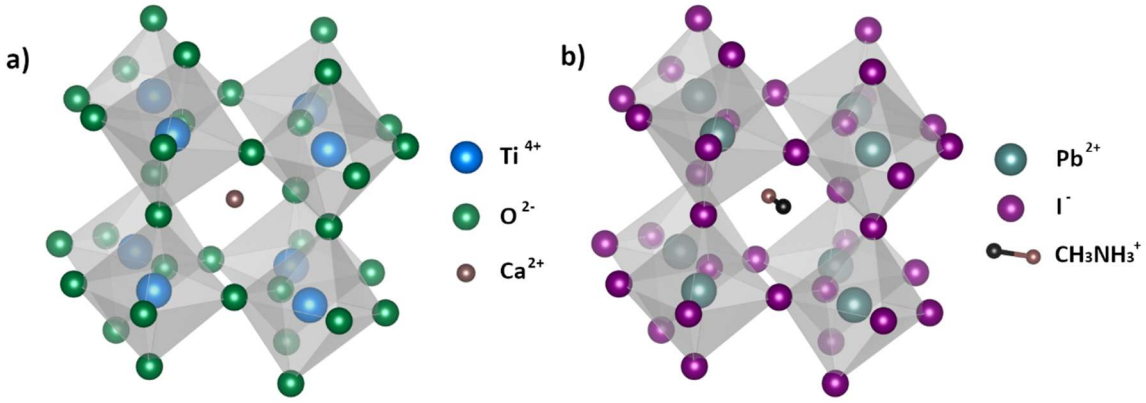

Figure 3.12 ABX_3 perovskite unit cells: **a)** calcium titanate ($CaTiO_3$) and **b)** methyl ammonium lead iodide ($CH_3NH_3PbI_3$) Visual representation created with VESTA, adapted from CIF data [30]

Organic-inorganic hybrid perovskites have been first considered as novel semiconductor materials by Mitzi et al. in 1994, in their search for high-T_c superconductors.[31] In these halide perovskites, an organic cation sits on the A site of the ABX_3 perovskite structure (e.g. $CH_3NH_3^+$) surrounded by a cubic lattice of a metallic cation (e.g. Pb^{2+}) in the B site, which are themselves surrounded by octahedra of a halide (e.g. I^-) as shown in Figure 3.12 b).

Almost two centuries later, these halide based perovskite materials are widely used in high tech devices like solar cells,[32, 33] LEDs,[34, 35] transistors,[36, 37] or sensors, like scintillators,[38, 39] or humidity sensors.[40] Miyasaka and his co-workers were the first to report results on perovskite

solar cells in 2006,[41] by using the organic-inorganic metal halide material $CH_3NH_3PbBr_3$ embedded in a mesoporous TiO_2 scaffold layer, which was historically utilized as an electron transport material (ETM) in Grätzel's dye-sensitized solar cells (DSSCs).[42] At that time, perovskite solar cells were using an organic electrolyte containing lithium halide as the hole contact material (HCM), reaching a power conversion efficiency of 2,2%. In 2009 Miyasaka and his group replaced the bromide part of the perovskite with iodide and increased the efficiency to 3,8 %.[43] In 2011, Park and his co-workers could optimize the perovskite solar cells, reaching an efficiency of 6.5 %.[44] The problem remained that the perovskite dissolved in the HCM electrolyte, with rapid degradation of the material. In 2012, Park, Grätzel and colleagues replaced the problematic liquid electrolyte with the solid hole transport material (HTM) spiro-MeOTAD (2,2',7,7'-tetrakis(N,N-di-p-methoxyphenylamine)-9,9'-spirobifluorene), which was commonly used in LEDs,[45] to produce the first all-solid perovskite solar cell, which reached an efficiency of 9,7 %. Since then, the efficiency of laboratory scaled perovskite solar cells grew unprecedently fast compared to other technologies, with the current record held by a group at the Korea University with a 25,2 % efficiency (see. Figure 3.11). The current record for a perovskite/Si tandem solar cell, which may potentially produce efficiencies beyond the Shockley-Queisser limit is held by the Helmholtz-Zentrum Berlin (HZB) with 29,1%. To date, there are over 9000 publications on perovskite solar cells with an ever increasing research interest over the years (see Figure 3.13).

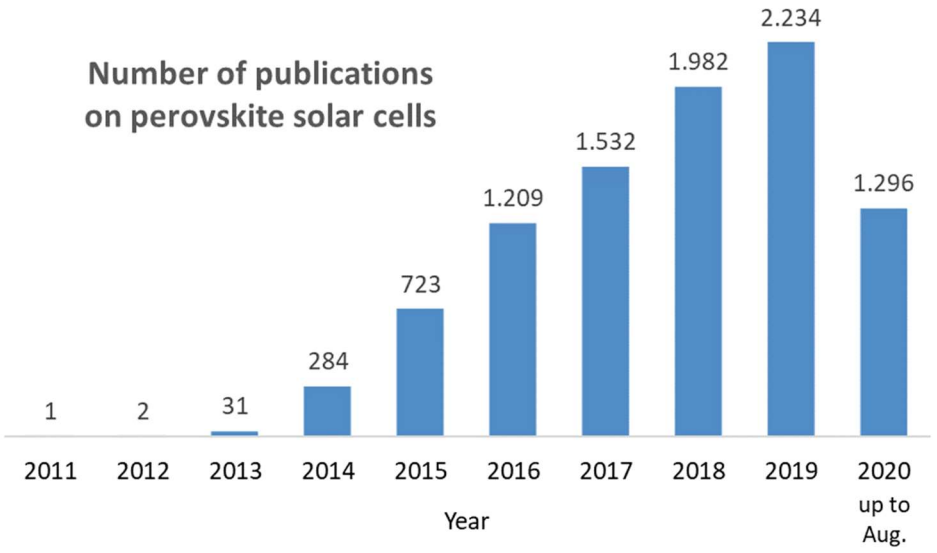

Figure 3.13 Number of publications on perovskite solar cells with data gathered from the Web of Science Core Collection. The number of publications add up to 9294 until Aug. 2020

A classical architecture of a perovskite solar cell can be seen in Figure 3.14. This solar cell uses the absorber perovskite material methylammonium lead iodide ($CH_3NH_3^+ Pb^{2+} I^-_3$, MAPI), sandwiched between the ETM: TiO_2 and the HTM: spiro-MeOTAD, with FTO (fluorine doped tin oxide, F : SnO_2) as the front contact and gold (Au) as the back contact. The mesoporous titania layer (m-TiO_2) is an optional layer, that is used in the spin coating process, because the spreading of a liquid on a rough, porous surface works better than on a smooth, compact one. According to theory, the solution infiltrates the pores of the m-TiO_2 through capillary forces.[44] After the solvent evaporates, a high contact area between the MAPI and the m-TiO_2 allows a proper transport of the electrons. On the other hand, if the MAPI material is mostly defect free, having a high mean free path of the charge carriers, a compact titania layer (c-TiO_2) with proper band properties should suffice in transporting the electrons and blocking the holes.

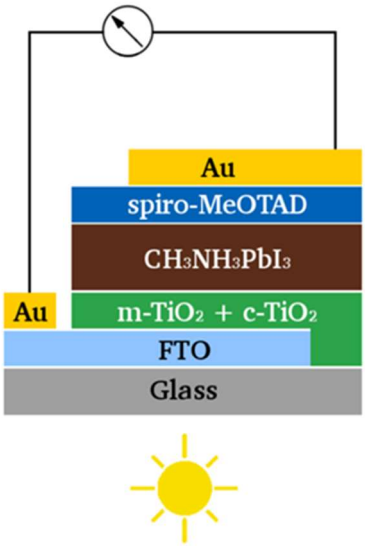

Figure 3.14 Classical architecture of a perovskite solar cell

Figure 3.15 illustrates the working principles of perovskite solar cells. There are two alternative architectures that can be used in a principle consideration when building perovskite solar cells, a p-i-n configuration and an n-i-p configuration. In the p-i-n configuration, the intrinsic perovskite material is sandwiched between the p-type HTM, that is deposited directly on the substrate, and the n-type ETM which is placed on top of the perovskite. In the n-i-p configuration, the n-type material is first deposited on the substrate and the p-type material is deposited on top of the intrinsic perovskite. Either version can be employed, depending on the materials used, their properties and their deposition methods.

In the band diagrams from Figure 3.15, light with a high enough energy that can overcome the band gap of the perovskite absorber can excite electrons from its valence band to its conduction band. The electrons are transferred to the energetic lower conduction band of the ETM, being blocked by the high energy LUMO of the HTM, further being conducted by the TCO (transparent conductive oxide), respectively by the metal contact of the circuit. In turn, the holes that form in the perovskite's valence band by the excitation of the electrons are conducted to the HOMO of the HTM and blocked by the deep laying valence band of the ETM.

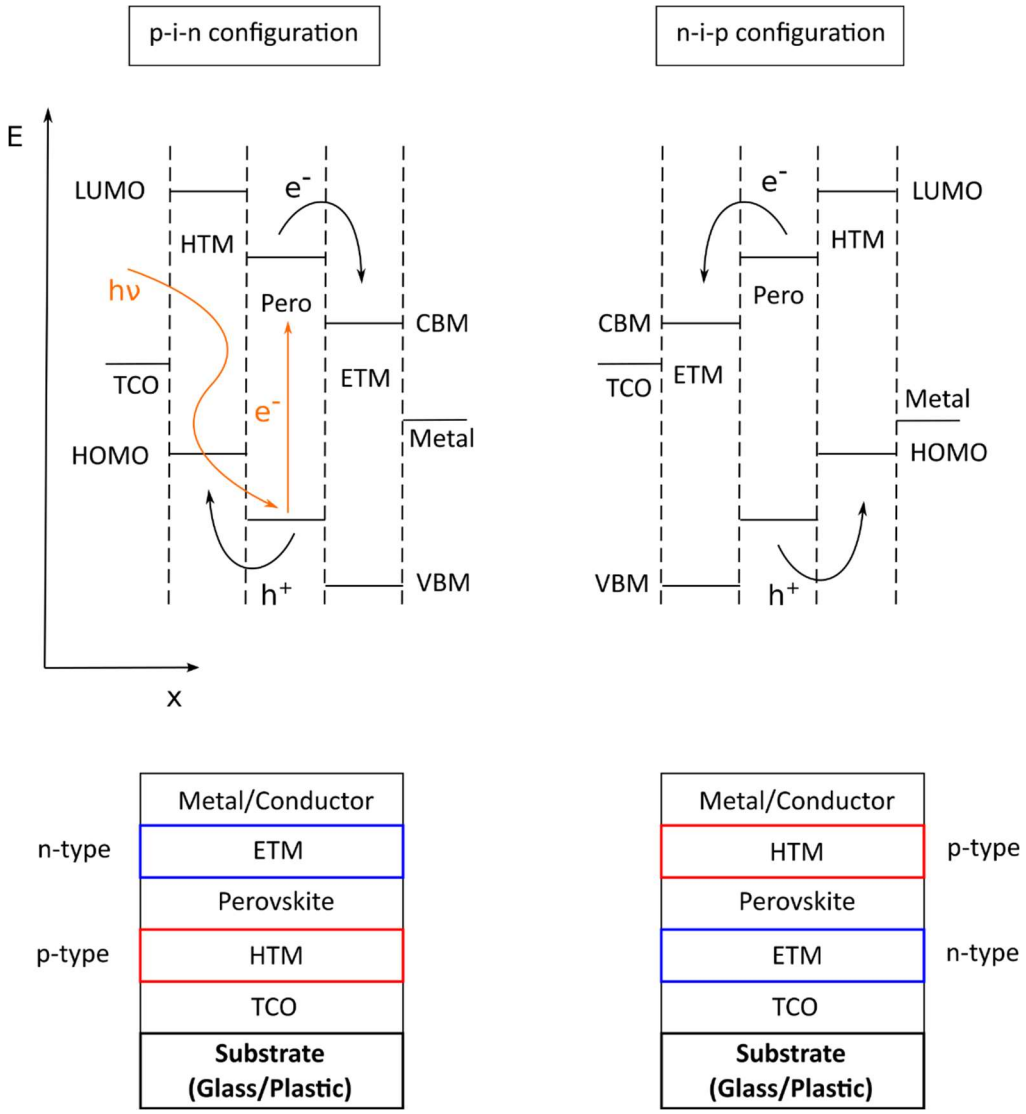

Figure 3.15 Band diagrams and architectures of the p-i-n and n-i-p configurations of perovskite solar cells. **LUMO:** lowest unoccupied molecular orbital. **HOMO:** highest occupied molecular orbital. **TCO:** transparent conductive oxide. **HTM:** hole transport material. **ETM:** electron transport material. **CBM:** conduction band minima. **VBM:** valence band maxima

A number of different perovskites with varying opto-electronic properties have been synthesized and used as the absorber layer in solar cells. Besides the most popular perovskite methylammonium lead iodide (MAPI, $CH_3NH_3PbI_3$),[46, 47] alternatives that replace the iodide with bromide,[48, 49] or chloride[50, 51] are used, as well as combinations of these halides, e.g. $CH_3NH_3PbBr_xI_{3-x}$, for which the width of the band gap can be tuned depending on the ratio of bromide and iodide.[52, 53] Colorful perovskite solar cells like yellow, orange, red, or brown can

be achieved in this way. The organic part methylammonium (MA, $CH_3NH_3^+$) can be replaced with other organic molecules like formamidinium (FA, $CH_5N_2^+$),[54, 55] or guanidinium (G, $C(NH_2)_3^+$),[56, 57] but also with inorganic components like caesium (Cs).[58, 59] Researchers go as far as combining several different organic and inorganic cations and halide anions into a mixed perovskite, like a quadruple cation, double anion lead perovskite containing MA^+, FA^+, Cs^+, K^+, I^- and Br^-, $K_xCs_{0.05}(FA_{0.85}MA_{0.15})_{0.95}Pb(I_{0.85}Br_{0.15})_3$, labeled KCsFAMA, which targets efficiency, as well as stability.[60]

Concerns over human- and ecotoxicity of lead (Pb^{2+}) contained in most solar cell perovskites used,[61] calls for a search for substitutes. MASI (methylammonium tin iodide, $CH_3NH_3SnI_3$) has been discussed as a possible non-toxic alternative in numerous publications.[62-64] However, new studies show that SnI_2, a possible decomposition material of MASI, has a higher aquatic toxicity for certain organisms than PbI_2.[64] Intakes of both Pb^{2+} and Sn^{2+} compounds have negative effects on human health. [61, 65] An advantage of tin based perovskites is their lower band gap which would allow a higher maximum theoretical efficiency compared to their lead counterpart. Efforts in this direction have been made by Noel et al.,[62] who achieved a PCE of 6.4 % using MASI as an absorber. The best-known efficiency with lead-free perovskite solar cells has been achieved by Shao et al.,[66] who used FASI (formamidinium tin iodide, $CH_5N_2SnI_3$), reaching a PCE of 9%. The challenge with tin based perovskites is their chemical instability in atmospheric conditions, where they can easily decompose. [62, 67, 68]

One big advantage of perovskite solar cells is their low projected Levelized Cost of Electricity (LCoE). According to the European Perovskite Initiative (EPKI, Whitepaper Sep. 2019), “Perovskite PV modules can be produced within a cost range of 20 Euro-cent/Wp in the coming 5 to 10 years and could go down further towards 10 and maybe even to 4 Euro-cent/Wp, depending on the learning curve and actual efficiency values of the scaled perovskite PV modules.” In comparison, according to a study by Fraunhofer ISE from 2018 entitled “Levelized Cost of Electricity – Renewable Energy Technologies”, the specific system cost of PVs today lies between 60 Euro-cent/Wp and 1,4 Euro/Wp, primarily depending on the type of plants. Perovskite solar cells could dramatically lower the cost of electricity produced by photovoltaic systems.

Another advantage of perovskite solar cells over conventional solar cell technologies is their ability to be manufactured on flexible and lightweight substrates, instead of rigid glass. Applications of flexible solar cells would be building integration, wearables, portable devices, or vehicle integration. A number of flexible substrate types are currently used in research for the fabrication of perovskite solar cells, like Corning's borosilicate Willow Glass,[69, 70] CPI (colorless polyimide),[71] PEN (polyethylene naphthalate),[72, 73] or PET (poly(ethylene terephthalate)).[74, 75] Willow Glass and CPI, although more costly, can withstand a higher processing temperature than PEN, or PET. Suitable ETL materials that would replace the widely used TiO_2, which needs a high temperature of up to 450°C to reach the needed anatase modification, would be buckminsterfullerene (C_{60}),[76, 77] zinc oxide (ZnO),[78-80] or tin oxide (SnO_2).[81-83] More cost effective and promising alternatives to the most expensive part of PSCs, the HTL spiro-MeOTAD, are PEDOT:PSS (poly(3,4-ethylenedioxythiophene) polystyrene sulfonate),[84-86] PTAA (poly(triaryl amine)),[87-89] or the inorganic alternative nickel oxide (NiO_x).[90-92] Depending on the regular n-i-p (used in this work), or inverted p-i-n architecture, several material alternatives are available for the front and back contact electrodes, instead of the FTO and gold (Au) combination used in this work, like carbon black (C),[93-95] nickel (Ni) mesh,[96, 97] silver (Ag),[98, 99] or graphene (C).[73, 100, 101] Promising up-scalable processing techniques for the production of PSCs are slot-die coating,[102, 103] inkjet printing,[11, 104] physical vapor deposition (PVD),[105, 106] or chemical vapor deposition (CVD).[107, 108]

Commercial companies working on the emerging perovskite solar cell technology already exist, like Oxford PV, Infinity PV, Solliance, Saule Technologies, Greatcell Energy, Solaronix, Lightyear, Solibro, Meyer Burger, or Power Roll to name a few.

3.3 Methods of characterization

This chapter describes the fundamentals of all relevant characterization methods and devices used in this work.

3.3.1 Electrical characterization of solar cells

An ideal solar cell can be described with an equivalent circuit diagram, as shown in Figure 3.16 **a)**. For a more realistic representation, in addition to the diode D_1 and the photocurrent j_{ph}, symbolized here by a current source, two resistances must be considered, a parallel resistance (R_p) and a series resistance (R_s) as shown in Figure 3.16 **b)**. Physically, these correspond to short circuits that lead to premature recombination of the charged carriers, respectively to ohmic resistances that occur in the contacts.

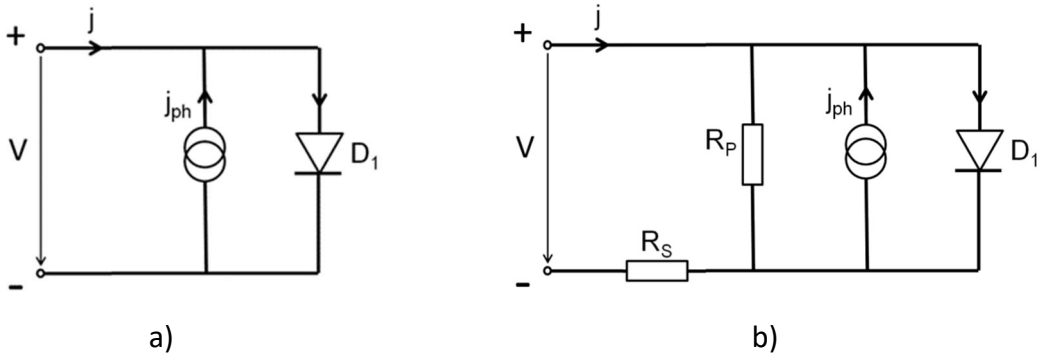

Figure 3.16 Equivalent circuits of a solar cell **a)** ideal circuit and **b)** a more realistic representation including the parallel resistance R_p and the series resistance R_s

For this more realistic representation of a solar cell as shown in Figure 3.16 **b)** the current density *j(V)* of a solar cell depending on the voltage is given by Figure 3.5, where j_{Ph} is the photocurrent density, j_0 is the reverse saturation current of the diode, R_s is the series resistance, V the voltage, k_B is Boltzmann's constant, T for Temperature and R_p is the parallel resistance.

Equation 3.5 $$j(V) = j_{ph} - j_0\, e^{\frac{V + R_S \cdot j(V)}{k_B T}} - 1 - \frac{V + R_S \cdot j(V)}{R_P}$$

By measuring the current-voltage curve of a solar cell, essential parameters can be determined. Figure 3.17 shows typical curves of an ideal solar cell under dark and under illumination. The dark curve follows the diode Equation 3.2. Zooming into the curve near the x-axis, a negative current unveils, given by the thermal excitation of the charge carriers at room temperature which excites some electrons to the conduction band, generating a small current flow. By illuminating the solar cell, the curve shifts to negative values with the amount of the photovoltage j_{Ph} according to Equation 3.3.

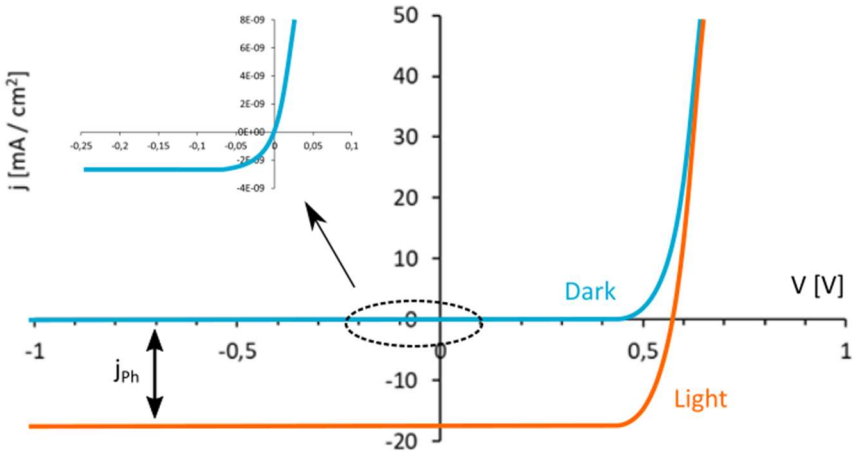

Figure 3.17 Linear plot of the characteristic current-voltage curves of an ideal solar cell at room temperature in dark and under illumination

Solar cell parameters can be read from a semi-logarithmic plot of the current-voltage curves as shown in Figure 3.18. The open circuit voltage V_{OC} and the short circuit current density j_{SC} can be read directly from the intersection with the axis, as in the linear plot from Figure 3.17 V_{OC} = $V(j=0)$ and $j_{SC} = j(V=0)$. The value of the reverse saturation current j_0 of the diode can only be obtained from the semi-logarithmic plot, by extrapolating a straight line for small positive voltages on the y-axis for the dark curve and reading out the current at V = 0 V. The series resistance R_S and the parallel resistance R_P of unideal solar cells can be easily determined from

the semi-logarithmic plot by choosing voltage and current density pairs at high, resp. low voltages in the linear region and dividing them by each other according to $R = U / I$.

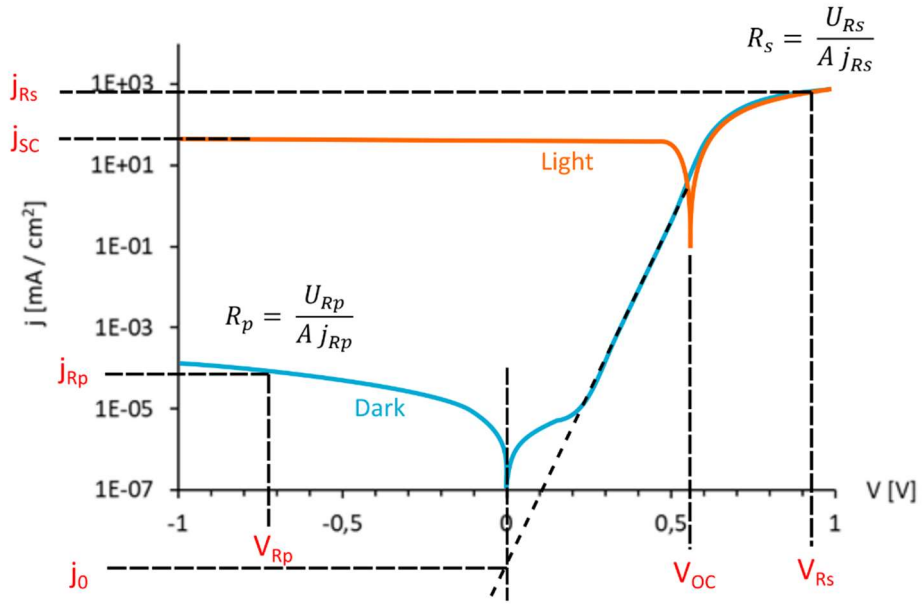

Figure 3.18 Characteristic values and semi-logarithmic plot of the current-voltage curves of a solar cell at room temperature in dark and under illumination

For an easier readability, a linear plot of the IV-curve can be mirrored from currents with negative values from the fourth quadrant (see Figure 3.17), into the first quadrant of the coordinate system as shown in Figure 3.19, to have currents with positive values. Figure 3.19 also contains a power curve P plotted against the voltage V, calculated from current and voltage pairs from the IV-curve according to $P = U \cdot I$. The maximum value of the $P(V)$ curve is called the maximum power point (MPP) of the solar cell. A solar cell should operate at its V_{MPP} and I_{MPP} for a maximum power output.

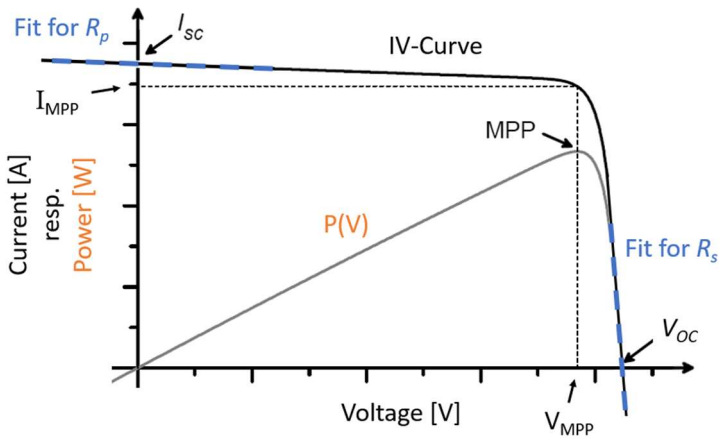

Figure 3.19 Current-voltage and power curves with characteristic solar cell parameters

The Fill Factor (*FF*) of a solar cell is the ratio of the maximum obtainable power (MPP) to its product of its maximum current density (short circuit current density j_{SC}) and its maximum voltage (open circuit voltage V_{OC}), as shown by Equation 3.6. The *FF* is a parameter for measuring and comparing the performance of solar cells and for assessing the "squareness" of the IV-curve.

Equation 3.6 $$FF = \frac{j_{MPP}\, V_{MPP}}{j_{SC}\, V_{OC}} = \frac{MPP}{j_{SC}\, V_{OC}}$$

For calculating the efficiency η of a solar cell (Equation 3.7), its output power $P_{electrical}$, equal to the MPP, is divided by the input power $P_{optical}$ of the illuminating light, which for an easy comparison between solar cells is defined as a standardized 1 Sun = 1000 W / m^2.

Equation 3.7 $$\eta = \frac{P_{electrical}}{P_{optical}} = \frac{MPP}{1000\ {}^{W}/_{m^2}} = \frac{FF\, j_{SC}\, V_{OC}}{1000\ {}^{W}/_{m^2}}$$

A schematic draft of the solar simulator used in this work can be seen in Figure 3.20. It is built by LOT Quantum Design, model LSH102, manufacturing date July 1990, using a USHIO UXL-150SO-Xenon lamp and an AM1.5G (air mass, global) filter.

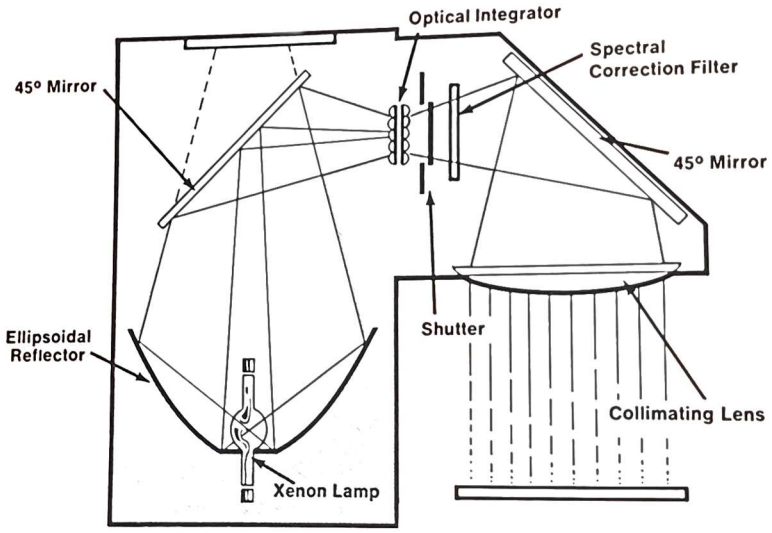

Figure 3.20 Schematic draft of the LOT Quantum Design LSH102 solar simulator setup

Source: manual of the device

In Figure 3.21, the solar simulator illuminates a bolometer calibration device (model CM 11, Kipp & Zonen Holland), which absorbs the irradiance of the incoming rays in an array of thermistors. The bolometer is used to calibrate the light intensity of the solar simulator to 840 W/m^2, by tuning the power of the lamp to 300 W $\pm$ 20 W. In this way, the solar simulator spectrum matches an AM1.5G spectrum in the range of the band gap of our perovskite solar cells. This calibration method is adopted from the company Antec, that used this solar simulator setup in the past to measure CdTe solar cells, having a similar band gap to the MAPI perovskite. The current and voltage characteristics of the cells are measured with a Keithley 2400 digital multimeter, by scanning the cells in a forward and backward direction from -0.2 V to 1.2 V in 0.1 V/s steps. Before each measurement, a quick voltage sweep was applied in dark conditions, ranging from -1 V to 1.5 V. The voltage sweep is applied to fill potential deep trap states that may occur in the materials due to defects. The efficiency of the solar cells is measured using a maximum power point tracking (MPPT) protocol, independent of the measurement of the IV curves of the devices. The exact J_{SC} and V_{OC} values are also measured separately and are not calculated from the IV curves of the respective devices.

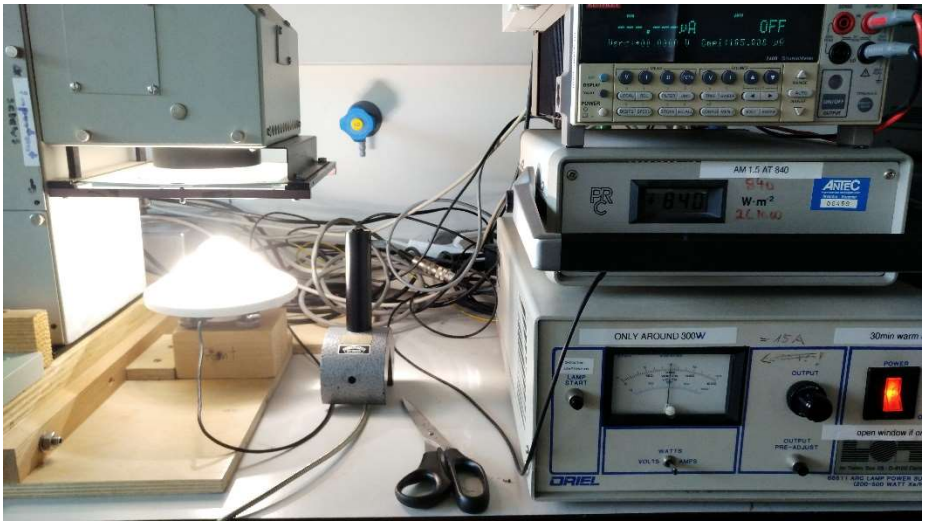

Figure 3.21 Solar simulator illuminating a bolometer calibration device

3.3.2 UV/Vis absorption spectroscopy

For measuring the band gaps of the materials applied in solar cells, a UV/Vis absorption spectroscopy method has been employed, using a Perkin Elmer Lambda 900, which has an Ulbricht sphere that was calibrated using barium(II)sulfate ($BaSO_4$) in a total reflection approach. A schematic drawing of the setup can be seen in Figure 3.22.

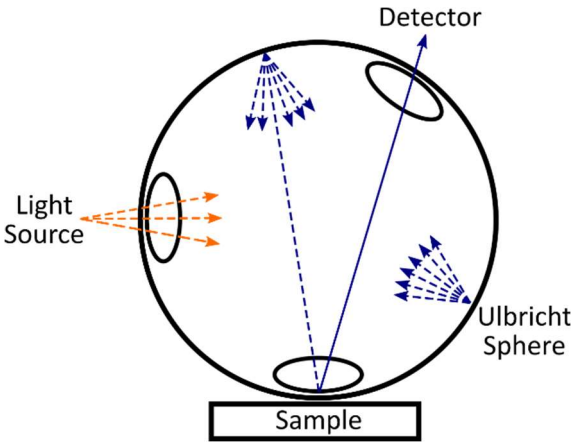

Figure 3.22 Schematic drawing of the UV/Vis absorption spectroscopy setup, featuring an Ulbricht sphere

In this setup, the light from the source is reflected inside the Ulbricht sphere. When light rays hit the sample, part of its energy is absorbed, while another part is reflected. In this setup, it can be assumed that no light is transmitted through the sample. The difference between the initial light intensity from the source, I_0 and the reflected light intensity inside the Ulbricht sphere, R is the absorbed intensity by the sample, A as shown by Equation 3.8.

$$A = I_0 - R \qquad \text{Equation 3.8}$$

As soon as the energy of the monochromatized light source surpasses the energy of the band gap of the material, the light will be absorbed. Since the light source can be set to distinct wavelengths with the help of a monochromator, the sample's band gap will control the absorption onset in an absorption vs. wavelength graph, as illustrated in Figure 3.23.

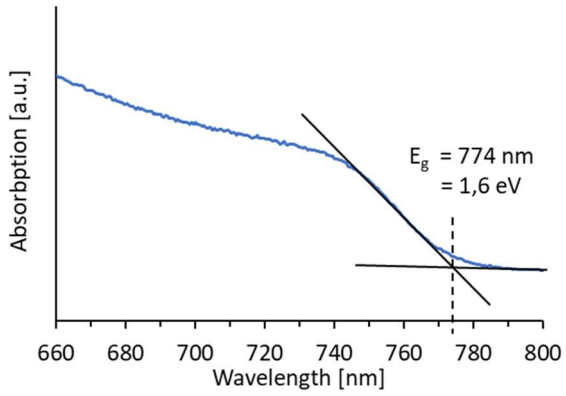

Figure 3.23 Example of a UV/Vis spectra with a linear fit in the onset region of the absorption and readout of the band gap E_g

3.3.3 Photoluminescence spectroscopy (PL)

Photoluminescence is emission of light from any form of matter after the absorption of photons. In this work, a Varian Cary Eclipse setup has been used to measure the photoluminescence of perovskite materials. By assessing the luminescence, the approximate band gap of a material can be determined and compared to UV/Vis absorption spectroscopy measurements.

By illuminating the material, electrons are excited from the valence band to the conduction band. The energetic values of photoluminescence photons in a semiconductor are usually somewhat smaller than the actual band gap of the material, because once excited into the conduction band, electrons can relax into shallow defect states right below the CB and from there recombine with holes in the VB, emitting photons with a smaller energy than the band gap. The intensity of light emitted by the excited material is recorded with respect to the wavelength.

A schematic of the photoluminescence setup is shown in Figure 3.24. The light intensity from the source of the setup can be adjusted through a variable slit of 5, 10, 15, or 20 nm. The bigger the opening of the slit, the more light will shine on the substrate and the more intense the photoluminescence will be. The slit should be adjusted between higher values to be able to produce a measurable amount of PL photons and lower values, for measuring below the saturation of the detector. The device has a variable monochromator that can be set to an excitation light of a fixed wavelength. A photograph depicting a perovskite sample that is illuminated with 480 nm can be seen in Figure 3.25. The device has manually interchangeable emission filter windows that transmit photons with wavelengths larger than their respective specification, e.g. >550 nm. The emission filter windows are used to block reflections that come from the excitation light. After the photoluminescence light passes through another adjustable slit, it can be detected by photodiodes with respect to its wavelength.

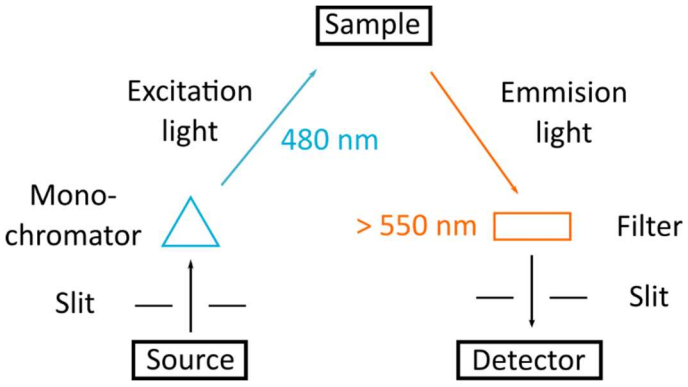

Figure 3.24 Schematic drawing of the photoluminescence setup used in this work with an example excitation wavelength of 480 nm and an example emission filter of >550 nm

Figure 3.25 Perovskite sample being illuminated by light of 480 nm in the Varian Cary Eclipse photoluminescence spectroscope

Figure 3.26 shows a typical photoluminescence spectrum of a methylammonium lead iodide sample with settings as shown in Figure 3.24 and as measured in Figure 3.25. The maximum of this spectrum is at 771 nm = 1,61 eV, which is close to the literature band gap of MAPI of 1,60 eV.[26, 109]

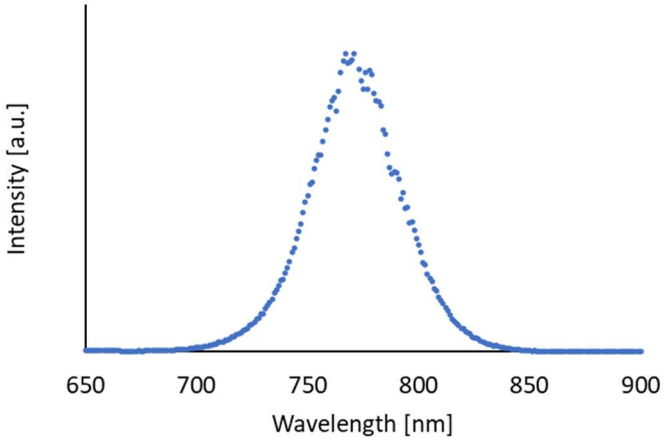

Figure 3.26 Typical photoluminescence spectrum of a methylammonium lead iodide thin film with a maximum at 771 nm = 1,61 eV

3.3.4 Scanning electron microscopy (SEM)

With the help of a scanning electron microscope (SEM), the surface morphology of samples can be recorded in the µm to nm range. An SEM device uses a focused, narrow electron beam as a source, generated by a thermal field emission cathode, which has an energy in the range of 10 keV – 30 keV. The generated electrons pass a series of lenses and apertures, focusing on the surface of the sample (see Figure 3.27 Right). By using scan coils situated above the objective lens, the beam can raster (scan) the surface of the sample to reveal a larger area than the focused point. Measurements are carried out in a vacuum chamber to prevent perturbances from surrounding air molecules. Many signals are produced during the electron-sample interaction, coming from Auger electrons, secondary electrons (SE), backscattered electrons (BSE) or characteristic X-rays (see Figure 3.27 Left).

Elastic scattering occurs when primary electrons are deflected by the atomic nuclei of the sample, or by electrons in the valence shells. In this kind of interaction, there is a negligible kinetic energy loss during the collisions. Electrons that are elastically scattered in an angle larger than 90° are called back scattered electrons (BSE) and can be used to image the sample. The number of elastically scattered electrons increases with the atomic number of elements, so BSE electrons can result in an elemental contrast of the sample.

Depending on the acceleration voltage, the primary electrons from the source can penetrate the sample up to a few microns. In inelastic scattering, the primary electrons transfer energy to the electrons and atoms of the sample, under circumstances even degrading unstable materials. The primary beam can ionize atoms, leading to the generation of secondary electrons (SE), coming from a depth of 1 nm to 10 nm, which is dictated by their mean free path through the sample. SE can be picked up by an Everhart-Thornley detector and translated to a grayscale image that reveals the surface topology of the sample in a characteristic three-dimensional appearance.

In the energy-dispersive X-ray spectroscopy (EDS, or EDX), characteristic X-rays can provide chemical information from the surface of the sample. When a primary electron collides with an electron from an inner shell of on atom, displacing it, an electron from an outer shell can re-combine with the created hole, emitting a characteristic X-ray with an energy that is the difference between the two electronic states. The energy of the emitted X-rays is characteristic for the respective elements that are analyzed, giving information on the chemical composition of the surface of the sample up to 5 µm depth.

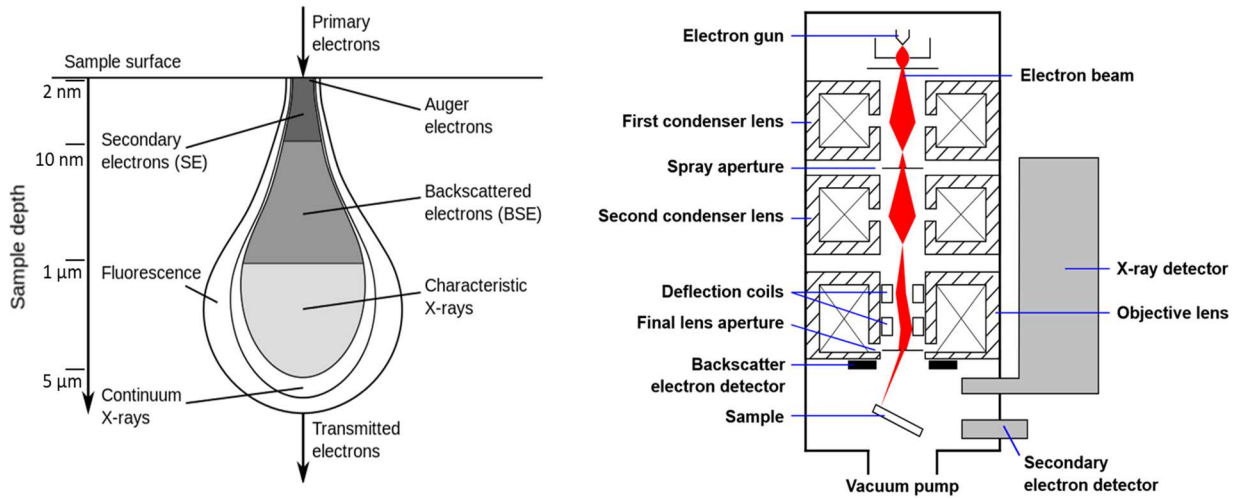

Figure 3.27 **Left:** Excitation volumes for excited species using a primary electron beam (Creative Commons 1.0 License, Wikimedia) **Right:** Schematics of a scanning electron microscope (SEM)

Creative Commons Attribution-Share Alike 1.0 Generic License, Wikimedia, Credit: Steff, modified by ARTE

For this work, an FEI/Philips model FEX XL 30 scanning electron microscope was used, that has a Schottky-type electron source. For recording clear images, parameters such as the acceleration voltage, spot size, focus, contrast & brightness, lens modulation, astigmatism, or scan speed can be varied.

In this work, the morphology of the surfaces of produced films have been analyzed using the SE detector. For measuring cross sections of the layers of the fabricated solar cells, the glass of the samples was broken in half and the sample was tilted in the sample holder of the SEM at 70° with the cross section facing towards the primary electron beam.

3.3.5 X-ray diffraction (XRD)

X-ray diffractometry (XRD) is a method for characterizing crystalline materials. It enables the determination of the crystal structure and if applicable the different phases present in a sample. The XRD method is based on the diffraction of X-rays on a crystal lattice as shown in Figure 3.28 on the left.

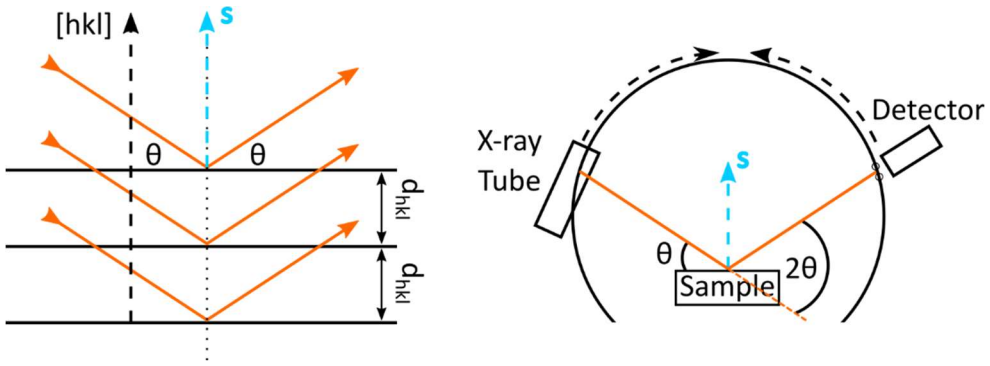

Figure 3.28 **Left:** Diffraction of X-rays on a crystal lattice. **Right:** Schematic of the Bragg-Brentano XRD geometry

When a monochromatic X-Ray beam with a wavelength in the range of the distance between the lattice planes hits the crystal, it gets diffracted by the electron clouds of the lattice atoms. These diffracted waves can interfere with each other constructively, or destructively. The radiation coming from constructive interferences can be measured by a detector. Whether constructive interference occurs, depends on the distance between the crystal planes and the angle of incidence of the X-ray beam and can be derived from the Bragg equation shown in Equation 3.9.

Equation 3.9 $$n \cdot \lambda = 2d_{hkl} \cdot \sin(\theta)$$

In this equation, λ is the wavelength of the incident radiation, d_{hkl} is the distance between the lattice planes, *hkl* being the Miller indices describing the planes of crystal (Bravais) lattices and θ is the incident angle of the beam on the lattice. For constructive interference to occur, the

optical path difference of the parallel incident X-rays, diffracted on parallel lattice planes should be an integer multiple *n* of the wavelength of the incident X-rays.

The X-ray diffraction patterns in this work were recorded on a Bruker D8 Advance in Bragg-Brentano geometry with Cu Kα radiation and a VANTEC detector. A schematic of the Bragg-Brentano geometry is shown in Figure 3.28 on the right. In this geometry, the diffraction vector *s* is always normal to the surface of the sample, bisecting the angle between the incident and the scattered beam. The incident angle θ is defined between the X-ray source beam and the sample. The diffraction angle, 2θ is defined between the incident beam and the detector. Both the X-ray tube (source) and the detector move on the so called goniometer circle, recording the constructive interference of the diffracted X-ray beams, by varying the diffraction angle.

3.3.6 X-ray photoelectron spectroscopy (XPS)

X-Ray Photoelectron Spectroscopy (XPS) was developed in the 1960s by Kai Siegbahn and his research group at the University of Uppsala in Sweden, at that time known as ESCA (Electron Spectroscopy for Chemical Analysis). In 1981 Siegbahn received the Nobel Prize in Physics for his work on the XPS technique.

In the surface analysis technique XPS, an X-ray is used to knock out electrons from the sample, their kinetic energy being detected. Usually X-ray sources like Mg Kα (1253,6 eV) and Al Kα (1486,6 eV) are used. The kinetic energy of the emitted electrons can be calculated by the Einstein relationship:

Equation 3.10 $$E_{Kin} = h\nu - BE - \phi_S + \Delta\phi$$

where E_{Kin} is the kinetic energy of an electron coming from the sample, *hv* is the photon energy of the X-rays, *BE* is the binding energy of the electron, ϕ_S is the sample work function and $\Delta\phi$ is the difference between the sample work function ϕ_S and the analyzer work function ϕ_A. Since the measured kinetic energy E'_{kin} contains the contact potential $\Delta\phi = \phi_S - \phi_A$,, the sample work

function ϕ_S in Equation 3.10 cancels out, while the analyzer work function is calibrated by referencing measurements, Equation 3.10 can be simplified to Equation 3.11:

Equation 3.11 $$BE = h\nu - E'_{Kin}$$

A photoelectron is created when an electron from an inner shell of an atom, e.g. K shell (1s orbital) is excited to reach the vacuum level and the atom is thus ionized, as Figure 3.29 Left illustrates. The binding energy can be regarded as the energy difference between the initial state and the final state after the photoelectron has left the atom. Since the X-ray photon energy *hv* is constant, by measuring the kinetic energy E_{Kin} of the electrons, the binding energy *BE* can be calculated. With help of the element specific binding energy *BE*, the chemical species in a sample and their surrounding atoms can be identified (chemical shift), since *BE* correlates to all electrostatic forces influencing an electron. For example, when comparing the two compounds lead(II)oxide and lead(II)selenide, although the lead cation is in the formal oxidation form 2+ in both cases, the binding energy for the Pb $4f_{7/2}$ in PbO is ca. 138,8 eV, while in PbSe it is ca. 137,5 eV.[110] Pauling's electronegativity for oxygen is 3,44, while for selenium it is smaller with 2,55. When an oxide anion attracts valence electrons of lead towards itself, the positive electrostatic force in the nucleus of lead becomes stronger on electrons in the inner shells (e.g. 4f orbital), resulting in a higher binding energy than in PbSe, where selenium is a more electropositive element. Thus, the related chemical shift in XPS measurements can be used to identify chemical compounds.

XPS measurements are surface sensitive with a depth of information in the order of 10 nm, because only photoelectrons which did not experience inelastic scattering (primary electrons) are used for analysis. This information depth depends on the mean free path of the photoelectrons, the distance they can travel without experiencing inelastic scattering, which is related to their kinetic energy.

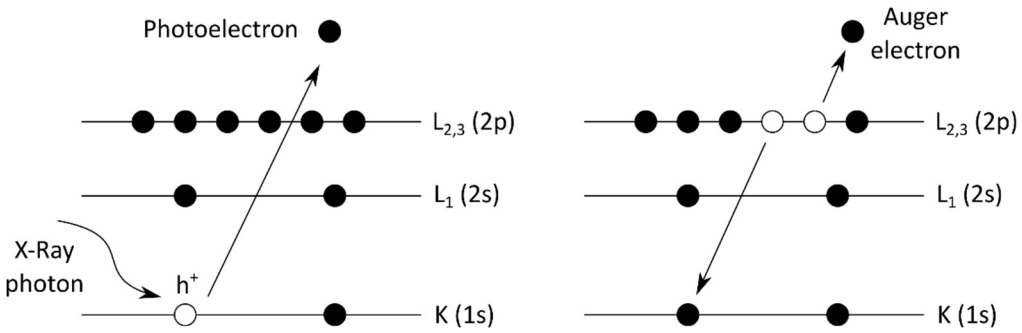

Figure 3.29 Principle of the creation of a photoelectron **(Left)** and of an Auger electron **(Right)**

In the photoemission process, another type of electrons can be emitted besides photoelectrons, so called Auger electrons (see Figure 3.29 Right). In the Auger process, an electron from a higher energetic shell can fill the hole created by the X-ray and the emission of a photoelectron from a lower energetic shell. Almost instantaneously, another electron from the same higher energetic shell is emitted as an Auger electron. The kinetic energy of the Auger electron is equal to the difference between the energy of the initial ion and the doubly charge final ion. Usually in photoionization, both a photoelectron and an Auger electron are emitted.

The spin-orbit coupling is a final state effect given by the electromagnetic interaction between an electron's magnetic dipole (spin), its orbital motion and the electrostatic field of the positively charged nucleus. This effect gives rise to a splitting of the spectral lines for electrons that leave behind holes in orbitals with an orbital angular momentum l different than 0 (for p, d, f orbitals, $l_p = 1$, $l_d = 2$, $l_f = 3$). With an electron having a spin $s = \pm ½$, the total angular momentum j can have two distinct results $j = l \pm ½$. The two emission lines corresponding to the two states, will have an intensity ratio $(2j+1)$, according to the degeneracy of states. Figure 3.30 shows an example for an XPS spectrum of electrons coming from the 3d orbital of iodine, where the electron from the left signal has a total angular momentum $j = 2 - ½ = 3/2$ and for the signal on the right $j = 2 + ½ = 5/2$.

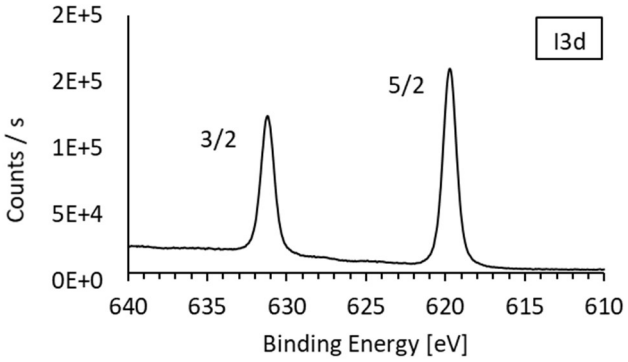

Figure 3.30 Typical XPS spectrum for an iodine species in methylammonium lead iodide ($CH_3NH_3PbI_3$) with spin-orbit splitting

The experiments of this work were carried using a ThermoFisher Scientific ESCALAB 250X XPS machine. Figure 3.31 illustrates the working principle of an XPS apparatus. After the electrons leave the sample due to the impact of the X-ray beam, they are focused by a set of electrostatic lenses and apertures into the concentric hemispherical analyzer. One hemisphere is charged positively, while the other is charged negatively and the electrons are deflected with the retardation voltage V_R to the pass energy E_{pass}. Only electrons that have a kinetic energy in the range of E_{pass} can pass through the analyzer and reach the channeltron detector array. All other electrons will fall onto the steel walls of the analyzer and will not be detected. Depending on the respective kinetic energy of the electrons, they will be detected by different channeltrons that are correspondingly spatially arranged and whose signals will be preamplified and sent to a signal processing unit.

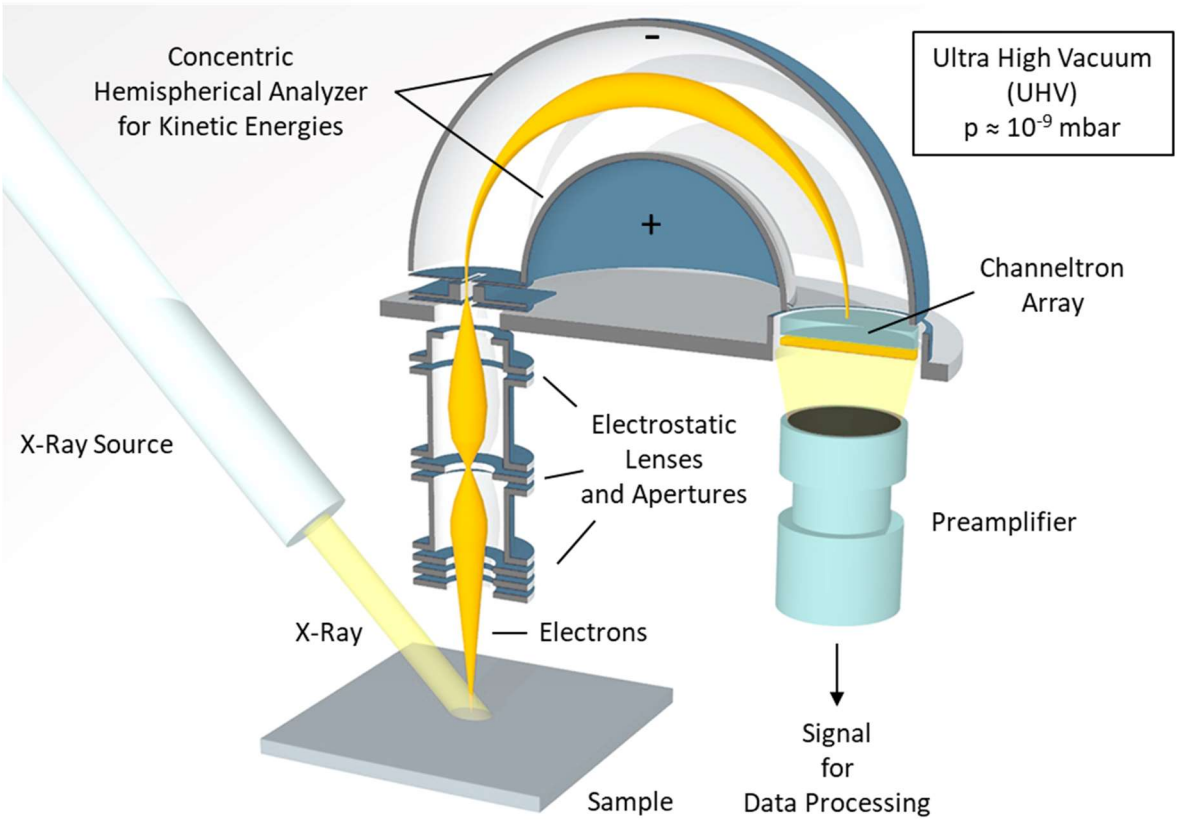

Figure 3.31 Schematic drawing of an X-Ray Photoelectron Spectrometer (XPS)

Graphic modified from a public domain image on Wikimedia

4. Experiments, results and discussion

4.1 Two-step process: spin coating and chemical bath

This chapter describes a reference process, including a detailed recipe for producing and subsequently measuring the performance of perovskite solar cells, as has been developed in a group effort in our Surface Science department.

The stack of materials for the reference solar cell can be seen in Figure 4.1. It comprises of Glass/FTO/c-TiO_2/m-TiO_2/MAPI/spiro-MeOTAD/Au.

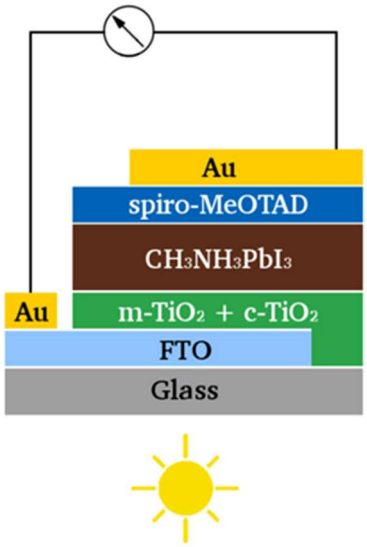

Figure 4.1 Material stack of a perovskite solar cell

The so called “two-step” approach refers to the production of the perovskite film, that uses the spin coating process in a first step and a chemical bath in a second step. The whole process for producing the solar cell uses four main production techniques: spray pyrolysis, spin coating, chemical bath and plasma sputter coating. These techniques will be shortly introduced in the following.

4.1.1 Experimental setup

Figure 4.2 shows a schematic draft of a spray pyrolysis setup and Figure 4.3 shows the actual setup used in this work, in a laboratory hood. In this process, a solution is pushed out of a nozzle by air pressure, being pulverized to an aerosol by a carrier gas. The spray reaches the substrates on a hot plate, the active substance being pyrolyzed to a thin film of the desired material. This technique is used to produce the compact titania layer (c-TiO_2) throughout this work.

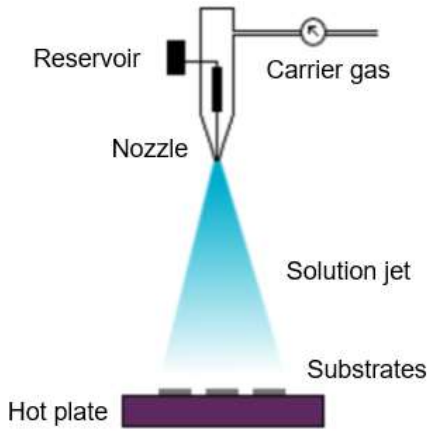

Figure 4.2 Schematics of a spray pyrolysis setup

Figure 4.3 Spray pyrolysis setup in a laboratory hood

Spin coating is a facile technique for producing thin films on a given substrate, from a solution. The stages of the spin coating process can be seen in Figure 4.4. In the first step, a solution of a desired material is pipetted onto a substrate. In a second step, the substrate is rotated for a set amount of time, at a given speed. The centrifugal force causes most of the solution to be expulsed from the surface of the substrate. In the third step, the remaining solution further spreads out across the substrate. In the fourth step, evaporation of the solvent occurs, leaving a solid film of the solvated material behind. This technique is being used to produce the m-TiO_2 layer, the PbI_2 layer (component of MAPI) and the spiro-MeOTAD layer throughout this work.

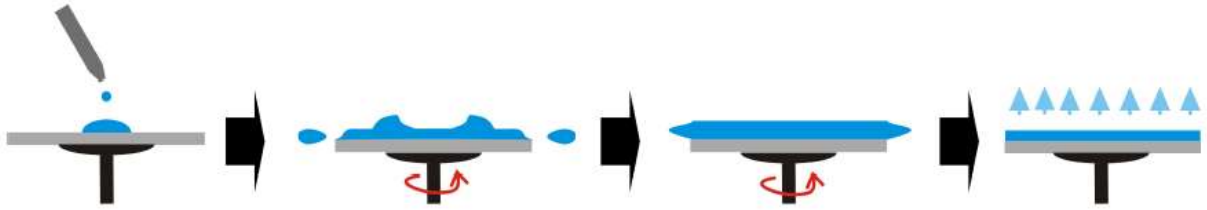

Figure 4.4 Schematic steps of the spin coating process

Graphic: public domain on Wikimedia

The spin coater device used in this work is shown in Figure 4.5. Since the device has been extensively used in our group with all sorts of materials, cleaning and thus wear of the device has been inevitable. To ensure a reproducible spinning speed and thus a reproducible layer thickness, a method for recalibrating the device is needed. For this purpose, a piece of adhesive tape is fixed to the rotating chuck, as seen in Figure 4.5. While spinning, the tape produces an audible feedback by hitting a hand-held spatula.

Figure 4.5 Spin coating device used in this work

Audio recordings of the cyclic event are captured with a smartphone, as shown in Figure 4.6. By tuning a potentiometer on the circuit board of the spin coater, the number of revolutions per second (rps) shown on the digital display of the device can be matched with that of the physical measurement.

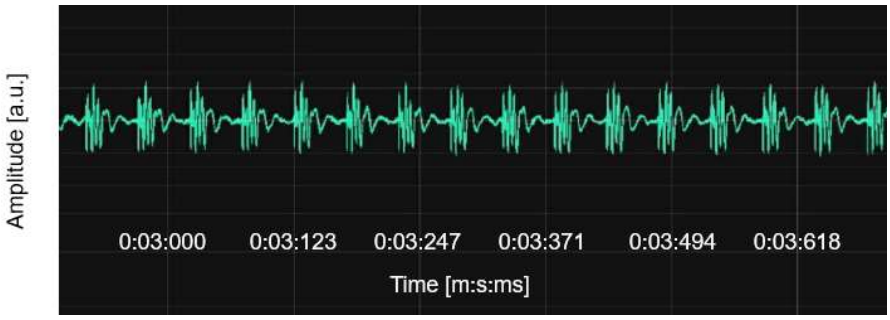

Figure 4.6 Audio feedback for the calibration of the spin coater's spinning speed of 22 rps; audio recording and plot made with the app WaveEditor for Android™

In the chemical bath process, a solution of MAI (methylammonium iodide, CH_3NH_3I) in 2-propanol, Figure 4.7 is poured onto the yellow spin coated PbI_2 layers, transforming them to MAPI perovskite ($CH_3NH_3PbI_3$), according to Equation 4.1. The brown MAPI perovskite is the light absorbing layer of the solar cell. Photographs of a PbI_2 covered substrate and of a substrate covered with MAPI after the MAI chemical bath are shown in Figure 4.8.

Figure 4.7 Chemical bath process for producing the MAPI ($CH_3NH_3PbI_3$) perovskite thin films in a glove-box. **Left**, the PbI_2 coated substrates in a Petri dish and a beaker with a solution of MAI (methylammonium iodide, CH_3NH_3I) in 2-propanol; **Right**, the reacted MAPI perovskite films after pouring the solution into the Petri dish

Equation 4.1 $PbI_2 + CH_3NH_3I \rightleftharpoons CH_3NH_3PbI_3$

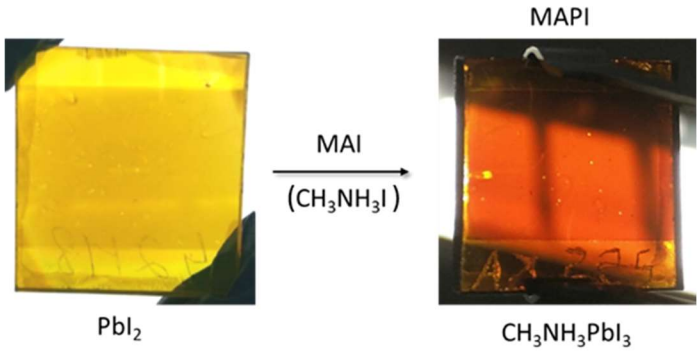

Figure 4.8 Glass/FTO/c-TiO_2/m-TiO_2 substrate covered with **left:** PbI_2 and **right:** MAPI perovskite ($CH_3NH_3PbI_3$)

In the plasma sputter coating process, Figure 4.9, a voltage and a current are applied, that ionize a sputtering gas, creating a plasma. The sputtering gas ions are directed towards a target, colliding with the material. Sputtered atoms are thus emitted and deposited onto a substrate as a thin film. Parameters like the sputtering current and time, define the thickness of the pro-

duced film. The plasma sputter coating device used in this work to deposit the gold (Au) layer can be seen in Figure 4.10.

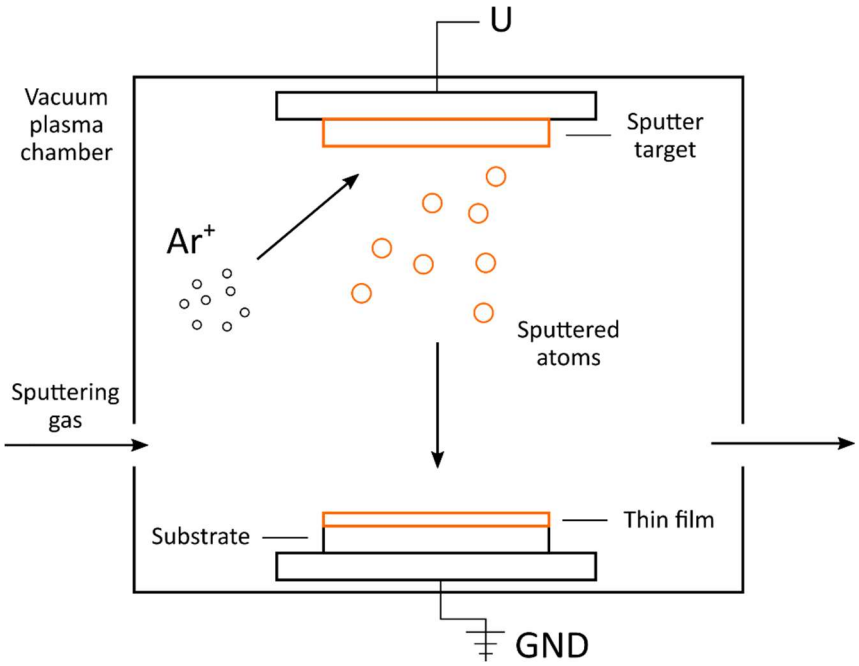

Figure 4.9 Schematic draft of the plasma sputter coating process

Figure 4.10 Plasma sputter coater - Quorum Technologies Q300TD, loaded with glass/FTO/c-TiO_2/m-TiO_2/MAPI/spiro-MeOTAD and metal masks

4.1.2 Architecture and recipe

This chapter describes a recipe used to produce MAPI perovskite solar cells in a “two-step” process, with details given for each layer from Figure 4.1 Material stack of a perovskite solar cell. Apart from the perovskite layer, all other contact layers are produced in the same way throughout this work.

A see-through image of a semi-transparent MAPI perovskite layer can be seen in Figure 4.11 left, having an orange/brown color. On the right, Figure 4.11 shows four substrates in a golden metal holder, each having four completed solar cells, which were made using the two-step spin coating and chemical bath deposition method.

Figure 4.11 **Left**: a see-through image of a substrate coated with MAPI perovskite; **Right**: four substrates in a metal holder, each having four completed solar cells

Figure 4.12 shows the dimensions of the substrate and the solar cells used in this work. A substrate is 2 x 2 cm^2 large, having 4 back contacts, which are defined by the gold layer and which are 3,25 x 10 mm^2 large. The dashed line is approximatly 3 mm away from the edge of the substrate and it delimits etched FTO, as explained in the following recipe.

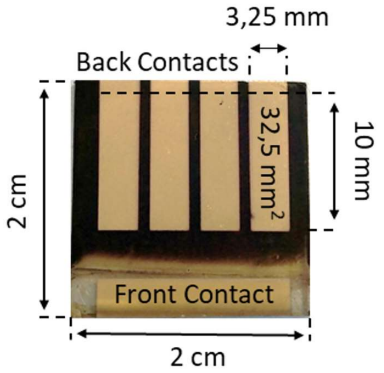

Figure 4.12 Substrate with four solar cells and physical dimensions

Glass coated with fluorine doped tin oxide (FTO): Pilkington NSG TEC15 FTO glass substrates have been used, cut as 2 cm x 2 cm squares, with a sheet resistance of 12-14 Ω/sq. and a glass thickness of 2.2 mm. From the edge of the substrate, 3 mm of the top FTO layer is removed to reveal glass, by etching it with zinc powder and a 6 M HCl solution, to later avoid short circuiting the front contact and the back contact, by piercing through all other layers with the pins of the solar simulator holder and risking to contact the FTO layer with both the plus and the minus pin. The substrates are cleaned with isopropanol, soap, tap water, distilled water and blown dry with a nitrogen gun.

c-TiO_2 layer: The compact TiO_2 layer is produced by spray pyrolysis on the glass/FTO substrates. 500 µL of titanium diisopropoxide bis(acetylacetonate), 75 wt. % in isopropanol (TIAA) from Merck is mixed with 18 mL reaction grade Ethanol. This solution is sprayed using oxygen carrier gas onto the glass/FTO substrates that have been treated for 5 min. in an oxygen plasma oven and heated to 450°C for 25 min. prior to deposition. During the spraying process the front contacts of the substrates are masked with a steel bar to avoid deposition of titania, leaving approximately 6 mm of Glass/FTO uncoated. After the spraying process the glass/FTO/c-TiO_2 substrates are annealed for 30 min. at 450°C in atmospheric conditions to form the desired anatase modification of titania.

m-TiO_2 layer: The mesoporous TiO_2 layer is deposited by spin coating 100 µL of a 1:7 weight ratio solution of 18NR-T Titania (TiO_2) paste from Greatcell Solar and reaction grade ethanol

onto each glass/FTO/c-TiO_2 substrates in atmospheric conditions. The solution is dropped onto a substrate, before spinning at 83 rps (revolutions per second) for 45 s. During the spin coating process, the front contacts of the substrates are masked with an adhesive tape to avoid deposition of titania. After drying for 10 min. at 70°C, an additional sintering step takes place for 45 min. at 450°C on a hot plate in atmospheric conditions.

PbI_2 layer: Prior to the deposition of the lead(II)iodide layer the glass/FTO/c-TiO_2/m-TiO_2 substrates are treated in a UV/ozone oven for 15 min. to clean off carbohydrate residues. The deposition takes place in a nitrogen (N_2) filled glovebox. After each substrate has been heated for 2 min. at 80°C on a hotplate, 100 µL of a 555 mg PbI_2 (Alfa Aesar 99.9985%, metal base) in 1 mL DMF (N,N-Dimethylformamide, Merck, 99.8%, anhydrous) solution, which has been stirred for at least half an hour at 80°C is dropped onto the hot substrates and then spun at 108 rps for 90 s. Each substrate is subsequently dried for 10 min. at 80°C.

MAPI layer: In a nitrogen glovebox, a solution of 400 mg methylammonium iodide (MAI, Greatcell Solar) and 40 mL anhydrous 2-propanol (99.5%, Merck) is stirred at 70°C until dissolved (forming a clear solution). After reaching room temperature, the solution is added to a Petri dish containing the glass/FTO/c-TiO_2/m-TiO_2/PbI_2 substrates. The substrates immediately turn from yellow to brown, see Figure 4.7. After 2 min. each substrate is rinsed in a clean 2-propanol bath of excess MAI and immediately blown dry with a pen blower. After additional drying on a hot plate for 15 min. at 50°C in the glovebox the substrates are annealed in a tube furnace, in atmospheric air for 20 min. at 120°C.

Spiro-MeOTAD layer: The deposition of the spiro-MeOTAD layer takes place on the glass/FTO/c-TiO_2/m-TiO_2/MAPI substrates in a nitrogen glovebox. 80 mg spiro-MeOTAD (Borun New Material, 99.9%) is mixed in 1 mL chlorobenzene (Merck, anhydrous, 99.8%) with 28.5 µL 4-tert-butylpyridine (Merck, 98%) and with 17.5 µL of a solution made from 260 mg Li-TFSI (bis(trifluoromethane)sulfonimide lithium salt, Merck, >99%) and 0.5 mL acetonitrile (Merck, anhydrous 99.8%). 100 µL of the resulted spiro-MeOTAD solution is dropped on a glass/FTO/c-

TiO_2/m-TiO_2/MAPI substrate. After a pause of 20 s it is spun at 23 rps for 30 s and left to dry at room temperature in the glovebox.

Gold layer: Before depositing the gold back contact layer, the front contact of the glass/FTO/c-TiO_2/m-TiO_2/MAPI/spiro-MeOTAD substrate is cleaned from the excess MAPI and spiro-MeOTAD material through rubbing off with a cotton swab, which was dipped in isopropanol, to reveal the glass/FTO layer, because no mask was used during the spin coating of the MAPI and spiro-MeOTAD layers. The gold (Au) layer is deposited by argon sputtering on top to the spiro-MeOTAD layer, in a Quorum Technologies Q300TD sputter coater machine with 30 mA current for 120 s using a steel mask for defining the contacts.

4.1.3 Results and discussion

Systematic optimizations of the two-step spin coating and chemical bath reference process have not been undertaken in the context of this work. This process was used to ensure the correct operation of all steps involved, which are also used in part for alternative processes, as well as for practical courses and demonstration purposes for bachelor and master students. Current-voltage performance data of solar cells made with the two-step process, for which obvious manufacturing, or measuring problems could be excluded, have been gathered in Appendix Table 9.1. A summary of the data is shown in Table 4.1. Out of 10 batches, having a total of 29 substrates and 113 cells, the average efficiency is 9 % with a standard deviation of 3,8 %. The average open circuit voltage is 1,01 V $\pm$ 0,09 and the average short circuit current is 161 A/m^2 $\pm$ 49. The average fill factor is 53 % $\pm$ 16. The best cell produced using the two-step method has an efficiency of 15.6 % with a V_{OC} of 1,08 V, a J_{SC} of 244 A/m^2 and a fill factor of 59 %. The IV-curve of this solar cell can be seen in Figure 4.13.

Table 4.1 Statistics of the performance of MAPI perovskite solar cells built using the two-step spin coating and chemical bath method. The complete set of data can be found in the Appendix Table 9.1

Nr. of	Batches 10	Substrates 29	Cells 113				
	Efficiency [%]	**V_{OC} [V]**	**J_{SC} [A/m^2]**	**FF**	**J_{WP} [A/m2]**	**V_{WP} [V]**	**MPP [W/m^2]**
Average	**9,0**	**1,01**	**161**	**0,53**	**131**	**0,66**	**90,3**
Sandard deviation	**3,8**	**0,09**	**49**	**0,16**	**49**	**0,13**	**38,3**
Best Cell	**15,6**	**1,08**	**244**	**0,59**	**212**	**0,74**	**155,8**

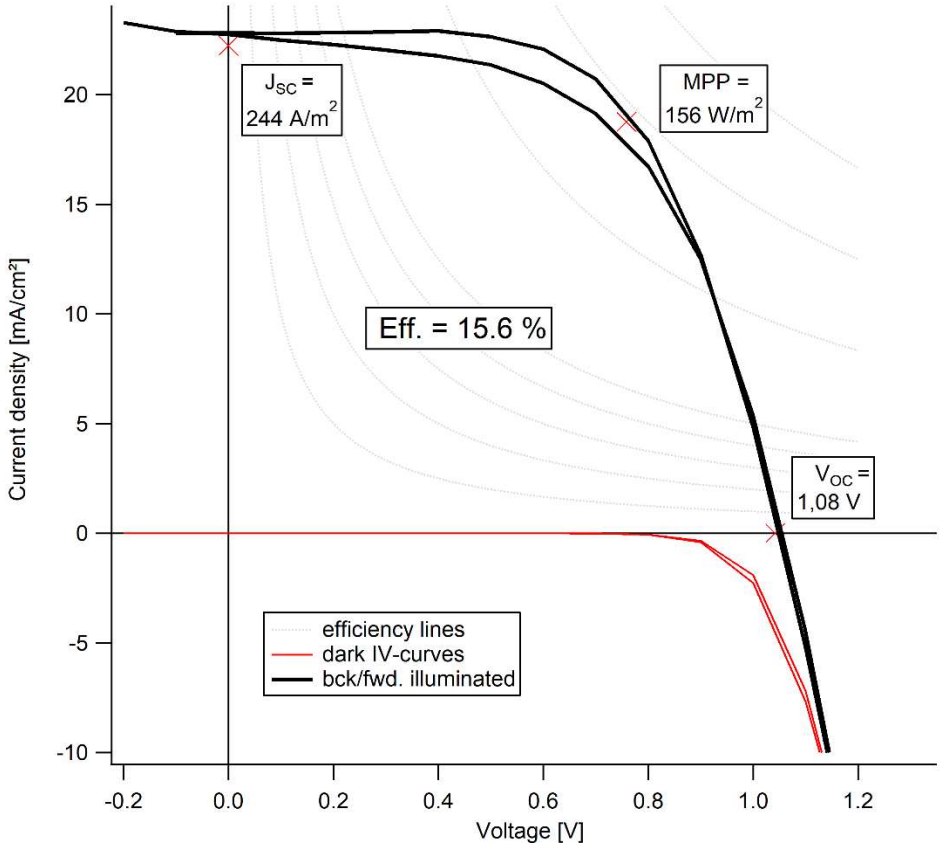

Figure 4.13 IV-curve of the best glass/FTO/c-TiO_2/m-TiO_2/MAPI/spiro-MeOTAD/Au cell produced using the two-step spin coating and chemical bath method

The large standard deviation for the efficiency of 3,8 % among 113 cells, reflects the high amount of manual work with many steps involved in producing functional solar cells, since even small changes can add up having a large effect on the outcome.

For example, one critical step for a visually uniform MAPI perovskite layer is the drying step after the chemical bath of MAI. The newly formed MAPI layers are rinsed in a bath of 2-propanol. The excess liquid on the surface of the substrates is blown off using a pen blower (Figure 4.14). The angle, the distance and the strength of the blow dictate the quality of the layer with visible ripples in the material, if done improperly. A solution to this problem would be a mechanical automation of this drying step.

Figure 4.14 Pen blower used to dry the MAPI layer after the 2-propanol bath

Another critical step in the formation of high quality perovskite layers is most likely the gas composition in the atmosphere of the nitrogen glovebox. When spin coating the solution of PbI_2 dissolved in DMF the atmosphere of the glovebox enriches with DMF vapor with increasing number of spin coated substrates. Since it is well known that DMF forms a coordinated complex with perovskites,[111, 112] its undefined quantity in the atmosphere of the glovebox when forming the MAPI perovskite layer can cause a variation in the quality of the films. A faster ventilation of the glovebox and a longer drying time for the PbI_2 layers would most likely give more homogeneous results.

A further limitation of the process is the cleanliness of the environment, as neither steps are carried out in clean rooms. Small dust particles can deposit onto the substrates at any point and produce defects in the layers. In Figure 4.15 (left), a transparent substrate with a Glass/FTO/c-TiO_2 layer can be seen, having small white dots that are visible with the naked eye. These particles could either be small titania crystallites that formed during the spray pyrolysis process, or dust particles that are deposited in the laboratory hood during the process. Small defects on the underlying layer will propagate and cause defects in the next layers, as Figure 4.15 (middle) shows. This is an image of a Glass/FTO/c-TiO_2/m-TiO_2/MAPI/spiro-MeOTAD layer under a microscope. The orange surface represents the MAPI perovskite having

diagonal lines from the liquid outflow of the spin coating process. The dark spots are most likely perovskite film defects, which form from material (dust) seeds during the formation of the crystal. Figure 4.15 (right) shows a MAPI substrate with a spin coated spiro-MeOTAD layer on top. Due to pointlike excess material, the spiro-MeOTAD layer is spin coated with a shadowing effect giving rise to material inhomogeneity that look like comet tails. A good practice to avoid dust depositions under the given conditions is blowing off the substrates with a gas stream after each deposition step and before beginning a new step.

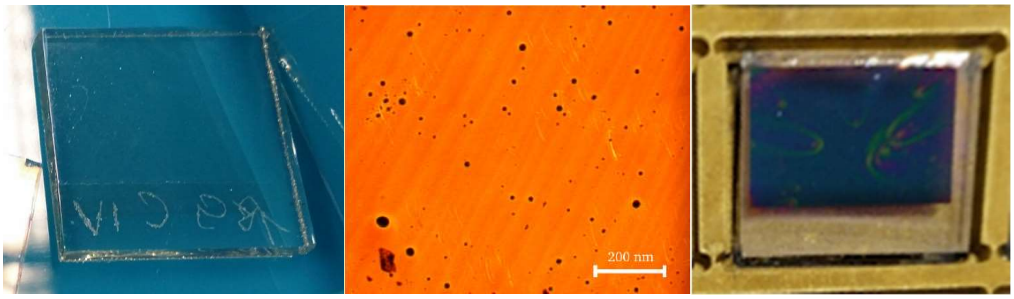

Figure 4.15 **Left**, a Glass/FTO/c-TiO_2 substrate with visible white spots. **Middle**, a Glass/FTO/c-TiO_2/m-TiO_2/MAPI/spiro-MeOTAD layer under an optical microscope. **Right**, a MAPI substrate after spin coating a spiro-MeOTAD layer on top

A different noteworthy issue concerns the performance measurement of the solar cells using the solar simulator. Theoretically, for an AM1.5G spectrum, an irradiance of 1000 W/m^2 should be used. We settled in our group to use a conservative irradiance of 840 W/m^2, this being an inherited knowledge from previous owners of our solar simulator. For the calculation of the efficiency of the solar cells, we still divide the power output of our solar cells by 1000 W/m^2 (1 sun), as Equation 3.7 shows (Page 41) . As the use of the 840 W/m^2 irradiance has not been made comprehensibly transparent, other than having the statement, that “for the band gap of 1,5 eV, the AM1.5G solar spectrum resembles that of the output of our solar simulator at 840 W/m^2”, spectral measurements have been carried out, unfortunately without a fruitful conclusion. To further test this statement, reference cadmium telluride and silicon solar cells as seen in Figure 4.16 have been sent to Fraunhofer ISE (Institute for Solar Energy Systems) for performance measurements with their equipment. Later, these cells have been measured with our solar simulator at an irradiance of 840 W/m^2 and 1000 W/m^2. The results can be seen in Table 4.2. The values show, that for the CdTe solar cells, measuring with an irradiance of 1000 W/m^2

at our solar simulator gives similar efficiencies as for the AM1.5G measurements by Fraunhofer ISE. The CdTe1 solar cell did not give reliable measurements and was declared broken. Given that the MAPI perovskite has a very similar band gap of 1,60 eV[26, 109] to CdTe (1,50 eV[113]), these results would mean that measuring with 1000 W/m^2 at our solar simulator would give correct results for our MAPI solar cells as well. For the silicon solar cell however, having a band gap of 1,12 eV[114], measuring with 1000 W/m^2 at our solar simulator would show a too high efficiency of 17,2 % instead of 15,7 %, as measured by Fraunhofer ISE.

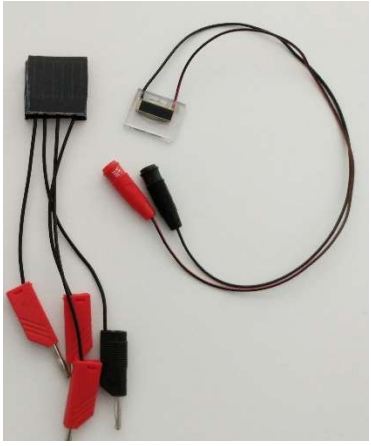

Figure 4.16 **Left**, 3 cadmium telluride (CdTe) solar cells in a module with connectors. **Right**, a silicon (Si) solar cell with connectors

Table 4.2 Comparison of the performances of cadmiun telluride (CdTe) and silicon (Si) solar cells from Figure 4.16, measured with AM1.5G settings by Fraunhofer ISE and measured at our solar simulator setup with an irradiance of 840 W/m^2 and 1000 W/m^2

Fraunhofer	Efficiency [%]	J_{sc} [mA/cm^2]	V_{oc} [V]
CdTe 1	12,2	24,0	0,79
CdTe 2	12,4	24,0	0,79
CdTe 3	11,6	23,4	0,78
Si	15,7	36,5	0,63

840 W/m^2	Efficiency [%]	J_{sc} [mA/cm^2]	V_{oc} [V]
CdTe 1	-	-	-
CdTe 2	11,1	22,5	0,77
CdTe 3	9,7	21,5	0,76
Si	14,3	37,7	0,60

1000 W/m^2	Efficiency [%]	J_{sc} [mA/cm^2]	V_{oc} [V]
CdTe 1	-	-	-
CdTe 2	12,4	26,9	0,77
CdTe 3	11,3	26,3	0,76
Si	17,2	42,7	0,61

A batch has been produced with the standard settings of the two-step process, but this time the cells have been measured with an irradiance of 1000 W/m^2 instead of the usual 840 W/m^2. The complete set of data for the produced solar cells can be seen in Appendix Table 9.2. With this irradiance value, the best solar cell produced shows an efficiency of 17.0 % (Figure 4.17), instead of the best cell produced and measured with 840 W/m^2, having 15,6 % (Figure 4.13).

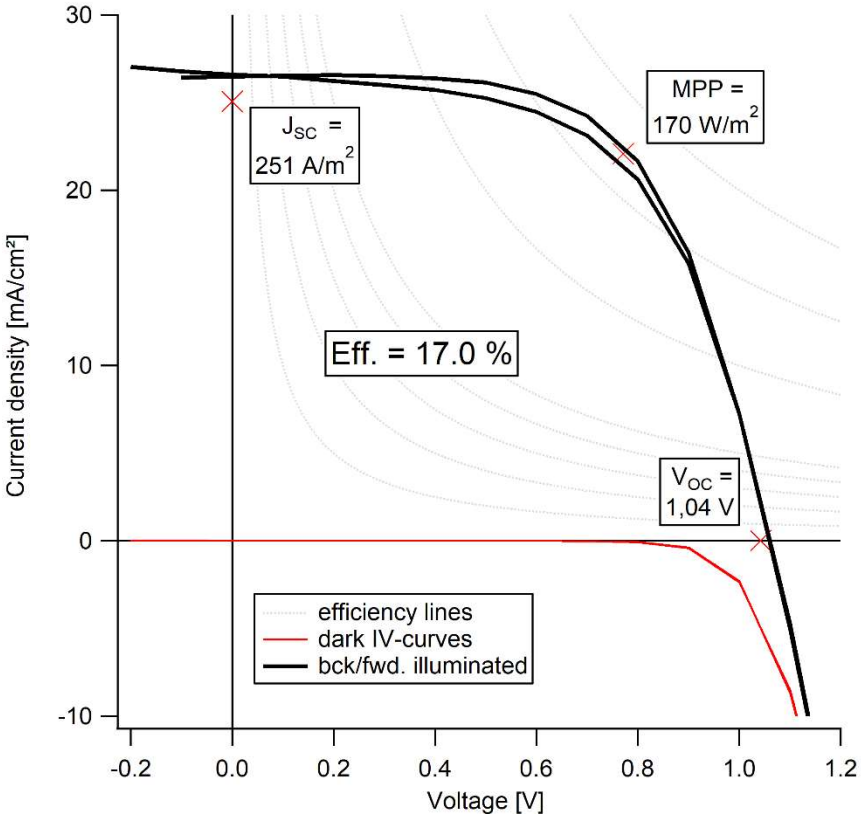

Figure 4.17 IV-curve of the best glass/FTO/c-TiO_2/m-TiO_2/MAPI/spiro-MeOTAD/Au cell produced using the two-step spin coating and chemical bath method, measured with 1000 W/m^2 with the solar simulator shown in Figure 3.20 and Figure 3.21

Nonetheless, all other solar cell performance values in this work have been recorded with the conservative irradiance of 840 W/m^2, still dividing the power by 1000 W/m^2 for obtaining the efficiency, as shows, so that we could have relative comparisons with all other historical results in our group.

4.2 One-step spin coating process

The following experiments of the one-step spin coating process have been conducted in close cooperation with Marco Melzi d'Eril, who wrote his Advanced Research Lab thesis in our Surface Science group on this topic under the author's supervision.

The one-step spin coating method refers to the processing of the perovskite layer, which is spin coated from one solution containing all the needed organic and inorganic components to form the perovskite dissolved in a mixture of solvents. This method has been employed to test how well the procedures used by our group for fabricating the solar cell devices compare to literature values. For this purpose, a recipe and method used in the publication entitled "How to Make over 20% Efficient Perovskite Solar Cells in Regular (n–i–p) and Inverted (p–i–n) Architectures" by M. Saliba et al.[1] for producing the perovskite layer has been adapted to the equipment in our labs. The procedures for all other layers (i.e. ETM, HTM, metal contact) and the performance measuring method have been kept the same as those used in the reference two-step spin coating and chemical bath process by our group, as described in Chapter 4.1.2.

The perovskite material used in the paper[1] is a mixed perovskite, that uses quadruple cations (Rb^+, Cs^+, MA^+ and FA^+) and double anions (Br^- and I^-) with a Pb^{2+} metal cation, having the chemical formula $(Cs_aRb_bMA_cFA_d)_1PbI_xBr_{3-x}$, in short called CsRbMAFA. The architecture of the solar cell is shown in Figure 4.18.

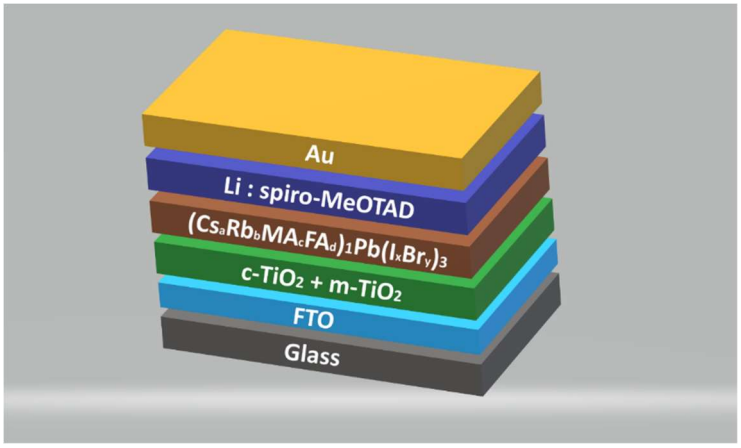

Figure 4.18 Material stack of a quadruple cations, double anions lead perovskite solar cell, produced by the one-step spin coating process

4.2.1 Recipe

The following recipe can be used to spin coat the CsRbMAFA perovskite. All steps occur in a nitrogen glovebox:

A solvent mixture of 4 mL DMF and 1 mL DMSO is made (**DMF/DMSO**).

The **PbI_2 stock solution** contains 1.5 g PbI_2 and 2,169 mL DMF/DMSO.

The **$PbBr_2$ stock solution** is made from 0,5 g $PbBr_2$ and 0,908 mL DMF/DMSO.

For the **$FAPbI_3$ stock solution**, 0,177 g FAI are mixed with 0,833 mL PbI_2 stock solution.

The **$MAPbBr_3$ stock solution** is made from 0,023 g MAI and 0,167 mL $PbBr_2$.

The **CsI stock solution** contains 0,1 g CsI and 0,256 mL DMSO.

The **RbI stock solution** contains 0,1 g RbI and 0,314 mL DMF/DMSO.

Mixing the $FAPbI_3$ stock solution with the $MAPbBr_3$ solution will give a **MAFA stock solution.**

Mixing 50 µL CsI stock solution in the MAFA stock solution will give a **CsMAFA final solution**, that can be spin coated. Optionally, 50 µL of the RbI stock solution can be added to the CsMAFA final solution to produce a **CsRbMAFA final solution**.

Prior to the deposition of the perovskite layer, the glass/FTO/c-TiO_2/m-TiO_2 substrates are treated in a UV/ozone oven for 15 min. In a nitrogen glovebox, 100 µL CsMAFA, or CsRbMAFA are dropped onto a Glass/FTO/c-TiO_2/m-TiO_2 substrate. After an initial spin-coating at 17 rps for 10 s, the substrate is spinned for another 20 s at 100 rps. 5 s before the end, 200 µL chlorobenzene as an antisolvent is dropped in the middle of the substrate at the correct dropping speed. The chlorobenzene interacts with the DMF/DMSO solvent mixture, quickly removing it from the substrate, while being an antisolvent to the perovskite layer. The exact mechanism of perovskite crystallization with the help of the antisolvent is still under discussion.[115, 116] According to the paper,[1] dropping the antisolvent too fast will result in an uncoated perovskite hole in the middle of the substrate, while dropping too slowly will result in cracks in the film. Removing the solvent vapor by force-purging the glovebox with a continuous flow of nitrogen during the spin coating process ensures reproducible performance results. Subsequently, the perovskite coated substrates are annealed at 100°C for 40 min. on a hot plate in the glovebox.

4.2.2 Results and discussion

Figure 4.19 is a photograph of four substrates, each having four completed CsRbMAFA solar cells that were produced by the one-step spin coating method.

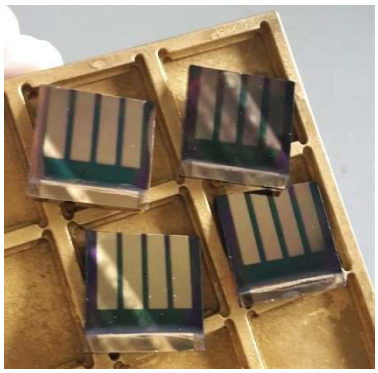

Figure 4.19 Photograph of four substrates on top of a golden metal holder, each having four solar cells produced by the one-step spin coating method

Current-voltage performance data of solar cells made with the one-step spin coating process, for which obvious manufacturing, or measuring problems could be excluded, have been gathered in Appendix Table 9.3. A summary of the data is shown in Table 4.3. Out of 5 batches, having a total of 20 substrates and 80 cells, the average efficiency is 12,7 % with a standard deviation of 2,91 %. The average open circuit voltage is 1,11 V $\pm$ 0,02 and the average short circuit current is 230 A/m^2 $\pm$ 25. The average fill factor is 49 % $\pm$ 9. The best CsRbMAFA solar cell produced using the one-step method has an efficiency of 18,0 % with a V_{OC} of 1,08 V, a J_{SC} of 264 A/m^2 and a fill factor of 63 %.

Table 4.3 Statistics of the performance of CsRbMAFA perovskite solar cells built using the one-step spin coating method. The complete set of data can be found in the Appendix

Nr. of	Batches 5	Substrates 20	Cells 80				
	Efficiency [%]	**V_{OC} [V]**	**J_{SC} [A/m^2]**	**FF**	**J_{WP} [A/m2]**	**V_{WP} [V]**	**MPP [W/m^2]**
Average	**12,7**	**1,11**	**230,0**	**0,49**	**176,3**	**0,72**	**127,1**
Sandard deviation	**2,91**	**0,02**	**24,93**	**0,09**	**31,80**	**0,07**	**29,10**
Best Cell	**18,0**	**1,08**	**264,3**	**0,63**	**227,1**	**0,79**	**180,1**

The paper[1] discusses that adding the RbI stock solution to the CsMAFA solution is optional. A batch has been made that excludes the rubidium component from the perovskite composition. The performance results of this batch can be seen in Table 4.4. The sample abbreviations l, ml, mr, and r refer to the four cells on a substrate, left, middle left, middle right and right, when the front contact is facing upwards. Out of 2 substrates and 8 cells, the average efficiency is 15,5 % with a standard deviation of 1,82 %. The average open circuit voltage is 1,07 V $\pm$ 0,03 and the average short circuit current is 238 A/m^2 $\pm$ 10. The average fill factor is 61 % $\pm$ 5.

Table 4.4 Performance data of CsMAFA perovskite solar cells built using the one-step spin coating method

Sample	Efficiency [%]	V_{OC} [V]	J_{SC} [A/m^2]	FF	J_{WP} [A/m2]	V_{WP} [V]	MPP [W/m^2]
1_l	15,4	-	-	-	219,6	-	153,7
1_ml	16,8	1,11	246,9	0,62	214,4	0,79	168,5
1_mr	15,0	1,08	231,5	0,60	201,8	0,74	149,6
1_r	15,7	1,06	227,6	0,65	200,0	0,78	156,5
2_l	15,0	1,06	238,0	0,59	209,3	0,72	150,2
2_ml	18,4	1,11	257,6	0,65	222,5	0,83	184,5
2_mr	11,6	1,01	230,6	0,50	163,5	0,71	115,9
2_r	16,0	1,08	232,3	0,64	189,3	0,85	160,3

Nr. of	Batches	Substrates	Cells
	1	2	8

	Efficiency [%]	V_{OC} [V]	J_{SC} [A/m^2]	FF	J_{WP} [A/m2]	V_{WP} [V]	MPP [W/m^2]
Average	**15,5**	**1,07**	**237,8**	**0,61**	**202,6**	**0,77**	**154,9**
Sandard deviation	**1,82**	**0,03**	**10,01**	**0,05**	**17,97**	**0,05**	**18,25**
Best Cell	**18,4**	**1,11**	**257,6**	**0,65**	**222,5**	**0,83**	**184,5**

The best CsMAFA solar cell produced using the one-step method has an efficiency of 18,45 % with a V_{OC} of 1,11 V, a J_{SC} of 257,6 A/m^2 and a fill factor of 65 %. The IV-curve of this solar cell can be seen in Figure 4.20.

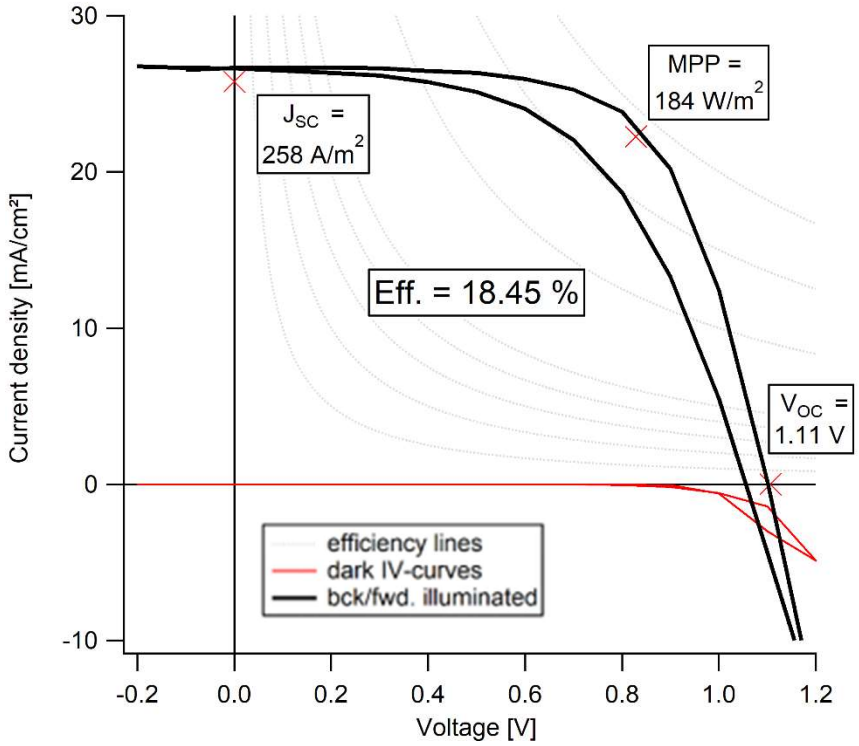

Figure 4.20 IV-curve of the best glass/FTO/c-TiO_2/m-TiO_2/CsMAFA/spiro-MeOTAD/Au cell produced using the one-step spin coating method

From these results it would seem that using the CsMAFA solution gives better results (15,5 % average efficiency) compared to using the CsRbMAFA solution (12,7 % average efficiency). However, comparing only 8 cells vs. 80 cells respectively is not representative. It can well be that by fabricating the CsMAFA solar cells at a later date than the CsRbMAFA solar cells the manual practice has improved.

The 20% efficiency for the one-step spin coating method could not be reached in our laboratory, as the title of the studied paper suggests.[1] Considering that our procedure of measuring the performance of the solar cells at the solar simulator uses a conservative irradiance of 840 W/m^2, instead of 1000 W/m^2, as discussed in Chapter 4.1.3, the 18,45 % efficient solar cell could have theoretically reached the 20 % mark, if measured with the latter irradiance value.

4.3 Flash evaporation process

As a first non-liquid process, the flash evaporation technique has been chosen to produce thin films of perovskites. This process is technically interesting due to its potential scalability. In the flash evaporation process, the perovskite material is brought onto the substrate in one step. In theory, by quickly heating the source “in a flash”, the material should sublimate stoichiometrically, far from thermodynamic evaporation equilibrium without decomposing into its constituents. The flash evaporation technique has been successfully proven to produce functional perovskite solar cells by Longo et al., who used MAPI prepared from the solvent DMF (dimethylformamide), reaching an efficiency of 12.2%.[117] In this work, a novel solvent-free approach has been tested, that uses different perovskites prepared by mechanochemical synthesis, flash evaporating them from their solid form.

4.3.1 Experimental setup

The custom-built flash evaporator device, shown in Figure 4.21, comprises of a glass cross with multiple KF-flanges. It can be evacuated with the help of a rotary vane pump to about $5 \cdot 10^{-3}$ mbar. The flash evaporator features a 4 cm^2 x 0.05 mm thin tantalum foil that can heat up the source material (i.e. perovskite powder) to high temperatures in a few seconds. The tantalum foil is fixed by two copper clamps, through which an adjustable alternating current with a maximum of 80 A and a constant voltage of 1 V can be passed. A temperature profile in dependence of the set electrical power is shown in Figure 4.22. The temperature has been measured by fixing a K-type thermocouple on the tantalum foil, in air. The temperature for the evacuated setup should be somewhat higher. For the height adjustable top part, the substrate can be brought into its holder by a drawer-like mechanism. Inside the glass cross, between the source and the substrate holder, a glass ring loosely limits the volume of evaporation, so that the material vapor is constrained mostly in this portion of the flash evaporator.

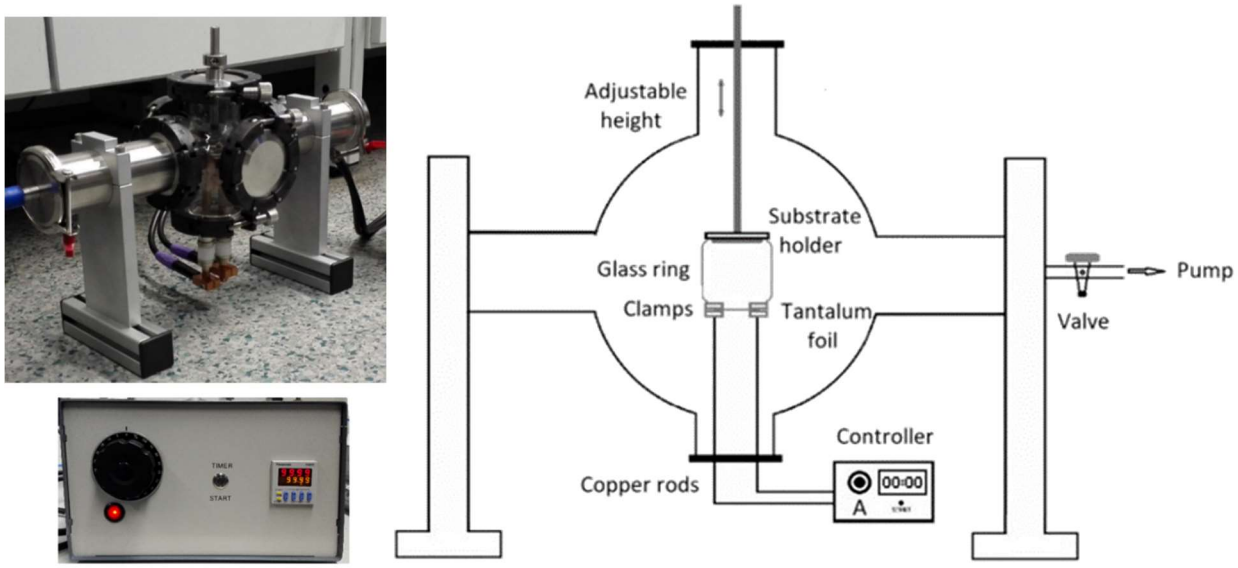

Figure 4.21 ***Left**, custom built flash evaporation apparatus,*

***right**, schematic view of the flash evaporator*

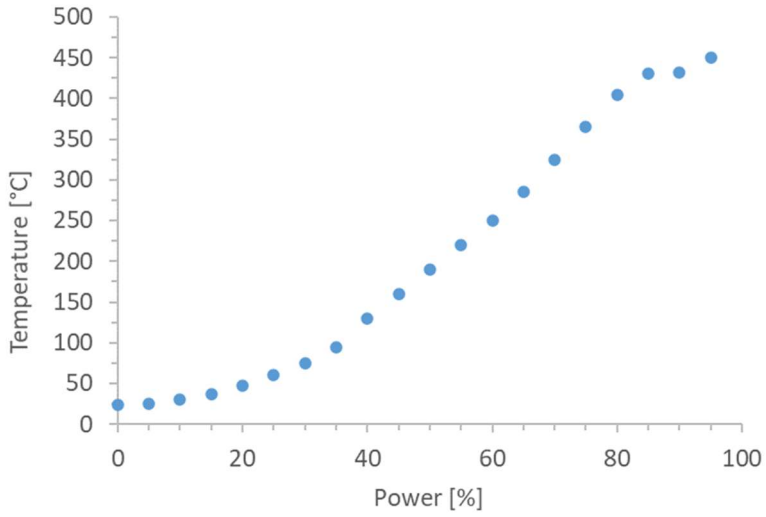

Figure 4.22 Temperature of the tantalum source foil of the flash evaporation device in dependence of the set power (1 V and 0 A – 80 A)

4.3.2 Methylammonium lead iodide (MAPI)

The MAPI source powder has been prepared via mechanochemical synthesis by thoroughly grinding PbI_2 (yellow) with MAI (CH_3NH_3I, white) in a 1:1 mol ratio in a ceramic crucible and in an argon glovebox. The mixture has been kept for a minimum of 2 h in the glovebox at room temperature prior to use. The educts react as shown in Equation 4.2 to form the MAPI perovskite (brown). The resulting MAPI powder can be seen in Figure 4.23.

Equation 4.2 $$PbI_2\ (s) + CH_3NH_3I\ (s) \rightleftharpoons CH_3NH_3PbI_3\ (s)$$

Figure 4.23 Appearance of the methylammonium lead iodide perovskite (MAPI, $CH_3NH_3PbI_3$) in the powder form

All steps of the flash evaporation process, from loading substrates to the evaporation of the films take place in an argon glovebox. The MAPI films are deposited onto a glass/ITO/c-TiO_2 substrate. 2 x 2 cm^2 ITO coated glass substrates are purchased from Pilkington, whereas the c-TiO_2 layer is deposited by spray pyrolysis as described in Chapter 4.1.2. The stack of materials is illustrated in Figure 4.24. As opposed to either the one- or the two-step wet chemical spin coating methods described in Chapter 4.1 and Chapter 4.2 , the material stack used for the flash evaporation process does not include the optional m-TiO_2 (mesoporous titania) electron transport layer.

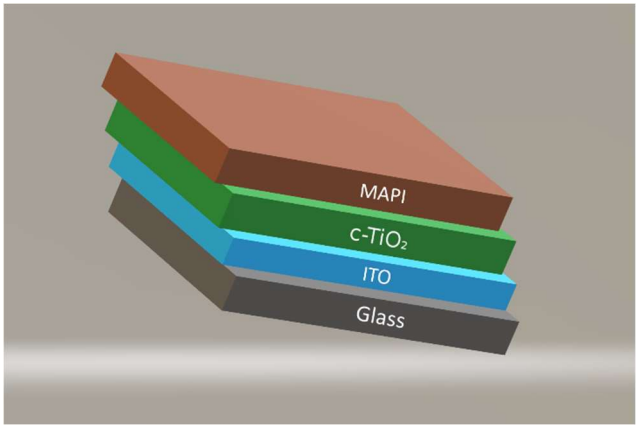

Figure 4.24 Material stack of flash evaporated MAPI perovskite substrates

Prior to the flash evaporation process, the Glass/FTO/c-TiO_2 substrates are treated in a UV/Ozone oven for 15 min. to clean them from surface contamination of hydrocarbons. For the flash evaporation process, the MAPI powder is placed onto the middle of the tantalum foil as shown in Figure 4.25 a). Due to a gradient in thermal conductivity towards the copper clamps, the middle portion of the tantalum foil is the hottest part, so the material is only placed on this middle portion of the tantalum foil. Figure 4.25 b) shows the substrate and the tantalum foil right after the deposition. It can be noticed how some of the material condenses near and on the copper clamps. Figure 4.25 c) is a photograph of a flash evaporated MAPI film. The optional annealing of the resulting films takes place in the argon glovebox on a hot place.

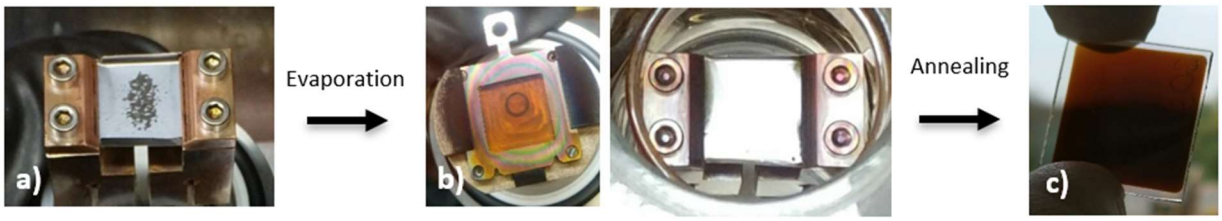

Figure 4.25 Images of the flash evaporation steps. **a)** the source: copper clamps holding a tantalum foil, onto which the MAPI perovskite powder ($CH_3NH_3PbI_3$) has been spread out. **b), left:** substrate holder with substrate after the flash evaporation. **b), right:** the source after the flash evaporation. **c)** the substrate with a MAPI film after annealing

Different evaporation temperatures have been tested, ranging from 250°C to 430°C, although the perovskite powder most likely evaporates at lower temperatures, in the first few seconds of the heat-up, before the tantalum foil reaches its thermal equilibrium after less than 10s. Successfully flashed films and their respective power, which was used to flash evaporate the source material, can be seen in Figure 4.26. Their parameters are summarized in Table 4.5. From the spin coating experience with working MAPI films, the correct brown/orange color and the transparency of the samples is known (compare Figure 4.11). A visual inspection of the flash evaporated samples shows that the sample produced at 60 % power is too yellowish and the ones flashed at the higher powers 75 % and 85 % appear gray. Some samples produced at 75% power have the desired orange/brown color as well, questioning the reproducibility of the process. The samples flashed at 65 % and 70 % have the correct orange/brown color and transparency. The sample flashed in between, at 67,5% turned out somewhat opaque but having the correct color as well (color not visible in the photograph).

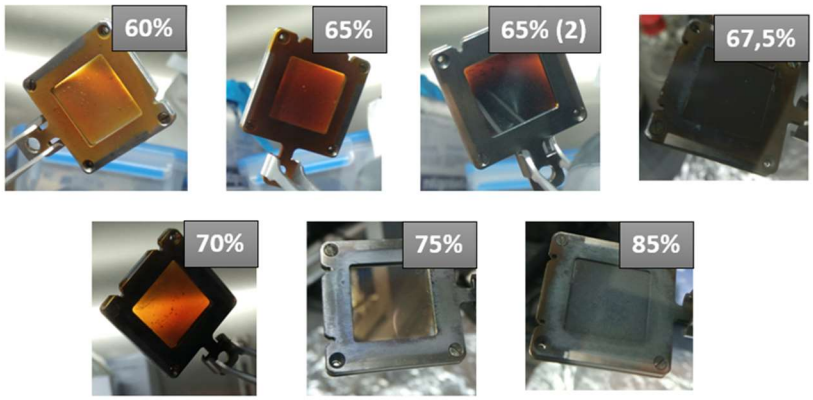

Figure 4.26 Different MAPI perovskite films produced in a glovebox via flash evaporation at their respective electrical power of the source

Table 4.5 Parameters for different $CH_3NH_3PbI_3$ (MAPI) films produced using the flash evaporation device, along with atomic concentration ratios of the elements Pb, C, N and I, calculated from XPS spectra

Sample	**I**	**II**	**III**	**IV**	**V**	**VI**	**VII**
Power [%]	60	65	65 (2)	67,5	70	75	85
Temperature [°C]	250	285	285	300	325	365	430
Time [s]	60	20	20	20	20	20	20
Amount [mg]	100	100	20	25	25	20	20
Annealed 100°C	no	no	yes	yes	no	yes	yes

The flash evaporated films from Figure 4.26 and Table 4.5 have been analyzed using XPS. Spectra of the elements contained in the $CH_3NH_3PbI_3$ MAPI perovskite film, i.e. lead, carbon, nitrogen and iodine have been recorded and can be found on page 201 in the Appendix Figure 9.1 – Figure 9.7. The element oxygen could not be found on the samples (expected binding energy range: 528 eV – 534 eV), excluding either a contamination of tantalum oxide from the tantalum source foil, or other surrounding contaminants (see survey plots in Appendix Figure 9.8).

For all these flash evaporated MAPI film measurements, the XPS setup was not calibrated using reference samples. In addition, due to faults in the potential control, these spectra can be shifted with up to 1 eV from their real value, so a comparison with literature values cannot be made. Nonetheless, atomic concentration ratios were calculated from the fits of the XPS spectra (Appendix Figure 9.1 – Figure 9.7) using the software Avantage 5.9911, which utilizes spectrometer specific corrected Scofield factors. The values can be found in Figure 4.27, showing percentages of the composition that add up to 100. Table 4.6 shows values for each film, which have been normalized with respect to the lead content in the respective film. In an ideal case, the atomic concentration ratios of the elements contained in MAPI ($CH_3NH_3PbI_3$) are 1: 1: 1: 3 for Pb: C: N: I. A second carbon peak (C2) can be seen in most films (see XPS carbon plots in Appendix Figure 9.1 to Figure 9.7), which can be attributed to surface contamination.[118] None of the films have an ideal composition. The films closest to ideal ratios are Nr. III (65 % (2)) and IV (67,5%), both having a nearly ideal amount of Pb: N: I with 1: 1,1: 3,1, but too much carbon with 1,6 resp. 1,8. It is possible that this larger amount of carbon also results from contamination of the devices and surroundings involved. Sample VII also seems to have the right composition from its atomic concentration ratios of 1: 1,2: 3 for Pb: N: I, having too much carbon as well with 1,8, but given the gray color of the film, instead of the needed orange/brown color, it is doubtful that this sample contains a working MAPI perovskite deposited, the color being

directly related to the band gap of the material. In any case, XPS provides a fast analysis of the films, but suffers from its pronounced surface sensitivity.

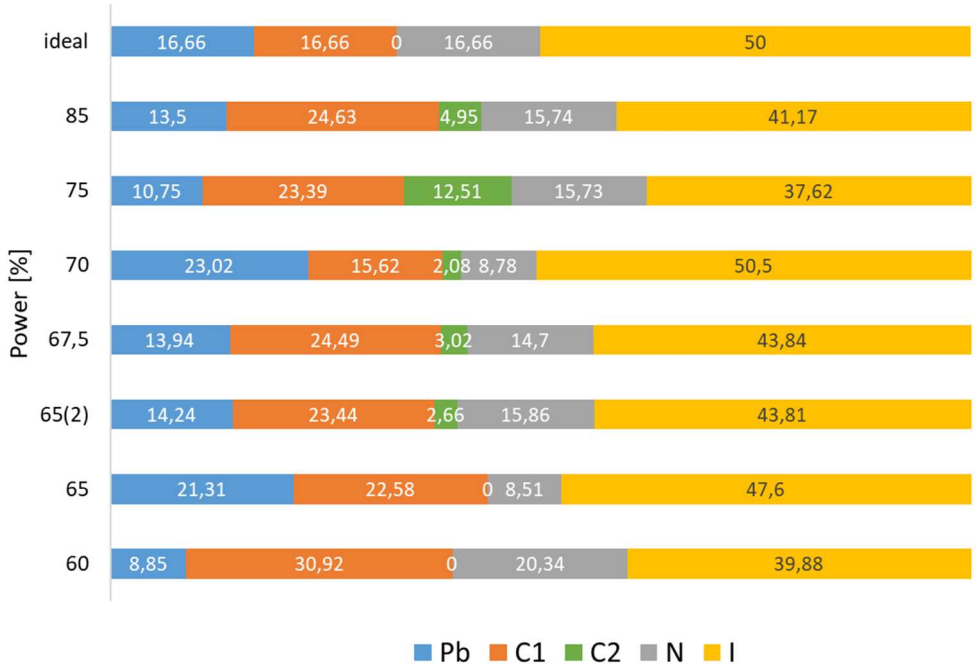

Figure 4.27 Atomic concentration ratios of MAPI perovskite films produce via flash evaporation, calculated from the XPS spectra found in the Appendix Figure 9.1 – Figure 9.7

Table 4.6 Atomic concentration ratios of MAPI perovskite films produce via flash evaporation, calculated from the XPS spectra found in the Appendix Figure 9.1 – Figure 9.7

Sample	**Source power**	**Atomic concentration ratios**				
		Pb	**C1**	**C2**	**N**	**I**
ideal		1	1	0	1	3
I	60 %	1	3,5	0	2,3	4,5
II	65 %	1	1,1	0	0,4	2,2
III	65 % (2)	1	1,6	0,2	1,1	3,1
IV	67,5 %	1	1,8	0,2	1,1	3,1
V	70 %	1	0,7	0,1	0,4	2,2
VI	75 %	1	2,2	1,2	1,5	3,5
VII	85 %	1	1,8	0,4	1,2	3,0

All films from these experiments deposited by flash evaporation show small pointlike defects on the surface, visible with the naked eye. Upon closer inspection using a scanning electron microscope (SEM) on a representative sample flashed at 75% power (Figure 4.28 and Figure 4.29), excess material shaped like half spheres can be observed (colorized in purple in Figure 4.28). These spheres indicated that droplets of a liquid phase form, either by liquifying of the source material upon heating, or in the vapor on the way between the source and the substrate, or upon condensation on the substrate. The 500 nm scale SEM image in Figure 4.29 shows that the morphologies of the film and that of the half sphere are the same, suggesting that both are in fact the same material. Additional defects can be observed, which look like craters from which the half spheres have fallen off after solidifying (colorized in green in Figure 4.28). The excess material with irregular shapes colorized in red indicates that not all powder from the source is deposited by evaporation, but some of the grains are evidently mechanically transmitted in the solid form to the substrate.

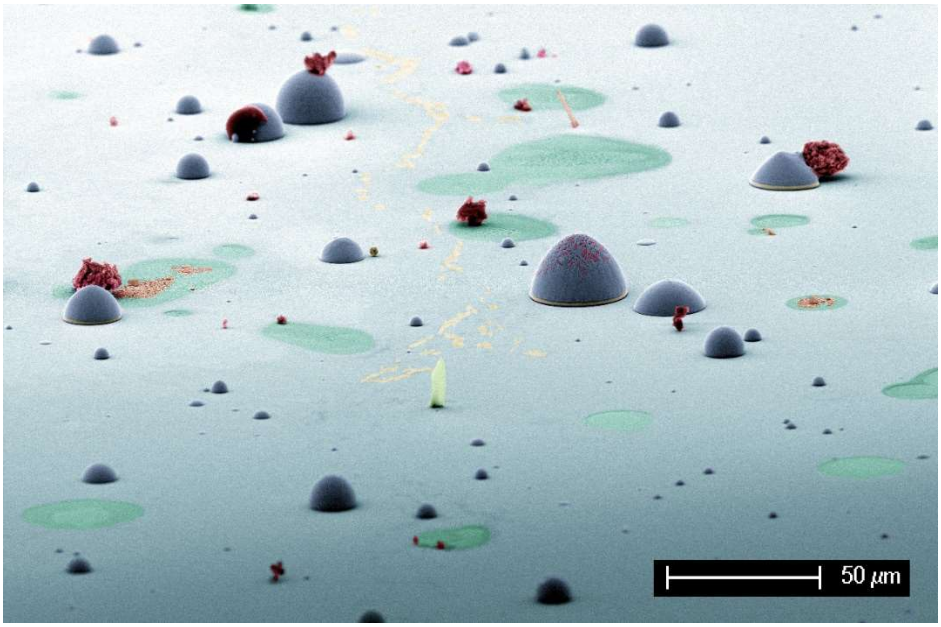

Figure 4.28 Colorized scanning electron microscopy (SEM) image of the surface of a flash evaporated MAPI perovskite film (light blue), with half spherical defects (purple), craters (green) and irregular defects (red). Sample tilted at 70°

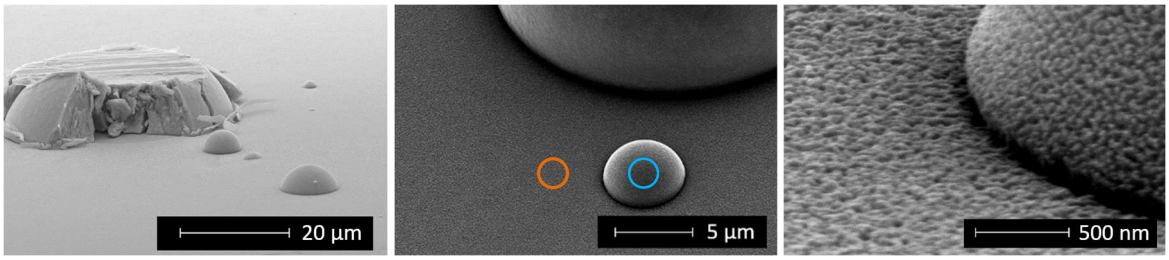

Figure 4.29 Scanning electron microscopy (SEM) images at different magnifications of the surface of a flash evaporated MAPI perovskite film, with defects. Sample tilted at 70°. The orange and the blue circles represent the spot locations of the EDS measurements shown in Figure 4.30

To further analyze the composition of the half spheres and that of the film formed, EDS measurements have been conducted on the film (orange) and on a half sphere (blue) on the spots highlighted in Figure 4.29. The recorded EDS spectra are shown in Figure 4.30. Both spots show peaks belonging to the elements contained in the MAPI perovskite ($CH_3NH_3PbI_3$): carbon (C), nitrogen (N), lead (Pb), and iodine (I). This fact indicates that the spheres, as well as the film are indeed both made of the MAPI perovskite. Since the EDS electron beam penetration depth and the characteristic X-rays depth are in the micrometer range, all other elements contained on the Glass/ITO/c-TiO_2 substrate are visible on the film, but not on the thicker half spheres. For the measurement conducted on the film, additional elements present in the soda lime glass of the substrate as oxides, appear: silicon (Si), sodium (Na), magnesium (Mg), aluminum (Al) and calcium (Ca). On both measurement spots, indium (In) and tin (Sn) from the conductive indium tin oxide layer and titanium from the titania (c-TiO_2) layer are also present. The peak assignments for the elements in the EDS measurements have been carried out with the help of the periodic table “Energy table for EDS analysis” by JEOL.

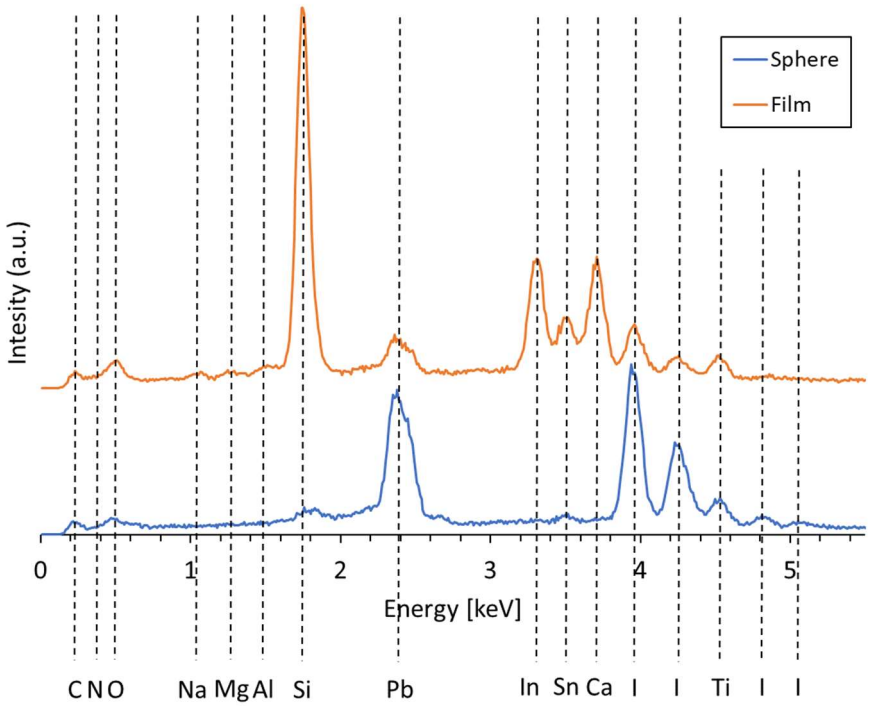

Figure 4.30 EDS spectra recorded on MAPI sample flash evaporated at 70% power on the spots highlighted in Figure 4.29, with blue being on a half sphere and orange on the film

The cross-section SEM image of the flash evaporated sample at 75% power and using 20 mg of source material, shown in Figure 4.31, reveals a thickness of the perovskite of ca. 400 nm, which is in the correct range needed for working solar cells.[119-121]

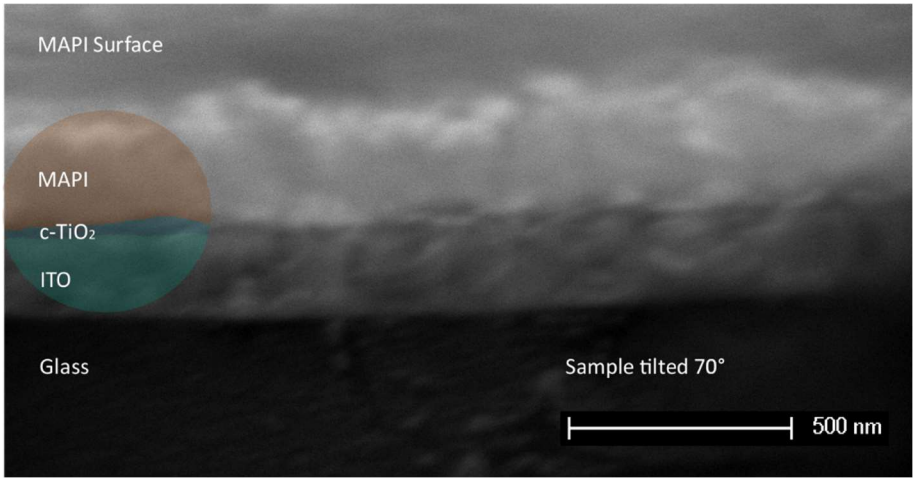

Figure 4.31 Cross-sectional scanning electron microscopy (SEM) image of a flash evaporated MAPI perovskite substrate. Partially colorized to indicate the different materials. Tilted at 70°

A further close-up on the surface of the film using SEM reveals its morphology, shown in Figure 4.32. On the left, a flash evaporated film that has not been annealed is displayed. The film is not continuous, showing a porous surface with separated grains, which is not an appropriate morphology for the absorber layer. When spin coating the spiro-MeOTAD hole transport layer, material would deposit through the holes, onto the c-TiO_2 electron transport layer, allowing undesired recombinations between these two layers. On the right, after the film has been annealed for 30 min. at 100°C, an increase of the grain sizes can be observed, but the material still shows the undesired porosity.

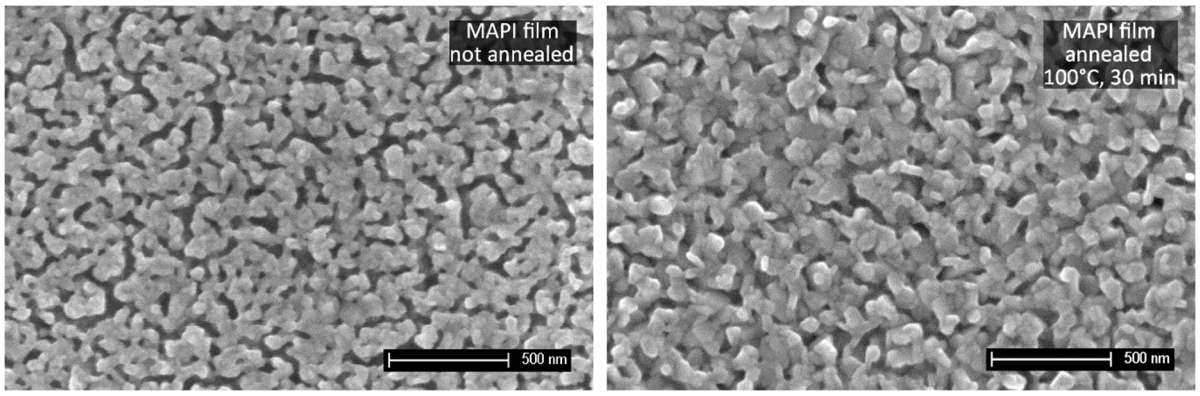

Figure 4.32 Close-up scanning electron microscopy (SEM) images of the surface of flash evaporated MAPI perovskite films. **Left:** a film without post-annealing, **right**: annealed at 100°C for 30 min.

Figure 4.33 shows photoluminescence measurements of a flash evaporated MAPI film as flashed, then after annealing at 80°C, having almost the same intensity of photoluminescence. In comparison the luminescence of a film, which has been annealed at 120°C for 30 min. is shown, for which the photoluminescence is almost inexistent. On the one hand, annealing a material should increase its grain sizes, healing grain boundary defects and allowing recrystallization, but on the other hand, annealing it at a too high temperature for too long will change the composition of the material, with possible evaporation of the constituents.

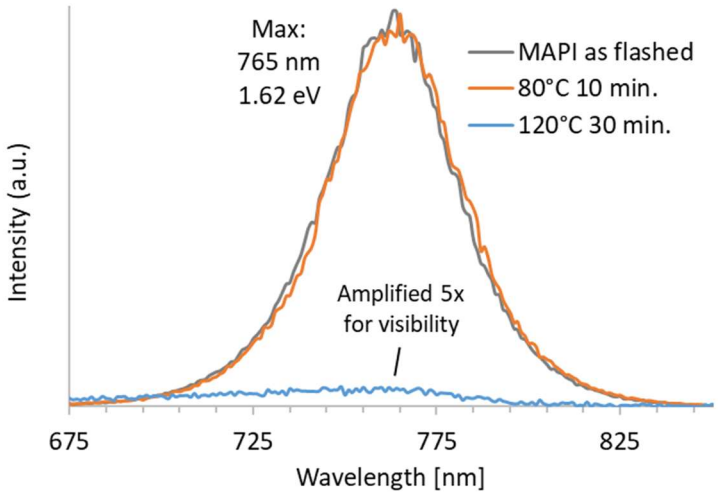

Figure 4.33 Comparison of photoluminescence measurements of flash evaporated MAPI samples with different post-annealing treatments

One possibility has been followed to mitigate the number of half-spherical defects shown in the SEM image Figure 4.28. The method involves evaporating the MAPI source powder onto another tantalum foil first and to then use this tantalum foil deposited with a smooth MAPI film as a source, evaporating the material onto the actual Glass/FTO/c-TiO_2 substrate. The images in Figure 4.34 illustrate the process. The MAPI powder has been evaporated at 75% power onto another tantalum foil first, creating a brown/orange film. The Ta/MAPI foil has then been used as a source to evaporate the material at 70% power onto a Glass/FTO/c-TiO_2 substrate. Indeed, the half-spherical defects decreased in number, as shown by the optical microscopy images of Figure 4.35. A solar cell has been completed by spin coating spiro-MeOTAD and sputter coating gold on top. The still remaining defects on top of the MAPI film show comet tail-like defects when spin coating the spiro-MeOTAD film, due to the shadowing effect. This solar cell had only a low efficiency of 1,3 %.

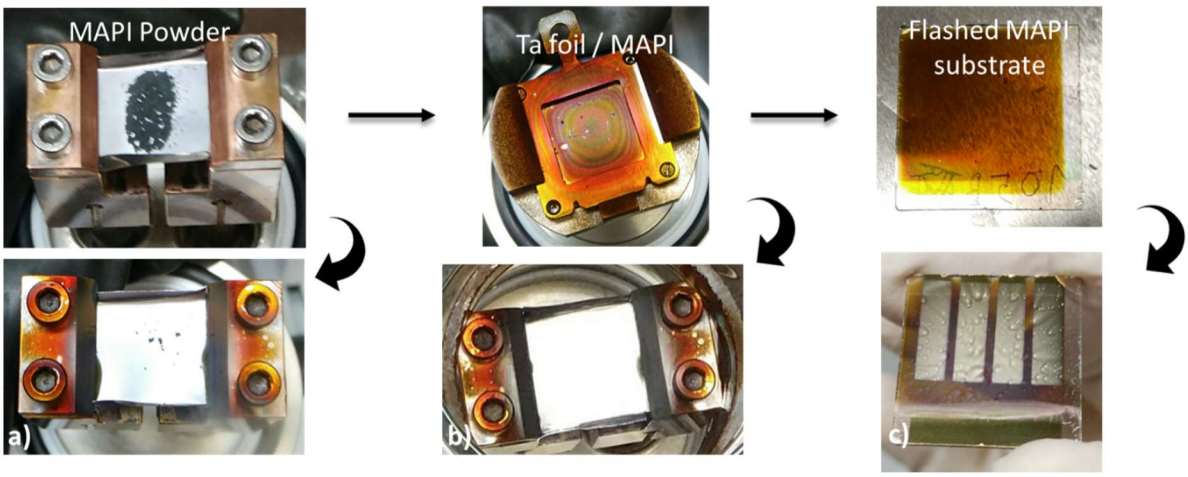

Figure 4.34 Images illustrating a flash evaporation process, which involves a second tantalum foil as an intermediary source, for depositing a smoother film. **a)** A Ta foil with MAPI powder on top and the residuals after evaporating the material at 75% power on **b)** another Ta foil covered with a film of MAPI and the residuals after evaporating the material at 70% power on **c)** a Glass/FTO/c-TiO_2, now having a MAPI film on top and the final solar cell with the stack Glass/FTO/c-TiO_2/MAPI/spiro-MeOTAD/Au

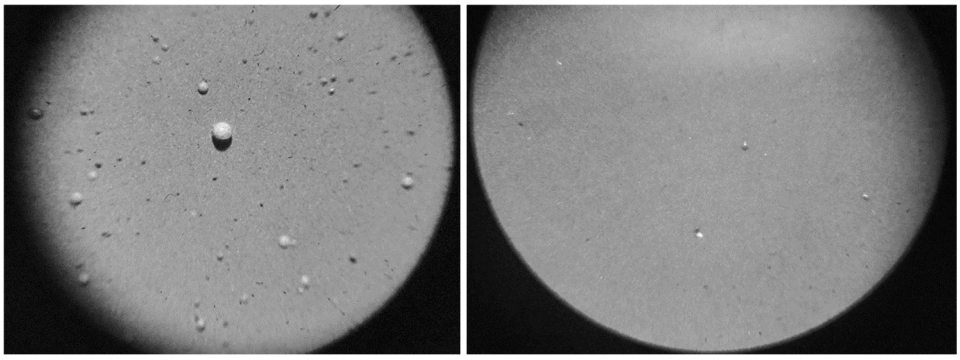

Figure 4.35 Optical microscopy images at 4x magnification of **left,** a flash evaporated MAPI film at 70% power directly from MAPI powder, using the regular technique and **right,** a flash evaporated MAPI film made by flash evaporating from a tantalum foil as a source, which was itself deposited with a MAPI film by flash evaporating from MAPI powder as shown in Figure 4.34

To summarize, MAPI solar cells made with the flash evaporation process had low performances of 0% (not working at all) to 1.75%. At this point, optimization of the MAPI flash evaporation process has been discontinued as other approaches seem to be more promising. Further possible improvements of the device would have been to integrate a heating cartridge in the sub-

strate holder, to avoid the quick condensation of the half-spheres from the vapor and to improve the porous morphology of the film. In addition, a heatable glass ring using a Kapton heating film, which would keep the vapor between the source and the substrate hot, would have further improved the quality of the film, reducing the formation of droplets in the vapor.
The low efficiencies of the flash evaporated MAPI films cannot be blamed entirely on the quality of the evaporated MAPI film. Other experiments from our group showed that there is a misalignment in the semiconductor bands of our produced c-TiO_2 and MAPI. In other experiments, the introduction of a thin layer of C_{60} between the c-TiO_2 and MAPI drastically improved the efficiency of the solar cells with the planar architecture, without the use of a mesoporous m-TiO_2 layer.

4.3.3 Methylammonium tin iodide (MASI)

In this chapter, a new one-step flash evaporation technique is presented, which uses MASI powder produced by a solvent free, mechanochemical synthesis method to create MASI films for use in solar cell devices.

The results of this chapter have been summarized in a publication in the journal Physica Status Solidi A with the title: *Preparation of Methylammonium Tin Iodide ($CH_3NH_3SnI_3$) Perovskite Thin Films via Flash Evaporation.*[122]

The MASI source material has been synthesized by thoroughly grinding SnI_2 with CH_3NH_3I (MAI) in a 1:1 mol ratio, in an argon glovebox. During grinding, the pink colored tin iodide and the white MAI turn into a black powder, indicating the formation of MASI. Subsequently, the mixture has been heated up in a closed tube filled with 1 bar argon for 2 h at 200°C in a tube furnace to further promote the reaction. In this mechanochemical synthesis, the educts react according to the chemical Equation 4.3, to form the MASI perovskite in the cubic phase, the black appearance of which can be seen in Figure 4.36.

Equation 4.3 SnI_2 (s) + CH_3NH_3I (s) ⇌ $CH_3NH_3SnI_3$ (s)

Figure 4.36 Appearance of the black source material methylammonium tin iodide (MASI, $CH_3NH_3SnI_3$) in the powder form

To highlight the difficulty of handling MASI in atmosphere, an experiment has been conducted in which the MASI powder has been left in air for 5 days, prior to recording its XRD pattern. For comparison, the MASI material that was stored in an argon glovebox, has been measured in a gas tight holder. The results can be seen in Figure 4.37.

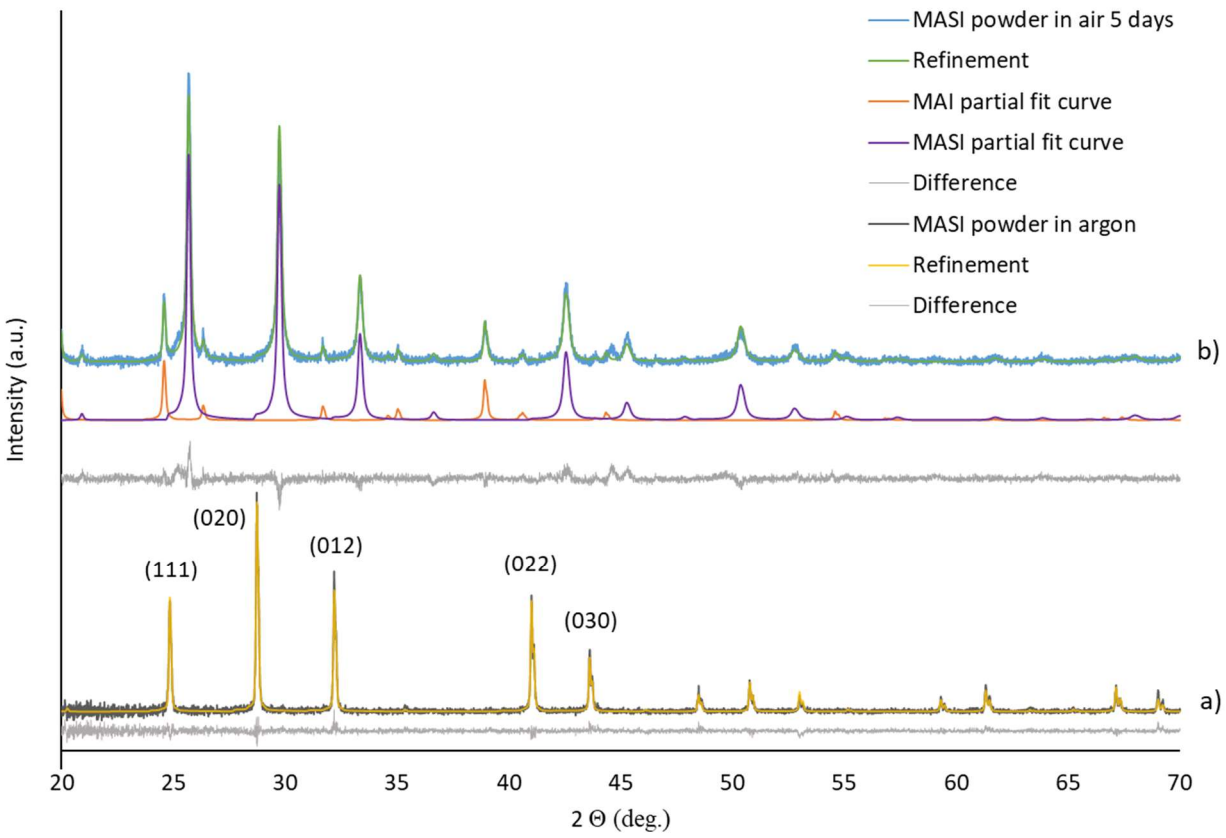

Figure 4.37 Rietveld refinements of the source material used for Flash Evaporation, **a)** without exposure to air vs. **b)** after 5 days of exposure to air

The Rietveld analysis of the XRD patterns have been done in close cooperation with Prof. O. Clemens from the Material Science department of TU Darmstadt, using the software TOPAS V. 5.0.

The patterns of the powders can be refined using the tetragonal structural model with *P4mm* symmetry as described by Hao et al.[123]

Neither measurement indicates a tetragonal distortion. A suitable fit for the measured MASI powder in argon could be obtained by constraining the cell to a pseudo-cubic cell metric with a ≈ c = 6.240(6) Å. The XRD of the MASI powder produced by the mechanochemical synthesis method shows an excellent fit with the refinement used, with no impurity phase present.

After air exposure, the powder was found to have decomposed under the formation of large amounts of methylammonium iodide (MAI). In addition, a chemical modification of the MASI is indicated from a strong decrease of the lattice parameter (a ≈ c = 6,009(5) Å, ΔV ≈ - 12 %),

which could be expected from a decomposition under formation of MAI. The decomposition of MASI in air has been also been reported by Noel and Wang, showing the formation of MAI, with possible formations of amorphous tin oxide species, where tin would get oxidized from a +II state to a +IV oxidation state. [15,124] It is expected that the material decomposes much faster than the 5 days it has been left in air in this experiment.

For producing the thin films, small amounts from a batch of the MASI source material are heated up quickly to the sublimation point using the flash evaporation device and deposited on a Glass/FTO/c-TiO_2 substrate as shown in Figure 4.38. The cleaning of the Glass/FTO substrates and the c-TiO_2 deposition by spray pyrolysis are described in Chapter 4.1.2. All processes starting from the synthesis of the MASI, filling of the flash evaporation source, and the flash evaporation are performed in the argon filled glovebox.

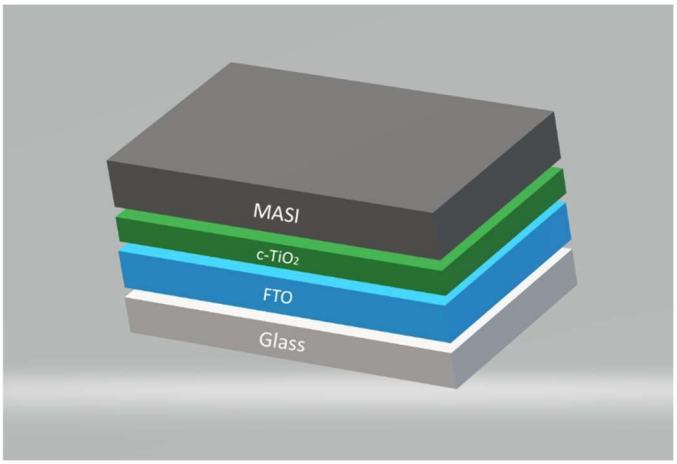

Figure 4.38 Material stack of a flash evaporated MASI perovskite substrate

For finding optimal deposition parameters for stoichiometric MASI thin films varied parameters include the amount of the source material, the pressure in the flash evaporator, source temperature and heating time. Details on notable experiments can be found in Figure 4.39 and Table 4.7

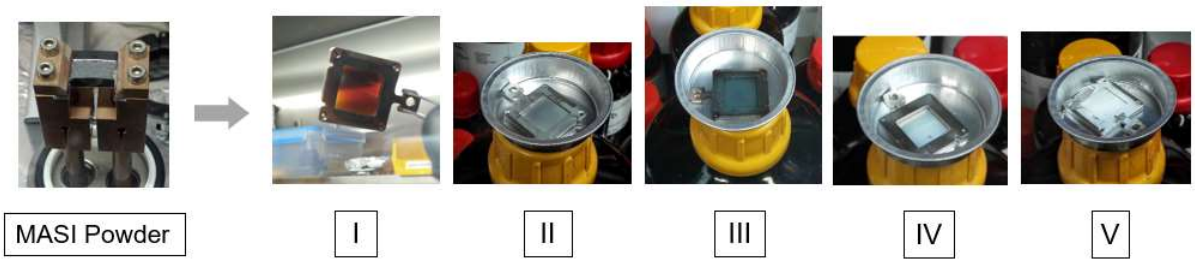

Figure 4.39 Different $CH_3NH_3SnI_3$ (MASI) films produced by the flash evaporation process, using parameters from Table 4.7

Table 4.7 Parameters for different $CH_3NH_3SnI_3$ (MASI) films produced using the flash evaporation device, along with atomic concentration ratios of the elements Sn, C, N and I, calculated from XPS spectra

Sample	**I**	**II**	**III**	**IV**	**V**
Time [s]	60	60	60	5	5
Power [%]	35	37	40	45	60
Temperature [°C]	210	230	250	300	400
Pressure [mbar]	$5 \cdot 10^{-3}$	100	$5 \cdot 10^{-3}$	100	100
Sn: C: N: I Ideal 1: 1: 1: 3	1: 6: 5: 7	1: 25: 53: 52	1: 1.2: 0.93: 3.15	--	--

MASI films show a gray color in appearance. By using too high temperatures and/or pressures, unfavorable colorless (white) films are formed, i.e. sample IV and V, Table 4.7**,** indicating a degradation of the source material. A too low temperature with good vacuum will produce an unfavorable orange film (sample I). Samples II and III are gray in color. A first factor for judging the success of the flash evaporation process is to analyze the atomic concentration ratios from XPS measurements. The best film produced, sample III, has near-stoichiometric ratios of 1.2: 0.93: 1: 3.15 for C: N: Sn: I, which is close to the ideal case of 1: 1: 1: 3 for $CH_3NH_3SnI_3$. These atomic concentration ratios have been calculated from the XPS Spectra displayed in Figure 4.40. The comparison of the concentration factors of samples I and II, which have been evaporated at almost the same temperatures, but at different argon pressures, reveals that the sample evaporated at the higher pressure contains more of the elements C, N and I (see Table 4.7). A hypothesis explaining this finding is that the MASI source material decomposes into SnI_2 and MAI when heating. At a lower surrounding pressure, i.e. $5 \cdot 10^{-3}$ mbar, more tin iodide can be evaporated at the set temperature, as observed for sample I. At a higher surrounding pressure,

i.e. 100 mbar (sample II), more of the MAI (CH_3NH_3I) component reaches the sample, since its boiling point is lower than that of the SnI_2. For this reason, the fast heating flash evaporation technique has been chosen for a one-step process, in order to evaporate the source material congruently, far from the thermodynamic evaporation equilibrium, avoiding fragmentation into MAI and SnI_2.

Sample III was deposited under optimized parameters at a maximum tantalum foil temperature of 250°C and a pressure of $5 \cdot 10^{-3}$ mbar (Table 4.7). The calculated atomic ratios from the XPS spectra, displayed in Figure 4.39**,** are close to ideal stoichiometry and the material features a pseudo-cubic perovskite structure as determined by the XRD shown in Figure 4.44**.** XPS Peak positions are $I3d_{5/2}$ at 619.0 eV and $Sn3d_{5/2}$ at 486.1 eV indicating pure Sn^{2+} (as Sn^{4+} would be expected at 487.3 eV and Sn^0 at 484.0 eV)[110] and N1s at 402.1 eV. Unlike the emissions of the elements tin, iodine and nitrogen, carbon shows an asymmetry. Deconvolution of the C1s signal reveals three species of carbon present in the sample, with a main signal at 285.9 eV, an additional emission at 286.5 eV and a small emission at 284.4 eV (Table 4.8). The main signal at 285.9 eV can be attributed to the C1s of the methylammonium component belonging to the perovskite. The other carbon signals could arise from surface defects at the MASI grains resulting from decomposition of the source material during heating, or from impurities from the deposition setup. MAI can be excluded from being a component of the film surface, since its C1s signal would be expected at 287 eV.[125] Reactions with atmospheric species can be excluded as well, since the transport of the deposited films from the glovebox to the XPS system is achieved with the help of an air-tight shuttle. A measurement in the region of the O1s electron binding energy of 526 eV to 536 eV did not feature any signal.

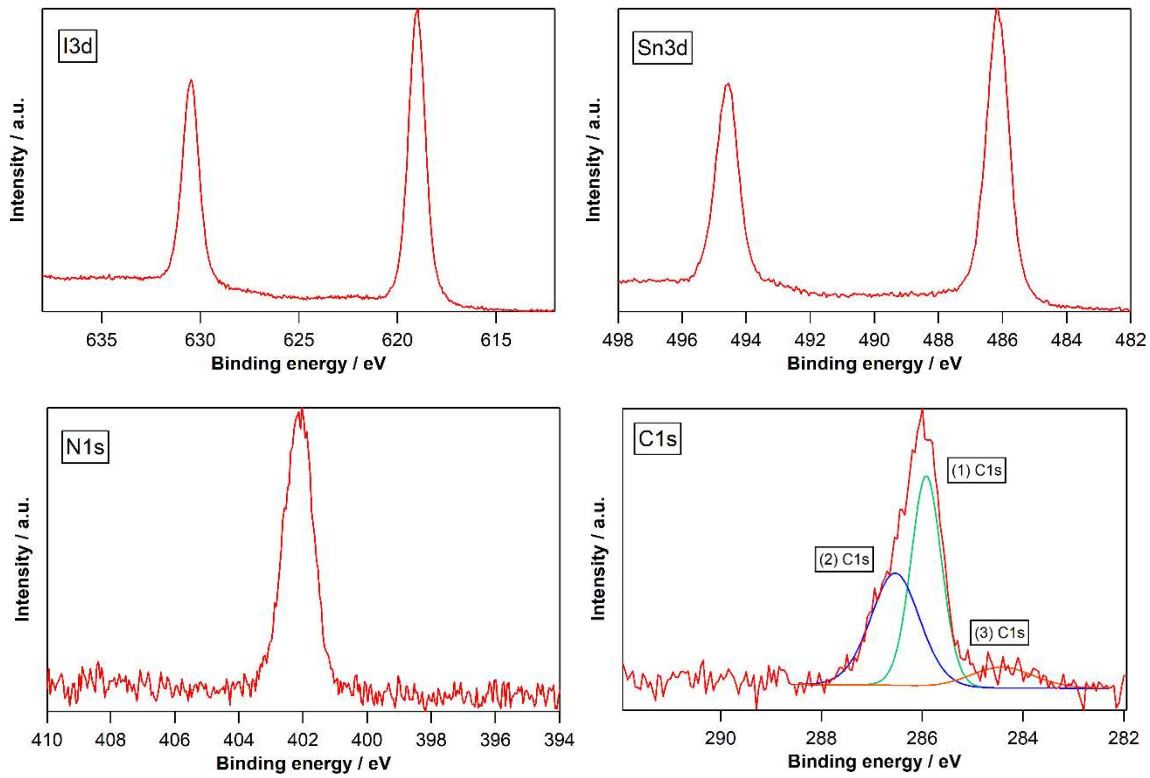

Figure 4.40 Detailed XPS measurements for the elements contained in the MASI ($CH_3NH_3SnI_3$) perovskite film Nr. III (Figure 4.39), produced by flash evaporation

Table 4.8 Core level positions and valence band maximum determined by XPS measurements of the MASI film Nr. III (Figure 4.39) belonging to Figure 4.40

Core Level of Element	Binding Energy
Sn3d 5/2	486.1
I3d 5/2	619.0
N1s	402.1
(1) C1s	285.9
(2) C1s	286.5
(3) C1s	284.4
VBM	0.4

For determining the valence band maximum binding energy position of the MASI film, an XPS measurement was recorded in the valence band region of the material, ranging from an energy of -3 eV to 10 eV, as shown in Figure 4.41. A common procedure for finding the value of the valence band maximum from photoemission valence band spectra is to linearly extrapolate the

strong onset of the emission to background intensity. The small extra emission above this onset might be attributed to shallow gap states near the valence band maximum. The measurement shows that MASI, produced by this method, is a p-type material with VBM - E_F of 0.4 eV, having a band gap of 1.3 eV (Figure 4.42). Using a work function Φ of 4.75 eV for UHV deposited MASI,[126] a band diagram can be drawn as displayed in Figure 4.41, which may be used for a first selection of appropriate hole and electron extraction layers according to the simple vacuum level alignment.

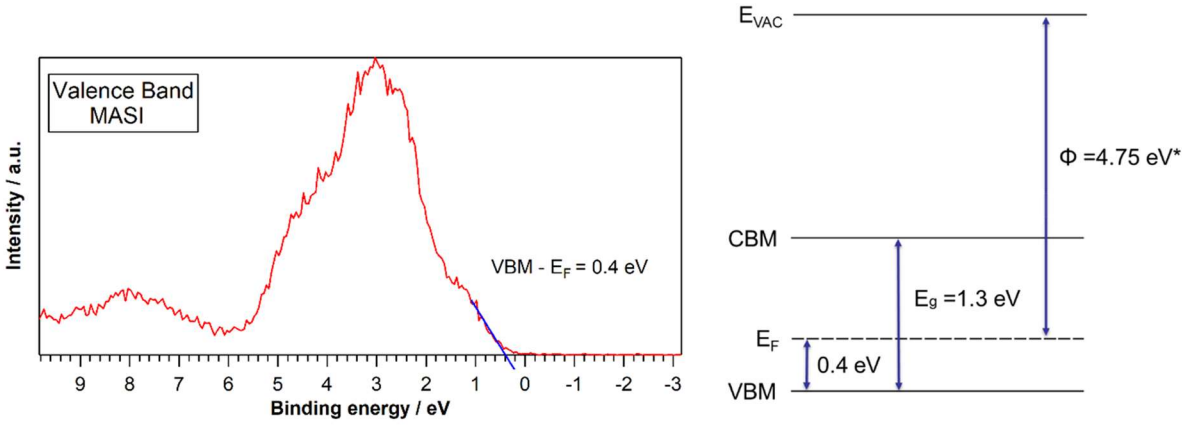

Figure 4.41 **Left**, XPS of the valence band region of the MASI film Nr. III (Figure 4.39); **Right**, concluded band diagram. The value of the band gap E_g is taken from our UV-/Vis measurement in Figure 4.42 and for the work function Φ, marked with an asterisk (*), from [126]

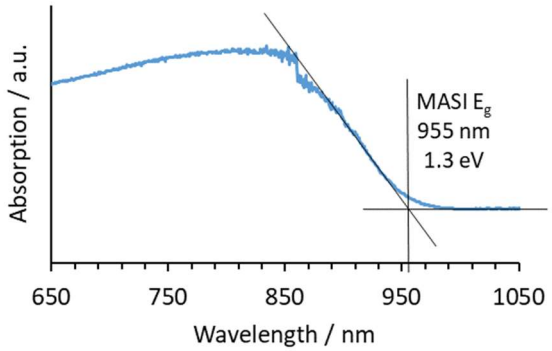

Figure 4.42 UV-/Vis spectrum of the flash evaporated MASI film III (Figure 4.39)

As a comparison to the film spectra and to further characterize the MASI source powder produced by the mechanochemical synthesis method, an XPS measurement has been conducted on the powder, which was pressed onto an indium foil. Since air exposure could be avoided with an air-tight shuttle for the transportation of the material to the XPS setup, no oxygen O1s signals are present in any films, which would be expected in a binding energy range of 528 eV – 534 eV (see survey plots in Appendix Figure 9.9). Figure 4.43 shows the spectra of the elements contained in the MASI powder. The signals in Figure 4.43 are shifted towards higher binding energies compared to the signals of the film in Figure 4.40. To correct this effect of charging, the positions of the signals for the respective elements in Table 4.9 have been shifted by 0.4 eV to lower binding energies from their originally measured values plotted in Figure 4.43. This charging effect in the photoelectron spectra can be observed, since there is an unfavorable contact between the grains of the powder to allow a good transport of the electrons to the indium foil substrate and the ground of the machine. The atomic ratios of the powder calculated from the spectra in Figure 4.43 are 1.46: 1.1: 1: 3.4 for C: N: Sn: I, while the ideal stoichiometry would be 1: 1: 1: 3. In comparison, the produced film from this powder does have an almost ideal stoichiometry of 1.2: 0.93: 1: 3.15, although the values for carbon and iodine are somewhat off in the data of the powder.

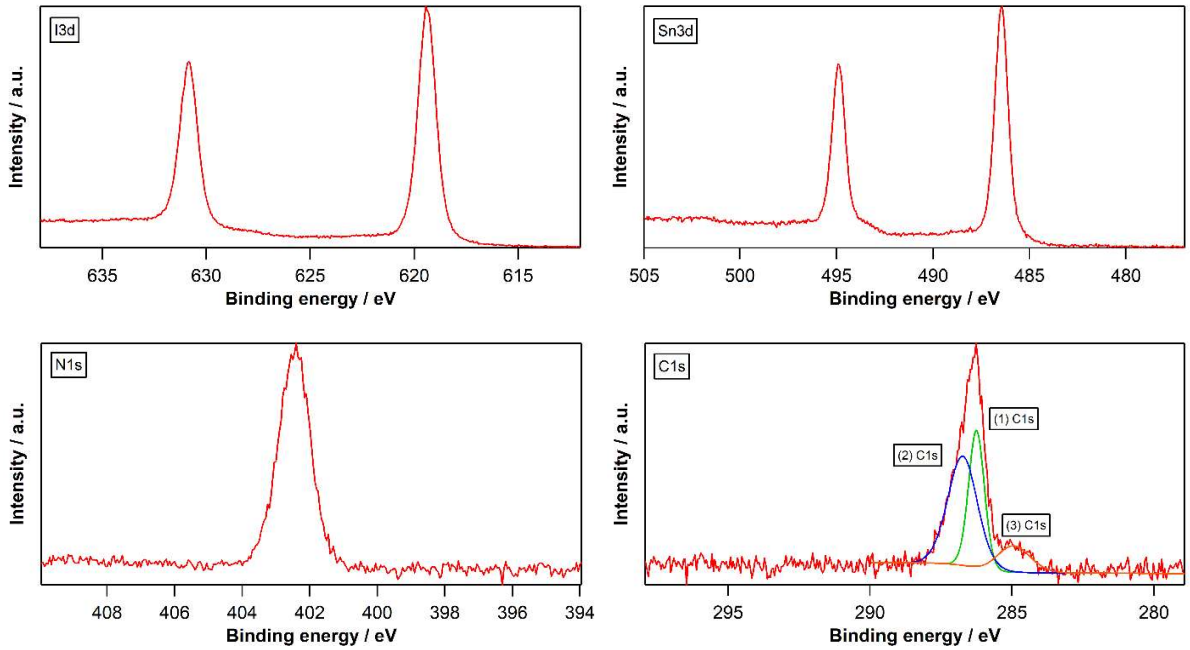

Figure 4.43 Detailed XPS measurements for the elements contained in the MASI ($CH_3NH_3SnI_3$) source material produced by mechanochemical synthesis

Table 4.9 Core level positions and valence band maximum of the MASI source material from the XPS data in Figure 4.43. All values in the table have been shifted by 0.4 eV from their original values in Figure 7 to compensate for charging of the powder

Core Level of Element	Binding Energy
Sn3d 5/2	486.1
I3d 5/2	619.0
N1s	402.0
(1) C1s	285.9
(2) C1s	286.4
(3) C1s	284.6

The XRD pattern in Figure 4.44 shows the measurement of a MASI film produced with the same settings as the one for the XPS measurement. The deposited material shows a very similar lattice parameter to that of the initial source material with pseudo-cubic symmetry: a ≈ c = 6.239(8) Å, i.e. a negligible deviation of the unit cell volume ΔV of around - 0.1 %, indicating an excellent transfer of the sample composition and structure of the source material to the film. Apart from the SnO_2 reflections of the FTO substrate, only a small amount of an additional impurity phase was found (marked with asterisks, *), which could not be matched to any phases within the ICSD database, but which could be possibly explained by a small amount of a (00l) textured MAI phase. Furthermore, the crystallite size of the material after deposition was found to be in the order of 53 nm, which is smaller than what is found for the precursor powder of 139 nm.

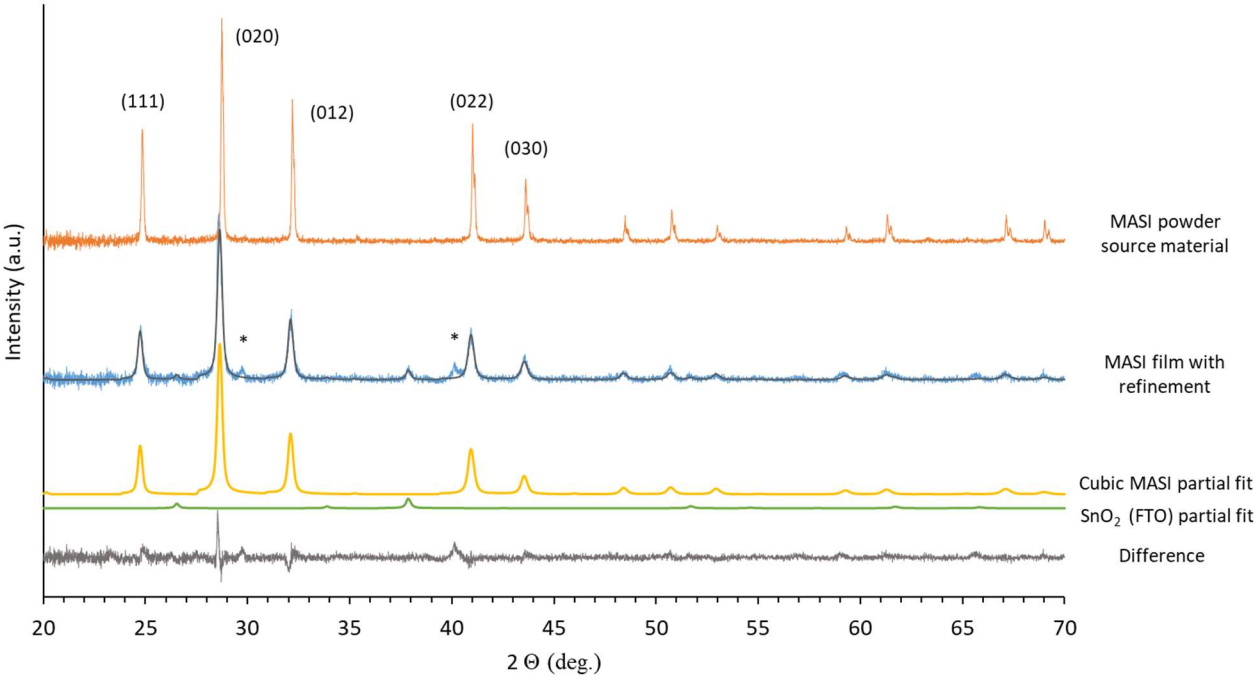

Figure 4.44 Rietveld analysis of diffraction data of a MASI film Nr. III (Figure 4.39) prepared via Flash Evaporation in comparison to the analysis of the source powder

A visual inspection of film III (Figure 4.39) deposited on the transparent substrate does not indicate pinholes. The morphology of the film was determined by SEM. Image a), Figure 4.45 features conglomerates of 300-500 nm in size and grains of 50 nm. The 50 nm grain sizes of the film found by SEM match the grain sizes calculated from the refinement of the XRD pattern of 53 nm. Recording SEM images of the MASI film has proven to be difficult, since at high magnifications the electron beam quickly degrades the material in a matter of a few seconds, leading to a highly blurred image. Image a), Figure 4.45 measured with 10 kV at 35.000x magnification, has been taken by fine tuning the focus of the electron microscope using several spots on the film, degrading the material locally, then quickly moving to the specific spot a) (Figure 4.45) and recording the image after only a quick scan. Image b), Figure 4.45 shows the material with a magnification of 200x on a micrometer scale. The defects found at this scale are identical to the half-spheres described in Chapter 4.3.2 for the MAPI perovskite, which are caused either by a liquid phase forming on the source, or by droplets condensing in the vapor phase between

the source and the substrate, or by gas directly condensing as a liquid on the film and then crystallizing as a solid.

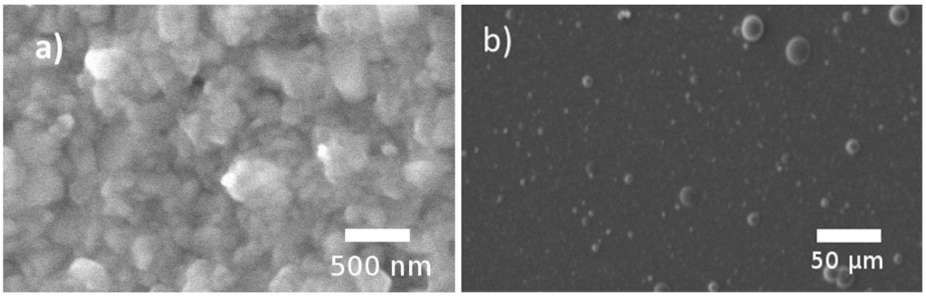

Figure 4.45 SEM images of film III (Figure 4.39). a) represents the morphology of the film on a nanometer scale and b) shows the micrometer scale structure

These experiments show that MASI can be congruently evaporated using the technique of flash evaporation to form a film which has a high chemical purity, measured by XPS and a single crystallographic phase, measured by XRD. The morphology of the film still shows many defects in the form of solidified droplets. The flash evaporation device could be improved in this respect as described in the previous Chapter 4.3.2. For measuring completed MASI solar cells, an encapsulation technique would need to be established, which would prevent the degradation of the material in air.

4.4 Chemical vapor deposition (CVD) process

Many of the following experiments of the CVD process have been conducted in close cooperation with Moritz Buchhorn and Marco Melzi d'Eril, who each wrote their Master Thesis in our Surface Science group on this topic under the author's supervision.

The first three subchapters, 4.4.1, 4.4.2 and 4.4.3 can be considered as pre-experiments that lead to the successful CVD process presented in 4.4.4.

Popular routes to forming the photo-active perovskite methylammonium lead iodide ($CH_3NH_3PbI_3$, MAPI) are either from solution, by spin coating, or from the gas phase, by evaporating the two precursor salts lead(II)iodide (PbI_2) and methylammonium iodide, (CH_3NH_3I, MAI), following the Equation 4.4.

Equation 4.4 $CH_3NH_3I + PbI_2 \rightleftharpoons CH_3NH_3PbI_3$

Since CH_3NH_3I can decompose at elevated temperatures above 170°C to ammonia (NH_3) and methyl iodide (CH_3I), Equation 4.5,[127] or above 110°C to hydrogen iodide (HI) and methylamine (CH_3NH_2, MA), Equation 4.6,[128] a chemical vapor deposition route to forming the MAPI perovskite seems to be possible, by mixing either combinations of the decomposition precursors with lead(II)iodide (PbI_2).

Equation 4.5 $CH_3NH_3I \rightleftharpoons NH_3 + CH_3I$

Equation 4.6 $CH_3NH_3I \rightleftharpoons HI + CH_3NH_2$

The standard route to synthesize the MAI salt is by mixing an ethanol, or methanol - MA solution with hydroiodic acid, HI (aq.).[129-131] For further purification and recrystallization, a considerable amount of solvents like diethyl ether, or isopropanol are used. Synthesizing MAPI from PbI_2 by directly using either the combination of MA and HI with the respective boiling temperatures of -6 ° and -35 °C, or NH_3 and CH_3I (-33.1°C, resp. 42,1°C) would thus present alternative routes. An industrially established process that could achieve this would be within reach as it would allow the development of a highly up-scalable chemical vapor deposition (CVD) process.

For testing different combinations of precursors for the production of perovskites, a custom-built CVD device has been developed and employed, as presented in Figure 4.46 and Figure 4.47.

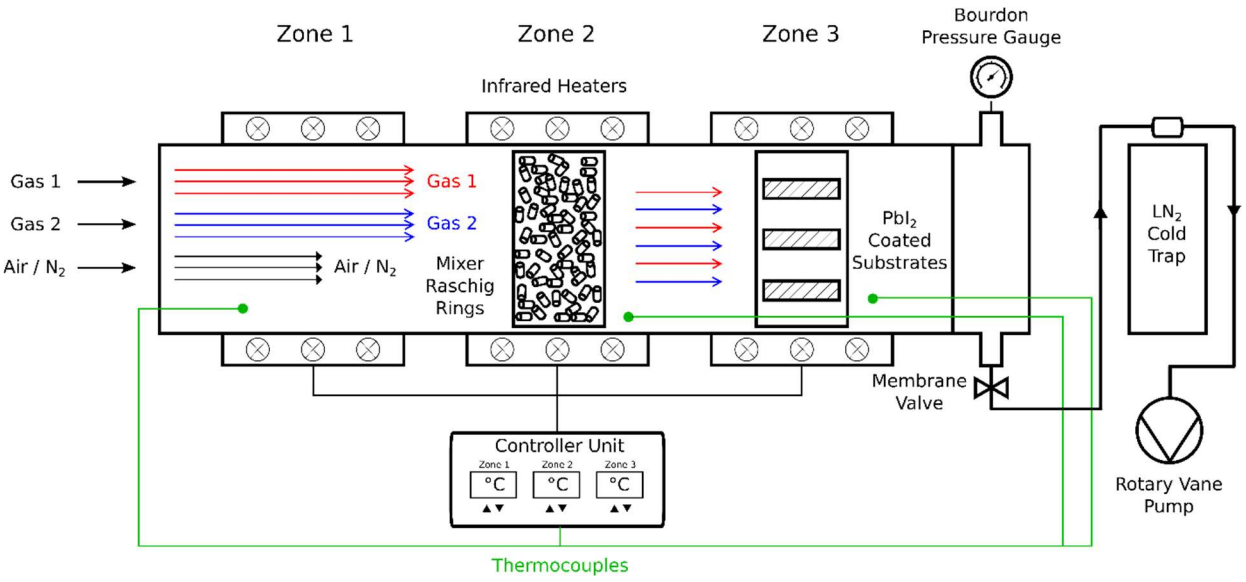

Figure 4.46 Schematic draft of the Chemical Vapor Deposition (CVD) setup

Figure 4.47 Chemical Vapor Deposition (CVD) setup in a laboratory hood

The main body consists of a three-zone tube furnace equipped with infra-red heaters and a reaction glass tube (78 cm length and 5 cm diameter) with KF (klein flange) vacuum flanges. The temperature in each zone can be controlled by feedback-loops of K-type thermocouples with feedthroughs inside the glass tube. Metal holders can hold up to three substrates, stacked

vertically. In this setup, different types of gases can be inserted into the reaction tube, the pressure of which can be monitored using a Bourdon pressure gauge. Surrounding air, or nitrogen is filled in by a manually controlled ball valve. The complete setup can be evacuated to about 1 mbar (measured with a Pirani pressure gauge) with the help of a magnetic coupling rotary vane pump for corrosive gases. A manual membrane valve is used to disconnect the vacuum line from the reaction tube. To hinder condensation of the reactive gases inside the rotary vane pump, a cold trap with liquid nitrogen (LN_2) is connected between the reaction tube and the pump.

4.4.1 $CH_3I + NH_3$

Since there are no known publications on using the combination of the precursors CH_3I and NH_3 reacting with a substrate coated with PbI_2 to form the MAPI perovskite ($CH_3NH_3PbI_3$), it would be a novelty, if conditions were found, which would prove their reaction according to the proposed Equation 4.7. To test the combination of these chemicals, a simple laboratory apparatus has been set up as seen in Figure 4.48. It comprises of a glass bell having a hose inlet covering a Petri dish, which holds **a)** a glass container with liquid methyl iodide (CH_3I) next to a Glass/FTO/c-TiO_2/m-TiO_2/PbI_2 substrate, prepared as described in Chapter 4.1.1 and **b)** an aluminum dish with a Glass/FTO/c-TiO_2/m-TiO_2/PbI_2 substrate immersed in methyl iodide. To evaporate the methyl iodide (T_{boil} = 42,1°C), the Petri dish is heated to 60°C, creating a CH_3I atmosphere under the glass bell. Through a hose, a light flow of ammonia gas (NH_3) can be passed under the glass bell from a steel lecture bottle. The pressure regulator of the steel bottle can be flushed with argon gas.

Equation 4.7 $$PbI_2 + CH_3I + NH_3 \overset{?}{\rightleftharpoons} CH_3NH_3PbI_3$$

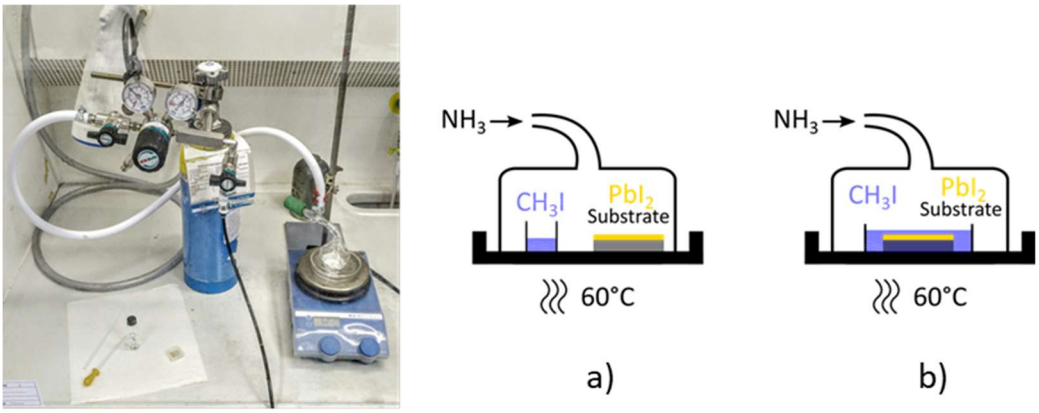

Figure 4.48 Apparatus und a laboratory hood having a glass bell connected to an ammonia (NH_3) lecture bottle and covering a Petri dish on a hot plate. Setup **a)** a glass container with liquid methyl iodide (CH_3I) next to a Glass/FTO/c-TiO_2/m-TiO_2/PbI_2 substrate. Setup **b)** an aluminum dish with a Glass/FTO/c-TiO_2/m-TiO_2/PbI_2 substrate immersed in methyl iodide (CH_3I)

For setup **a)** in Figure 4.48, passing ammonia under the glass bell, immediately turns the yellow PbI_2 substrate transparent. In the glass container with the CH_3I, a small amount of white precipitate forms, presumably MAI (CH_3NH_3I). Upon flushing the pressure regulator and the glass bell with argon, the transparent substrate immediately turns back to yellow, indicating a metastable complex forming between the NH_3 and the PbI_2. No brown coloration on the yellow PbI_2 substrate is visible, which would be attributed to MAPI. Upon immersing the PbI_2 substrate in the liquid methyl iodide as Figure 4.48 **b)** shows, the yellow substrate immediately turns transparent again while inserting the NH_3 gas, even though the substrate is immersed in the liquid CH_3I. This time no white precipitate can be observed. The transparent substrate immediately turns back to yellow when purging with argon. Under these chosen conditions Equation 4.7 does not take place.

Studies of complexes which form between ammonia and lead(II)iodide are found in literature.[132, 133] Species like $PbI_2(NH_3)_{1.3}$, $PbI_2(NH_3)_{2.47}$ or $PbI_2(NH_3)_4$ can form, whereas the latter compound is completely transparent, while the complexes with less ammonia content are reported to be white to pale yellow.

Other experiments involving ammonia (NH_3) and methyl iodide (CH_3I) have been carried out in a prototype CVD apparatus as seen in Figure 4.49. In a glass tube wrapped with an electrical heating band, ammonia can be inserted from a lecture bottle. Liquid methyl iodide is also connected to the tube, using a glass valve. The tube can be evacuated with the help of a rotary vane pump that is also connected to the tube with a glass valve in between. Methyl iodide with a boiling temperature of 42,1°C at standard pressure, easily evaporates into the tube at lower pressures, when using the pump, even at room temperature.

Figure 4.49 **Left:** prototype of the chemical vapor deposition apparatus. **Right:** experiment of passing methyl iodide (CH_3I), resp. ammonia (NH_3) over a MAPI substrate produced in a two-step spin coating and chemical bath process

A noteworthy experiment using this setup is shown on the right in Figure 4.49. When passing CH_3I and NH_3 over an FTO/c-TiO_2/m-TiO_2/MAPI substrate, which was produced in the two-step spin coating and chemical bath process (Chapter 4.1.1), an obvious discoloration of the brown MAPI can be observed in both cases. An irreversible discoloration towards yellow (color of PbI_2) due to ammonia is most prominent. This means that even if conditions were found, under which the substances PbI_2, NH_3 and CH_3I would react, special care would have to be taken, to avoid that excess NH_3, or CH_3I would decompose the perovskite. A possible reaction between the MAPI perovskite and NH_3 is proposed in Equation 4.8.

Equation 4.8 $$CH_3NH_3PbI_3 + NH_3 \overset{?}{\rightleftharpoons} CH_3NH_2\uparrow + PbI_2 + NH_4I$$

In an experiment performed in a version of the CVD apparatus shown in Figure 4.47, CH_3I and NH_3 are inserted together into the reaction tube, alongside a substrate spin coated with PbI_2. As seen in Figure 4.50, NH_3 can be filled into the reaction tube from a lecture bottle using a standard gas bottle pressure regulator. A glass tube containing CH_3I is connected to the CVD reaction tube with a ball valve and a ball check valve, whose spring was calibrated to close at ca. 400 mbar against normal pressure. In the evacuated CVD reaction tube, ca. 400 mbar CH_3I are inserted by heating its glass container to 65°C in a water bath. NH_3 is then added to the CVD reaction tube, filling the atmosphere to ca. 1 bar. The gases are left to react with a substrate coated with a film of spin coated PbI_2 for several hours at 100°C.

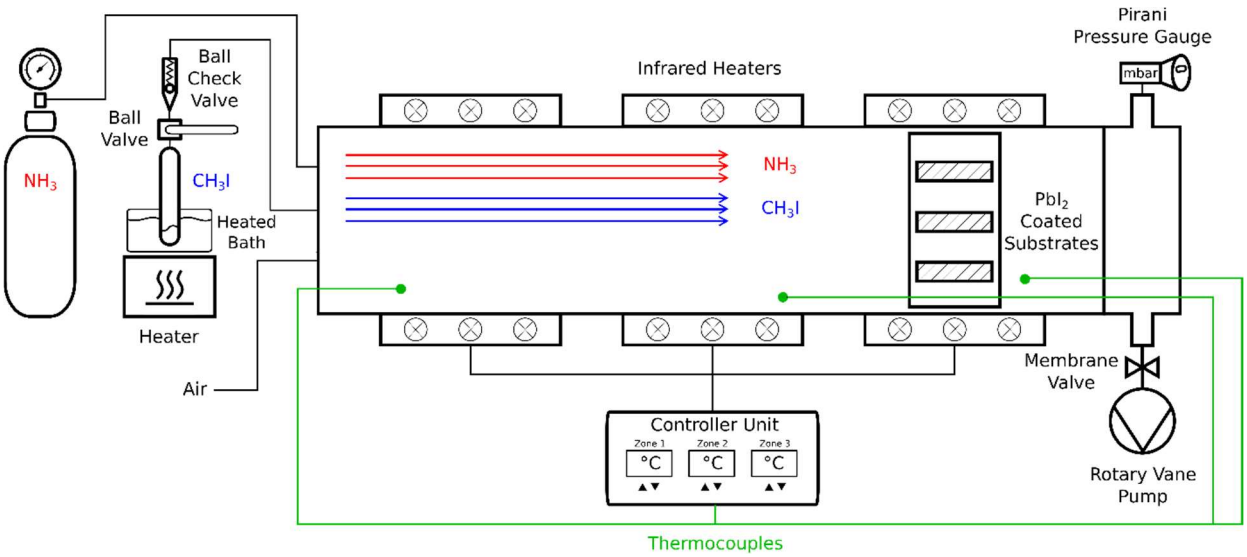

Figure 4.50 Schematic draft of the Chemical Vapor Deposition (CVD) setup, in the ammonia (NH_3) and methyl iodide (CH_3I) version

During the insertion of the NH_3, the yellow PbI_2 substrate becomes completely transparent, indicating the formation of the $PbI_2 \cdot xNH_3$ complex. After several hours, the reacted substrate appears white, with a few brown spots, as seen in Figure 4.51 and does not turn fully dark brown as expected for the MAPI perovskite.

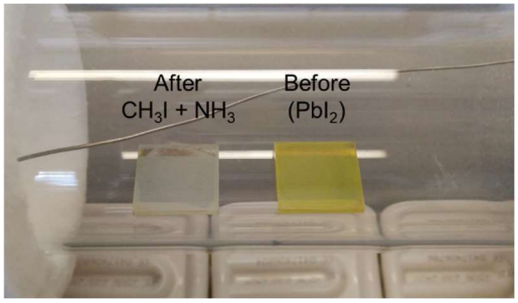

Figure 4.51 **Left,** reacted substrate after treatment with an atmosphere of CH_3I and NH_3 for several hours. **Right,** the appearance of a representative Glass/FTO/c-TiO_2/m-TiO_2/PbI_2 substrate, before the treatment

Another method of synthesizing a perovskite is through cationic exchange. For example, the methylammonium ($CH_3NH_3^+$) component in MAPI can be replaced by formamidinium ($CN_2H_5^+$) in a formamidine (CN_2H_4) atmosphere to produce the perovskite FAPI (formamidinium lead iodide, $CN_2H_5PbI_3$).[134] Another example is the replacement of ammonium (NH_4^+) in NH_4PbI_3 with methylammonium ($CH_3NH_3^+$) in a methylamine (CH_3NH_2) atmosphere to form MAPI.[135] Since methylamine and formamidine are both gases at standard conditions, they are suitable for use in the CVD process. Furthermore, both reactions are self-limiting and selective. The wet chemical synthesis of NH_4PbI_3 is published.[136] This material would be suitable as a precursor to synthesize both MAPI and FAPI in a CVD procedure, using methylamine gas, resp. formamidine gas through cationic exchange.

An attempt to synthesize NH_4PbI_3 in the CVD device is made from the $PbI_2 \cdot xNH_3$ complex and hydrogen iodide gas (HI), according to the assumed reaction in Equation 4.9. The manufacturing method of the hydrogen iodide gas will be explained later, in the next Chapter 4.4.2.

Equation 4.9 $$PbI_2 + NH_3 + HI \overset{?}{\rightleftharpoons} NH_4PbI_3$$

A spin coated PbI_2 substrate is inserted in the CVD reaction tube, which is evacuated and filled with 1 bar of NH_3 for 24 hours. After evacuation of the ammonia, the substrate turns from transparent, back to yellow. Subsequently the substrate is treated with an atmosphere of HI

gas for 20 hours, evacuated and characterized by XRD in air. The resulting measurement is shown in Figure 4.52. A comparison of this measurement with a reference NH_4PbI_3 spectra shows that the desired material did not form. A reaction did take place, as the reacted substrate is not covered with PbI_2 any longer, as shown by the comparison with the PbI_2 reference spectra. Noticing that the desired material did not form, this reaction pathway was not followed further.

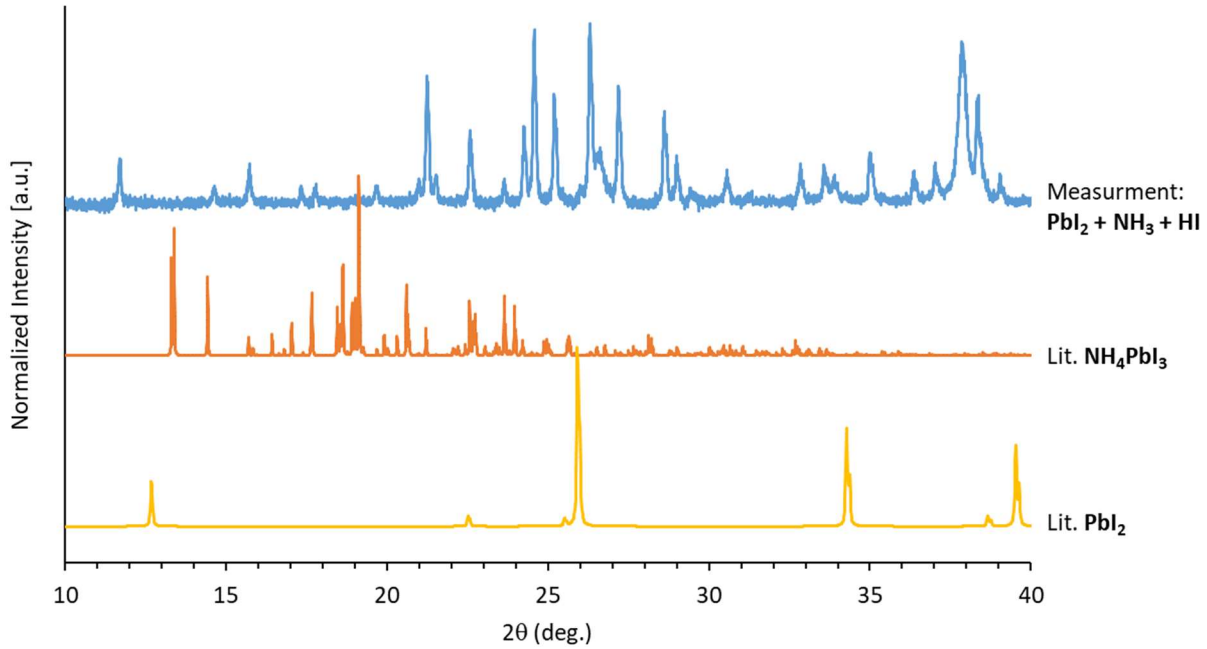

Figure 4.52 XRD measurement of a Glass/FTO/c-TiO_2/m-TiO_2/PbI_2 substrate treated first in an atmosphere of NH_3 gas, then in an atmosphere of HI gas, in comparison to literature reference patterns of NH_4PbI_3 [137] and PbI_2 [138]

4.4.2 $HPbX_3$ powders

Hydrogen lead iodide ($HPbI_3$) was first reported in 2015 by Wang et al.,[139] who used it as a precursor to produce the FAPI perovskite, formamidinium lead iodide. To synthesize $HPbI_3$, the authors use PbI_2 as a precursor reacting it with a surplus of hydroiodic acid ($HI_{aq.}$), in the solvent DMF (dimethylformamide), as shown by Equation 4.10.

Equation 4.10 $$PbI_2 + HI_{aq.} \overset{DMF}{\rightleftharpoons} HPbI_3$$

Afterwards they have mixed the synthesized $HPbI_3$ in a 1:1 mol ratio with FAI (CN_2H_5I) in DMF to spin coat layers of FAPI perovskite ($CN_2H_5PbI_3$). Their solar cells reach a reported efficiency of up to 17,5%.
Cheng et al. and Pang et al.[140, 141] used spin coated $HPbI_3$ to form the MAPI perovskite using methylamine gas and produced solar cells with efficiencies of 13,2%, resp. 18,2%.

Thus $HPbI_3$ seems to be a well-suited precursor to produce the MAPI and the FAPI perovskites using the CVD method. In this chapter the novel synthesis attempt of $HPbI_3$ in a CVD approach is described, starting from a spin coated layer of PbI_2 and self-produced HI gas, according to Equation 4.11, without the use of the solvent DMF.

Equation 4.11 $$PbI_2\,(s) + HI\,(g) \overset{?}{\rightleftharpoons} HPbI_3\,(s)$$

In addition, the novel synthesis attempt of mixed bromide and iodide containing species like $HPbBr_3$, $HPbIBr_2$ and $HPbI_2Br$ are described. These species would also be suited to synthesize a range of iodide and bromide lead perovskites which have a larger band gap and thus a larger open circuit voltage V_{OC} than perovskites containing only the iodide component.[142, 143]

First, the synthesis of the species $HPbI_3$, $HPbI_2Br$, $HPbIBr_2$ and $HPbBr_3$ is attempted, by using the solvent DMF, following the recipe presented in the paper by Wang et al. for $HPbI_3$.[139] The respective PbX_2 salts (X = halide) are mixed with the HX aqueous acids in a 1 : 1.5 mol ratio in the solvent DMF in four glass vials. The assumed reactions are shown in

Equation 4.12 – Equation 4.15. The amounts of the respective substances are summarized in Table 4.10. A more detailed table including the densities, molar masses and the number of moles for the respective precursors is shown in the Appendix Table 9.4.

Equation 4.12 PbI_2 (DMF) + HI (aq.) $\overset{?}{\rightleftharpoons} HPbI_3$

Equation 4.13 PbI_2 (DMF) + HBr (aq.) $\overset{?}{\rightleftharpoons} HPbI_2Br$

Equation 4.14 $PbBr_2$ (DMF) + HI (aq.) $\overset{?}{\rightleftharpoons} HPbIBr_2$

Equation 4.15 $PbBr_2$ (DMF) + HBr (aq.) $\overset{?}{\rightleftharpoons} HPbBr_3$

Table 4.10 Amounts of precursors to produce the hydrogen lead halide compounds: $HPbI_3$, $HPbI_2Br$, $HPbIBr_2$ and $HPbBr_3$

Solution	DMF Solvent [mL]	Substance	Mass [g]	Substance	Volume [mL]
1	2	PbI_2	1	$HI_{aq.}$ (57w%)	0,429
2	2	PbI_2	1	$HBr_{aq.}$ (47w%)	0,376
3	2	$PbBr_2$	1	$HI_{aq.}$ (57w%)	0,540
4	2	$PbBr_2$	1	$HBr_{aq.}$ (47w%)	0,472

An image of the four solutions after 17 h of stirring at 70°C is shown in Figure 4.53 **left**. On the **right**, the resulting powders are shown, after the DMF has been evaporated in a laboratory hood in atmosphere at 150°C on a hot plate and washed twice with diethyl ether. For additional drying, the powders are kept 20 h under low vacuum at room temperature.

Figure 4.53 **Left:** DMF precursor solutions for the hydrogen lead halide compounds, from left to right: PbI_2 + $HI_{aq.}$ (orange), $PbBr_2$ + $HI_{aq.}$ (yellow), PbI_2 + $HBr_{aq.}$ (yellow) and $PbBr_2$ + $HBr_{aq.}$ (white). **Right:** The powder precipitates from the respective DMF solutions, from left to right: PbI_2 + $HBr_{aq.}$ (yellow), PbI_2 + $HI_{aq.}$ (yellow), $PbBr_2$ + $HBr_{aq.}$ (white), and $PbBr_2$ + $HI_{aq.}$ (yellow)

Powder XRD measurements were conducted on the four compounds from Figure 4.53 **Right**, shown in Figure 4.54. The peak positions and relative intensities are summarized in Table 4.11.

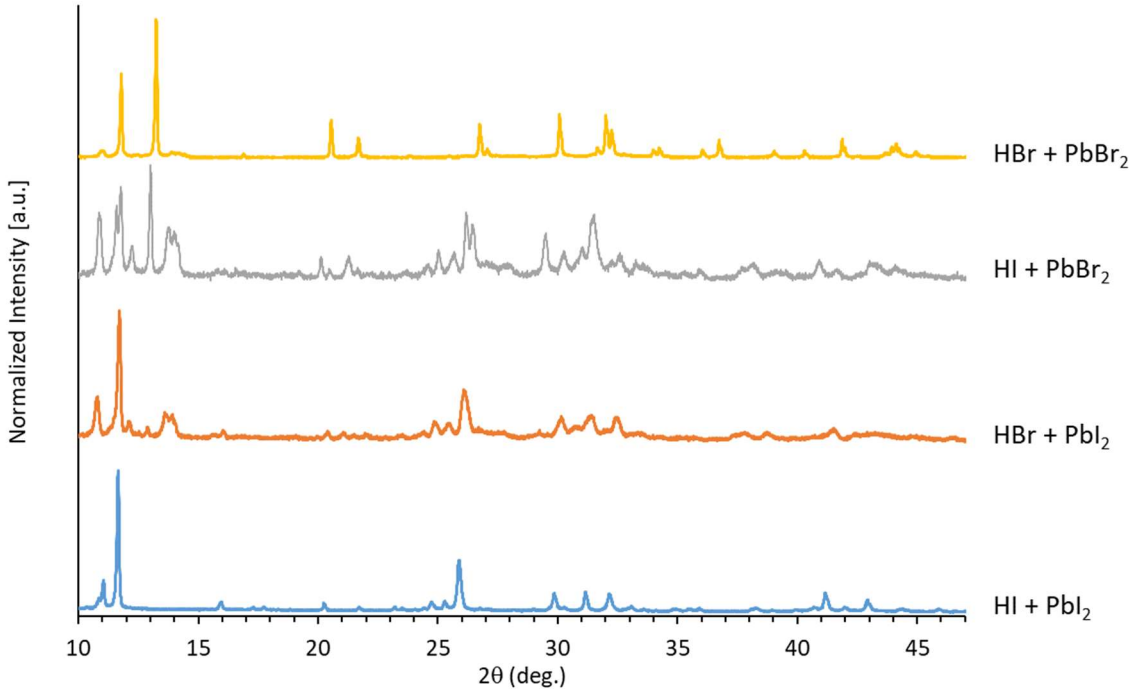

Figure 4.54 XRD measurements of powders made from aqueous halide acids (HI and HBr) and the respective lead halide salts (PbI_2 and $PbBr_2$) in the solvent DMF

The XRD pattern of the powder HI + PbI_2 from DMF (Figure 4.54, in blue) coincides with both measurements reported by Wang et al.[139] and Pang et al.[140, 141] for $HPbI_3$. Merely the first peak at 11,0° 2θ is missing in the publications and could be attributed to an impurity phase in the product. Published XRD data about the other three compounds that include the bromide component could not be found in literature.

Table 4.11 Peak positions and relative intensities of the XRD measurements in Figure 4.54 of powders made from aqueous halide acids (HI and HBr) and the respective lead halide salts (PbI_2 and $PbBr_2$) in the solvent DMF

HI + PbI_2 (DMF)		**HBr + PbI_2 (DMF)**		**HI + $PbBr_2$ (DMF)**		**HBr + $PbBr_2$ (DMF)**	
2 θ [°]	Rel. Intensity [%]	2 θ [°]	Rel. Intensity [%]	2 θ [°]	Rel. Intensity [%]	2 θ [°]	Rel. Intensity [%]
11,0	23,6	10,8	71,0	10,8	85,2	11,0	80,0
11,7	100,0	11,7	100,0	11,5	86,1	11,8	93,3
16,0	8,4	13,8	65,2	11,7	91,5	13,2	100,0
20,2	8,8	14,0	63,8	12,1	77,6	20,6	84,8
24,7	9,0	24,8	63,3	12,7	100,0	21,7	81,8
25,2	9,0	25,5	62,4	13,7	82,0	26,7	84,0
25,9	35,6	26,2	73,3	13,9	82,0	30,1	85,5
29,9	15,4	30,2	64,8	20,0	75,7	32,0	85,8
31,0	15,0	31,5	65,2	21,0	75,7	32,3	82,8
32,2	14,7	32,5	65,2	25,0	77,6	36,8	80,8
41,2	13,8	41,6	61,9	25,6	77,0	41,9	81,5
43,0	8,3			26,2	86,1	44,1	81,0
				26,4	82,6		
				29,4	81,1		
				30,1	77,3		
				30,9	78,2		
				31,4	85,2		
				32,4	76,3		
				38,0	75,4		
				40,8	76,3		

The $HPbI_3$ powder was tested once in a solar cell device by spin coating an $HPbI_3$/DMF solution, combined with the CVD procedure. 709 mg $HPbI_3$ were dissolved in 1 mL DMF (1,2 M solution) at 80°C in an argon glovebox. The Glass/FTO/c-TiO_2/m-TiO_2 substrate, produced as described in Chapter 4.1.2 is first treated 15 min. in a UV/ozone oven, then heated at 80°C for 2 min. in the argon glovebox. 100 µL of the $HPbI_3$/DMF solution is spin coated onto the hot substrate at 108 rps for 90 s, then dried 10 min. at 80°C. For transforming the $HPbI_3$ to MAPI perovskite accord-

ing to Equation 4.16, a methylamine (CH_3NH_2) gas bottle is connected to the CVD setup as shown in Figure 4.55.

Equation 4.16 $HPbI_3 + CH_3NH_2 \rightleftharpoons CH_3NH_3PbI_3$

The Glass/FTO/c-TiO_2/m-TiO_2/$HPbI_3$ substrate is inserted in the CVD reaction tube, evacuated to ca. 1 mbar, then filled with 100 mbar of methylamine. At this step, the substrate turns from a light gray colored film ($HPbI_3$), to completely transparent (methylamine complex) as seen in Figure 4.56. After several seconds, the reaction tube is evacuated. At this point the transparent substrate (methylamine complex) immediately turns brown (MAPI perovskite), see Figure 4.56. After filling the reaction tube with 1 bar of air, the substrate is annealed 10 min. at 130°C.

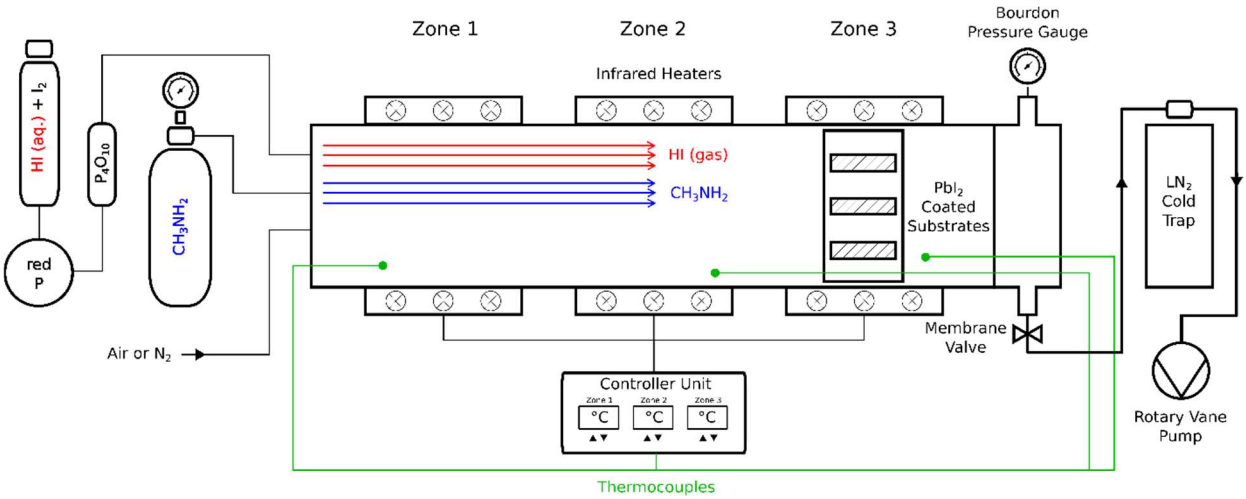

Figure 4.55 Schematic draft of the Chemical Vapor Deposition (CVD) setup, in the hydrogen iodide (HI) gas and methylamine (CH_3NH_2) version

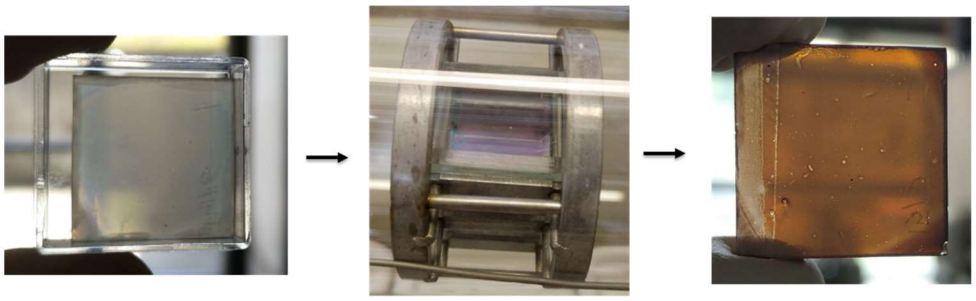

Figure 4.56 **Left:** light gray colored $HPbI_3$ covered substrate. **Middle:** transparent substrate in the CVD reaction tube surrounded by methylamine gas. **Right:** MAPI ($CH_3NH_3PbI_3$) perovskite substrate after the CVD reaction, photographed in air

The Glass/FTO/c-TiO_2/m-TiO_2/MAPI substrate produced from spin coating $HPbI_3$ and treating it with methylamine gas in the CVD apparatus is now spin coated with the spiro-MeOTAD hole transport layer and sputtered with gold as described in Chapter 4.1.2, to complete the solar cell. The average efficiency of the 4 solar cells on the substrate made by spin coating $HPbI_3$, then treating it with MA gas in the CVD device amounts to 6,5 %. The IV-curve of the best solar cell, including all relevant information like maximum power point, open circuit voltage and short circuit current are shown in Figure 4.57, having an efficiency of 7,7 % (measured with the maximum power point tracking protocol). A 10 h tracking of the efficiency of this solar cell can be seen in Figure 4.58. After 2,5 h illumination with an AM1.5G spectrum, the solar cell exhibits its maximum efficiency with 8,45 %. This increase in efficiency could either be attributed to an annealing effect of the perovskite due to the heat of the solar simulator lamp, by which defects could be healed, or to a further enhancement of the reaction of still free MA gas and $HPbI_3$ on the substrate, forming additional MAPI perovskite. After 10 h, the substrate still shows an efficiency of 7,1 %. The intermittent sharp decreases and increases of the efficiency seen in this graph (Figure 4.58) are caused by a fault in the electronics of the solar simulator at the time of this measurement. A defective micro-transformer caused the lamp to flicker, giving rise to an irregular intensity of the light. For the same reason, the measurements of the solar cell from Figure 4.57 are questionable as well.

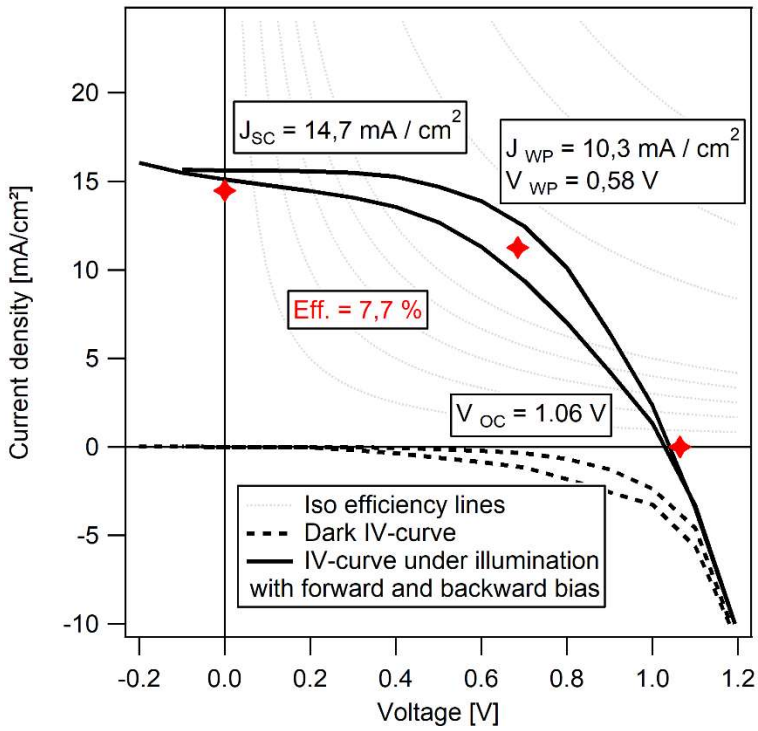

Figure 4.57 IV-curve of the best glass/FTO/c-TiO_2/m-TiO_2/MAPI/spiro-MeOTAD/Au cell produced by spin coating a layer of $HPbI_3$ on the m-TiO_2 and treating it with methylamine (MA) gas in the CVD setup from Figure 4.55

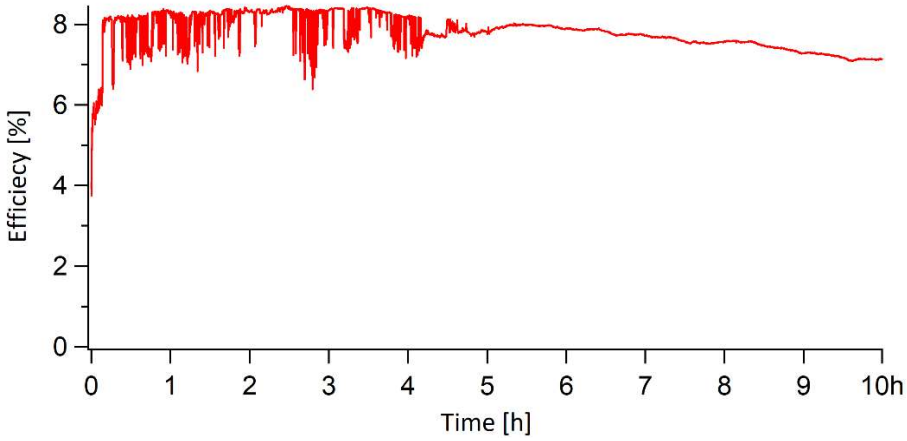

Figure 4.58 Ten hour measurement of the efficiency of the solar cell from Figure 4.57 (glass/FTO/c-TiO_2/m-TiO_2/MAPI/spiro-MeOTAD/Au), produced by spin coating a layer of $HPbI_3$ on the m-TiO_2 and treating it with methylamine (MA) gas in the CVD setup from Figure 4.55

As already discussed, preparing the hydrogen lead iodide ($HPbI_3$) species by a wet chemical route from lead iodide (PbI_2) in dimethylformamide (DMF) and hydroiodic acid ($HI_{aq.}$) has already been published.[139-141] Since DMF is toxic, an alternative method to transform a film of lead iodide (PbI_2) to $HPbI_3$ in a CVD procedure using hydrogen iodide (HI) gas would be favorable. Finding a vendor who sells bottled HI gas has been unsuccessful. For this reason, a chemical glass apparatus has been built and connected to the CVD reaction tube as shown in Figure 4.55, to produce self-made HI gas from hydroiodic acid ($HI_{aq.}$), according to literature.[144]

The glass setup used to produce the HI gas can be seen in Figure 4.59. Hydroiodic acid ($HI_{aq.}$, 57 wt%, Merck), mixed with solid iodine (I_2, double sublimated, generic, Laborladen) in a 1:2 weight ratio is added from a dropping funnel to a round-bottom flask containing excess red phosphorous (P_{red}, min. 98%, generic, Laborladen).[144] The evolving HI gas is passed through the drying agent phosphorus pentoxide (P_4O_{10}, Sicapent, Merck), before entering the reaction tube, further removing possible water vapor from the formed gas.

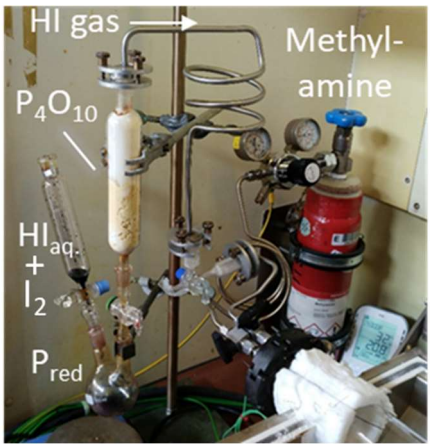

Figure 4.59 Glass apparatus used for the production of hydrogen iodide (HI) gas, which is connected to the CVD reaction tube, seen in Figure 4.47 and Figure 4.55

To try forming the $HPbI_3$ species in the CVD setup, a Glass/FTO/c-TiO_2/m-TiO_2/PbI_2 substrate produced as described in Chapter 4.1.2 is placed in the CVD reaction tube and evacuated to ca. 1 mbar. Ca. 200 mbar of HI gas are inserted, produced by dropping the $HI_{aq.}/I_2$ solution on P_{red} and passed through P_4O_{10}. The PbI_2 substrate is left in the HI atmosphere for 20 h. In this

amount of time, air from the surroundings fill the non-airtight CVD reaction tube. After the treatment, the substrate still appears as yellow as before, indicating lead iodide and does not exhibit the light gray color seen from the spin coated $HPbI_3$ in Figure 4.56. An XRD measurement of the film is recorded, to check whether a small amount of $HPbI_3$ has formed under the given conditions. The blue curve in Figure 4.60 represents the measurement of the PbI_2 substrate treated with HI gas. Comparing the position of the peaks with the produced $HPbI_3$ powder and a literature curve of PbI_2,[138] it is clear that the substrate did not react and is still only covered with PbI_2, with no trace of the $HPbI_3$ compound.

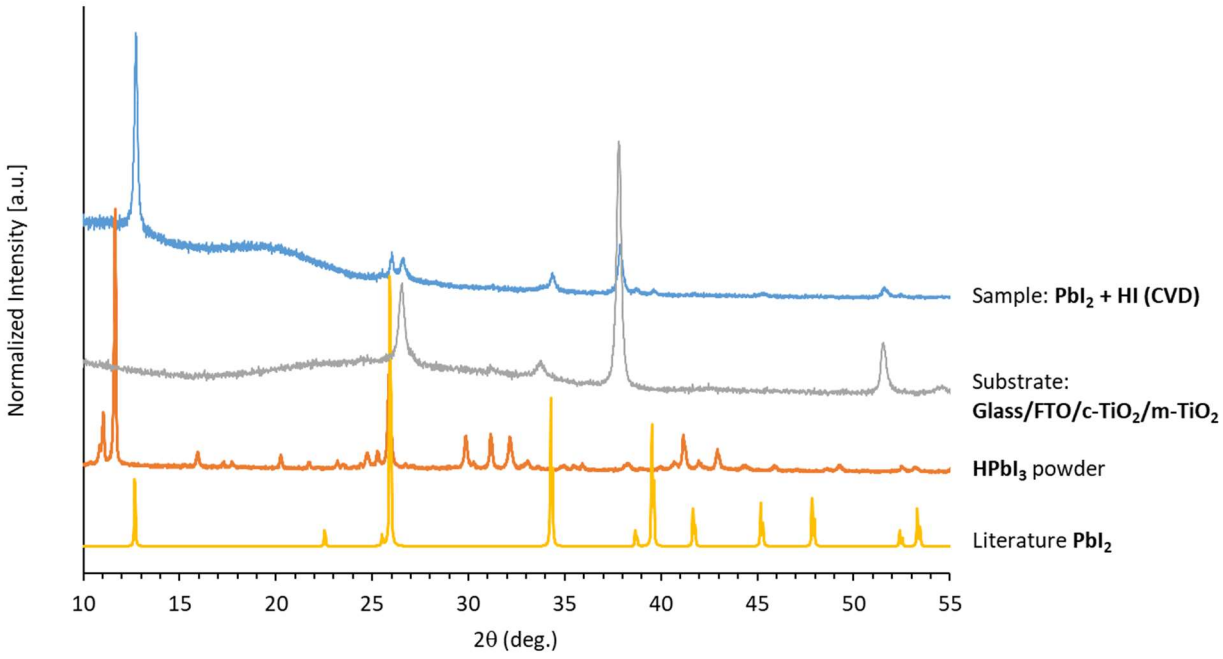

Figure 4.60 XRD measurement of a Glass/FTO/c-TiO_2/m-TiO_2/PbI_2 substrate treated in an HI gas atmosphere, then in an atmosphere of HI gas, alongside literature reference spectra of NH_4PbI_3 [137] and PbI_2 [138]

This experiment raises the question whether the reaction of PbI_2 with hydroiodic acid ($HI_{aq.}$) forming $HPbI_3$ only works in the presence of the solvent dimethyl formamide (DMF). To test this hypothesis in an experiment, a series of solvents have been used to mix the lead iodide salt (PbI_2) with hydroiodic acid ($HI_{aq.}$): DMF, ethanol, methanol, water, γ-butyrolactone (GBL), DMSO and acetone in the same amount as the original recipe with DMF (2 mL). The resulting powders can be seen in Figure 4.61. Only the powder in DMF exhibits the neon-yellow color of

$HPbI_3$ (glass vial Nr. 2 in Figure 4.61). All other powders have either the same color as the lead iodide from glass vial Nr. 1, or a brown (DMSO) or even black color (acetone). This simple visual inspection leads to the conclusion that $HPbI_3$ only forms from PbI_2 + $HI_{aq.}$ in the solvent DMF.

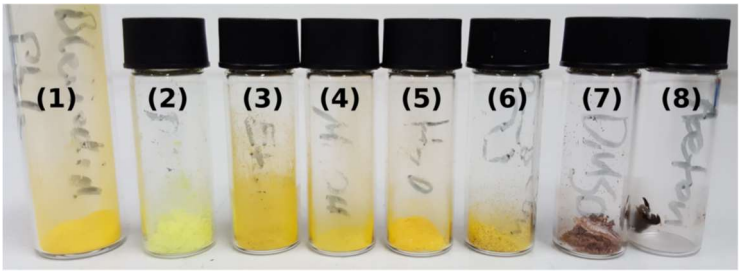

Figure 4.61 Experiment of mixing PbI_2 (**(1)**: reference powder) with $HI_{aq.}$ In a series of solvents: **(2):** DMF, **(3):** ethanol, **(4):** methanol, **(5):** water, **(6):** γ-butyrolactone (GBL), **(7):** DMSO and **(8):** acetone

A recent study published in Nature Communications by Ke et al. called "Myths and reality of $HPbI_3$ in halide perovskite solar cells"[145] prove through NMR and XRD measurements that the compound previously thought to be $HPbI_3$ is in fact $DMAPbI_3$: dimethylammonium lead iodide. Both compounds have the same XRD pattern, but different 1H-NMR spectra.[145] The mechanism of the reaction involves the solvent dimethyl formamide (DMF), that can hydrolyze, forming dimethylamine (DMA) and formic acid (HCOOH). The hydroiodic acid (HI) significantly accelerates the reaction shown in Equation 4.17, shifting the equilibrium towards the dissociation products of DMF. The dimethylammonium iodide (DMAI) can react with PbI_2 forming the perovskite $DMAPbI_3$.

Equation 4.17 $HCON(CH_3)_2$ (DMF) + HI + $H_2O \rightleftharpoons (CH_3)_2NH_2I$ (DMAI) + HCOOH

In conclusion, the reactions between the lead salts PbX_2 (X= I, Br) and the halide acids (HI and HBr) prepared in DMF as shown in Figure 4.53 and Figure 4.54 are most likely dimethylammonium lead halides $DMAPbX_3Y_{x-3}$ (X, Y = I and Br) and CVD reactions of lead halide films, PbX_2 (X= I, Br) and the halide acid gases HI and HBr are evidently not possible.

4.4.3 CH_3NH_2 + HI (aq.)

As mentioned in the introduction in Chapter 4.4 and in Equation 4.6, methylammonium iodide, a common precursor for the MAPI perovskite can decompose to methylamine (MA, CH_3NH_2) and HI gas when heated.[128] It would thus make sense to bring the two components MA and HI together onto PbI_2 to form the MAPI perovskite according to Equation 4.18

Equation 4.18 $$CH_3NH_2 + HI + PbI_2 \overset{?}{\rightleftharpoons} CH_3NH_3PbI_3$$

One possibility would be to insert the two gases MA and HI together in the CVD setup, forming MAI, according to Equation 4.19. The salt ($CH_3NH_3^+ I^-$), that is solid at room temperature would have had to be kept above its boiling point to be able to transport it properly through the CVD tube to reach the PbI_2 substrates and form the MAPI perovskite. Presumably, the salt would evaporate either as its constituting compounds, or as clusters of the crystal lattice. This process has not been attempted for several reasons. Challenges like blockage of the gas pipes through condensation of the MAI salt in them, or an excess amount of MAI deposition on top of the eventually formed MAPI film with an additional layer of unwanted MAI, would have had to be overcome. Additionally, a number of publications already exist that describe CVD processes for creating the MAPI perovskite from the MAI salt. In 2013, Chen et al.[146] introduced a new process called VASP (vapor assisted solution process), that involves spin coating the PbI_2 salt wet chemically, then exposing it to a vapor of heated MAI in a closed chamber to create the MAPI perovskite. Their solar cells achieved a PCE of 12,9 %. Similar, improved processes have been published since, many involving tubular arrangements to transport the MAI vapor to PbI_2 layers,[147-153] of which the best known reported efficiency for MAPI solar cells is 18,9 %.[154]

Equation 4.19 $$CH_3NH_2\ (MA) + HI \rightleftharpoons CH_3NH_3I\ (MAI)$$

In this work, a different approach was targeted instead, by adding the MA and the HI sequentially, hoping for a facile controllability of the process. Furthermore this approach would not

allow the two components to react already in the gas phase, with a condensation of MAI powder in the reaction tube and everywhere else in the apparatus, making the process more clean for a reusable, industrial, up-scaled process.

When the following experiment was performed, it was not yet known that PbI_2 would not react in the presence of HI alone, to form $HPbI_3$ (as described in the previous Chapter 4.4.2), therefore a process has been tried of using two cycles of alternating hydrogen iodide (HI) and methylamine (MA) exposure to spin coated layers of lead iodide (PbI_2) in the CVD setup shown in Figure 4.62. The idea was to first convert the PbI_2 to $HPbI_3$ with the HI and then to convert the $HPbI_3$ with methylamine gas (MA) to MAPI, the absorber of perovskite solar cells, as shown by the Equation 4.20 and Equation 4.21 below. After observing that the first sequence of HI and MA transformed the yellow PbI_2 substrate into a light brown material, that from experience was not yet as dark as the spin coated MAPI, a second sequence (cycle) of HI and then MA was used hoping for of a more thorough conversion of the PbI_2. This indeed turned the substrate to a darker brown.

Equation 4.20 $$PbI_2 + HI \overset{?}{\rightleftharpoons} HPbI_3$$

Equation 4.21 $$HPbI_3 + CH_3NH_2 \rightleftharpoons CH_3NH_3PbI_3$$

The procedure is as follows. A Glass/FTO/c-TiO_2/m-TiO_2/PbI_2 substrate (prepared as described in Chapter 4.1.2) with a spin coated layer of PbI_2 is inserted in the CVD setup shown in Figure 4.62. The reaction tube is evacuated to ca. 1 mbar. A glass tube containing hydroiodic acid (57 wt%, Merck) is heated to 180°C in a water bath to saturate the reaction tube with hydroiodic acid vapor. At this point the pressure gauge does not show any increase in pressure, because the $HI_{aq.}$ vapor is a liquid/gaseous phase which does not interact with the Bourdon mechanism that detects gases. The $HI_{aq.}$ vapor is left in the tube for 10 min. An image of this stage can be seen in Figure 4.63. In the next step, the tube is evacuated and ca. 200 mbar methylamine (MA) gas are inserted. At this point the substrate immediately becomes transparent due to the formation of the $PbI_2 \cdot x\ CH_3NH_2$ complex. The MA gas is left in the reaction tube for ca. 2 min.

Upon evacuation, the substrate quickly becomes brown, indicating the formation of the MAPI perovskite. The HI and the MA steps are repeated, to have two cycles of each in the end. The substrate was then annealed at 100°C in vacuum for 1 min.

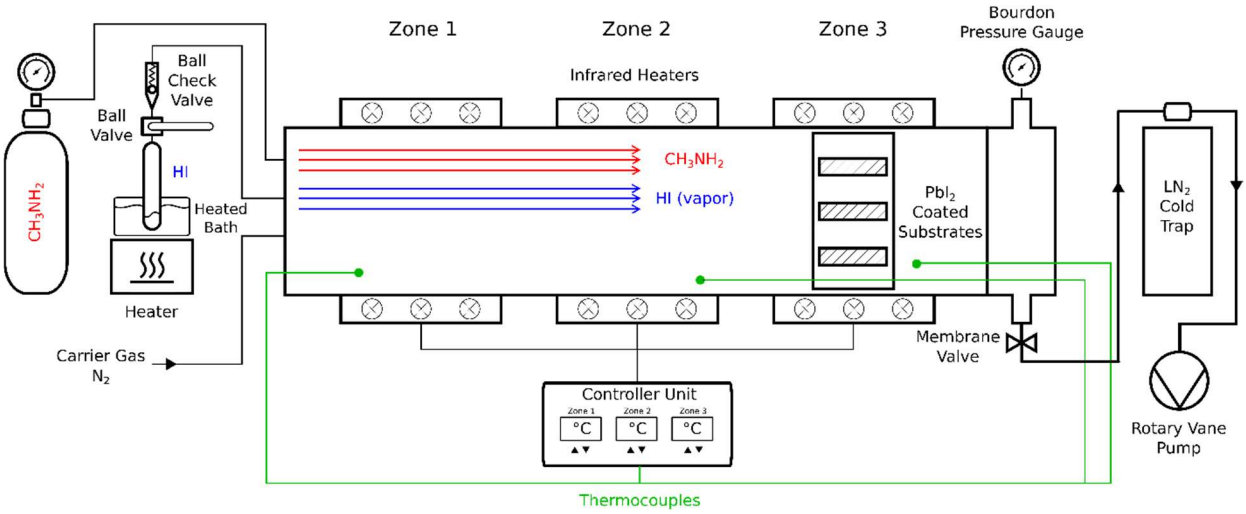

Figure 4.62 Schematic draft of the Chemical Vapor Deposition (CVD) setup, in the hydroiodic acid ($HI_{aq.}$) and methylamine (CH_3NH_2) version

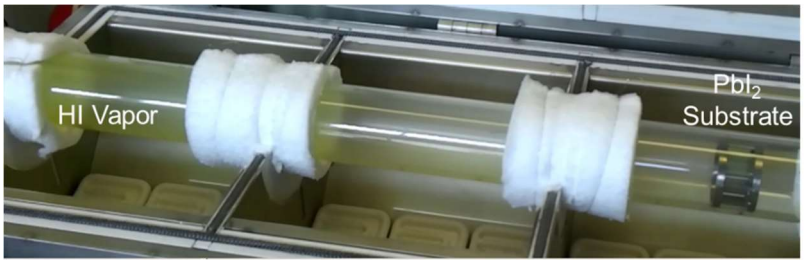

Figure 4.63 CVD reaction tube filled with hydroiodic acid ($HI_{aq.}$) and holding a substrate coated with a layer of PbI_2

Figure 4.64 a) and b) show the Glass/FTO/c-TiO_2/m-TiO_2/MAPI substrate made through the HI and MA 2-cycle CVD process. Image a) shows the substrate with light coming from the back through the substrate and image b) shows the substrate with light reflecting from above. The substrate has been completed with spiro-MeOTAD and gold layers (described in Chapter 4.1.2) as shown in image c). The best solar cell on this substrate has a low efficiency of 3,2 %. The IV curves are presented in Figure 4.65. The open circuit voltage of this solar cell of 1,04 V is com-

parable to well working cells made with the spin coating and chemical bath deposition method, but the short circuit current density of 5,2 mA / cm^2 is rather low compared to the one of a well working cell from Figure 4.13 of 24,4 mA / cm^2. The low J_{SC} could be attributed to defects in the crystal of the MAPI perovskite caused by excess of water present in the hydroiodic acid vapor ($HI_{aq.}$). Large holes are visible all over the substrate even with the naked eye (Figure 4.64), that are cause by condensation of the $HI_{aq.}$ on the surface of the substrate and also it is known from literature that water can have a detrimental impact on the performance of the cells. Water in moderate amounts can facilitate nucleation and crystallization of the perovskite, but after a certain level, it can destroy the perovskite material irreversibly, creating hydrate defects that drastically increase the band gap of the material.[155]

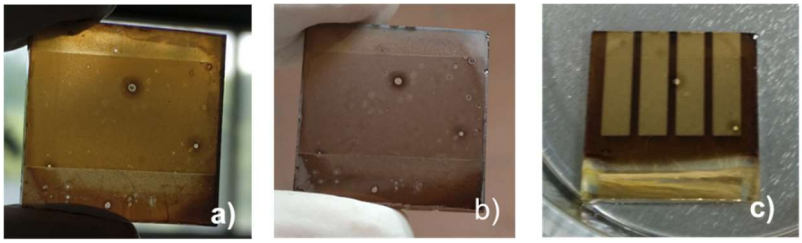

Figure 4.64 Substrate with a MAPI perovskite ($CH_3NH_3PbI_3$) layer made by a 2-cycle hydroiodic acid ($HI_{aq.}$) and methylamine (MA) CVD process. Image a) substrate covered with a MAPI film with light coming from behind, b) with light reflecting from above and c) a substrate completed with solar cells Glass/FTO/c-TiO_2/m-TiO_2/MAPI/spiro-MeOTAD/Au

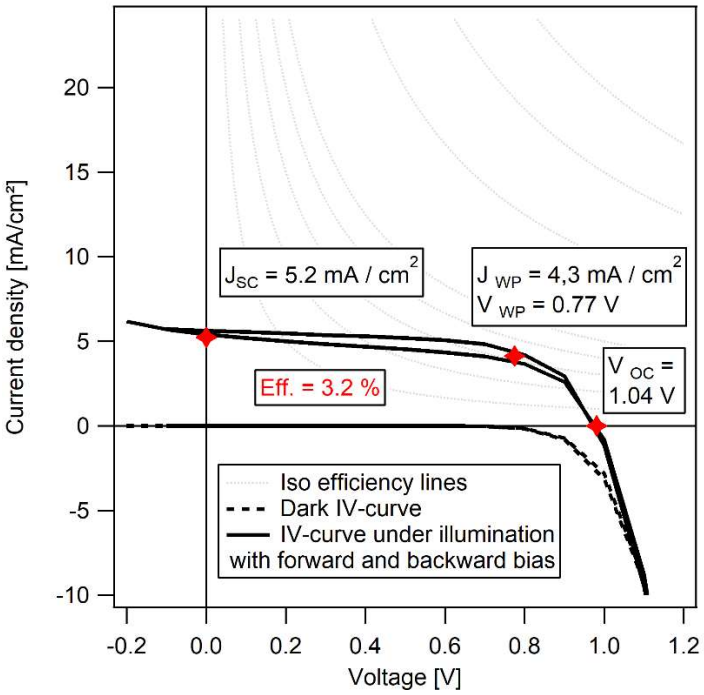

Figure 4.65 IV-curve of the best glass/FTO/c-TiO_2/m-TiO_2/MAPI/spiro-MeOTAD/Au cell produced by the 2-cycle hydroiodic acid ($HI_{aq.}$) and methylamine (MA) CVD process in the CVD setup from Figure 4.62

In the case of this type of CVD process using the hydroiodic acid ($HI_{aq.}$), the excess water hinders the formation of a smooth and continuous MAPI perovskite layer. The resulting film has many pin holes exposing the underlying m-TiO_2 layer, as shown by the optical microscopy image Figure 4.66, with a 4x magnification of a representative sample.

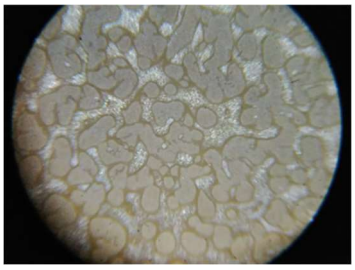

Figure 4.66 Optical microscopy image with a 4x magnification of a Glass/FTO/c-TiO_2/m-TiO_2/MAPI sample, produced by the 2-cycle hydroiodic acid ($HI_{aq.}$) and methylamine (MA) CVD process

Experiments with changed parameters like heating between steps, less amount of hydroiodic acid, different annealing temperatures, etc. have been carried out to optimize the 2-cycle $HI_{aq.}$

and MA CVD process, but the results are so far not promising, with solar cell efficiencies of 0 % to 3,2 %. A process is evidently needed, that does not involve an excess amount of water.

4.4.4 CH_3NH_2 + HI gas

The results of this sub-chapter are considered to be the most important part of this dissertation and have been summarized and published in the journal Energy Science and Engineering with the title: *Preparation of Methylammonium Lead Iodide ($CH_3NH_3PbI_3$) Thin Film Perovskite Solar Cells by Chemical Vapor Deposition (CVD) Using Methylamine Gas (CH_3NH_2, MA) and Hydrogen Iodide Gas (HI).*[156]

The previous chapter discussed the preparation of MAPI perovskite from a spin coated film of PbI_2 along with hydroiodic acid vapor ($HI_{aq.}$) and methylamine (MA) gas in the CVD setup. Since it was shown that water vapor from the $HI_{aq.}$ is detrimental for the formation of a high-quality film of MAPI perovskite, a process is introduced in this chapter that allows the production and use of pure HI gas from hydroiodic acid ($HI_{aq.}$). While in the previous chapter $HI_{aq.}$ and MA were exposed at first in this sequence, the procedure described in this chapter will reverse the sequence of use, i.e. MA then HI in multiple cycles, due to recent findings in literature of a new type of mechanism involving PbI_2, MA, H_2O and HI.

In 2015, Zhou et al.[157] was one of the first scientist to report the use of MA for healing MAPI perovskite films, describing the formation of a $CH_3NH_3PbI_3 \cdot xCH_3NH_2$ liquid phase during the perovskite-gas interaction. Many other publications have appeared soon after, which use the so-called methylamine (MA) induced defect-healing (MIDH) effect on perovskites.[141, 158-167] Raga et al.[168] reported a synthetic route to forming MAPI perovskite thin films, which implies exposure of a PbI_2 film to an atmosphere of heated methylamine from ethanol ($MA_{Eth.}$) in combination with an atmosphere of heated hydroiodic acid ($HI_{aq.}$) on a hot plate. With this method they achieved an efficiency of 12.7 % with a sequential $MA_{Eth.}$ / $HI_{aq.}$ process and 15.3 % with a simultaneous $HI_{aq.}$ + $MA_{Eth.}$ process in a beaker, on a hot plate. The paper established a reaction mechanism between the MA, HI and PbI_2, as shown in Equation 4.22 to Equation 4.26.

Water from the atmosphere is needed for the reactions in Equation 4.22 and Equation 4.23 to take place. In the MA step, Equation 4.23 and Equation 4.24, the formation of lead oxide (PbO) and lead hydroxide $Pb(OH)_2$ can be observed. These species would then be regenerated to lead iodide (PbI_2) in the HI step, according to Equation 4.25 and Equation 4.26.

Equation 4.22 $CH_3NH_2 + H_2O \rightleftharpoons CH_3NH_3OH$

Equation 4.23 $3\ PbI_2 + 2\ CH_3NH_2 + H_2O \rightleftharpoons 2\ CH_3NH_3PbI_3 + PbO$

Equation 4.24 $3\ PbI_2 + 2\ CH_3NH_3OH \rightleftharpoons 2\ CH_3NH_3PbI_3 + Pb(OH)_2$

Equation 4.25 $Pb(OH)_2 + 2\ HI_{aq.} \rightleftharpoons PbI_2 + H_2O$

Equation 4.26 $PbO + 2\ HI_{aq}. \rightleftharpoons PbI_2 + H_2O$

The version of the CVD device used in the experiments from this chapter is shown in Figure 4.67. In this setup, methylamine (MA) gas can be dosed into the reaction tube from a lecture bottle, using a standard pressure regulator. The HI gas is self-made: hydroiodic acid ($HI_{aq.}$), mixed with solid iodine (I_2) in a 1:2 weight ratio is added from a dropping funnel to a round-bottom flask containing excess red phosphorous (P_{red}).[144] The evolving HI gas is optionally passed through the drying agent phosphorus pentoxide (P_4O_{10}), before entering the reaction tube, further removing possible water vapor from the formed gas. The glass setup used to create the HI gas is shown in Figure 4.68 **left** and the CVD apparatus, while in a laboratory hood can be seen in Figure 4.68 **right**. Up to 6 substrates are inserted into the reaction tube, 3 in each of the 2 holders.

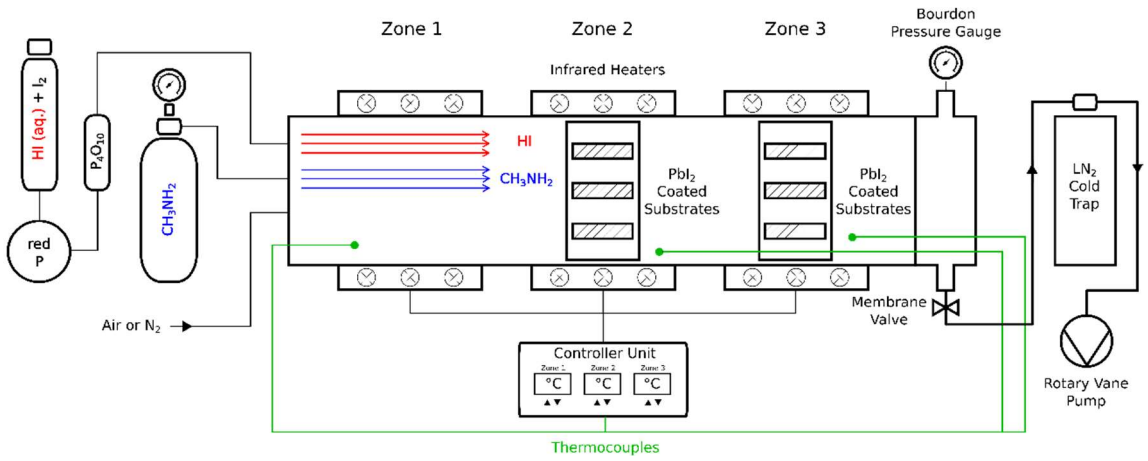

Figure 4.67 Schematic draft of the Chemical Vapor Deposition (CVD) setup, in the hydrogen iodide gas (HI) and methylamine (CH_3NH_2) version

Figure 4.68 **Left:** Glass apparatus used for the production of hydrogen iodide (HI) gas, which is connected to the CVD reaction tube seen in Figure 4.67. **Right:** Chemical Vapor Deposition (CVD) setup in a laboratory hood

For transforming PbI_2 to MAPI, MA and HI are introduced in the reaction tube sequentially and in multiple cycles. A half cycle (0.5, 1.5 and 2.5) refers to a methylamine step and a whole cycle (1.0 and 2.0) refers to an HI step. Prior to loading the spin coated PbI_2 samples, the reaction tube is heated to 100°C for at least an hour under vacuum to remove any residuals that may adhere to the walls. All further steps take place at room temperature. For the methylamine

step, 400 mbar of surrounding (humid) air is introduced into the reaction tube. After inserting an additional 200 mbar of methylamine, the yellow PbI_2 coated substrates immediately turn transparent, as seen in Figure 4.69.

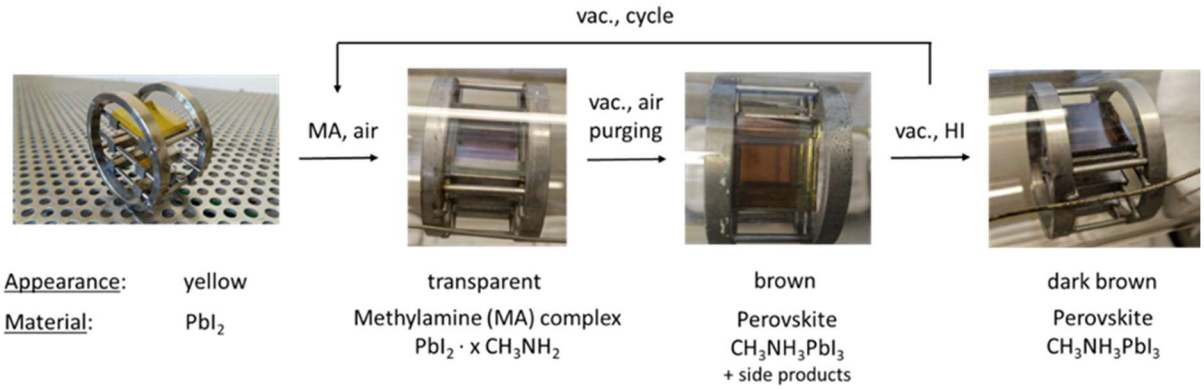

Figure 4.69 Process diagram of the methylamine (MA) and hydrogen iodide (HI) CVD process, with images of the intermediate stages

Minuscule droplets can be observed on the surface, that indicate the formation of a liquid phase of the methylamine and PbI_2 complex. This intermediate phase is one of the advantages of the methylamine process, since the resulting film becomes exceptionally smooth, independent of the roughness of the initial precursor layer of PbI_2, as shown by the SEM images in Figure 4.70.

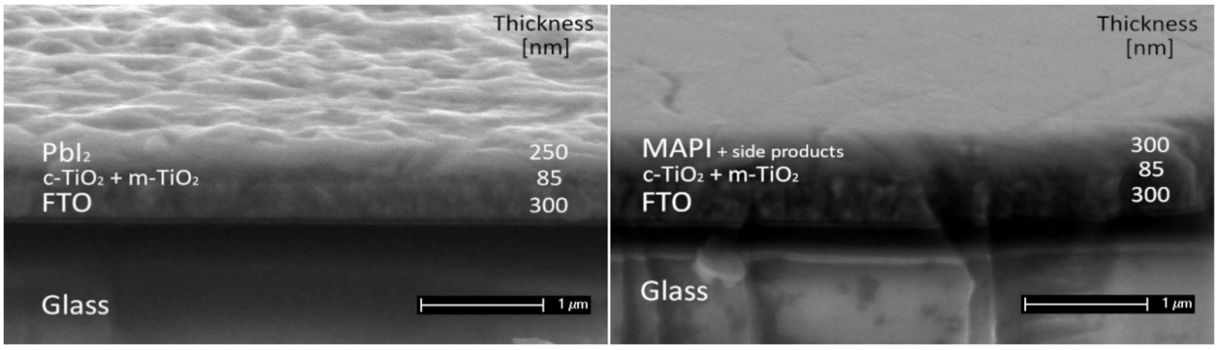

Figure 4.70 Cross-section SEM images; **Left:** detail of the surface of a spin coated lead iodide (PbI_2) layer vs. **Right:** detail of the surface of the MAPI layer, after treatment of the lead iodide layer in the CVD process for 0.5 cycles with methylamine (MA). Samples are tilted at 70°

After 15 s, a 600 mbar air flow for 1 min. removes the methylamine gas from the tube. In the first few seconds of removing the methylamine gas, the substrate turns light brown, with gradual darkening as shown in Figure 4.71.

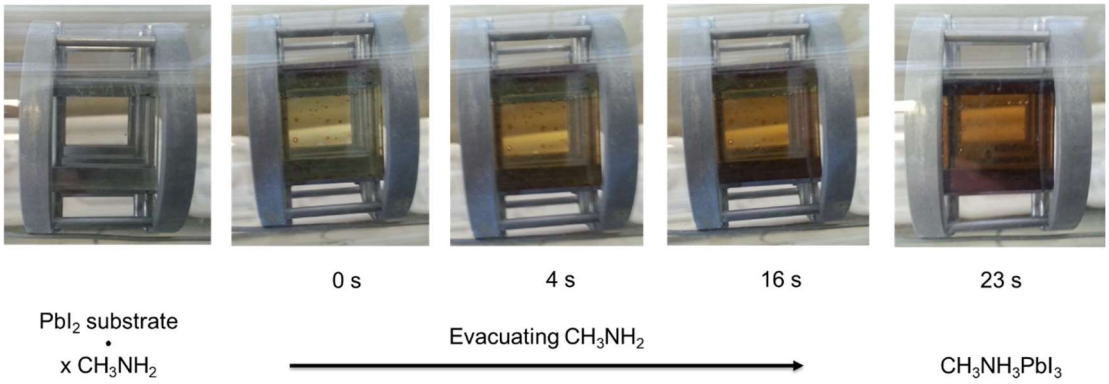

Figure 4.71 Formation of the MAPI layer when purging the PbI2 · x CH_3NH_2 complex with an airflow

To remove all excess methylamine and air from the reaction tube, it is purged three times with nitrogen (filling to 1 bar and evacuating to 1 mbar). In the next step, 200 - 300 mbar of self-made HI gas is added to the evacuated tube. The HI gas is optionally passed through the drying agent phosphorous pentoxide (P_4O_{10}), to further remove excess water vapor, before entering the reaction tube. After 10 min. reaction time, the HI gas is removed by purging three times with nitrogen. The dark brown color of the substrate after the HI step can be seen in Figure 4.69. After evacuating, the MA and HI steps are repeated for 2.5 cycles. To complete the solar cell devices, spiro-MeOTAD is spin coated and gold is sputtered onto the substrates, as explained in Chapter 4.1.2. The cell architecture, the substrate dimensions and a cross section SEM image of the layers of a MAPI perovskite solar cell produced with the MA and HI gas CVD method are shown in Figure 4.72. Compared to the PbI_2 layer thickness of 250 nm, the MAPI layer shows a 60 % increase to 400 nm after the 2.5 cycles of MA and HI (compare Figure 4.70 **left** and Figure 4.72 **right**). In comparison to the layer thickness of 300 nm of the MAPI layer after only one treatment of the PbI_2 layer with MA (0.5 cycles), the final MAPI layer shows an increase of 33 % to 400 nm thickness after completing all 2.5 cycles (compare Figure 4.70 **right** and Figure 4.72 **right)**.

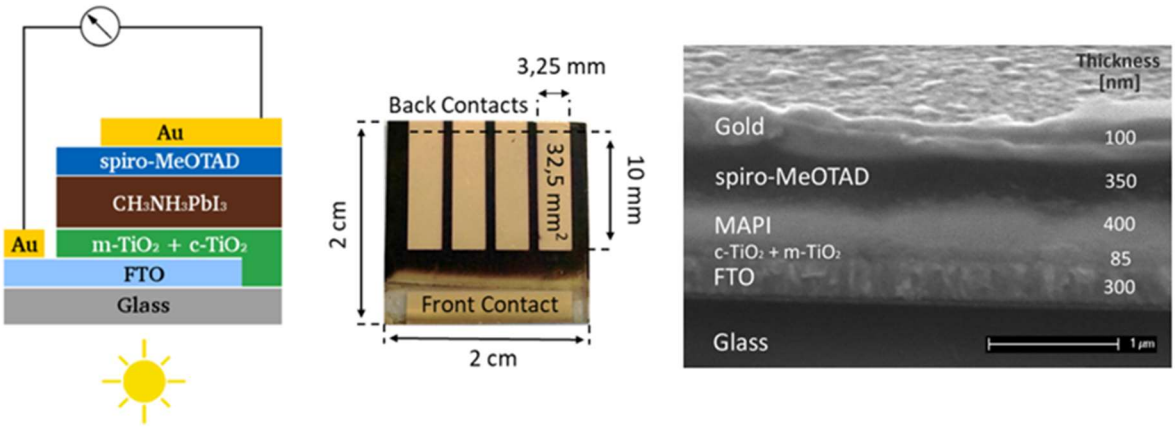

Figure 4.72 **Left:** Material stack of a MAPI perovskite solar cell. **Middle:** Substrate with four solar cells and physical dimensions. **Right:** Cross-section SEM image of a completed MAPI perovskite solar cell, using the MA and HI gas CVD method. Sample tilted at 70°

Figure 4.73 shows current voltage curves of the champion cells under the AM1.5G illumination (measured with a 840 W/m^2 light intensity in our solar simulator – see Chapter 4.1.3), which were produced *without* and *with the drying agent* P_4O_{10} in the HI step, respectively. The best solar cell produced with the drying agent reached a 12,9 % efficiency under MPPT (maximum power point tracking), while the one without the drying agent reached an efficiency of 11,7 %, each for a 32,5 mm^2 cell on a 4 cm^2 substrate. The size of these solar cells can be considered as being a mini-module.

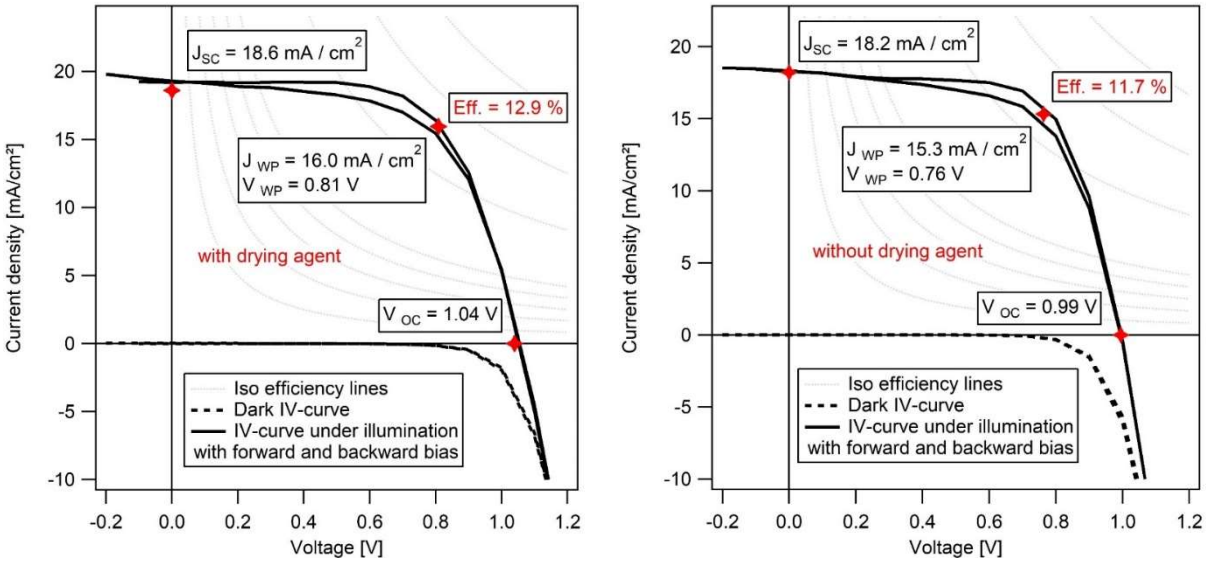

Figure 4.73 IV-curves of MAPI solar cells from the MA and HI gas CVD process with MPPT values. **Left:** without using the drying agent P_4O_{10} for the HI step. **Right:** using the drying agent for the HI step

Among 8 solar cells on 2 substrates (4 cells on each substrate), the spread of the efficiencies for the cells made with the drying agent (HI production step) is 1,9 % with an average of 11,1 % and the spread for the cells made without the drying agent is 1,4 % with an average of 9,4 %. The individual values for the efficiencies, the open circuit voltages (V_{OC}), the short circuit currents (J_{SC}) and the fill factors for representative solar cells are given in Table 4.12. The low fill factors with an average value of around 60 % may be related to small amounts of PbO and $Pb(OH)_2$ species that have been mentioned by Raga et al.[168] and that are involved in the mechanism of formation of the MAPI perovskite. These species have also been confirmed on the surface of the films by XPS measurements in this work and will be shown and discusses thoroughly later on (see Figure 4.80).

Table 4.12 Solar simulator performance characteristics of MAPI perovskite solar cells, built up using the MA and HI gas CVD process

		With drying agent (HI gas)				Without drying agent (HI gas)			
	Cell	Efficiency [%]	V_{OC} [V]	J_{SC} [A/m^2]	Fill Factor [%]	Efficiency [%]	V_{OC} [V]	J_{SC} [A/m^2]	Fill Factor [%]
	1	4,2	1,04	76	53	8,1	0,84	180	54
Sample	2	11,8	1,06	176	63	10,1	1,01	170	59
I	3	11,9	1,04	181	63	6,4	0,74	167	52
	4	10,3	1,03	175	57	10,0	1,02	144	68
	5	12,8	1,08	183	64	8,0	0,95	150	56
Sample	6	11,8	1,04	173	65	**11,7**	0,99	182	65
II	7	**12,9**	1,04	186	67	11,0	0,99	172	65
	8	12,8	1,04	188	65	9,6	0,98	161	61
	Average	**11,1**	1,05	167	62	**9,4**	0,94	166	60

The substrates of the intermediate steps of the MA and HI gas CVD process, seen in Figure 4.74, have been characterized by photoluminescence spectroscopy (PL), UV/vis spectroscopy, SEM, XRD and XPS. One set of the samples was produced without the drying agent P_4O_{10} in the HI production step, and another set was produced with the help of the drying agent. The results and the differences will be discussed in the following.

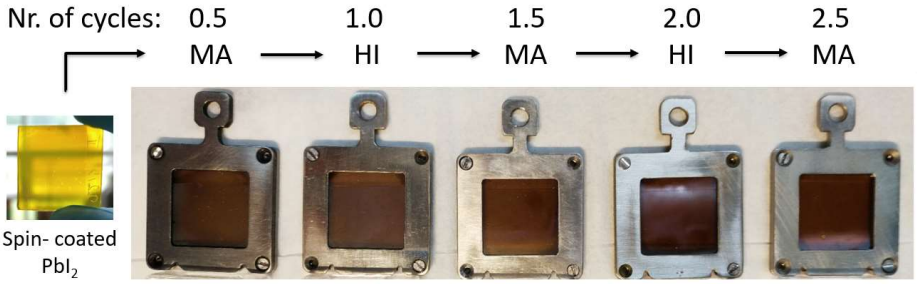

Figure 4.74 Appearance of substrates for each step of the MA and HI gas CVD process, having the stack of materials Glass/FTO/c-TiO_2/m-TiO_2/MAPI

Figure 4.75 shows UV/Vis spectra of the samples of each step of the CVD process, **left:** made *with the drying agent* in the HI production step, and **right:** *without the drying agent*. The optical band gap E_g of the materials formed is red shifted through progressing cycles, following the trend of a decreasing band gap. For the sample from the set made *with the drying agent*, the band gap is 1,63 eV (759 nm) for the PbI_2 layer that was treated only once with methylamine in the first half-cycle (0.5 MA). In comparison, the band gap of the first half-cycle (0.5 MA) sample

from the set made *without the drying agent* is with 1,61 eV (768 nm) slightly lower, although they are made with seemingly the same settings. These deviations in the results can be expected from production with a high amount of manual work. For the last step of the process (2.5 MA), the band gap of the material produced *with the drying agent* is 1,60 eV (776 nm). In comparison, the band gap of the sample produced *without the drying agent* is close to the latter value with 1,59 eV (778 nm), with only 2 nm difference. The decreasing band gap of the samples through the cycles indicate an increasing amount of MAPI and an increase in its crystallinity. These band gaps are in accordance with literature values for MAPI.[26, 109]

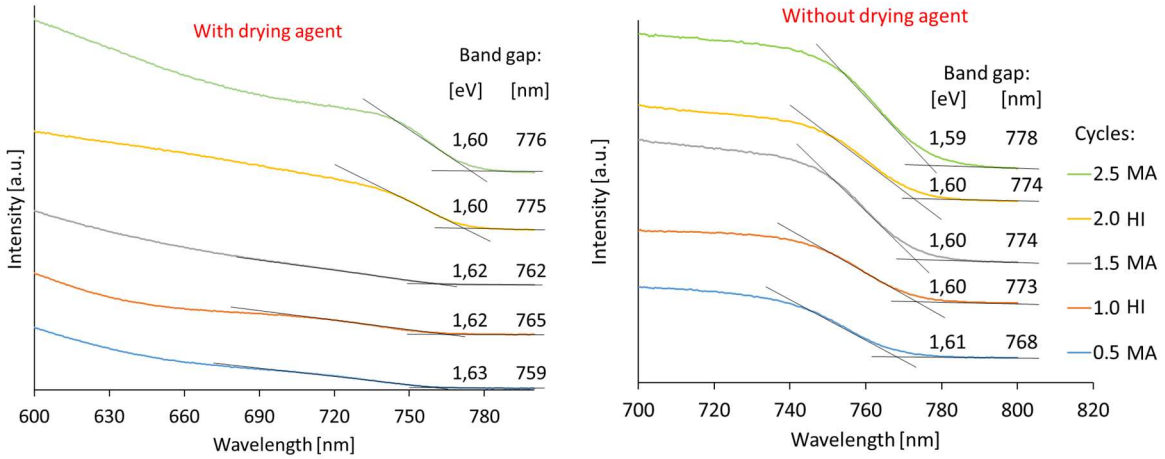

Figure 4.75 UV/Vis spectra of the samples of each cycle in the MA and HI gas CVD process. **Left:** with the drying agent in the HI production step. **Right:** without the drying agent

The measured PL bands of the MAPI samples for the final, 2.5 MA steps (Figure 4.76) are 1,61 eV (769 nm), resp. 1,63 eV (762 nm) (with / without the drying agent). These values are comparable to PL literature values of 1,61 eV [169] and they are also within the range of the measured optical band gaps of 1,60 eV (776 nm), resp. 1,59 eV (778 nm) (see Figure 4.75). According to theory (see Chapter 3.3.3), the PL values should be lower than the optical band gaps. We attribute the relatively small differences to different distribution of defect states around the fundamental gap (Urbach tails) which are expected for samples without perfect crystallinity.

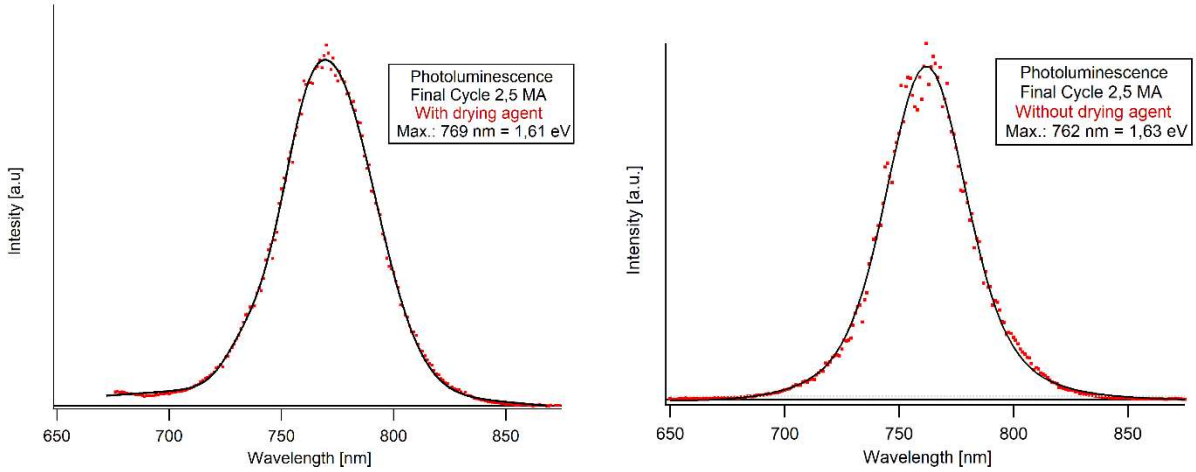

Figure 4.76 Photoluminescence (PL) measurements of the 2.5 MA final cycle of the MA and HI gas CVD process. **Left:** made without the drying agent for the HI step, **right:** with the drying agent

Figure 4.77 shows cross-sectional SEM images of the samples from all the steps of the MA and HI gas CVD process, which were obtained without using the drying agent in the HI production step. An overall increase in roughness in progressing cycles can be observed. The images also show that the surfaces of the samples after the MA half cycle, i.e. a) 0.5 MA, c) 1.5 MA and e) 2.5 MA are smoother than those of the samples after the HI gas half cycle, i.e. b) 1.0 HI, d) 2.0 HI and f) 3.0 HI. The surfaces after the MA treatment might be smoother because of the intermediate liquid complex phase of $PbI_2 \cdot x\ CH_3NH_2$ and $MAPI \cdot x\ CH_3NH_2$, allowing the material to better spread over the surface.

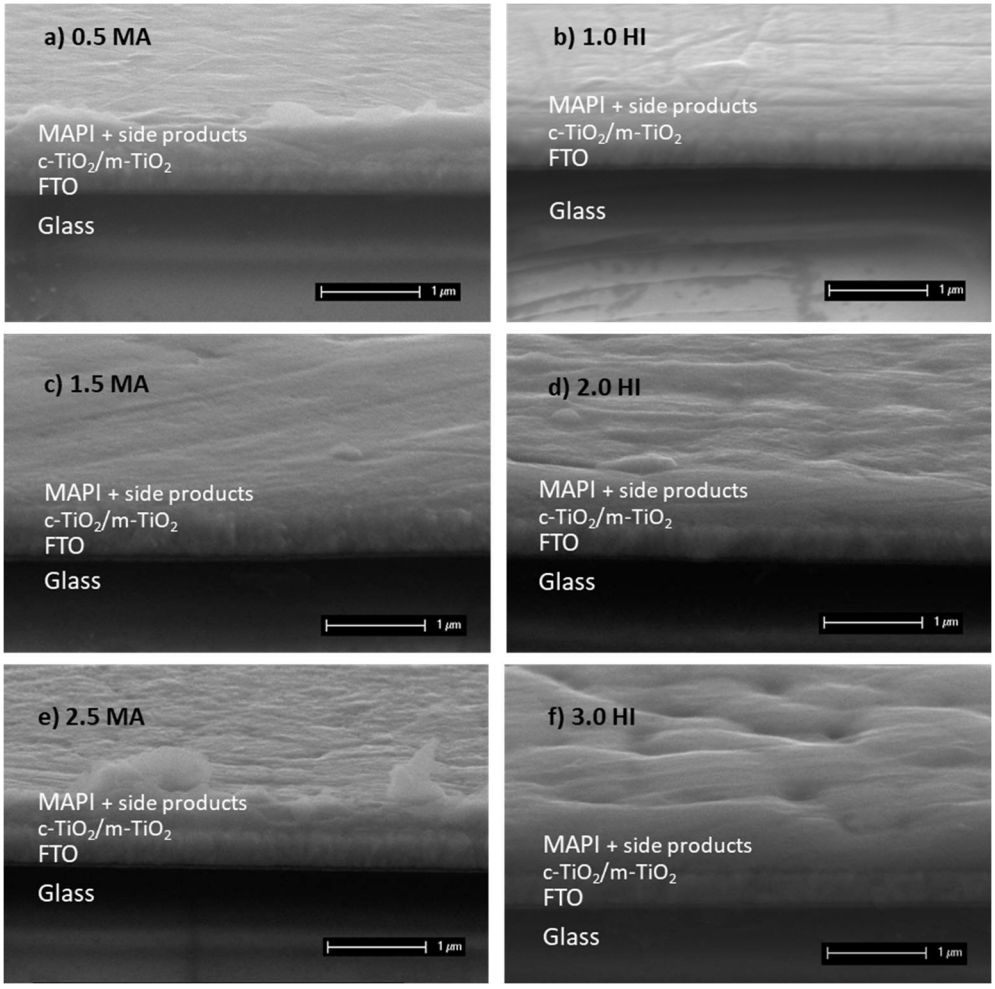

Figure 4.77 Cross-sectional SEM images of the different stages of the MA and HI gas CVD process, for samples obtained without the drying agent for the HI production step. The samples after the MA half cycle, i.e. a) 0.5 MA, c) 1.5 MA and e) 2.5 MA have a smoother surface than the samples after the HI gas half cycle, i.e. b) 1.0 HI, d) 2.0 HI and f) 3.0 HI, which show a rougher surface. Samples are tilted at 70°

The samples made for the following XRD measurements have been prepared without using the drying agent in the HI production step. Figure 4.78 shows that in all steps of the CVD process a high amount of oriented MAPI forms, showing a (100) reflex at 14.2°, a (200) reflex at 28.5° and a (300) reflex at 43.4°, which indicates strong texturing of the samples. These values are in accord to literature.[30, 170] Although from Equation 4.23 and Equation 4.24 the formation of PbO and $Pb(OH)_2$ are expected,[168] neither species can be found in the XRD patterns of the samples. However, XPS measurements that will be shown later on, do indicate the formation of PbO and $Pb(OH)_2$ (see Figure 4.80). These species seem to merely form on the surface of the samples,

only being detected by the surface sensitive XPS technique. Another explanation would be that they could exist as amorphous phases, or having very small crystallites spread out throughout the material, that could make them undetectable by the bulk measuring method XRD.

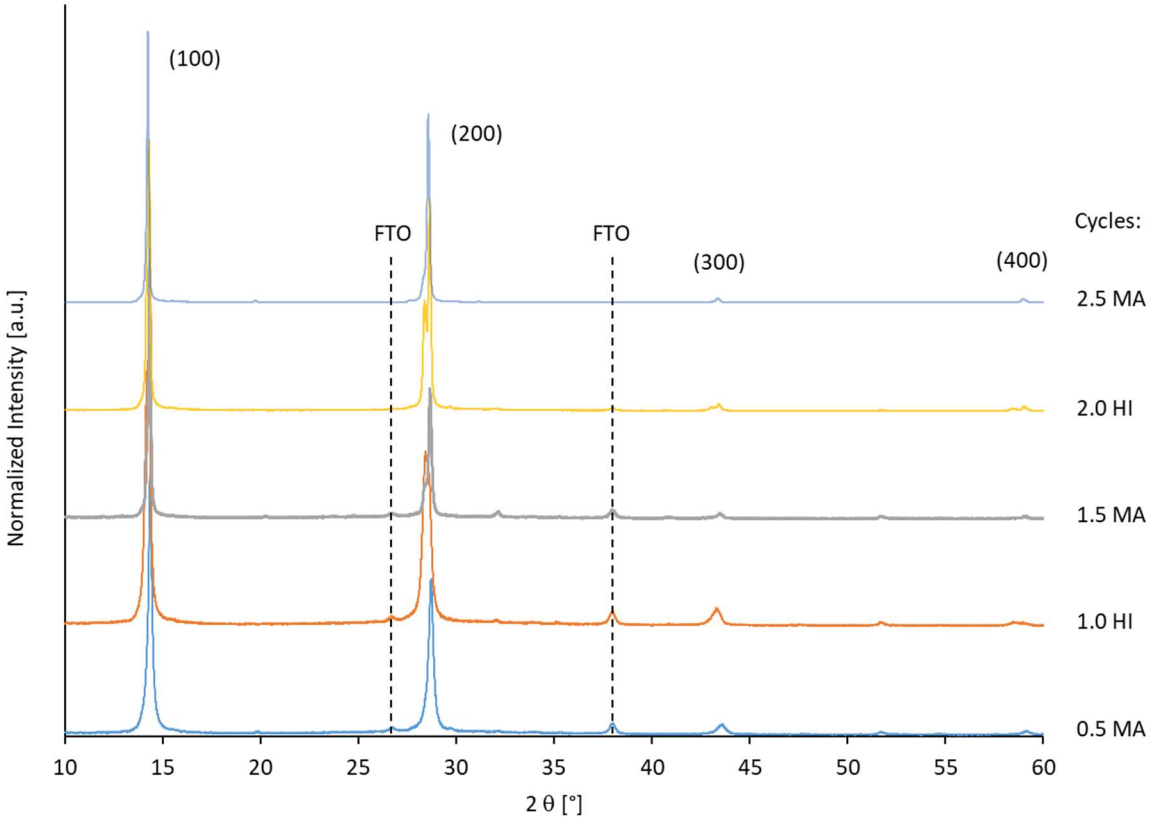

Figure 4.78 XRD patterns of the MAPI substrates from all intermediate steps of the MA and HI gas CVD cycled process, made without the drying agent in the HI production step

The following Rietveld fittings have been performed by Prof. Clemens in the software TOPAS 5.0, for the whole measured 2θ-range (10° - 90°). The further analysis of this data has been made in close cooperation with Prof. Clemens. The texture parameters required to fit the perovskite phases were calculated by application of the March Model[171], in relation to the (100) plane for the cubic phase, or the (100)/(001) planes for the tetragonal model.

Rietveld refinements of the XRD measurements displayed in Figure 4.79 (2.5 MA sample), indicate the presence of a mixture of a cubic (lower volume) and a tetragonal (higher volume) MA-

PI perovskite phase. Rietveld refinements of the samples 1.0. HI, 1.5 MA and 2.0. HI (Appendix Figure 9.11 to Figure 9.13) also feature a mixture of the two phases. In contrast, the 0.5 MA sample from the Appendix Figure 9.10 could be fitted with a cubic phase only. Results of the lattice parameters, phase fraction distributions, texture parameters and volumes per ABX_3 unit are summarized in Table 4.13. The low values of the refined March Dollase parameters, ranging from 0.16 to 0.21, indicate highly textured film growth with the (001) plane in parallel to the film surface. Two perovskite phases can be found within most of the films. These are high volume phases, indicated to be predominantly tetragonal when found in high quantities, as well as low volume phases, predominantly cubic.[172] Their quantities show a strong dependence on the treatment step, where the low volume phase becomes predominant after the MA treatment. Literature studies show that the electronic behavior (i.e. performance of the solar cells) is insensitive to the structural phase of either cubic or tetragonal perovskite.[109, 173, 174]

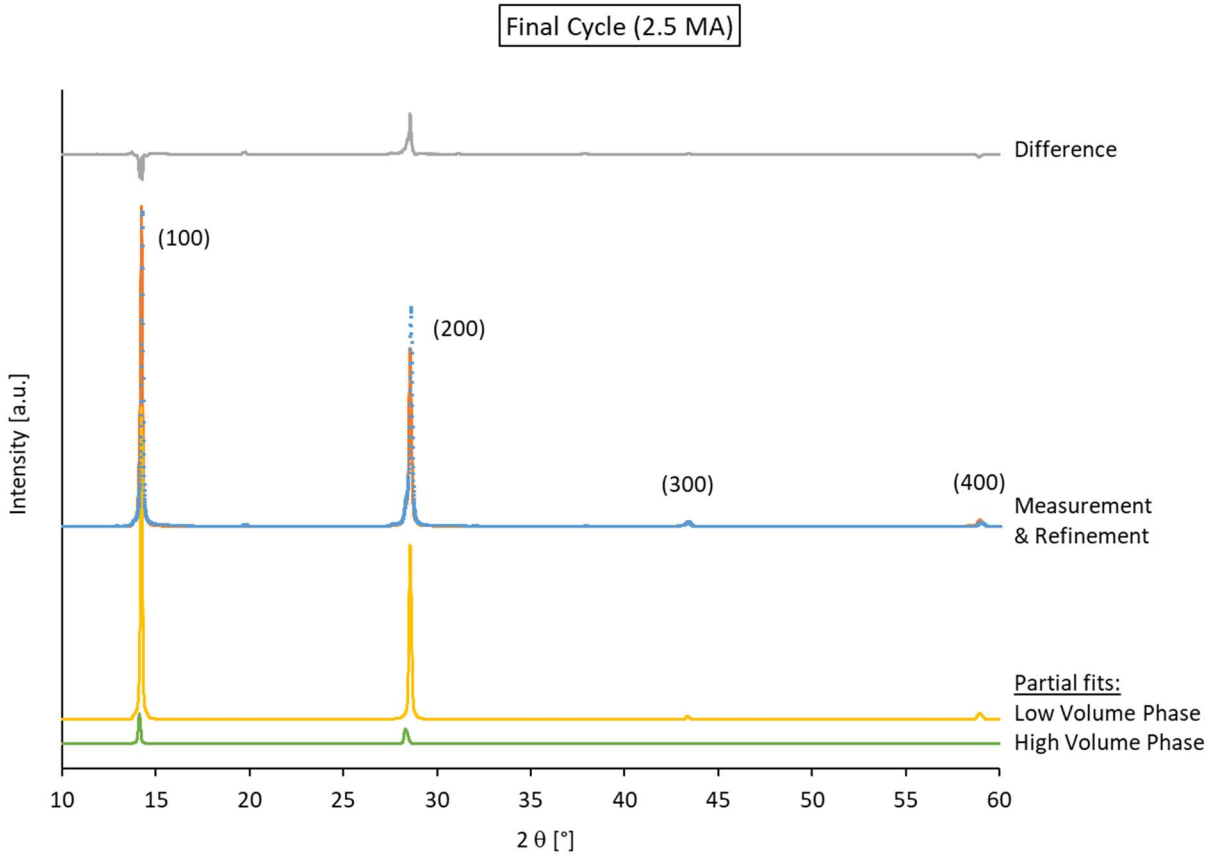

Figure 4.79 XRD pattern and refinements of the substrate measured after the final cycle of the MA and HI gas CVD process, 2.5 MA, made without using the drying agent for the HI production

Table 4.13 Refined parameters of the phases in the perovskite mixture produced in the cycles of the MA and HI gas CVD process, without using the drying agent for the HI production

		Low Volume Phase			High Volume Phase			
Sample	Texture Parameter	a [Å]	Fraction [%]	Volume per ABX_3 unit [$Å^3$]	a [Å]	c [Å]	Fraction [%]	Volume per ABX_3 unit [$Å^3$]
0.5 MA	0.20	8.870(7)	100	246.8	8.971(7)	12.654(8)	0	--
1.0 HI	0.21	8.901(5)	31.5	249.3	8.967(9)	12.614(7)	68.5	254.6
1.5 MA	0.21	8.877(7)	78.1	247.4	8.953(0)	12.692(0)	21.9	253.6
2.0 HI	0.19	8.883(2)	65.2	247.5	8.950(0)	12.610(5)	34.8	254.3
2.5 MA	0.16	8.879(0)	89.4	250.8	8.967(9)	12.565(2)	10.6	253.1

In the following section, XPS measurements of the samples made using the step-by-step cycled MA and HI gas CVD process from Figure 4.74 will be presented and discussed.

The samples were transfered from the CVD device into the UHV (ultra-high vacuum) XPS system through air.

The spectra shown in Figure 4.80 - Figure 4.85 belong to the set of samples that were prepared using the drying agent P_4O_{10} in the HI production step, measured with a ThermoFisher Scientific ESCALAB 250X using a Mg K_α source. The spectra show the respective elements, which are present in each sample (0.5 MA to 2.5 MA), as measured by XPS: oxygen (O1s), carbon (C1s), nitrogen (N1s), lead (Pb4f 7/2), iodine (I3d 5/2) and titanium (Ti2p). Each figure contains XPS measurements from all cycles of the process, shown in red, e.g. the O1s Figure 4.80, contains measurements for oxygen of each sample from the cycles: 0.5 MA, 1.0 HI, 1.5 MA, 2.0 HI and 2.5 MA. For each sample, e.g. 0.5 MA, the elements O, C, N, Pb, I and Ti have been measured, shown throughout the figures.

The calibration of the binding energies for the XPS measurements in Figure 4.80 - Figure 4.85 were made using pure Gold (Au), Silver (Ag) and Copper (Cu) standards, which were cleaned by argon sputtering prior to the measurements and the measured binding energies for each element (O, C, N, Pb, I, Ti) were shifted according to reference values, as shown in the Appendix: Table 9.5, Table 9.6 and Figure 9.14.

All spectra from the graphs in Figure 4.80 - Figure 4.84 have been deconvoluted for each element, to show the chemical species on all samples, using the software ThermoScientific Avantage 5.9911. The cross-deconvolution takes into account all spectra, literature binding energy positions for the respective species and the ideal atomic ratios of each molecule on the samples. Table 4.14. shows the ideal atomic ratios for the chemical species found on the samples. For example, the molecule MAOH (CH_3NH_3OH) contains 1 part carbon, 1 part nitrogen and 1 part oxygen; or lead(II)hydroxide, $Pb(OH)_2$ contains 1 part lead and 2 parts oxygen. These ratios have been used to deconvolute all spectra. The software Avantage integrates the area under a fitted curve and divides it by the Scofield sensitivity factor for the respective orbital of each element (see Table 4.15), to be able to calculate the ratios of the atomic concentrations for a species. For example, for the species MA (CH_3NH_2), present in the 0.5 MA sample in Figure 4.82 (C1s) and Figure 4.81 (N1s), the area under the fitted curve for the C1s spectrum is 138,6 cps · eV, with a Scofield factor of 1. The area under the fitted N1s spectrum is 239,7 cps · eV, divided by the Scofield factor of N: 1,8 makes 133,2 cps · eV, which is approximately the same as the fitted area under the C1s spectrum of the MA species, so a 1:1,04 ratio results (ideally 1:1, see Table 4.14). The intensity and the B.E. positions of the fitted curves have been manually adjusted to fulfill the conditions given in Table 4.14. All fitted curves, reconvoluted, will result in the envelope (drawn in blue) of the measured (red) spectra. All data from all fits, like the peak B.E. position, height (cps), area (cps · eV), etc. are shown in the Appendix Table 9.7 - Table 9.11. In these tables, the Atomic % for each sample, e.g. 0.5 MA, add up to 100 %.

Table 4.14 Atomic ratios of the molecules contained in the films produced in the CVD experiments

		Atomic Ratios				
Abbreviation	**Molecule**	**C**	**N**	**O**	**Pb**	**I**
	CH_3I	1				1
	I_2					1
MA	CH_3NH_2	1	1			
MAI	CH_3NH_3I	1	1			1
MAOH	CH_3NH_3OH	1	1	1		
MAPI	$CH_3NH_3PbI_3$	1	1		1	3
	$Pb(OH)_2$	1		2		
	Pb^0				1	
	PbI_2				1	2
	PbO			1	1	

Table 4.15 Scofield sensitivity factors for the Mg K_α source

Orbital	Scoffield Sensitivity Factos Mg K-alpha
O1s	2,8
C1s	1,0
N1s	1,8
Pb4f	12,8
I3d	19,3

In the following, the fitted spectra and their respective species from Figure 4.80 - Figure 4.84 will be compared and discussed for all samples, which were made using the MA and HI gas CVD method and a mechanism of the MAPI perovskite formation involving specific chemical reactions will be concluded. Table 4.16 shows literature reference binding energy positions for all species found on the samples that were used as an approximate starting point to fit the measured spectra.

Table 4.16 Literature XPS reference binding energies for the species found on the samples made by the MA and HI gas CVD process

Molecule	XPS - B.E. position [eV]					Citation
	C1s	N1s	O1s	Pb4f 7/2	I3d 5/2	
CH_3I	285,3				618,3/620,5	[175]
I_2 (on Ag)					619,4	[176]
CH_3NH_2 (MA)	284,9					[177]
	285,4					[178]
	284,8					[179]
	285,9	397,9				[180]
CH_3NH_3I (MAI)	287,0	402,4				[125]
	286,5	402,1			619,1	[181]
	286,9	402,4				[179]
CH_3NH_3OH (MAOH)			531,2			[182]
$CH_3NH_3PbI_3$ (MAPI)	286,4	402,4		138,4	619,3	[183]
	286,4	402,5		138,6	619,4	[184]
	286,5					[179]
$Pb(OH)_2$				137,95		[185]
				138,6		[186]
			531,8			[187]
			532,4			[188]
Pb^0				137,0		[189]
PbI_2				138,5	619,5	[190]
				138,35		[185]
				138,7		[191]
PbO			529,3	137,9		[192]
			530,9	137,7		[193]
C (adventitious)	285,0					[194]
	285,1					[195]
	285,3					[118]
Adsorbed H_2O			533,5			[196]

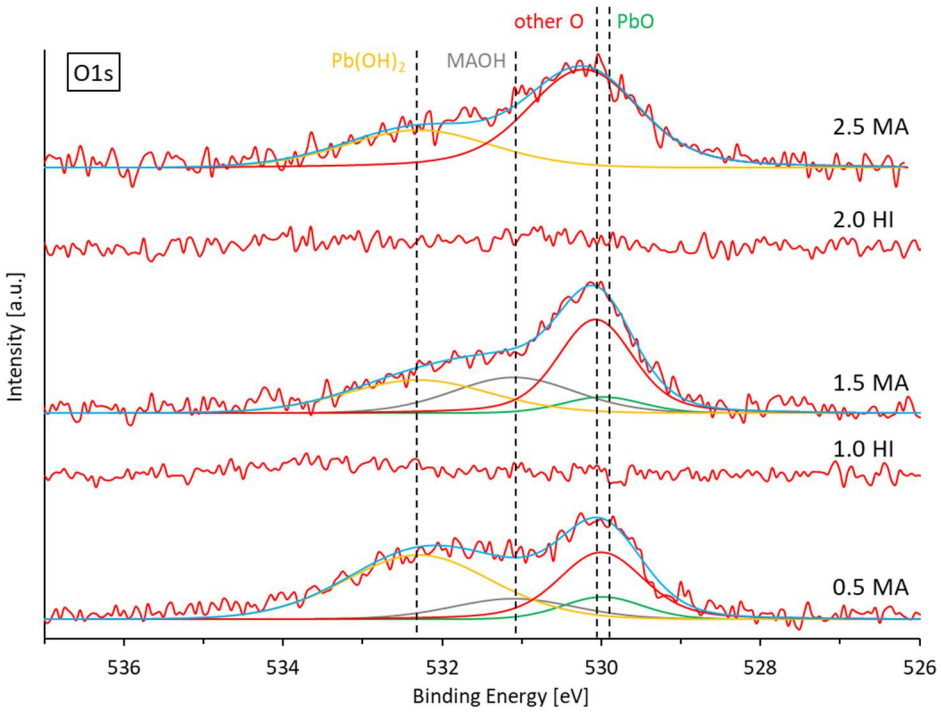

Figure 4.80 O1s XPS measurements of samples from the MA and HI gas CVD process, which were made using the drying agent P_4O_{10} in the HI production step

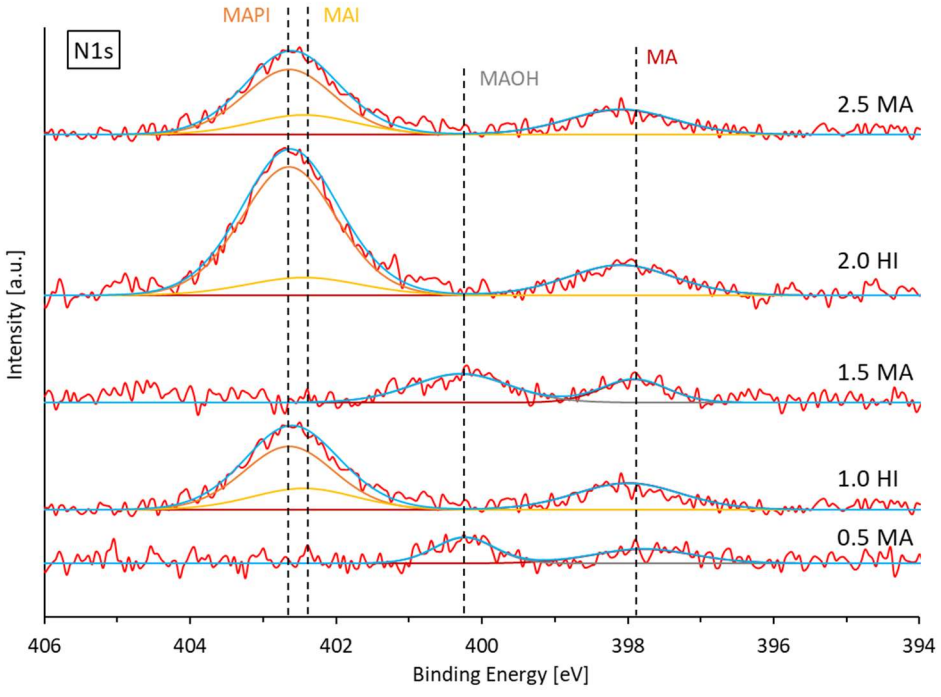

Figure 4.81 N1s XPS measurements of samples from the MA and HI gas CVD process, which were made using the drying agent P_4O_{10} in the HI production step

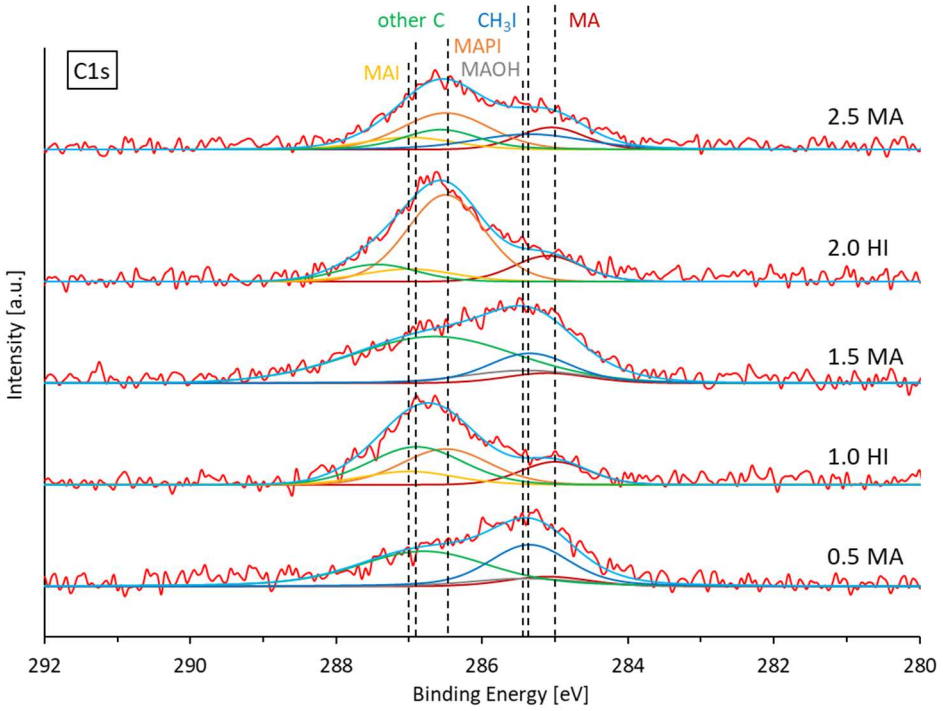

Figure 4.82 C1s XPS measurements of samples from the MA and HI gas CVD process, that were made using the drying agent P_4O_{10} in the HI production step

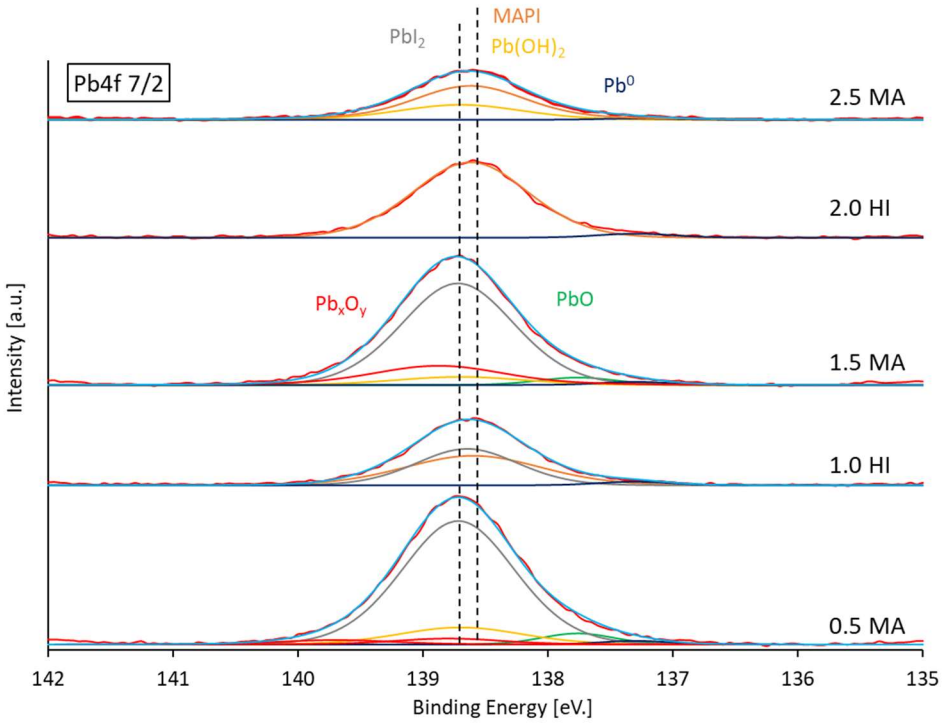

Figure 4.83 Pb4f 7/2 XPS measurements of samples from the MA and HI gas CVD process, which were made using the drying agent P_4O_{10} in the HI production step

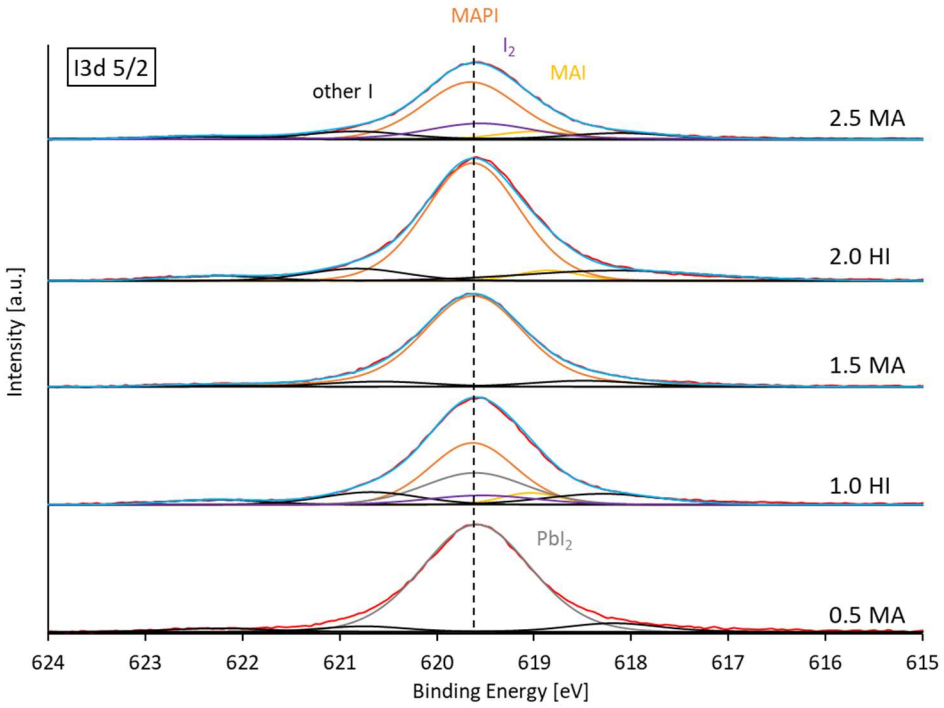

Figure 4.84 I3d 5/2 XPS measurements of samples from the MA and HI gas CVD process, which were made using the drying agent P_4O_{10} in the HI production step

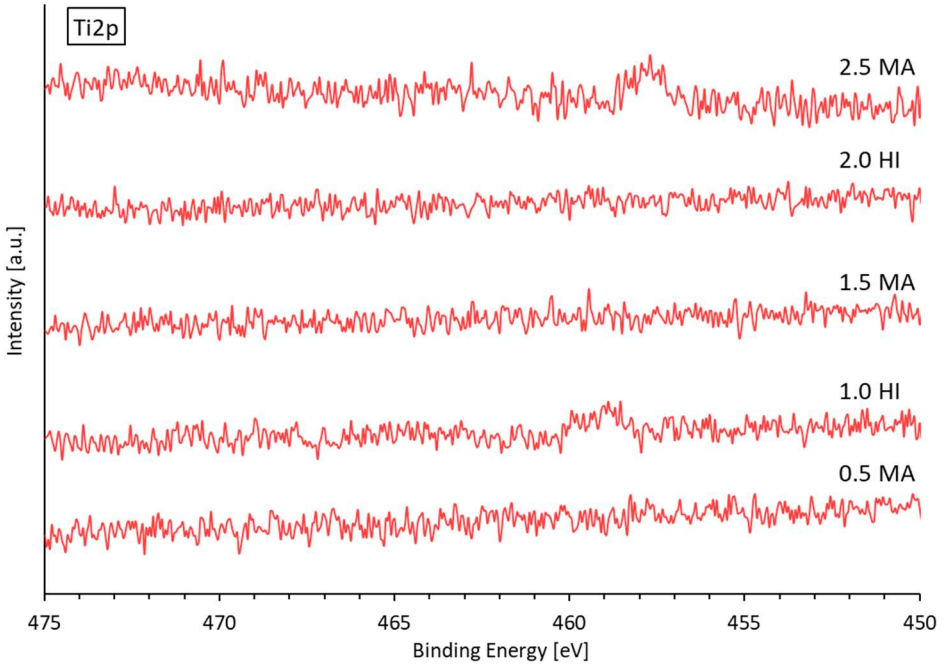

Figure 4.85 Ti2p XPS measurements of samples from the MA and HI gas CVD process, which were made using the drying agent P_4O_{10} in the HI production step

Figure 4.80 shows the O1s spectra. In the steps in which the MA (CH_3NH_2) gas and ambient air (containing humidity) are introduced into the reaction tube onto PbI_2 coated layers, the oxygen species MAOH (CH_3NH_3OH, 531,1 eV), $Pb(OH)_2$ (532,3 eV), and PbO (529,98 eV) form, according to Equation 4.27 - Equation 4.30. The MAOH species does not appear in the 2.5 MA sample (unlike in the 0.5 MA and 1.5 MA). This species is missing from the N1s spectra of the 2.5 MA sample (Figure 4.81). The PbO species is missing as well in the 2.5 MA O1s spectra, because it could not be fitted in the Pb4f 7/2 spectra (Figure 4.83), after all other necessary species have been introduced. These two species could have formed as well on the sample, but since the XPS measuring method is surface sensitive, they do not show up in the spectra, since they might be covered by other substances on the surface of the 2.5 MA sample. These surface species will be discussed in the explanation of the C1s spectra later on.

Equation 4.27 $CH_3NH_2 + H_2O \rightleftharpoons CH_3NH_3OH$

Equation 4.28 $PbI_2 + 2\ CH_3NH_3OH \rightleftharpoons 2\ CH_3NH_3I + Pb(OH)_2$

Equation 4.29 $3\ PbI_2 + 2\ CH_3NH_3OH \rightleftharpoons 2\ CH_3NH_3PbI_3 + Pb(OH)_2$

Equation 4.30 $3\ PbI_2 + 2\ CH_3NH_2 + H_2O \rightleftharpoons 2\ CH_3NH_3PbI_3 + PbO$

Figure 4.81 shows the N1s spectra. The mainly desired photo-active perovskite MAPI N1s component (402,65 eV) surfaces according to the N1s spectra is observed after the 1.0 HI, 2.0 HI steps and the 2.5 MA step. It can form in an HI step according to Equation 4.31 from PbI_2, HI and MA gas which is still absorbed by the film from the MA step, or according to Equation 4.32 from PbI_2 (which is still unreacted, or that has been regenerated from $Pb(OH)_2$ (Equation 4.34) and PbO (Equation 4.35) in the HI step) and MAI. The MAI component can form in the HI step from MAOH and HI according to Equation 4.33. In an MA step, MAPI can form according to Equation 4.32 from PbI_2 and MAI, since MAI can also form in an MA step (as well as in an HI step), according to Equation 4.28. MAPI can also form in an MA step according to Equation 4.29 and Equation 4.30 from PbI_2 and MAOH, resp. PbI_2, MA and water. Although all XRD spectra in Figure 4.78 clearly show that MAPI forms in all steps of the CVD reactions, it is not present in the XPS spectra of the 0.5 MA and 1.5 MA steps. An explanation could be that in these

steps, the surfaces of the substrates are covered with oxide species and the MAPI component lies underneath. The MAI N1s component (402,45 eV) appears in parallel to MAPI in the 1.0 HI, 2.0 HI and 2.5 MA steps. This observation can also be explained by the coverage of the surface of the substrates in the 0.5 MA and 1.5 MA with oxide species, since MAI can form in both an MA and an HI step (Equation 4.28 resp. Equation 4.33). In all steps of the N1s spectra, a species with a BE between 397,8 and 398,1 eV is present, which according to literature values[180] could be attributed to adsorbed MA (CH_3NH_2); see Table 4.16. This species can also be fitted in all C1s spectra (285,0 eV – 285,1 eV, see Figure 4.82), to have a ratio of 1 part carbon to 1 part nitrogen. Longer, and more thorough purging between steps, or a heating step might have eliminated this redundant component from the film. The MAOH (CH_3NH_3OH) species in the 0.5 MA and 1.5 MA steps (400,2 eV – 400,3 eV) forms according to Equation 4.27 and reacts with HI according to Equation 4.28 and Equation 4.29 and it cannot be found in all other steps. The MAI (CH_3NH_3I) component (402,45 eV) can either form according to Equation 4.28 from MAOH and PbI_2 in an MA step, or in an HI step according to Equation 4.33 from MAOH and HI.

Equation 4.31 $PbI_2 + x\ CH_3NH_2 + HI \rightleftharpoons CH_3NH_3PbI_3 \cdot x\text{-}1\ CH_3NH_2$

Equation 4.32 $PbI_2 + CH_3NH_3I \rightleftharpoons CH_3NH_3PbI_3$

The spectra of the HI steps in Figure 4.80 (O1s spectra) are flat (only noise), not showing any oxygen species on the samples 1.0 HI and 2.0 HI. According to Equation 4.33 - Equation 4.35, the species MAOH, $Pb(OH)_2$ and PbO can regenerate with HI to MAI, resp. PbI_2, under the formation of water. It is important that the HI gas is free of water, since according to Le Chatelier's principle of equilibrium, the chemical equations Equation 4.33 - Equation 4.35 shift further to the right side in the absence of water, which forms during these reactions.

Equation 4.33 $CH_3NH_3OH + HI \rightleftharpoons CH_3NH_3I + H_2O\uparrow$

Equation 4.34 $Pb(OH)_2 + 2\ HI \rightleftharpoons PbI_2 + H_2O\uparrow$

Equation 4.35 $PbO + 2\ HI \rightleftharpoons PbI_2 + H_2O\uparrow$

In all MA steps of Figure 4.80 (O1s spectra), a fitted species called “other O” (drawn in red) is present in large amounts (530 eV – 530,2 eV). This species cannot be unambiguously identified, but it disappears in the HI steps as well. It might be attributed to other Pb_xO_y species of higher oxidation states, that could also be found in the Pb4f 7/2 spectra (138,8 eV - 138,9 eV, Figure 4.83). Another origin of these species could be hydrocarbons containing oxygen on the surface of the film, which might be correlated to the “other C” species found in the C1s spectra (286,6 eV – 287,4 eV) shown later on. Adsorbed water can be excluded from the identification of the “other O” species, since water would be expected at a much higher B.E. of 533,5 eV.[196]

The C1s spectra in Figure 4.82 contains 6 species. The MAPI (286,45 eV – 286,5 eV) and MAI (287,0 eV) components appear in the 1.0 HI, 2.0 HI and 2.5 MA spectra, analogous to the N1s spectra from Figure 4.81. The MAOH (285,4 eV) component appears as well analogous to the N1s spectra from Figure 4.81, in the 0.5 MA and 1.5 MA steps. The MA component (285,0 eV – 285,1 eV) is present in all steps. The component called “other C” (286,6 eV – 287,4 eV), drawn in green, could be a contamination on the surface of the substrates, which is also present in literature[125], measured on a bare silicon substrate, in the same binding energy region. The carbon component drawn in blue at a B.E. position of 285,35 eV, present in the 0.5 MA, 1.5 MA and 2.5 MA steps, could either be attributed to adventitious carbon that is generally present on ex-situ samples (see Table 4.16), but since it disappears in the 1.0 HI and 2.0 HI samples, it could be a species that reacts with HI. A plausible species that could appear at this B.E. position would be according to literature,[175] methyl iodide, CH_3I (see Table 4.16). CH_3I could react in an HI step forming methane (CH_4), that would easily evaporate, and I_2.

The Pb4f 7/2 spectra in Figure 4.83 contains 6 species. The MAPI component (138,6 eV) follows the trend explained in the N1s and C1s spectra, appearing after the 1.0 HI, 2.0 HI and 2.5 MA step. In the 2.0 HI step, the main component of the Pb4f 7/2 spectra is MAPI. The envelope has not been drawn in this graph to not cover MAPI’s fitting curve. The lead oxide species $Pb(OH)_2$ (138,7 eV) and PbO (137,8 eV) regenerate in the HI steps to PbI_2. The fits drawn in red (0.5 MA and 1.5 MA steps) could be attributed to other higher stoichiometry lead oxide species Pb_xO_y at a B.E. position of 138,8 eV - 139,7 eV. An example would be Pb_3O_4, that could form as shown

in Equation 4.36. PbI_2 (138,7 eV) is prominent in the first three steps and inexistent in the last two steps. The content of PbI_2 is indeed expected to decrease through progressing cycles due to its gradual transformation to MAPI. A small amount of elemental lead, Pb^0, appears in all samples. This component is known to form due to the degradation of non-encapsulated MAPI films.[189]

Equation 4.36 $$11\ PbI_2 + 8\ CH_3NH_2 + 4\ H_2O + I_2 \rightleftharpoons 8\ CH_3NH_3PbI_3 + Pb_3O_4$$

In Figure 4.84, the I3d 5/2 spectra of all steps of the process are shown. In the first spectrum (0.5 MA) the main fit consists of PbI_2 (619, 6 eV). This is expected at the beginning of the reaction, that starts with a PbI_2 film. For this spectrum, the envelope is not drawn, to not cover the fitted curve. Analogous to the lead spectra, PbI_2 is present in the first three steps and inexistent on the surface of the last two samples of the process. Throughout the samples, two iodine containing species in small amounts are present at binding energies of 618,1 eV – 618,5 eV, resp. 620,6 – 620,8 eV, that cannot be unambiguously identified. These could possibly be hydrocarbons containing iodine. The satellite peak between 622,2 eV – 622,4 eV is always present in iodine spectra measured with a Mg Ka source, according to ref.[110] MAPI (619,6 eV) and MAI (618,85 eV – 619,0 eV) follow the trend of the C1s, N1s and Pb4f spectra, appearing in the 1.0 HI, 2.0 HI and 2.5 MA steps. To achieve the correct shape of the envelope that fits the measured spectra in the 1.0 HI and 2.5 MA steps, an additional component is needed, drawn in violet, at a binding energy of 619,55 eV - 619,6 eV. According to[176] (see Table 4.16) , this species could be attributed to iodine, I_2, that could form through the degradation of PbI_2, MAPI, MAI, or other iodine containing species on the samples.

Spectra in the binding energy range of titanium Ti2p states (450 eV – 475 eV, Figure 4.85) have been measured, to assess whether pin holes are present on the measuring spot, that would reach to the substrate's TiO_2 layer. For electrons coming from the 2p orbitals of the anatase modification of titania, a doublet at 459,5 eV ($Ti2p_{1/2}$) and 465,2 eV ($Ti2p_{3/2}$)[197] would be expected due to the spin orbit coupling effect. Except for the 1.0 HI and the 2.5 MA sample, the spectra show only noise, so no pin holes are present. The 1.0 HI and the 2.5 MA samples show

weak signals, which most likely do not belong to titania, since no doublet is present. These weak artefact signals might come from electrons of other elements.

In Table 4.17, the main reactions of the MA and HI gas CVD process derived from the XPS data are summarized, split into reactions that occur in the MA steps and those that occur in the HI steps of the process.

Table 4.17 Reactions deduced from the XPS analysis of the MA and HI steps of the CVD process

MA-Step (0.5 / 1.5 / 2.5 steps)	**HI-Step (1.0 / 2.0 steps)**
$PbI_2 + x\ CH_3NH_2 \rightleftharpoons PbI_2 \cdot x\ CH_3NH_2$	$CH_3NH_3OH + HI \rightleftharpoons CH_3NH_3I + H_2O\uparrow$
$CH_3NH_2 + H_2O \rightleftharpoons CH_3NH_3OH$	$PbI_2 + CH_3NH_3I \rightleftharpoons CH_3NH_3PbI_3$
$PbI_2 + 2\ CH_3NH_3OH \rightleftharpoons 2\ CH_3NH_3I + Pb(OH)_2$	$PbI_2 + x\ CH_3NH_2 + HI \rightleftharpoons CH_3NH_3PbI_3 \cdot (x\text{-}1)\ CH_3NH_2$
$3\ PbI_2 + 2\ CH_3NH_3OH \rightleftharpoons 2\ CH_3NH_3PbI_3 + Pb(OH)_2$	$Pb(OH)_2 + 2\ HI \rightleftharpoons PbI_2 + H_2O\uparrow$
$3\ PbI_2 + 2\ CH_3NH_2 + H_2O \rightleftharpoons 2\ CH_3NH_3PbI_3 + PbO$	$PbO + 2\ HI \rightleftharpoons PbI_2 + H_2O\uparrow$
$PbI_2 + CH_3NH_3I \rightleftharpoons CH_3NH_3PbI_3$	

The samples for the XPS measurements explained above (Figure 4.80 - Figure 4.85) were made using the drying agent P_4O_{10} in the production of the HI gas. To highlight the importance of the drying agent in the preparation of the HI gas, O1s XPS measurements of a set of samples is shown in Figure 4.86, which were prepared without the drying agent in the HI production. When the drying agent is not present, the HI gas that is produced by dropping hydroiodic acid ($HI_{aq.}$) on red phosphorous will contain humidity, which affects the end-products. In the O1s spectra of Figure 4.86, unwanted, omnipresent peaks appear throughout all samples at around 533,5 eV, which do not disappear in the HI steps, unlike all peaks in the samples produced using the drying agent in the HI production step (Figure 4.80). According to literature,[196] this O1s B.E. position can be attributed to adsorbed water, which most likely comes from the humidity of the produced HI gas/vapor. Since higher power conversion efficiencies are reported by fabrication under completely dry atmosphere conditions,[198] avoiding water in the formation process of the MAPI perovskite is desired. All other XPS spectra of the elements N, C, I, Pb and Ti

for the samples produced without the drying agent in the HI production step, are shown for completion in the Appendix Figure 9.15 - Figure 9.19.

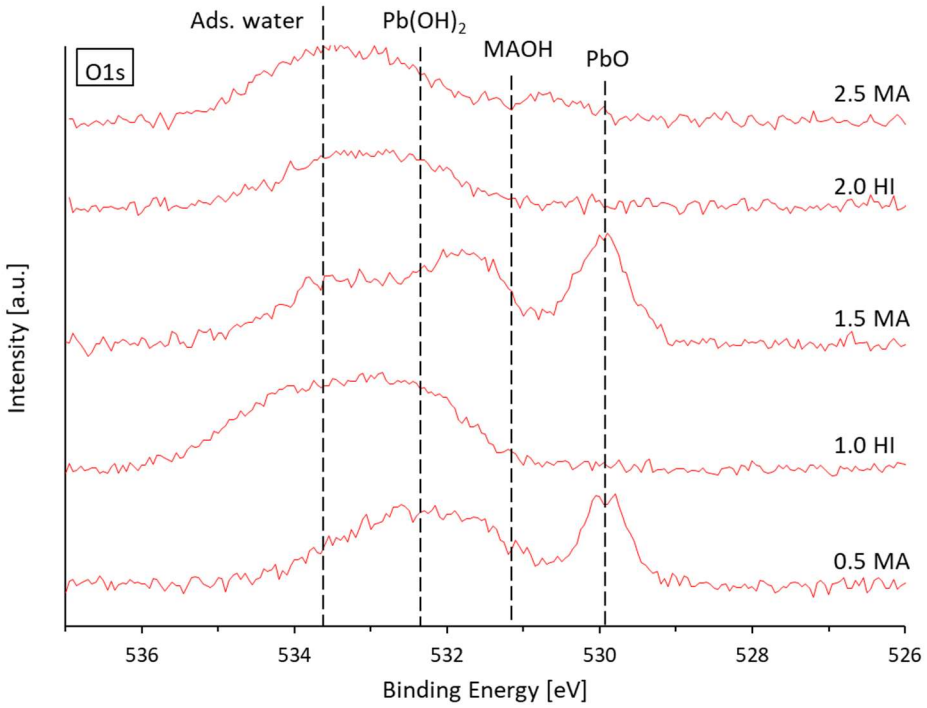

Figure 4.86 O1s XPS measurements of samples from the MA and HI gas CVD process, which were made without a drying agent in the HI production step

In conclusion, this type of upscalable CVD reaction involving PbI_2, MA, water and HI does produce a working MAPI perovskite material that achieved up to 12,9 % efficient solar cells (see Figure 4.76), but unwanted side products will always be present on the substrate, i.e. lead oxides and hydroxide in the MA step, or lead(II)iodide in the HI step. In this type of mechanism, the PbI_2 precursor film will never react completely to MAPI, since according to the equations in Table 4.17, in the best case, 3 molecules of PbI_2 will react to only 2 molecules of MAPI in a full cycle. No matter how many cycles are used, small amounts of PbI_2 will always remain on the substrate after a full cycle.

Although an acceptable efficiency has been achieved with the MA and HI gas CVD process through optimizations, the process could still be optimized further. In the following, notable

problems and challenges that could be overcome are presented and possible solutions are proposed.

Under certain circumstances, an unwanted white smoke can be observed in the reaction tube of the CVD apparatus, during the introduction of either the MA or the HI gas. In the case of the appearance of the white smoke during the introduction of the HI gas, a likely explanation is the formation of hydroiodic acid vapor from humidity (water) that still exists in the reaction tube, due to an incomplete evacuation, or not enough purging with N_2 gas. The white smoke appears at times after an MA step, only after HI gas has already been introduced and then evacuated in a previous step. Most likely fine particles of MAI form through the addition of MA and HI gas as shown in Equation 4.37. The HI gas could remain in the reaction tube due to an incomplete evacuation and not enough purging with N_2 gas, before the introduction of the MA gas. To avoid the formation of a white smoke in this sequential MA and HI gas type of reaction, an apparatus could be constructed with separate chambers for each of the two gases, with a mechanism that would allow a simple back and forth transfer of the substrate.

Equation 4.37 $CH_3NH_2 + HI \rightleftharpoons CH_3NH_3I$

Another challenge of the MA and HI gas CVD process are the pinholes that form on the substrates with progressing cycles. In Figure 4.87, image **a)** shows a Glass/FTO/c-TiO_2/m-TiO_2/PbI_2 substrate that has been treated once with MA. The substrate already shows more pinholes than the PbI_2 coated substrate alone (see Figure 4.8 in Chapter 4.1.1, Page 59 as a reference). The next image, **b)**, shows the same substrate that has gone through all 2.5 cycles (i.e. 3 x MA gas treatments and 2x HI gas treatments). The pinholes appear bigger and in a higher number. In image **b)**, the black rectangles indicate the positions on which gold will be later sputtered on in a subsequent step, which will define the area of the solar cells. The pinholes (on which MAPI material is most likely missing) might create contacts between the later deposited hole transport material (HTM) spiro-MeOTAD and the electron transport material (ETM) TiO_2, which most likely causes a loss in efficiency. Although many pinholes are present, the cells still feature a high average photovoltage of 1,05 V. The solar cell “mr” showed the highest measured

efficiency of all CVD produced solar cells of this work, with 12,9 %. The solar cell labeled “ml”, showed an efficiency of 11,8 % and the solar cell labeled “r”, had 12,8 %. Image **c)** shows the same substrate with completed solar cells, which has already been illuminated with an AM1.5G spectrum and measured for 15 h in the solar simulator. An obvious discoloration from brown (color of MAPI) to yellow (color of PbI_2) is visible, which indicates the degradation of the material due to MAI evaporation. Image **d)** is the same as image **c)**, with the addition of a red rectangle that indicates the actual illuminated area in the solar simulator. All other parts of the substrate are covered by the solar simulator’s plastic holder. It can be observed that the parts surrounding the red rectangle show less discoloration and degradation (compare images **c)** and **d)**), so MAI evaporation is accelerated by light exposure as confirmed by Das et al. through in-operando XPS measurements in vacuum.[189]

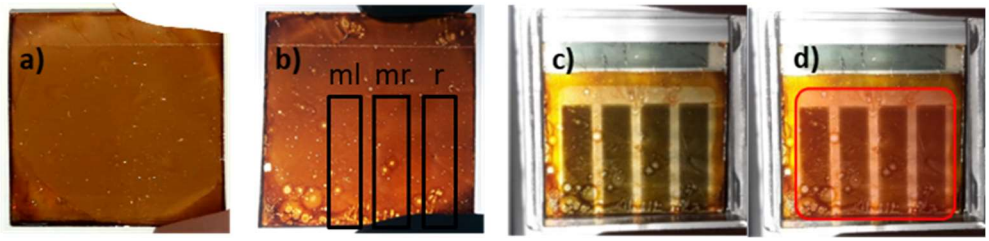

Figure 4.87 **a)** Glass/FTO/c-TiO_2/m-TiO_2/PbI_2 substrate that has been treated once with the MA gas. **b)** substrate from a) that underwent all 2.5 cycles of the CVD process (i.e. 3 x MA gas treatments and 2x HI gas treatments). The black rectangles indicate the position of the solar cells, which will be later defined by the gold contacts. **c)** completed solar cells from substrate b), which have been illuminated and measured for 15 h under an AM15.G spectrum. **d)** the same image as c) with the addition of a red rectangle that indicates the illuminated area in the holder of the solar simulator, the rest being covered by the plastic holder

A 15 hour measurement of the efficiency of the best solar cells from Figure 4.87 **c)** produced using the MA and HI gas CVD process, which had a starting efficiency of 12,9% is shown in Figure 4.88. The solar cell experiences an exponential decrease in efficiency due to degradation, with a value of under 2 % after 15 hours, measured continuously with the AM1.5G spectrum of the solar simulator. It is expected that the organic compound (i.e. MAI) evaporates from the MAPI film, leaving behind the PbI_2, that could also further degrade to elemental lead

(Pb^0) and I_2.[189] A common way of preventing this degradation would be encapsulating the substrate[199-201] with another piece of glass glued to the sides, on top of the active substrate, under inert atmosphere. The difficulty of encapsulation lies in choosing the right type and amount of glue and creating contacts to the outside, which would be compatible to the measuring device. These issues have not been considered any further in our own experiments.

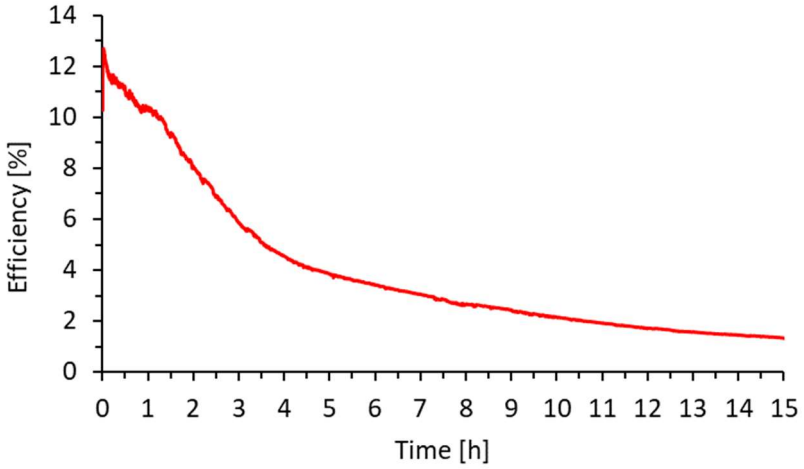

Figure 4.88 A 15 hour efficiency measurement of a solar cell produced with the MA and HI gas CVD method

To further analyze the aforementioned pinhole defects on the substrates, top view SEM images of a Glass/FTO/c-TiO_2/m-TiO_2/MAPI substrate, produced in 2.5 cycles in the MA and HI gas CVD process have been recorded and are shown in Figure 4.89. In the **left** image, needle like crystal defects on the MAPI film can be observed, which are most likely a conglomerate of MAPI crystals, also observed in literature.[202-204] These irregular crystals can form from surface impurities (dust from the surrounding), which act like a seed, as seen in the **middle** image. In the image on the **right**, another type of defect is shown, which has a large, presumably MAPI crystal in the middle, surrounded by a crater, which most likely exposes the titania layer underneath the MAPI. These kinds of defects appear by the naked eye as pinholes.

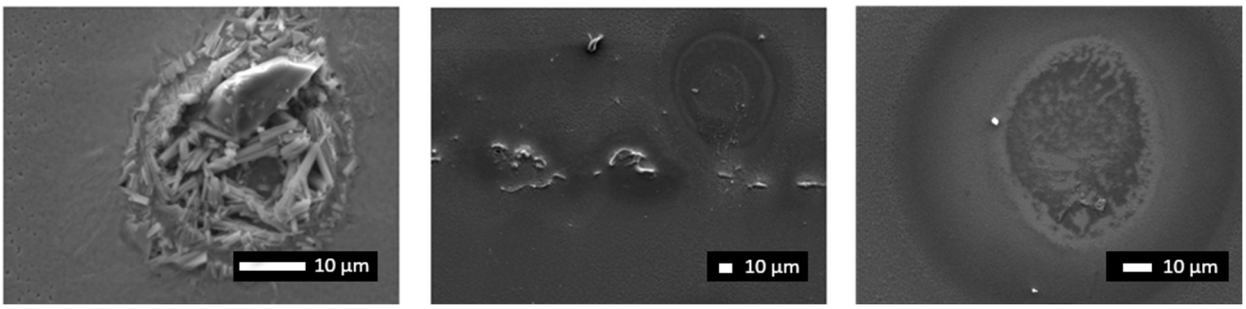

Figure 4.89 Top view scanning electron microscopy (SEM) images of MAPI films and defects from substrates produced using the MA and HI gas CVD method

Two types of possible mechanisms of the formation of the defects on the CVD prepared substrates are proposed in the following. I) The bubble model: tearing of the surface during the MA evacuation. The excess methylamine reversibly forms a liquid complex with MAPI.[205, 206] If the excess methylamine does not leave this complex evenly and diffuses out of the lower layers, tiny bubbles can form. Due to the low pressure to which the material is exposed during evacuation, gas bubbles break open and tear a hole into the surface. A gentler (slower) evacuation with an optional heating step could possibly suppress this phenomenon. II) Crystallization model: undesired crystallization on impurities or steps on the substrate. These crystallization nuclei and impurities arise from the condensation of water, methylammonium iodide smoke, particles from the sample holder and deposits that are brought onto the substrate from the gas inlet tubes. If the liquid complex that forms in each methylamine step is converted into the perovskites by evacuation of the excess MA, this germination can lead to crystallization. Since liquefaction occurs in each reaction cycle, these crystals can grow by attracting and incorporating MAPI from their surroundings. Possible solutions for mitigating these crystallization defects would be working in a clean room, which has ideally no dust and the separation of the MA and the HI gas reaction tubes to hinder the formation of MAI, which could lead to deposition of MAI crystallites from the “white smoke” on the surface of the substrates.

Another challenge of the CVD apparatus was that a large amount of material deposited inside the vacuum pump. The Pfeiffer Vacuum Duo 5 MC pump, although being especially designed for corrosive gases and having a magnetic coupling that separates the motor from the rotary

vane chamber, had difficulties of running with a constant suction power with an intermittent, audible beat, due to the deposition of large amounts of impurities as see in Figure 4.90. Image **a)** shows the inside of the pump covered by a brown slag, deposited from the large amounts of $HI_{aq.}$, humidity, MA, HI and other gases that have been used during the CVD process. In the carcass of the pump, image **b)**, white crystals formed, presumably organic-inorganic in nature, e.g. MAI from the addition of MA and HI. Image **c)** shows the perfluoropolyether (P4) pump oil, containing a brown slag, that could be easily filtered out, to recycle the rather expensive, inert P4 oil. The pump had to be disassembled several times (see Figure 4.91), cleaned in an ultra-sonic bath and reassembled to ensure a constant vacuum power. A solution to this problem would have been choosing a larger liquid nitrogen cold trap, that would have solidified a larger amount of the vapors and gasses used in the CVD processes, before entering the pump.

Figure 4.90 **a)** Image of the inside of the Pfeiffer Vacuum Duo 5 MC pump covered by a brown slag. **b)** Carcass of the pump with white crystallites build-up. **c)** Perfluoropolyether (P4) pump oil filtering from brown slag

Figure 4.91 Disassembled Pfeiffer Vacuum Duo 5 MC pump for cleaning

4.4.5 Formamidine gas – formamidinium lead iodide perovskite (FAPI)

Another mentionable experiment has been conducted, with the scope of producing formamidinium lead iodide (FAPI, $CN_2H_5PbI_3$) in the CVD device, a perovskite that is also commonly used as an absorber in well working solar cells.[207-209]

A modification of the CVD setup has been used as shown in Figure 4.92. In the round bottom flask, 2,3 g (0,058 mol) sodium hydroxide (NaOH) is mixed with 5,0 g (0,048 mol) formamidinium acetate (FA^+ac^-, $CN_2H_5^+CH_3COOH^-$).[210] The dropping funnel contains ca. 1 mL of dest. water. The drying tube is filled with calcium oxide (CaO), a commonly used material for drying alkaline gases. After inserting a Glass/FTO/c-TiO_2/m-TiO_2/PbI_2 substrate in the reaction tube, it is evacuated to ca. 1mbar. The water from the funnel is dropped onto the mixture of NaOH and FAac and mixed with a magnet stirrer. The substances react according to Equation 4.38, forming the formamidine gas (CN_2H_4). A valve that connects the round bottom flask, the drying tube and the reaction tube is slowly opened. The gas is left to react with the PbI_2 coated substrate for 20 min. After a short heat-up of several minutes at 100°C, an XRD of the substrate is measured in air that can be seen in Figure 4.93.

Equation 4.38 $NaOH + CN_2H_5^+CH_3COOH^- + H_2O \rightleftharpoons NaCH_3COOH + 2\,H_2O + CN_2H_4\uparrow$

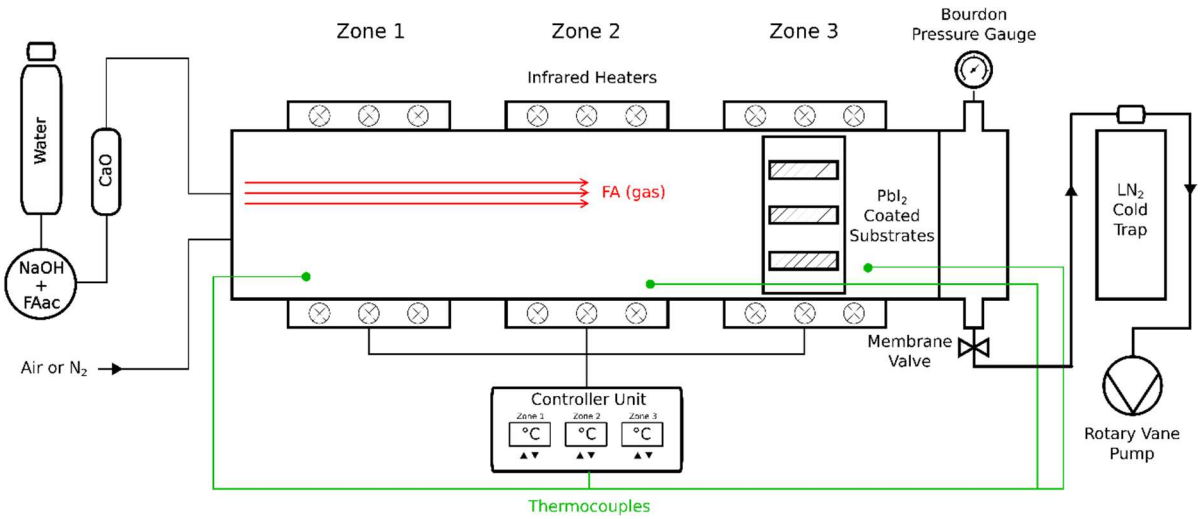

Figure 4.92 Schematic draft of the Chemical Vapor Deposition (CVD) setup, in the formamidinium (FA) gas version

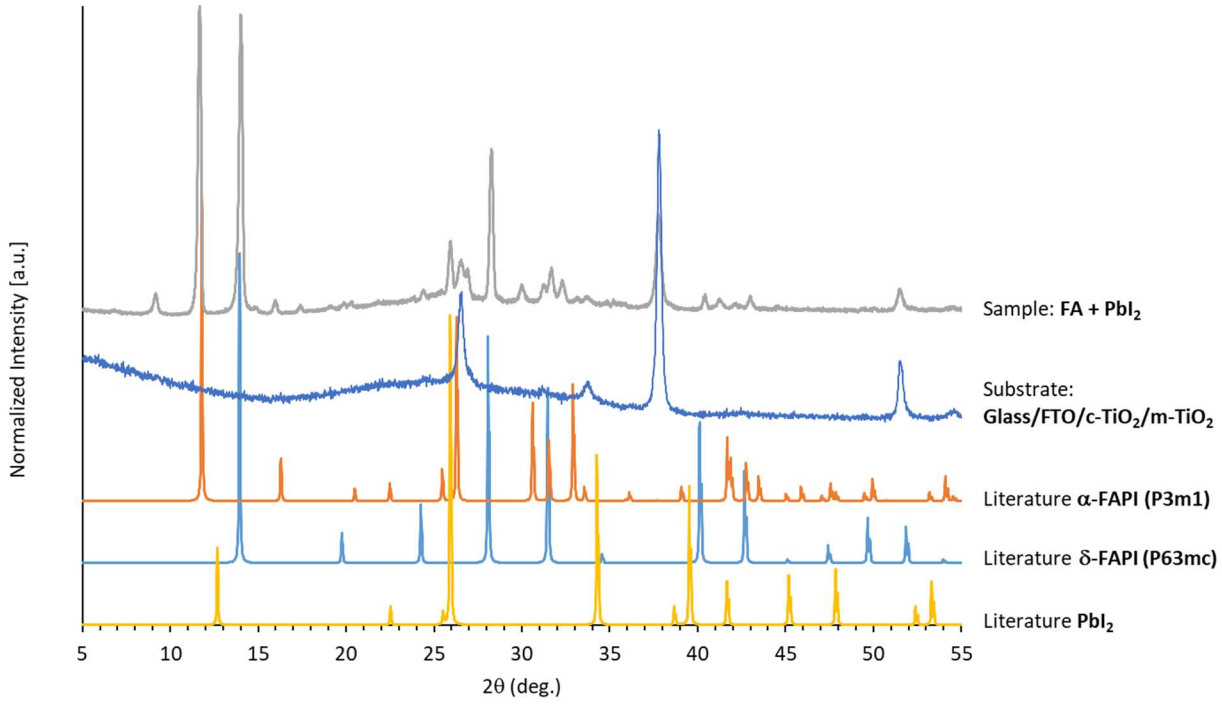

Figure 4.93 XRD patterns from top to bottom of: the Glass/FTO/c-TiO_2/m-TiO_2/PbI_2 substrate that was treated in the CVD setup with formamidine (FA) gas, a reference XRD measurement of the Glass/FTO/c-TiO_2/m-TiO_2 substrate, literature XRD patterns of the trigonal α-phase and the hexagonal δ-phase of the formamidinium lead iodide (FAPI)[211], and XRD patterns of lead iodide (PbI_2) [138]

Since the FA (CN_2H_4) gas does not bring an iodide anion needed to form the FAPI perovskite ($CN_2H_5PbI_3$) from PbI_2, a similar reaction mechanism is expected to take place, analogous to the PbI_2 + MA gas reaction as described in the previous Chapter 4.4.4, in which several PbI_2 molecules from the lattice would share iodides to form the perovskite. Water from the not completely dried FA gas most likely takes part in the reaction as well, to form the formamidinium cation ($CN_2H_5^+$) from the formamidine gas (CN_2H_4). Side products like PbO, or $Pb(OH)_2$ can be expected here as well.

Both the PbI_2 substrate and the substrate after the PbI_2 + FA gas reaction have a yellow color.

The XRD pattern of the substrate from the PbI_2 + FA gas reaction (Figure 4.93, gray curve) shows that FAPI indeed forms, indicating a successful reaction. A comparison with an XRD pattern of PbI_2[138] shows no match, suggesting completely reacted PbI_2. The comparison to literature XRD patterns of the α-phase and the δ-phase of the formamidinium lead iodide (FAPI) polymorph[211] shows that both phases are present on the reacted substrate. According to[212], the α-phase (space group *P3m1*) is a photo-active "black" perovskite phase, while the δ-phase (space group *$P6_3mc$*) is a non-perovskite "yellow" phase. Both phases are stable at room temperature. The annealing temperature of only 100°C used in this experiment was too low to form a completely black phase of FAPI perovskite. According to[211] a temperature of 150°C is needed to transform the δ-phase into the α-phase, while in the experiment only 100°C were used.

4.4.6 Transformation of a flash evaporated film of PbO to PbI_2, using $HI_{aq.}$

Another mentionable side experiment is the transformation of a flash evaporated film of PbO to PbI_2, using $HI_{aq.}$, as a precursor for perovskite solar cells, according to Equation 4.39.

Equation 4.39 $PbO + 2\ HI \rightleftharpoons PbI_2 + H_2O$

This method could be potentially upscaled in a CVD type of process. The motivation behind using the PbO coated film is a patent published in 2015 by Belcher et al. from the MIT (USA),[213] in which the authors describe a method of recycling lead acid car batteries, using lead from the anode and lead oxide from the cathode, transforming them with the help of heat, acetic acid, nitric acid and potassium iodide (KI) into PbI_2 and further processing it with MAI to form the MAPI perovskite and to build solar cells.

To flash evaporate a film of lead(II)oxide (PbO), the flash evaporation apparatus described in Chapter 4.3.1 is used. A few milligrams of PbO (Merck, ACS reagent, ≥99.0%) are placed on the tantalum source foil as seen in Figure 4.94 a). The material is evaporated at 100 % power (roughly 450°C) and $5 \cdot 10^{-3}$ mbar for 15 s onto a Glass/FTO/c-TiO_2/m-TiO_2 substrate. The remaining material on the tantalum source foil can be seen in Figure 4.94 b). The resulting film can be seen in photographs with light coming from the top in Figure 4.94 c) and d) and with light shining through the sample in Figure 4.94 e).

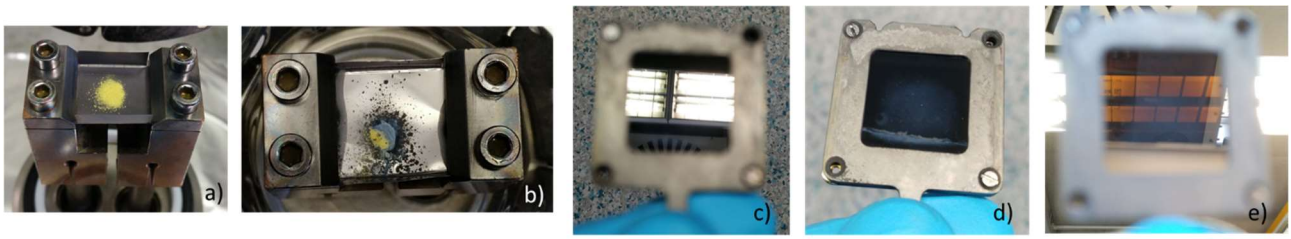

Figure 4.94 **a)** Lead(II)oxide, PbO (yellow) on top of the tantalum foil of the Flash Evaporation Apparatus from Chapter 4.3.1. **b)** Residual after the flash evaporation process at 100 % power (roughly 450°C) and $5 \cdot 10^{-3}$ mbar for 15 s. **c), d) and e)** The Glass/FTO/c-TiO_2/m-TiO_2/PbO substrate after the flash evaporation

The brown/reddish flashed Glass/FTO/c-TiO_2/m-TiO_2/PbO substrate is broken in half. One half is measured as is with XRD. The other half is transformed to PbI_2 as shown in Figure 4.95. The substrate is fixed with a double-sided adhesive tape to the bottom of a beaker and placed bottoms up on a Petri dish that holds a drop of concentrated hydroiodic acid ($HI_{aq.}$) The Petri dish is heated on a hot plate at 60°C. Figure 4.95 shows the gradual steps in time of the conversion process. After 15 min., the now yellow substrate is measured as well with XRD.

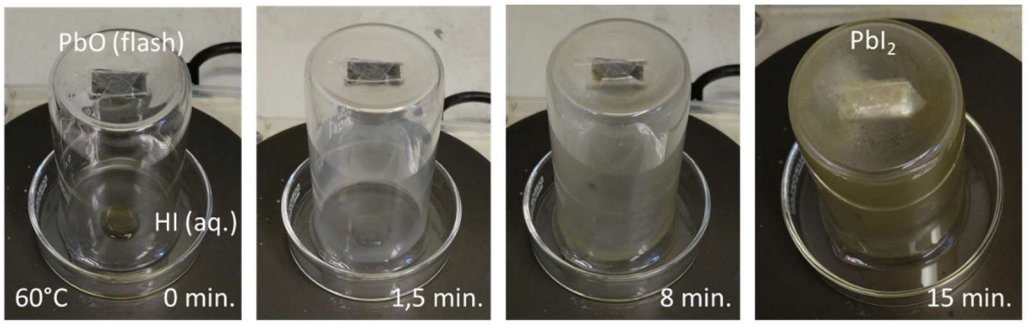

Figure 4.95 Steps in time of the transformation of lead(II)oxide (PbO), that was flash evaporated on a Glass/FTO/c-TiO_2/m-TiO_2 substrate, to lead(II)iodide (PbI_2), using a drop of hydroiodic acid ($HI_{aq.}$) and a temperature of 60°C

Figure 4.96 shows a side-by-side comparison of the substrate covered with PbO (brown/reddish) and the transformed substrate now covered with PbI_2 (yellow).

Figure 4.96 **Left,** a Glass/FTO/c-TiO_2/m-TiO_2/PbO sample and **right,** a Glass/FTO/c-TiO_2/m-TiO_2/PbI_2 sample

Figure 4.97 shows the XRD patterns of the two samples from Figure 4.96, compared to literature patterns of PbO and PbI_2[214] and also a measurement of the underlying Glass/FTO/c-TiO_2/m-TiO_2 substrate. The measurements clearly show that PbO has been successfully flashed onto the Glass/FTO/c-TiO_2/m-TiO_2 substrate and successfully transformed to PbI_2 using heated hydroiodic acid. Both XRD measurements of the PbO and the PbI_2 substrates correlate to reference spectra of the materials.[214]

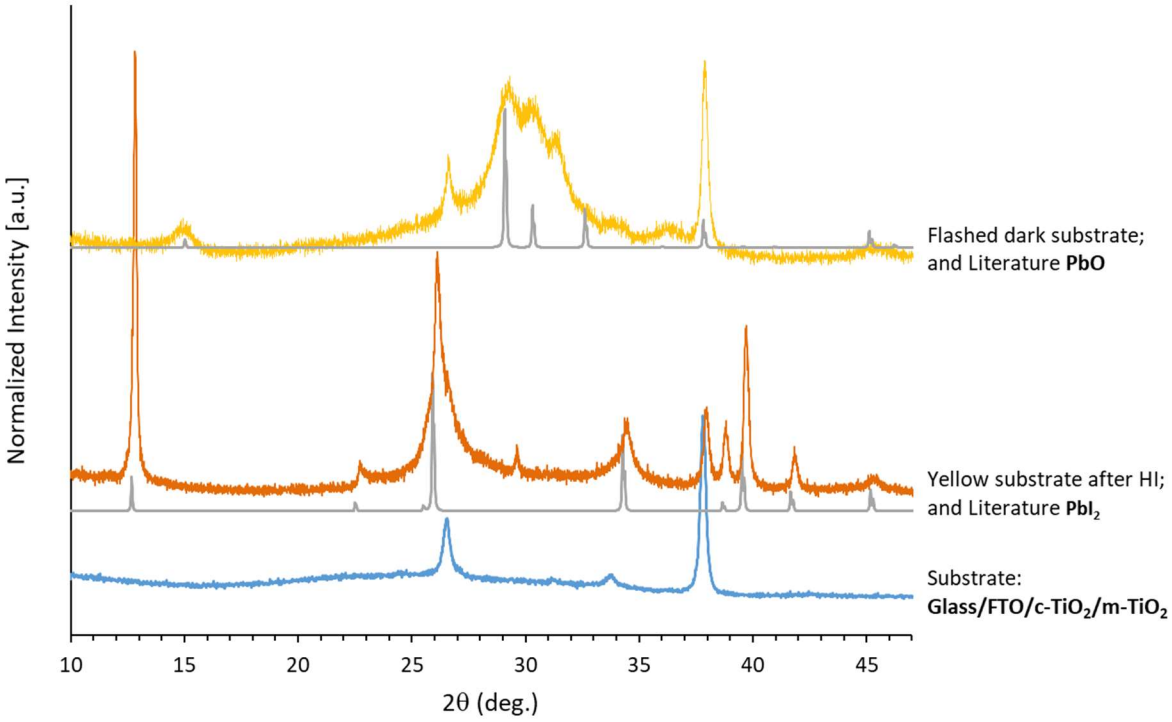

Figure 4.97 XRD measurements of the Glass/FTO/c-TiO_2/m-TiO_2 substrate and those of the substrates shown in Figure 4.96, which are covered with a layer of lead(II)oxide (PbO), resp. lead(II)iodide (PbI_2), alongside literature XRD patterns of PbO and PbI_2[214]

This experiment shows that the abundant material lead(II)oxide (PbO), can be easily transformed with the help of hydroiodic acid ($HI_{aq.}$) to lead(II)iodide (PbI_2), which is a common precursor for perovskite solar cell. This method could be upscaled to a CVD type of process.

5. Conclusion and Outlook

Thin film perovskite solar cells with different compositions have been manufactured throughout this work, using spin coating, spray pyrolysis, etching, sputtering, chemical bath deposition, flash evaporation and chemical vapor deposition (CVD). The solar cells and their materials have been characterized electrically at the solar simulator setup, and in addition using UV/Vis absorption spectroscopy, photoluminescence (PL), scanning electron microscopy (SEM), X-ray diffraction (XRD) and X-ray photoelectron spectroscopy (XPS).

Chapter 4.1 describes a recipe for building solar cells with the stack of materials: Glass/FTO/c-TiO_2/m-TiO_2/MAPI/spiro-MeOTAD/Au, in which the perovskite methylammonium lead iodide ($CH_3NH_3PbI_3$, MAPI) is the absorber. For this configuration, the maximum obtained efficiency is 15,6 % with a solar cell dimension of 32,5 mm^2 and a mini-module substrate dimension of 4 cm^2. This liquid process recipe could be further upscaled to manufacture panels using ink-jet printing, or slot-die coating, instead of the spin-coating process, which is otherwise a fast, lab-scale process that has limited scalability. In the next Chapter, 4.2 a one-step spin coating process is discussed, which uses a perovskite ink containing a triple cation, double anion, lead perovskite ($(Cs_aMA_bFA_c)_1PbI_xBr_{3-x}$). This recipe, having the same contact materials as the two-step process, resulted in an even higher efficiency of 18,5 %. The addition of caesium, formamidinium and bromide to the previously discussed methylammonium lead iodide improves device performance and should also improve the long-term stability of the solar cells.

In Chapter 4.3 a new home-built flash evaporation device was used to evaporate perovskite powders (produced by mechanochemical synthesis) under low vacuum. This non-liquid, one-step evaporation process did not result in any noteworthy solar cell efficiencies using MAPI. The morphology of the film showed many defects in the form of solidified droplets as characterized by SEM. The flash evaporation device could be further improved in this respect as described in Chapter 4.3.2. To address the concern of lead (Pb) toxicity in perovskite solar cells, films of the tin (Sn) containing perovskite methylammonium tin iodide ($CH_3NH_3SnI_3$, MASI) have also been produced via flash evaporation. These experiments show that MASI can be

congruently evaporated using the technique of flash evaporation to form a film that has a high chemical purity, measured by XPS and a single crystallographic phase, measured by XRD. For characterizing completed MASI solar cells, an encapsulation technique would need to be established, which would prevent the quick degradation of the material in air. If further optimized, the flash evaporation process could be considered as a viable alternative to the multi-source physical vapor deposition (PVD) process, for creating thin films of perovskite materials in one step and from one source, by using high quality perovskite powders produced by non-liquid processes such as ball milling.

In Chapter 4.4 a new home-built chemical vapor deposition (CVD) setup was used to produce MAPI and FAPI perovskites. To produce the MAPI perovskite, several precursor combinations have been tested, most notably involving a layer of PbI_2 that in one approach was treated with the gases ammonia (NH_3) and methyl iodide (CH_3I) and in another approach with the gases methylamine (MA, CH_3NH_2) and hydrogen iodide (HI), instead of the solid methylammonium iodide (CH_3NH_3I), which is commonly used. While for the first approach conditions for a successful reaction could not be found, the latter approach involving MA and HI has produced well working solar cells. For this reaction, the underlying mechanism of reaction has been clarified through XRD and XPS measurements and analysis. The PbI_2, MA and HI CVD reaction involves water from the atmosphere and thus unwanted side products will always be present on the substrate, i.e. lead oxides and hydroxide in the MA step, or lead(II)iodide in the HI step. In this type of mechanism, the PbI_2 precursor film will never react completely to MAPI. Nevertheless, acceptably high efficiencies have been achieved with this process with a maximum of 12,9 %. The FAPI perovskite was also successfully synthesized from a PbI_2 layer and formamidine gas via the CVD setup. A combination of MA, FA and even the use HBr gas instead of HI and $PbBr_2$ as a precursor film instead of PbI_2 could result in more stable and efficient perovskites with tunable band gaps. The CVD technique has a high commercial importance in fabrication of semiconducting materials and could well be established as one of the fabrication methods for perovskite solar cells.

Further improvements could be expected by introducing a better control of the flow of reactants as well as a higher purity of chemicals, a further optimization task outside the scope of this thesis.

A big advantage of thin film perovskite solar cells is their projected fabrication cost, in which a much smaller amount of materials is needed in comparison to the established silicon solar cells technology, potentially resulting in a lower levelized cost of electricity. Substitution of the contact materials like the expensive, organic spiro-MeOTAD with inorganic alternatives like NiO_x would further reduce the cost of production. The ability of perovskite solar cells to be manufactured on flexible and lightweight substrates, instead of rigid glass opens up the new application field of flexible solar cells that could be used in buildings and vehicles integration, in wearables, or portable devices. Another important advantage of perovskite solar cells is their ability to be used in tandem configurations, either by complementing silicon to achieve even higher power conversion efficiencies, or by using a number of different perovskite compositions in multi-perovskite tandem solar cells.

For all these applications the possible use of a CVD process as shown in this PhD thesis would be of interest. However, further improvements of the deposition technology would be needed.

6. Bibliography

[1] Saliba, M., Correa-Baena, J.-P., Wolff, C.M., Stolterfoht, M., Phung, N., Albrecht, S., et al. How to Make over 20% Efficient Perovskite Solar Cells in Regular (n–i–p) and Inverted (p–i–n) Architectures. Chem Mater. 2018, 30, 4193-201.

[2] Darmstädter Exzellenz-Graduiertenschule für Energiewissenschaft und Energietechnik (English: Darmstadt Graduate School of Excellence Energy Science and Engineering) www.ese.tu-darmstadt.de

[3] Smith, I.C., Hoke, E.T., Solis-Ibarra, D., McGehee, M.D., Karunadasa, H.I. A Layered Hybrid Perovskite Solar-Cell Absorber with Enhanced Moisture Stability. Angew Chem Int Edit. 2014, 53, 11232-5.

[4] Szostak, R., Marchezi, P.E., Marques, A.D., da Silva, J.C., de Holanda, M.S., Soares, M.M., et al. Exploring the formation of formamidinium-based hybrid perovskites by antisolvent methods: in situ GIWAXS measurements during spin coating. Sustain Energ Fuels. 2019, 3, 2287-97.

[5] Tong, G., Li, H., Li, D., Zhu, Z., Xu, E., Li, G., et al. Dual-Phase CsPbBr3–CsPb2Br5 Perovskite Thin Films via Vapor Deposition for High-Performance Rigid and Flexible Photodetectors. 2018, 14, 1702523.

[6] Bonomi, S., Marongiu, D., Sestu, N., Saba, M., Patrini, M., Bongiovanni, G., et al. Novel Physical Vapor Deposition Approach to Hybrid Perovskites: Growth of MAPbI(3) Thin Films by RF-Magnetron Sputtering. Sci Rep-Uk. 2018, 8.

[7] Di Giacomo, F., Shanmugam, S., Fledderus, H., Bruijnaers, B.J., Verhees, W.J.H., Dorenkamper, M.S., et al. Up-scalable sheet-to-sheet production of high efficiency perovskite module and solar cells on 6-in. substrate using slot die coating. Sol Energ Mat Sol C. 2018, 181, 53-9.

[8] Ciro, J., Mejia-Escobar, M.A., Jaramillo, F. Slot-die processing of flexible perovskite solar cells in ambient conditions. Sol Energy. 2017, 150, 570-6.

[9] Leyden, M.R., Ono, L.K., Raga, S.R., Kato, Y., Wang, S.H., Qi, Y.B. High performance perovskite solar cells by hybrid chemical vapor deposition. J Mater Chem A. 2014, 2, 18742-5.

[10] Leyden, M.R., Lee, M.V., Raga, S.R., Qi, Y.B. Large formamidinium lead trihalide perovskite solar cells using chemical vapor deposition with high reproducibility and tunable chlorine concentrations. J Mater Chem A. 2015, 3, 16097-103.

[11] Mathies, F., Eggers, H., Richards, B.S., Hernandez-Sosa, G., Lemmer, U., Paetzold, U.W. Inkjet-Printed Triple Cation Perovskite Solar Cells. Acs Appl Energ Mater. 2018, 1, 1834-9.

[12] Dou, B., Whitaker, J.B., Bruening, K., Moore, D.T., Wheeler, L.M., Ryter, J., et al. Roll-to-Roll Printing of Perovskite Solar Cells. Acs Energy Lett. 2018, 3, 2558-65.

[13] Shockley, W., Queisser, H.J. Detailed Balance Limit of Efficiency of P-N Junction Solar Cells. J Appl Phys. 1961, 32, 510-&.

[14] Ruhle, S. Tabulated values of the Shockley-Queisser limit for single junction solar cells. Sol Energy. 2016, 130, 139-47.

[15] Phung, N., Félix, R., Meggiolaro, D., Al-Ashouri, A., Sousa e Silva, G., Hartmann, C., et al. The Doping Mechanism of Halide Perovskite Unveiled by Alkaline Earth Metals. J Am Chem Soc. 2020, 142, 2364-74.
[16] Physics of Semiconductor Devices. Kluwer Academic Publishers, 2002.
[17] Rioult, M. Hematite-based epitaxial thin films as photoanodes for solar water splitting. 2015.
[18] Basnet, P., Dissertation: Metal Oxide Photocatalytic Nanostructures Fabricated By Dynamic Shadowing Growth 2015.
[19] Kittel, C. Introduction to solid state physics. Wiley. 2005.
[20] Becquerel, A.E. Memoire sur les Effects d'Electriques Produits Sous l'Influence des Rayons Solaires. Comptes Rendus de l'Academie des Sciences. 1839, Vol. 9, pp. 561-7.
[21] W. Adams, R.D. The action of light on selenium. Proceedings of the Royal Society of London. 1876, 25, pp. 113–7.
[22] Fritts, C.E. On the fritts selenium cells and batteries. Journal of the Franklin Institute. 1885, 119, 221-32.
[23] Siemens, W. On the electro motive action of illuminated selenium, discovered by Mr. Fritts, of New York. Journal of the Franklin Institute. 1885, 119, 453-IN6.
[24] Hutter, E.M., Gélvez-Rueda, M.C., Osherov, A., Bulović, V., Grozema, F.C., Stranks, S.D., et al. Direct–indirect character of the bandgap in methylammonium lead iodide perovskite. Nat Mater. 2017, 16, 115-20.
[25] Sarritzu, V., Sestu, N., Marongiu, D., Chang, X., Wang, Q., Masi, S., et al. Direct or Indirect Bandgap in Hybrid Lead Halide Perovskites? 2018, 6, 1701254.
[26] Wang, T., Daiber, B., Frost, J.M., Mann, S.A., Garnett, E.C., Walsh, A., et al. Indirect to direct bandgap transition in methylammonium lead halide perovskite. Energ Environ Sci. 2017, 10, 509-15.
[27] Burger, B. "Fraunhofer ISE: Photovoltaics Report, updated: 27 August 2018". 2018.
[28] Telahun, Y. Estimation of global solar radiation from sunshine hours, geographical and meteorological parameters. Solar & Wind Technology. 1987, 4, 127-30.
[29] Webmineral. http://webmineral.com/data/Perovskite.shtml#.XywhLTWxWUk.
[30] Baikie, T., Fang, Y.N., Kadro, J.M., Schreyer, M., Wei, F.X., Mhaisalkar, S.G., et al. Synthesis and crystal chemistry of the hybrid perovskite (CH3NH3) PbI3 for solid-state sensitised solar cell applications. J Mater Chem A. 2013, 1, 5628-41.
[31] Mitzi, D.B., Feild, C.A., Harrison, W.T.A., Guloy, A.M. Conducting Tin Halides with a Layered Organic-Based Perovskite Structure. Nature. 1994, 369, 467-9.
[32] Green, M.A., Ho-Baillie, A., Snaith, H.J. The emergence of perovskite solar cells. Nat Photonics. 2014, 8, 506-14.
[33] Jena, A.K., Kulkarni, A., Miyasaka, T. Halide Perovskite Photovoltaics: Background, Status, and Future Prospects. Chem Rev. 2019, 119, 3036-103.
[34] Lin, K.B., Xing, J., Quan, L.N., de Arquer, F.P.G., Gong, X.W., Lu, J.X., et al. Perovskite light-emitting diodes with external quantum efficiency exceeding 20 per cent. Nature. 2018, 562, 245-+.
[35] Sun, C., Zhang, Y., Ruan, C., Yin, C.Y., Wang, X.Y., Wang, Y.D., et al. Efficient and Stable White LEDs with Silica-Coated Inorganic Perovskite Quantum Dots. Adv Mater. 2016, 28, 10088-94.

[36] Yu, W.L., Li, F., Yu, L.Y., Niazi, M.R., Zou, Y.T., Corzo, D., et al. Single crystal hybrid perovskite field-effect transistors. Nat Commun. 2018, 9.
[37] Senanayak, S.P., Abdi-Jalebi, M., Kamboj, V.S., Carey, R., Shivanna, R., Tian, T., et al. A general approach for hysteresis-free, operationally stable metal halide perovskite field-effect transistors. Sci Adv. 2020, 6.
[38] Chen, Q.S., Wu, J., Ou, X.Y., Huang, B.L., Almutlaq, J., Zhumekenov, A.A., et al. All-inorganic perovskite nanocrystal scintillators. Nature. 2018, 561, 88-93.
[39] Xie, A., Hettiarachchi, C., Maddalena, F., Witkowski, M.E., Makowski, M., Drozdowski, W., et al. Lithium-doped two-dimensional perovskite scintillator for wide-range radiation detection. Communications Materials. 2020, 1, 37.
[40] Xu, W., Li, F.M., Cai, Z.X., Wang, Y.R., Luo, F., Chen, X. An ultrasensitive and reversible fluorescence sensor of humidity using perovskite CH3NH3PbBr3. J Mater Chem C. 2016, 4, 9651-5.
[41] Kojima, A., Teshima, K., Miyasaka, T., Shirai, Y. Novel Photoelectrochemical Cell with Mesoscopic Electrodes Sensitized by Lead-Halide Compounds (2). 2006.
[42] Gratzel, M. Dye-sensitized solar cells. J Photoch Photobio C. 2003, 4, 145-53.
[43] Kojima, A., Teshima, K., Shirai, Y., Miyasaka, T. Organometal Halide Perovskites as Visible-Light Sensitizers for Photovoltaic Cells. J Am Chem Soc. 2009, 131, 6050-+.
[44] Im, J.H., Lee, C.R., Lee, J.W., Park, S.W., Park, N.G. 6.5% efficient perovskite quantum-dot-sensitized solar cell. Nanoscale. 2011, 3, 4088-93.
[45] Salbeck, J., Yu, N., Bauer, J., Weissortel, F., Bestgen, H. Low molecular organic glasses for blue electroluminescence. Synthetic Met. 1997, 91, 209-15.
[46] Momblona, C., Malinkiewicz, O., Roldan-Carmona, C., Soriano, A., Gil-Escrig, L., Bandiello, E., et al. Efficient methylammonium lead iodide perovskite solar cells with active layers from 300 to 900 nm. Apl Mater. 2014, 2.
[47] Ava, T.T., Al Mamun, A., Marsillac, S., Namkoong, G. A Review: Thermal Stability of Methylammonium Lead Halide Based Perovskite Solar Cells. Appl Sci-Basel. 2019, 9.
[48] Sheng, R., Ho-Baillie, A., Huang, S.J., Chen, S., Wen, X.M., Hao, X.J., et al. Methylammonium Lead Bromide Perovskite-Based Solar Cells by Vapor-Assisted Deposition. J Phys Chem C. 2015, 119, 3545-9.
[49] Mhamdi, A., Mehdi, H., Bouazizi, A., Garcia-Belmonte, G. One-step methylammonium lead bromide films: Effect of annealing treatment. J Mol Struct. 2019, 1192, 1-6.
[50] Sarkar, P., Mazumder, J., Tripathy, S.K., Baishnab, K.L., Palai, G. Structural, optoelectronic, and morphological study of indium-doped methylammonium lead chloride perovskites. Appl Phys a-Mater. 2019, 125.
[51] Binek, A., Grill, I., Huber, N., Peters, K., Hufnagel, A.G., Handloser, M., et al. Control of Perovskite Crystal Growth by Methylammonium Lead Chloride Templating. Chem-Asian J. 2016, 11, 1199-204.
[52] Calvo, M.E. Materials chemistry approaches to the control of the optical features of perovskite solar cells. J Mater Chem A. 2017, 5, 20561-78.
[53] Zhou, Y.Y., Yang, M.J., Wu, W.W., Vasiliev, A.L., Zhu, K., Padture, N.P. Room-temperature crystallization of hybrid-perovskite thin films via solvent-solvent extraction for high-performance solar cells. J Mater Chem A. 2015, 3, 8178-84.

[54] Murugadoss, G., Thangamuthu, R., Kumar, M.R. Formamidinium lead iodide perovskite: Structure, shape and optical tuning via hydrothermal method. Mater Lett. 2018, 231, 16-9.
[55] Zhao, Y.C., Tan, H.R., Yuan, H.F., Yang, Z.Y., Fan, J.Z., Kim, J., et al. Perovskite seeding growth of formamidinium-lead-iodide-based perovskites for efficient and stable solar cells. Nat Commun. 2018, 9.
[56] Dimesso, L., Quintilla, A., Kim, Y.M., Lemmer, U., Jaegermann, W. Investigation of formamidinium and guanidinium lead tri-iodide powders as precursors for solar cells. Mater Sci Eng B-Adv. 2016, 204, 27-33.
[57] Jodlowski, A.D., Roldan-Carmona, C., Grancini, G., Salado, M., Ralaiarisoa, M., Ahmad, S., et al. Large guanidinium cation mixed with methylammonium in lead iodide perovskites for 19% efficient solar cells. Nat Energy. 2017, 2, 972-9.
[58] Wang, K., Jin, Z.W., Liang, L., Bian, H., Bai, D.L., Wang, H.R., et al. All-inorganic cesium lead iodide perovskite solar cells with stabilized efficiency beyond 15% (vol 9, 4544, 2018). Nat Commun. 2018, 9.
[59] Thomas, C.J., Zhang, Y.N., Guillaussier, A., Bdeir, K., Aly, O.F., Kim, H.G., et al. Thermal Stability of the Black Perovskite Phase in Cesium Lead Iodide Nanocrystals Under Humid Conditions. Chem Mater. 2019, 31, 9750-8.
[60] Bu, T.L., Liu, X.P., Zhou, Y., Yi, J.P., Huang, X., Luo, L., et al. A novel quadruple-cation absorber for universal hysteresis elimination for high efficiency and stable perovskite solar cells. Energ Environ Sci. 2017, 10, 2509-15.
[61] WHO. Exposure to lead: a major public health concern. World Health Organization, Geneva, 2010.
[62] Noel, N.K., Stranks, S.D., Abate, A., Wehrenfennig, C., Guarnera, S., Haghighirad, A.-A., et al. Lead-free organic–inorganic tin halide perovskites for photovoltaic applications. Energ Environ Sci. 2014, 7, 3061-8.
[63] Babayigit, A., Thanh, D.D., Ethirajan, A., Manca, J., Muller, M., Boyen, H.G., et al. Assessing the toxicity of Pb- and Sn-based perovskite solar cells in model organism Danio rerio. Sci Rep-Uk. 2016, 6.
[64] Hao, F., Stoumpos, C.C., Cao, D.H., Chang, R.P.H., Kanatzidis, M.G. Lead-free solid-state organic–inorganic halide perovskite solar cells. Nat Photonics. 2014, 8, 489-94.
[65] Howe, P.W., Peter. Tin and inorganic tin compounds. In: 1954- & United Nations Environment Programme & International Labour Organisation & World Health Organization, Geneva, 2005.
[66] Shao, S.Y., Liu, J., Portale, G., Fang, H.H., Blake, G.R., ten Brink, G.H., et al. Highly Reproducible Sn-Based Hybrid Perovskite Solar Cells with 9% Efficiency. Adv Energy Mater. 2018, 8.
[67] Marshall, K.P., Walton, R.I., Hatton, R.A. Tin perovskite/fullerene planar layer photovoltaics: improving the efficiency and stability of lead-free devices. J Mater Chem A. 2015, 3, 11631-40.
[68] Liao, Y., Liu, H., Zhou, W., Yang, D., Shang, Y., Shi, Z., et al. Highly Oriented Low-Dimensional Tin Halide Perovskites with Enhanced Stability and Photovoltaic Performance. J Am Chem Soc. 2017, 139, 6693-9.

[69] Tavakoli, M.M., Tsui, K.H., Zhang, Q.P., He, J., Yao, Y., Li, D.D., et al. Highly Efficient Flexible Perovskite Solar Cells with Antireflection and Self-Cleaning Nanostructures. Acs Nano. 2015, 9, 10287-95.
[70] Dou, B.J., Miller, E.M., Christians, J.A., Sanehira, E.M., Klein, T.R., Barnes, F.S., et al. High-Performance Flexible Perovskite Solar Cells on Ultrathin Glass: Implications of the TCO. J Phys Chem Lett. 2017, 8, 4960-6.
[71] Park, J.I., Heo, J.H., Park, S.H., Il Hong, K., Jeong, H.G., Im, S.H., et al. Highly flexible InSnO electrodes on thin colourless polyimide substrate for high-performance flexible CH3NH3PbI3 perovskite solar cells. J Power Sources. 2017, 341, 340-7.
[72] Heo, J.H., Lee, M.H., Han, H.J., Patil, B.R., Yu, J.S., Im, S.H. Highly efficient low temperature solution processable planar type CH3NH3PbI3 perovskite flexible solar cells. J Mater Chem A. 2016, 4, 1572-8.
[73] Yoon, J., Sung, H., Lee, G., Cho, W., Ahn, N., Jung, H.S., et al. Superflexible, high-efficiency perovskite solar cells utilizing graphene electrodes: towards future foldable power sources. Energ Environ Sci. 2017, 10, 337-45.
[74] Yang, D., Yang, R.X., Zhang, J., Yang, Z., Liu, S.Z., Li, C. High efficiency flexible perovskite solar cells using superior low temperature TiO2. Energ Environ Sci. 2015, 8, 3208-14.
[75] Hou, L.X., Wang, Y.L., Liu, X.H., Wang, J., Wang, L.X., Li, X.W., et al. 18.0% efficiency flexible perovskite solar cells based on double hole transport layers and CH3NH3PbI3-xClx with dual additives. J Mater Chem C. 2018, 6, 8770-7.
[76] Liu, C., Cai, M., Yang, Y., Arain, Z., Ding, Y., Shi, X., et al. A C60/TiOx bilayer for conformal growth of perovskite films for UV stable perovskite solar cells. J Mater Chem A. 2019, 7, 11086-94.
[77] Wojciechowski, K., Leijtens, T., Siprova, S., Schlueter, C., Hörantner, M.T., Wang, J.T.-W., et al. C60 as an Efficient n-Type Compact Layer in Perovskite Solar Cells. The Journal of Physical Chemistry Letters. 2015, 6, 2399-405.
[78] Schutt, K., Nayak, P.K., Ramadan, A.J., Wenger, B., Lin, Y.H., Snaith, H.J. Overcoming Zinc Oxide Interface Instability with a Methylammonium-Free Perovskite for High-Performance Solar Cells. Adv Funct Mater. 2019, 29.
[79] Dehghan, M., Behjat, A. Deposition of zinc oxide as an electron transport layer in planar perovskite solar cells by spray and SILAR methods comparable with spin coating. Rsc Adv. 2019, 9, 20917-24.
[80] Shalan, A.E., El-Shazly, A.N., Rashad, M.M., Allam, N.K. Tin-zinc-oxide nanocomposites (SZO) as promising electron transport layers for efficient and stable perovskite solar cells. Nanoscale Adv. 2019, 1, 2654-62.
[81] Smith, J.A., Game, O.S., Bishop, J.E., Spooner, E.L.K., Kilbride, R.C., Greenland, C., et al. Rapid Scalable Processing of Tin Oxide Transport Layers for Perovskite Solar Cells. Acs Appl Energ Mater. 2020, 3, 5552-62.
[82] Liang, J.W., Chen, Z.L., Yang, G., Wang, H.B., Ye, F.H., Tao, C., et al. Achieving High Open-Circuit Voltage on Planar Perovskite Solar Cells via Chlorine -Doped Tin Oxide Electron Transport Layers. Acs Appl Mater Inter. 2019, 11, 23152-9.
[83] Abuhelaiqa, M., Paek, S., Lee, Y., Cho, K.T., Heo, S., Oveisi, E., et al. Stable perovskite solar cells using tin acetylacetonate based electron transporting layers. Energ Environ Sci. 2019, 12, 1910-7.

[84] Hu, L.J., Li, M., Yang, K., Xiong, Z., Yang, B., Wang, M., et al. PEDOT:PSS monolayers to enhance the hole extraction and stability of perovskite solar cells. J Mater Chem A. 2018, 6, 16583-9.
[85] Huang, D., Goh, T., Kong, J., Zheng, Y.F., Zhao, S.L., Xu, Z., et al. Perovskite solar cells with a DMSO-treated PEDOT: PSS hole transport layer exhibit higher photovoltaic performance and enhanced durability. Nanoscale. 2017, 9, 4236-43.
[86] Adam, G., Kaltenbrunner, M., Glowacki, E.D., Apaydin, D.H., White, M.S., Heilbrunner, H., et al. Solution processed perovskite solar cells using highly conductive PEDOT:PSS interfacial layer. Sol Energ Mat Sol C. 2016, 157, 318-25.
[87] Liu, X.L., Cheng, Y.H., Liu, C., Zhang, T.X., Zhang, N.D., Zhang, S.W., et al. 20.7% highly reproducible inverted planar perovskite solar cells with enhanced fill factor and eliminated hysteresis (vol 12, pg 1622, 2019). Energ Environ Sci. 2019, 12, 1718-.
[88] Xu, C.Y., Liu, Z.H., Lee, E.C. High-performance metal oxide-free inverted perovskite solar cells using poly(bis(4-phenyl)(2,4,6-trimethylphenyl)amine) as the hole transport layer. J Mater Chem C. 2018, 6, 6975-81.
[89] Zhao, Q., Wu, R.S., Zhang, Z.L., Xiong, J., He, Z., Fan, B.J., et al. Achieving efficient inverted planar perovskite solar cells with nondoped PTAA as a hole transport layer. Org Electron. 2019, 71, 106-12.
[90] Lin, Y.R., Liao, Y.S., Hsiao, H.T., Chen, C.P. Two-step annealing of NiOx enhances the NiOx-perovskite interface for high-performance ambient-stable p-i-n perovskite solar cells. Appl Surf Sci. 2020, 504.
[91] Chen, W., Pang, G.T., Zhou, Y.C., Sun, Y.Z., Liu, F.Z., Chen, R., et al. Stabilizing n-type hetero-junctions for NiOx based inverted planar perovskite solar cells with an efficiency of 21.6%. J Mater Chem A. 2020, 8, 1865-74.
[92] Li, R.J., Wang, P.Y., Chen, B.B., Cui, X.H., Ding, Y., Li, Y.L., et al. NiOx/Spiro Hole Transport Bilayers for Stable Perovskite Solar Cells with Efficiency Exceeding 21%. Acs Energy Lett. 2020, 5, 79-86.
[93] Li, H., Cao, K., Cui, J., Liu, S.S., Qiao, X.F., Shen, Y., et al. 14.7% efficient mesoscopic perovskite solar cells using single walled carbon nanotubes/carbon composite counter electrodes. Nanoscale. 2016, 8, 6379-85.
[94] Yang, Y.Y., Xiao, J.Y., Wei, H.Y., Zhu, L.F., Li, D.M., Luo, Y.H., et al. An all-carbon counter electrode for highly efficient hole-conductor-free organo-metal perovskite solar cells. Rsc Adv. 2014, 4, 52825-30.
[95] Wei, Z.H., Chen, H.N., Yan, K.Y., Zheng, X.L., Yang, S.H. Hysteresis-free multi-walled carbon nanotube-based perovskite solar cells with a high fill factor. J Mater Chem A. 2015, 3, 24226-31.
[96] Thakur, U.K., Kumar, P., Gusarov, S., Kobryn, A.E., Riddell, S., Goswami, A., et al. Consistently High Voc Values in p-i-n Type Perovskite Solar Cells Using Ni3+-Doped NiO Nanomesh as the Hole Transporting Layer. Acs Appl Mater Inter. 2020, 12, 11467-78.
[97] Troughton, J., Bryant, D., Wojciechowski, K., Carnie, M.J., Snaith, H., Worsley, D.A., et al. Highly efficient, flexible, indium-free perovskite solar cells employing metallic substrates. J Mater Chem A. 2015, 3, 9141-5.
[98] Lee, E., Ahn, J., Kwon, H.C., Ma, S., Kim, K., Yun, S., et al. All-Solution-Processed Silver Nanowire Window Electrode-Based Flexible Perovskite Solar Cells Enabled with Amorphous Metal Oxide Protection. Adv Energy Mater. 2018, 8.

[99] Lee, M., Jo, Y., Kim, D.S., Jun, Y. Flexible organo-metal halide perovskite solar cells on a Ti metal substrate. J Mater Chem A. 2015, 3, 4129-33.
[100] You, P., Liu, Z.K., Tai, Q.D., Liu, S.H., Yan, F. Efficient Semitransparent Perovskite Solar Cells with Graphene Electrodes. Adv Mater. 2015, 27, 3632-8.
[101] Liu, Z.K., You, P., Xie, C., Tang, G.Q., Yan, F. Ultrathin and flexible perovskite solar cells with graphene transparent electrodes. Nano Energy. 2016, 28, 151-7.
[102] Cotella, G., Baker, J., Worsley, D., De Rossi, F., Pleydell-Pearce, C., Carnie, M., et al. One-step deposition by slot-die coating of mixed lead halide perovskite for photovoltaic applications. Sol Energ Mat Sol C. 2017, 159, 362-9.
[103] Whitaker, J.B., Kim, D.H., Larson, B.W., Zhang, F., Berry, J.J., van Hest, M.F.A.M., et al. Scalable slot-die coating of high performance perovskite solar cells. Sustain Energ Fuels. 2018, 2, 2442-9.
[104] Mathies, F., List-Kratochvil, E.J.W., Unger, E.L. Advances in Inkjet-Printed Metal Halide Perovskite Photovoltaic and Optoelectronic Devices. Energy Technol-Ger. 2020, 8.
[105] Fan, P., Gu, D., Liang, G.X., Luo, J.T., Chen, J.L., Zheng, Z.H., et al. High-performance perovskite CH3NH3PbI3 thin films for solar cells prepared by single-source physical vapour deposition. Sci Rep-Uk. 2016, 6.
[106] Avila, J., Momblona, C., Boix, P.P., Sessolo, M., Bolink, H.J. Vapor-Deposited Perovskites: The Route to High-Performance Solar Cell Production? Joule. 2017, 1, 431-42.
[107] Tran, V.D., Pammi, S.V.N., Dao, V.D., Choi, H.S., Yoon, S.G. Chemical vapor deposition in fabrication of robust and highly efficient perovskite solar cells based on single-walled carbon nanotubes counter electrodes. J Alloy Compd. 2018, 747, 703-11.
[108] Leyden, M.R., Jiang, Y., Qi, Y.B. Chemical vapor deposition grown formamidinium perovskite solar modules with high steady state power and thermal stability. J Mater Chem A. 2016, 4, 13125-32.
[109] Quarti, C., Mosconi, E., Ball, J.M., D'Innocenzo, V., Tao, C., Pathak, S., et al. Structural and optical properties of methylammonium lead iodide across the tetragonal to cubic phase transition: implications for perovskite solar cells. Energ Environ Sci. 2016, 9, 155-63.
[110] Moulder, J.F., Chastain, J. Handbook of X-ray Photoelectron Spectroscopy: A Reference Book of Standard Spectra for Identification and Interpretation of XPS Data, Physical Electronics Division, Perkin-Elmer Corporation, 1992.
[111] Choi, Y.C., Lee, S.W., Jo, H.J., Kim, D.H., Sung, S.J. Controlled growth of organic-inorganic hybrid CH3NH3PbI3 perovskite thin films from phase-controlled crystalline powders. Rsc Adv. 2016, 6, 104359-65.
[112] Hamill, J.C., Schwartz, J., Loo, Y.L. Influence of Solvent Coordination on Hybrid Organic-I norganic Perovskite Formation. Acs Energy Lett. 2018, 3, 92-7.
[113] Fonthal, G., Tirado-Mejia, L., Marin-Hurtado, J.I., Ariza-Calderon, H., Mendoza-Alvarez, J.G. Temperature dependence of the band gap energy of crystalline CdTe. J Phys Chem Solids. 2000, 61, 579-83.
[114] Bludau, W., Onton, A., Heinke, W. Temperature dependence of the band gap of silicon. 1974, 45, 1846-8.
[115] Manion, J.G., Proppe, A.H., Hicks, G.E.J., Sargent, E.H., Seferos, D.S. High Throughput Screening of Antisolvents for the Deposition of High Quality Perovskite Thin Films. Acs Appl Mater Inter. 2020.

[116] Song, T.B., Yuan, Z.H., Babbe, F., Nenon, D.P., Aydin, E., De Wolf, S., et al. Dynamics of Antisolvent Processed Hybrid Metal Halide Perovskites Studied by In Situ Photoluminescence and Its Influence on Optoelectronic Properties. Acs Appl Energ Mater. 2020, 3, 2386-93.
[117] Longo, G., Gil-Escrig, L., Degen, M.J., Sessolo, M., Bolink, H.J. Perovskite solar cells prepared by flash evaporation. Chem Commun. 2015, 51, 7376-8.
[118] Conings, B., Drijkoningen, J., Gauquelin, N., Babayigit, A., D'Haen, J., D'Olieslaeger, L., et al. Intrinsic Thermal Instability of Methylammonium Lead Trihalide Perovskite. Adv Energy Mater. 2015, 5.
[119] Gelmetti, I., Cabau, L., Montcada, N.F., Palomares, E. Selective Organic Contacts for Methyl Ammonium Lead Iodide (MAPI) Perovskite Solar Cells: Influence of Layer Thickness on Carriers Extraction and Carriers Lifetime. Acs Appl Mater Inter. 2017, 9, 21599-605.
[120] Carretero-Palacios, S., Jimenez-Solano, A., Miguez, H. Plasmonic Nanoparticles as Light-Harvesting Enhancers in Perovskite Solar Cells: A User's Guide. Acs Energy Lett. 2016, 1, 323-31.
[121] Biccari, F., Gabelloni, F., Burzi, E., Gurioli, M., Pescetelli, S., Agresti, A., et al. Graphene-Based Electron Transport Layers in Perovskite Solar Cells: A Step-Up for an Efficient Carrier Collection. Adv Energy Mater. 2017, 7.
[122] Mortan, C., Hellmann, T., Clemens, O., Mayer, T., Jaegermann, W. Preparation of Methylammonium Tin Iodide (CH3NH3SnI3) Perovskite Thin Films via Flash Evaporation. Phys Status Solidi A. 2019, 216.
[123] Hao, F., Stoumpos, C.C., Cao, D.H., Chang, R.P.H., Kanatzidis, M.G. Lead-free solid-state organic-inorganic halide perovskite solar cells. Nat Photonics. 2014, 8, 489-94.
[124] Wang, F., Ma, J.L., Xie, F.Y., Li, L.K., Chen, J., Fan, J., et al. Organic Cation-Dependent Degradation Mechanism of Organotin Halide Perovskites. Adv Funct Mater. 2016, 26, 3417-23.
[125] Liu, L.J., McLeod, J.A., Wang, R.B., Shen, P.F., Duhm, S. Tracking the formation of methylammonium lead triiodide perovskite. Appl Phys Lett. 2015, 107.
[126] Hellmann, T., Wussler, M., Das, C., Dachauer, R., El-Helaly, I., Mortan, C., et al. The difference in electronic structure of MAPI and MASI perovskites and its effect on the interface alignment to the HTMs spiro-MeOTAD and CuI. J Mater Chem C. 2019, 7, 5324-32.
[127] Juarez-Perez, E.J., Hawash, Z., Raga, S.R., Ono, L.K., Qi, Y.B. Thermal degradation of CH3NH3PbI3 perovskite into NH3 and CH3I gases observed by coupled thermogravimetry-mass spectrometry analysis. Energ Environ Sci. 2016, 9, 3406-10.
[128] Baekbo, M.J., Hansen, O., Chorkendorff, I., Vesborg, P.C.K. Deposition of methylammonium iodide via evaporation - combined kinetic and mass spectrometric study. Rsc Adv. 2018, 8, 29899-908.
[129] Upadhyaya, A., Negi, C.M.S., Yadav, A., Gupta, S.K., Verma, A.S. Synthesis and Characterization of Methylammonium Lead Iodide Perovskite and its Application in Planar Hetero-junction Devices. Semicond Sci Tech. 2018, 33.
[130] Weiss, M., Horn, J., Richter, C., Schlettwein, D. Preparation and characterization of methylammonium tin iodide layers as photovoltaic absorbers (Phys. Status Solidi A 4⁄2016). 2016, 213, 841-.

[131] Levchuk, I., Hou, Y., Gruber, M., Brandl, M., Herre, P., Tang, X.F., et al. Deciphering the Role of Impurities in Methylammonium Iodide and Their Impact on the Performance of Perovskite Solar Cells. Adv Mater Interfaces. 2016, 3.
[132] Gurina, G.I., Savchenko, K.V. Intercalation and formation of complexes in the system of lead(II) iodide-ammonia. J Solid State Chem. 2004, 177, 909-15.
[133] Preda, N., Mihut, L., Baibarac, M., Baltog, I., Ramer, R., Pandele, J., et al. Films and crystalline powder of PbI2 intercalated with ammonia and pyridine. J Mater Sci-Mater El. 2009, 20, 465-70.
[134] Zhou, Y., Yang, M., Pang, S., Zhu, K., Padture, N.P. Exceptional Morphology-Preserving Evolution of Formamidinium Lead Triiodide Perovskite Thin Films via Organic-Cation Displacement. J Am Chem Soc. 2016, 138, 5535-8.
[135] Zong, Y., Zhou, Y., Ju, M., Garces, H.F., Krause, A.R., Ji, F., et al. Thin-Film Transformation of NH4 PbI3 to CH3 NH3 PbI3 Perovskite: A Methylamine-Induced Conversion-Healing Process. Angewandte Chemie (International ed. in English). 2016, 55, 14723-7.
[136] Dimesso, L., Wussler, M., Mayer, T., Mankel, E., Jaegermann, W. Inorganic alkali lead Iodide semiconducting APbI3 (A = Li, Na, K, Cs) and NH4PbI3 films prepared from solution: Structure, morphology, and electronic structure, AIMS Materials Science. 2016, Vol. 3, pp. 737-55.
[137] Fan, L.-Q., Wu, J.-H. NH4PbI3. Acta Crystallogr. E. 2007, 63, i189-i.
[138] Mcmurdie, H.F., Swanson, H.E. Standard X-Ray Powder Patterns at the National Bureau of Standards. Acta Crystallogr. 1960, 13, 1098-.
[139] Wang, F., Yu, H., Xu, H.H., Zhao, N. HPbI3: A New Precursor Compound for Highly Efficient Solution-Processed Perovskite Solar Cells. Adv Funct Mater. 2015, 25, 1120-6.
[140] Cheng, N.A., Li, W.W., Xiao, Z.Y., Sun, S.J., Zhao, Z.Q., Zi, W., et al. High performance hole transport material free perovskite solar cells from a low pure PbI2 source using a facile solid-gas reaction process. Org Electron. 2018, 53, 221-6.
[141] Pang, S.P., Zhou, Y.Y., Wang, Z.W., Yang, M.J., Krause, A.R., Zhou, Z.M., et al. Transformative Evolution of Organolead Triiodide Perovskite Thin Films from Strong Room-Temperature Solid-Gas Interaction between HPbI(3)-CH3NH2 Precursor Pair. J Am Chem Soc. 2016, 138, 750-3.
[142] Wu, C.-G., Chiang, C.-H., Chang, S.H. A perovskite cell with a record-high-Voc of 1.61 V based on solvent annealed CH3NH3PbBr3/ICBA active layer. Nanoscale. 2016, 8, 4077-85.
[143] Ng, C.H., Ripolles, T.S., Hamada, K., Teo, S.H., Lim, H.N., Bisquert, J., et al. Tunable Open Circuit Voltage by Engineering Inorganic Cesium Lead Bromide/Iodide Perovskite Solar Cells. Sci Rep-Uk. 2018, 8, 2482.
[144] Taylor, R. Vogel Textbook of Practical Organic-Chemistry, 5th Edition - Furniss,Bs, Hannaford,Aj, Smith,Pwg, Tatchell,Ar. Nature. 1989, 342, 629-.
[145] Ke, W.J., Spanopoulos, I., Stoumpos, C.C., Kanatzidis, M.G. Myths and reality of HPbI3 in halide perovskite solar cells. Nat Commun. 2018, 9.
[146] Chen, Q., Zhou, H.P., Hong, Z.R., Luo, S., Duan, H.S., Wang, H.H., et al. Planar Heterojunction Perovskite Solar Cells via Vapor-Assisted Solution Process. J Am Chem Soc. 2014, 136, 622-5.

[147] Luo, P.F., Liu, Z.F., Xia, W., Yuan, C.C., Cheng, J.G., Lu, Y.W. A simple in situ tubular chemical vapor deposition processing of large-scale efficient perovskite solar cells and the research on their novel roll-over phenomenon in J-V curves. J Mater Chem A. 2015, 3, 12443-51.
[148] Tavakoli, M.M., Gu, L.L., Gao, Y., Reckmeier, C., He, J., Rogach, A.L., et al. Fabrication of efficient planar perovskite solar cells using a one-step chemical vapor deposition method. Sci Rep-Uk. 2015, 5.
[149] Bhachu, D.S., Scanlon, D.O., Saban, E.J., Bronstein, H., Parkin, I.P., Carmalt, C.J., et al. Scalable route to CH3NH3PbI3 perovskite thin films by aerosol assisted chemical vapour deposition. J Mater Chem A. 2015, 3, 9071-3.
[150] Panzer, F., Hanft, D., Gujar, T.P., Kahle, F.J., Thelakkat, M., Kohler, A., et al. Compact Layers of Hybrid Halide Perovskites Fabricated via the Aerosol Deposition Process-Uncoupling Material Synthesis and Layer Formation. Materials. 2016, 9.
[151] Chen, S.Q., Briscoe, J., Shi, Y., Chen, K., Wilson, R.M., Dunna, S., et al. A simple, low-cost CVD route to high-quality CH3NH3PbI3 perovskite thin films. Crystengcomm. 2015, 17, 7486-9.
[152] Peng, Y.K., Jing, G.S., Cui, T.H. A hybrid physical-chemical deposition process at ultra-low temperatures for high-performance perovskite solar cells. J Mater Chem A. 2015, 3, 12436-42.
[153] Wang, B.H., Chen, T. Exceptionally Stable CH3NH3PbI3 Films in Moderate Humid Environmental Condition. Adv Sci. 2016, 3.
[154] Yin, J., Qu, H., Cao, J., Tai, H.L., Li, J., Zheng, N.F. Vapor-assisted crystallization control toward high performance perovskite photovoltaics with over 18% efficiency in the ambient atmosphere. J Mater Chem A. 2016, 4, 13203-10.
[155] Huang, J.B., Tan, S.Q., Lund, P.D., Zhou, H.P. Impact of H2O on organic-inorganic hybrid perovskite solar cells. Energ Environ Sci. 2017, 10, 2284-311.
[156] Mortan, C., Hellmann, T., Buchhorn, M., d'Eril Melzi, M., Clemens, O., Mayer, T., et al. Preparation of methylammonium lead iodide (CH3NH3PbI3) thin film perovskite solar cells by chemical vapor deposition using methylamine gas (CH3NH2) and hydrogen iodide gas. Energy Sci Eng. 2020; 8: 3165– 3173.
[157] Zhou, Z.M., Wang, Z.W., Zhou, Y.Y., Pang, S.P., Wang, D., Xu, H.X., et al. Methylamine-Gas-Induced Defect-Healing Behavior of CH3NH3PbI3 Thin Films for Perovskite Solar Cells. Angew Chem Int Edit. 2015, 54, 9705-9.
[158] Zhang, M.J., Wang, N., Pang, S.P., Lv, L., Huang, C.S., Zhou, Z.M., et al. Carrier Transport Improvement of CH3NH3PbI3 Film by Methylamine Gas Treatment. Acs Appl Mater Inter. 2016, 8, 31413-8.
[159] Huang, Y.Q., Wu, S.H., Chen, R., Fang, S.Y., Zhang, S.S., Wang, G., et al. Efficient Methylamine-Containing Antisolvent Strategy to Fabricate High-Efficiency and Stable FA(0.85)Cs(0.15)Pb(Br0.15I2.85) Perovskite Solar Cells. Acs Appl Mater Inter. 2019, 11, 18415-22.
[160] Zhao, T., Williams, S.T., Chueh, C.-C., deQuilettes, D.W., Liang, P.-W., Ginger, D.S., et al. Design rules for the broad application of fast (<1 s) methylamine vapor based, hybrid perovskite post deposition treatments. Rsc Adv. 2016, 6, 27475-84.

[161] Zhang, Y., Zhou, Z.M., Ji, F.X., Li, Z.P., Cui, G.L., Gao, P., et al. Trash into Treasure: delta-FAPbI(3) Polymorph Stabilized MAPbI(3) Perovskite with Power Conversion Efficiency beyond 21%. Adv Mater. 2018, 30.
[162] Shao, Z.P., Wang, Z.W., Li, Z.P., Fan, Y.P., Meng, H.G., Liu, R.R., et al. A Scalable Methylamine Gas Healing Strategy for High-Efficiency Inorganic Perovskite Solar Cells. Angew Chem Int Edit. 2019, 58, 5587-91.
[163] Yang, J.A., Qin, T.X., Xie, L.S., Liao, K.J., Li, T.S., Hao, F. Methylamine-induced defect-healing and cationic substitution: a new method for low-defect perovskite thin films and solar cells. J Mater Chem C. 2019, 7, 10724-42.
[164] Hong, L., Hu, Y., Mei, A.Y., Sheng, Y.S., Jiang, P., Tian, C.B., et al. Improvement and Regeneration of Perovskite Solar Cells via Methylamine Gas Post-Treatment. Adv Funct Mater. 2017, 27.
[165] Liu, Z.H., Qiu, L.B., Juarez-Perez, E.J., Hawash, Z., Kim, T., Jiang, Y., et al. Gas-solid reaction based over one-micrometer thick stable perovskite films for efficient solar cells and modules. Nat Commun. 2018, 9.
[166] Chen, H., Ye, F., Tang, W.T., He, J.J., Yin, M.S., Wang, Y.B., et al. A solvent- and vacuum-free route to large-area perovskite films for efficient solar modules. Nature. 2017, 550, 92-+.
[167] Noel, N.K., Habisreutinger, S.N., Wenger, B., Klug, M.T., Horantner, M.T., Johnston, M.B., et al. A low viscosity, low boiling point, clean solvent system for the rapid crystallisation of highly specular perovskite films. Energ Environ Sci. 2017, 10, 145-52.
[168] Raga, S.R., Ono, L.K., Qi, Y.B. Rapid perovskite formation by CH3NH2 gas-induced intercalation and reaction of PbI2. J Mater Chem A. 2016, 4, 2494-500.
[169] Yamada, Y., Nakamura, T., Endo, M., Wakamiya, A., Kanemitsu, Y. Near-band-edge optical responses of solution-processed organic-inorganic hybrid perovskite CH3NH3PbI3 on mesoporous TiO2 electrodes. Appl Phys Express. 2014, 7.
[170] Peng, W., Miao, X.H., Adinolfi, V., Alarousu, E., El Tall, O., Emwas, A.H., et al. Engineering of CH3NH3PbI3 Perovskite Crystals by Alloying Large Organic Cations for Enhanced Thermal Stability and Transport Properties. Angew Chem Int Edit. 2016, 55, 10686-90.
[171] Dollase, W.A. Correction of Intensities for Preferred Orientation in Powder Diffractometry - Application of the March Model. J Appl Crystallogr. 1986, 19, 267-72.
[172] Palazon, F., Perez-del-Rey, D., Danekamp, B., Dreessen, C., Sessolo, M., Boix, P.P., et al. Room-Temperature Cubic Phase Crystallization and High Stability of Vacuum-Deposited Methylammonium Lead Triiodide Thin Films for High-Efficiency Solar Cells. Adv Mater. 2019, 31.
[173] Schelhas, L.T., Christians, J.A., Berry, J.J., Toney, M.F., Tassone, C.J., Luther, J.M., et al. Monitoring a Silent Phase Transition in CH3NH3PbI3 Solar Cells via Operando X-ray Diffraction. Acs Energy Lett. 2016, 1, 1007-12.
[174] Wang, Q., Lyu, M.Q., Zhang, M., Yun, J.H., Chen, H.J., Wang, L.Z. Transition from the Tetragonal to Cubic Phase of Organohalide Perovskite: The Role of Chlorine in Crystal Formation of CH3NH3PbI3 on TiO2 Substrates. J Phys Chem Lett. 2015, 6, 4379-84.
[175] Farkas, A.P., Koos, A., Bugyi, L., Solymosi, F. Adsorption and Reaction of Methyl and Ethyl Iodide on Potassium-Promoted Mo2C/Mo(100) Surface. J Phys Chem C. 2008, 112, 18502-9.

[176] Moers H., K.-N.H., Pfennig G., Ache H.J. Fres. Z. Anal. Chem. 1987, 329, 61.
[177] Zhang, X., Su, Z., Zhao, B., Yang, Y., Xiong, Y., Gao, X., et al. Chemical interaction dictated energy level alignment at the N,N'-dipentyl-3,4,9,10-perylenedicarboximide/CH3NH3PbI3 interface. 2018, 113, 113901.
[178] Jung, M.C., Lee, Y.M., Lee, H.K., Park, J., Raga, S.R., Ono, L.K., et al. The presence of CH3NH2 neutral species in organometal halide perovskite films. Appl Phys Lett. 2016, 108.
[179] Hawash, Z., Raga, S.R., Son, D.Y., Ono, L.K., Park, N.G., Qi, Y.B. Interfacial Modification of Perovskite Solar Cells Using an Ultrathin MAI Layer Leads to Enhanced Energy Level Alignment, Efficiencies, and Reproducibility. J Phys Chem Lett. 2017, 8, 3947-53.
[180] Chen, J.J., Winograd, N. The Adsorption and Decomposition of Methylamine on Pd(111). Surf Sci. 1995, 326, 285-300.
[181] Dachauer, R., Clemens, O., Lakus-Wollny, K., Mayer, T., Jaegermann, W. Characterization of Methylammonium Lead Iodide Thin Films Fabricated by Exposure of Lead Iodide Layers to Methylammonium Iodide Vapor in a Closed Crucible Transformation Process. Phys Status Solidi A. 2019, 216.
[182] Kumar, G.R., Savariraj, A.D., Karthick, S.N., Selvam, S., Balamuralitharan, B., Kim, H.J., et al. Phase transition kinetics and surface binding states of methylammonium lead iodide perovskite. Phys Chem Chem Phys. 2016, 18, 7284-92.
[183] Zhang, X.N., Su, Z.H., Zhao, B., Yang, Y.G., Xiong, Y.M., Gao, X.Y., et al. Chemical interaction dictated energy level alignment at the N,N '-dipentyl-3,4,9,10-perylenedicarboximide/CH3NH3PbI3 interface. Appl Phys Lett. 2018, 113.
[184] Jiang, Y., Juarez-Perez, E.J., Ge, Q., Wang, S., Leyden, M.R., Ono, L.K., et al. Post-annealing of MAPbI3 perovskite films with methylamine for efficient perovskite solar cells. Mater Horiz. 2016, 3, 548-55.
[185] Pederson, L.R. J. Electron Spectrosc. Relat. Phenom. 1982, 28, 203.
[186] Allen, G.C., Paul, M. Catalytic Effect of Vanadium, Iron and Lead-Oxides on the Oxidation of Moderator Graphite. J Chem Soc Faraday T. 1995, 91, 3717-23.
[187] Malgras, V., Nattestad, A., Yamauchi, Y., Dou, S.X., Kim, J.H. The effect of surface passivation on the structure of sulphur-rich PbS colloidal quantum dots for photovoltaic application. Nanoscale. 2015, 7, 5706-11.
[188] Huang, W.X., Manser, J.S., Kamat, P.V., Ptasinska, S. Evolution of Chemical Composition, Morphology, and Photovoltaic Efficiency of CH(3)NH(3)Pbl(3) Perovskite under Ambient Conditions. Chem Mater. 2016, 28, 303-11.
[189] Das, C., Wussler, M., Hellmann, T., Mayer, T., Jaegermann, W. In situ XPS study of the surface chemistry of MAPI solar cells under operating conditions in vacuum. Phys Chem Chem Phys. 2018, 20, 17180-7.
[190] Nefedov V.I., S.Y.V., Keller X. Zh. Neorg. Khimii. 1979, 24, 2564.
[191] Morgan, W.E., Van Wazer, J. R. . J. Phys. Chem. . 1973, 77, 964.
[192] Baker J.M., J.R.W., Pollak R.A. J. Vac. Sci. Technol. 1979.
[193] Zingg, D.S., Hercules, D. M. J. Phys. Chem. 1978.
[194] Jain, S.M., Philippe, B., Johansson, E.M.J., Park, B.-w., Rensmo, H., Edvinsson, T., et al. Vapor phase conversion of PbI2 to CH3NH3PbI3: spectroscopic evidence for formation of an intermediate phase. J Mater Chem A. 2016, 4, 2630-42.

[195] Yang, J.M., Yuan, Z.C., Liu, X.J., Braun, S., Li, Y.Q., Tang, J.X., et al. Oxygen- and Water-Induced Energetics Degradation in Organometal Halide Perovskites. Acs Appl Mater Inter. 2018, 10, 16225-30.
[196] Dinh, C.T., Jain, A., de Arquer, F.P.G., De Luna, P., Li, J., Wang, N., et al. Multi-site electrocatalysts for hydrogen evolution in neutral media by destabilization of water molecules. Nat Energy. 2019, 4, 107-14.
[197] Zhu, L.J., Lu, Q.P., Lv, L.F., Wang, Y., Hu, Y.F., Deng, Z.B., et al. Ligand-free rutile and anatase TiO2 nanocrystals as electron extraction layers for high performance inverted polymer solar cells. Rsc Adv. 2017, 7, 20084-92.
[198] Aranda, C., Guerrero, A., Bisquert, J. Crystalline Clear or Not: Beneficial and Harmful Effects of Water in Perovskite Solar Cells. 2019, 20, 2587-99.
[199] Lee, Y.I., Jeon, N.J., Kim, B.J., Shim, H., Yang, T.-Y., Seok, S.I., et al. A Low-Temperature Thin-Film Encapsulation for Enhanced Stability of a Highly Efficient Perovskite Solar Cell. 2018, 8, 1701928.
[200] Weerasinghe, H.C., Dkhissi, Y., Scully, A.D., Caruso, R.A., Cheng, Y.-B. Encapsulation for improving the lifetime of flexible perovskite solar cells. Nano Energy. 2015, 18, 118-25.
[201] Matteocci, F., Cinà, L., Lamanna, E., Cacovich, S., Divitini, G., Midgley, P.A., et al. Encapsulation for long-term stability enhancement of perovskite solar cells. Nano Energy. 2016, 30, 162-72.
[202] Li, Y.H., Zhao, Z.H., Lin, F., Cao, X.B., Cui, X., Wei, J.Q. In Situ Observation of Crystallization of Methylammonium Lead Iodide Perovskite from Microdroplets. Small. 2017, 13.
[203] Zaman, M.M.U., Imran, M., Saleem, A., Kamboh, A.H., Arshad, M., Khan, N.A., et al. Potassium doped methylammonium lead iodide (MAPbI(3)) thin films as a potential absorber for perovskite solar cells; structural, morphological, electronic and optoelectric properties. Physica B. 2017, 522, 57-65.
[204] Burkitt, D., Searle, J., Worsley, D.A., Watson, T. Sequential Slot-Die Deposition of Perovskite Solar Cells Using Dimethylsulfoxide Lead Iodide Ink. Materials. 2018, 11.
[205] Jiang, Y., Juarez-Perez, E.J., Ge, Q.Q., Wang, S.H., Leyden, M.R., Ono, L.K., et al. Post-annealing of MAPbI(3) perovskite films with methylamine for efficient perovskite solar cells. Mater Horiz. 2016, 3, 548-55.
[206] Li, C.W., Pang, S.P., Xu, H.X., Cui, G.L. Methylamine Gas Based Synthesis and Healing Process Toward Upscaling of Perovskite Solar Cells: Progress and Perspective. Sol Rrl. 2017, 1.
[207] Min, H., Kim, M., Lee, S.-U., Kim, H., Kim, G., Choi, K., et al. Efficient, stable solar cells by using inherent bandgap of α-phase formamidinium lead iodide. 2019, 366, 749-53.
[208] Eperon, G.E., Stranks, S.D., Menelaou, C., Johnston, M.B., Herz, L.M., Snaith, H.J. Formamidinium lead trihalide: a broadly tunable perovskite for efficient planar heterojunction solar cells. Energ Environ Sci. 2014, 7, 982-8.
[209] Thote, A., Jeon, I., Lee, J.-W., Seo, S., Lin, H.-S., Yang, Y., et al. Stable and Reproducible 2D/3D Formamidinium–Lead–Iodide Perovskite Solar Cells. Acs Appl Energ Mater. 2019, 2, 2486-93.
[210] Zhou, Y.Y., Yang, M.J., Pang, S.P., Zhu, K., Padture, N.P. Exceptional Morphology-Preserving Evolution of Formamidinium Lead Triiodide Perovskite Thin Films via Organic-Cation Displacement. J Am Chem Soc. 2016, 138, 5535-8.

[211] Stoumpos, C.C., Malliakas, C.D., Kanatzidis, M.G. Semiconducting Tin and Lead Iodide Perovskites with Organic Cations: Phase Transitions, High Mobilities, and Near-Infrared Photoluminescent Properties. Inorg Chem. 2013, 52, 9019-38.
[212] Liu, T.H., Zong, Y.X., Zhou, Y.Y., Yang, M.J., Li, Z., Game, O.S., et al. High-Performance Formamidinium-Based Perovskite Solar Cells via Microstructure-Mediated delta-to-alpha Phase Transformation. Chem Mater. 2017, 29, 3246-50.
[213] Angela M. Belcher, P.-Y.C., Paula T. Hammond-Cunningham, Jifa Qi. Recycling car batteries for perovskite solar cells Patent US9590278B2. 2015, Massachusetts Institute of Technology
[214] Howard, E.S. Standard X-ray diffraction powder patterns. Section 3. Data for 51 substances, Washington, D.C. : National Bureau of Standards : for sale by the Supt. of Docs., U.S. Govt. Print. Off., 1964., 1964.

7. List of Figures

8. List of Tables

9. Appendix

Table 9.1 Performance data of MAPI perovskite solar cells produced with by the two-step spin coating and chemical bath process, measured with a solar simulator light intensity of 840 W/m2

Date	Sample	Efficiency [%]	V_{OC} [V]	J_{SC} [A/m^2]	FF	J_{WP} [A/m2]	V_{WP} [V]	MPP [W/m^2]
17.06.2016	1_l	12,6	1,04	205	0,59	191	0,66	125,9
	1_ml	11,8	1,03	200	0,57	181	0,65	117,7
	1_mr	11,2	1,03	195	0,56	171	0,66	112,5
	1_r	6,3	0,97	187	0,35	117	0,54	63,0
	2_l	0,00019	0,93	0,0076	0,27	0,0037	0,52	0,0019
	2_ml	10,5	1,04	192	0,53	176	0,60	105,1
	2_mr	9,5	1,03	177	0,52	155	0,61	94,6
	2_r	0,000045	1,03	165	0,00	0,0021	0,22	0,00045
16.08.2016	1_ml	10,6	1,03	179	0,58	155	0,69	106,0
	1_mr	10,9	1,03	181	0,58	159	0,68	108,5
	2_l	0,1	1,01	121	0,01	4	0,22	0,9
	2_ml	9,4	1,02	168	0,55	145	0,64	93,7
	2_mr	9,9	1,02	171	0,57	146	0,68	98,8
	3_l	6,0	1,03	121	0,49	101	0,60	60,3
	3_ml	8,4	1,03	153	0,54	130	0,65	84,1
	3_mr	7,5	1,02	140	0,53	114	0,66	75,4
	3_r	7,0	1,02	136	0,50	107	0,65	69,7
	4_l	9,1	1,04	175	0,50	146	0,63	91,4
	4_ml	9,2	1,03	162	0,55	137	0,67	91,7
	4_mr	9,2	1,03	166	0,54	146	0,63	92,3
	4_r	8,0	1,02	143	0,55	128	0,63	80,2
25.11.2016	1_l	9,6	1,05	161	0,57	142	0,68	96,4
	1_ml	8,5	1,05	145	0,56	128	0,66	84,5
	1_mr	8,0	1,04	133	0,58	115	0,70	80,2
	1_r	8,0	1,05	127	0,60	115	0,70	80,2
	2_l	11,6	1,06	206	0,53	174	0,67	116,2
	2_ml	9,9	1,04	177	0,54	153	0,65	99,0
	2_mr	10,8	1,04	180	0,58	160	0,67	107,9
	2_r	0,4	0,15	120	0,25	62	0,07	4,5
	3_l	15,0	1,07	206	0,68	186	0,81	149,7
	3_ml	12,1	1,05	181	0,63	157	0,77	120,6
	3_mr	11,8	1,04	181	0,63	162	0,73	118,3
	3_r	10,7	1,04	160	0,64	146	0,73	106,7
	4_l	14,4	1,06	198	0,68	179	0,81	144,1
	4_ml	12,8	1,04	175	0,70	159	0,80	127,8
	4_mr	11,8	1,03	167	0,68	160	0,73	117,7
	4_r	9,4	1,04	149	0,61	139	0,68	94,5
	5_l	12,1	1,05	197	0,58	179	0,68	120,8
	5_ml	0,000090	0,95	0,0033	0,28	0,0018	0,50	0,00090
	5_mr	0,000013	0,84	0,0006	0,25	0,0003	0,41	0,00013
	5_r	0,000030	0,89	0,0013	0,26	0,0006	0,48	0,00030
	6_l	12,0	1,06	171	0,66	163	0,74	120,0
	6_ml	13,4	1,04	192	0,67	185	0,73	134,3
	6_mr	12,8	1,04	187	0,66	176	0,73	128,3
	6_r	12,6	1,04	193	0,63	181	0,70	126,1

05.12.2016	1_l	8,2	1,05	232	0,34	151	0,54	81,8
	1_ml	8,6	1,05	211	0,39	159	0,54	86,0
	1_mr	9,7	1,05	217	0,43	164	0,59	96,8
	1_r	11,4	1,05	224	0,49	177	0,65	114,3
13.01.2017	1_l	12,4	1,04	201	0,59	173	0,71	123,6
	1_ml	0,027	1,00	195	0,00	1	0,21	0,3
	1_mr	10,6	1,00	166	0,64	143	0,74	106,0
	1_r	8,4	1,02	130	0,64	110	0,77	84,2
19.01.2017	1_l	4,7	1,03	181	0,25	103	0,46	46,9
	1_ml	5,4	1,03	169	0,31	105	0,52	54,0
	1_mr	6,4	1,03	176	0,35	118	0,54	64,0
	1_r	6,5	1,03	173	0,36	114	0,57	64,7
	2_l	7,9	1,03	181	0,42	136	0,58	78,6
	2_ml	8,4	1,03	167	0,49	136	0,62	83,9
	2_mr	9,2	1,03	169	0,53	140	0,66	91,6
	2_r	9,0	1,03	171	0,51	140	0,64	90,0
10.02.2017	1_l	11,4	1,04	201	0,54	167	0,68	113,9
	1_ml	9,3				142	0,65	92,5
	1_mr	10,1				149	0,68	100,6
09.06.2017	1_l	9,5	1,05	146	0,62	123	0,77	94,5
	1_ml	8,8	1,04	131	0,65	110	0,80	88,2
	1_mr	8,4	1,03	130	0,63	110	0,77	84,2
	1_r	8,5	1,03	140	0,59	112	0,76	85,4
09.08.2017	1_l	15,6	1,08	244	0,59	212	0,74	155,8
	1_ml	14,2	1,04	222	0,61	188	0,76	142,3
	1_mr	13,3	1,02	214	0,60	171	0,77	132,7
	1_r	12,5	1,03	205	0,59	167	0,75	124,6
	2_l	15,0	1,07	224	0,63	199	0,75	150,1
	2_ml	13,9	1,03	217	0,62	186	0,75	138,9
	2_mr	13,6	1,02	217	0,62	173	0,79	136,3
	2_r	13,3	1,02	217	0,60	173	0,77	133,0
	3_l	13,0	1,07	226	0,54	188	0,69	130,0
	3_ml	14,1	1,04	221	0,61	194	0,73	141,0
	3_mr	13,2	1,03	212	0,61	169	0,78	131,6
	3_r	12,2	1,03	200	0,59	159	0,77	121,9
	4_l	14,3	1,07	239	0,56	204	0,70	143,0
	4_ml	14,8	1,03	225	0,64	193	0,77	147,9
	4_mr	14,7	1,02	224	0,64	185	0,79	146,8
	4_r	13,4	1,03	217	0,60	180	0,75	134,3

29.05.2018	1_l	11,4	1,00	165	0,69	157	0,73	114,1
	1_ml	11,0	1,00	159	0,69	145	0,75	109,7
	1_mr	10,6	0,99	158	0,68	125	0,85	106,0
	1_r	10,4	0,98	160	0,67	138	0,75	104,3
	2_l	8,8	1,01	132	0,66	128	0,69	88,3
	2_ml	8,2				119	0,69	82,2
	3_ml	7,9	1,01	120	0,65	109	0,73	79,4
	3_mr	7,8	1,00	119	0,66	113	0,69	78,1
	3_r	8,0	0,99	129	0,63	116	0,69	80,4
	4_l	1,7	1,00	103	0,16	37	0,45	16,7
	4_ml	1,8	1,00	105	0,17	37	0,47	17,5
	4_mr	1,7	1,00	103	0,17	37	0,47	17,5
	4_r	1,6	0,99	84	0,19	31	0,51	16,0
	5_l	10,3	1,02	155	0,65	136	0,75	102,8
	5_ml	9,3	1,00	144	0,65	128	0,73	93,2
	5_mr	9,9	1,00	153	0,64	131	0,75	98,9
	5_r	8,5	0,99	139	0,62	112	0,76	85,2
	6_l	7,9	1,01	113	0,70	101	0,78	79,5
	6_ml	7,5	0,99	111	0,68	99	0,76	75,4
	6_mr	7,0	0,99	104	0,69	96	0,73	70,0
	6_r	6,3	0,99	95	0,67	87	0,73	63,2
	7_l	5,5	1,02	120	0,45	97	0,57	55,2
	7_ml	5,1	1,00	111	0,46	90	0,57	50,9
	7_mr	4,7	0,99	102	0,47	84	0,57	47,4
	7_r	4,6	0,99	107	0,44	82	0,57	46,5
	8_l	6,9	0,99	139	0,50	122	0,57	69,3
	8_ml	9,2	1,00	132	0,70	122	0,75	91,9
	8_mr	9,1	1,00	130	0,70	121	0,75	91,0
	8_r	8,3	0,99	119	0,70	110	0,75	82,6
	Nr. of cells	113						
	Best Cell	**15,6**	**1,08**	**244**	**0,59**	**212**	**0,74**	**155,8**
	Average	**9,0**	**1,01**	**161**	**0,53**	**131**	**0,66**	**90,3**
	Sandard deviation	**3,8**	**0,09**	**49**	**0,16**	**49**	**0,13**	**38,3**

Table 9.2 Performance data of MAPI perovskite solar cells produced by the two-step spin coating and chemical bath process, measured with a solar simulator light intensity of 1000 W/m2

Date	Sample	Efficiency [%]	V_{OC} [V]	J_{SC} [A/m^2]	FF	J_{WP} [A/m2]	V_{WP} [V]	MPP [W/m^2]
02.10.2018	1_l	9,1	1,04	206	0,42	159	0,57	90,7
	1_ml	11,2	1,03	216	0,50	177	0,63	112,3
	1_mr	11,7	1,03	231	0,49	186	0,63	117,4
	1_r	12,0	1,03	241	0,49	188	0,64	120,4
	2_l	8,2	1,05	189	0,41	144	0,57	81,6
	2_ml	12,1	1,05	204	0,57	176	0,69	121,3
	2_mr	12,6	1,04	193	0,63	173	0,73	126,1
	2_r	14,7	1,04	209	0,68	195	0,75	147,2
	3_l	10,6	1,05	189	0,54	148	0,72	106,3
	3_mr	15,8	1,07	226	0,65	186	0,85	158,1
	3_r	16,1	1,05	242	0,63	214	0,75	161,4
	4_l	13,6	1,06	219	0,59	184	0,74	135,8
	4_ml	16,5	1,05	236	0,67	208	0,79	164,7
	4_mr	17,0	1,04	251	0,65	221	0,77	170,2
	4_r	16,3	1,04	253	0,62	218	0,75	162,9
	5_l	9,7	1,04	180	0,52	141	0,69	97,3
	5_ml	15,3	1,03	223	0,66	203	0,75	152,9
	5_mr	16,1	1,03	238	0,66	214	0,75	161,4
	5_r	16,2	1,03	250	0,63	215	0,75	162,3
	Nr. of cells	19						
	Best cell	**17,0**	**1,04**	**251**	**0,65**	**221**	**0,77**	**170,2**
	Averages	**13,4**	**1,04**	**221**	**0,58**	**187**	**0,71**	**134,2**
	Standard deviation	**2,8**	**0,01**	**22**	**0,08**	**25**	**0,07**	**27,5**

Table 9.3 Performance data of CsRbMAFA perovskite solar cells produced by the one-step spin coating method, measured with an 840 W/m^2 irradiance at the solar simulator

Date	Sample	Efficiency [%]	V_{OC} [V]	J_{SC} [A/m^2]	FF	J_{WP} [A/m2]	V_{WP} [V]	MPP [W/m^2]
02.11.2018	1_l	5,2	1,11	146,6	0,32	76,9	0,67	51,5
	1_ml	5,7	1,09	156,3	0,33	87,4	0,65	56,8
	1_mr	5,9	1,08	163,2	0,33	92,4	0,64	59,0
	1_r	6,1	1,09	173,1	0,32	96,1	0,64	61,0
	2_l	13,2	1,14	237,6	0,49	183,4	0,72	131,6
	2_ml	12,6	1,12	227,2	0,50	168,1	0,75	126,3
	2_mr	11,8	1,12	224,4	0,47	164,4	0,72	118,0
	2_r	11,3	1,12	217,9	0,46	152,7	0,74	113,2
	3_l	16,9	1,12	262,2	0,58	221,0	0,77	169,5
	3_ml	14,8	1,09	248,5	0,55	201,7	0,73	147,8
	3_mr	15,0	1,08	250,7	0,56	204,1	0,74	150,2
	3_r	14,2	1,07	258,9	0,51	199,7	0,71	142,4
	4_l	10,1	1,11	214,3	0,42	151,1	0,67	101,5
	4_ml	10,8	1,11	205,8	0,47	144,0	0,75	108,5
	4_mr	10,0	1,11	202,0	0,45	136,1	0,74	100,3
	4_r	9,0	1,11	206,1	0,39	126,0	0,72	90,1
08.11.2018	1_l	5,3	1,08	221,5	0,22	105,4	0,50	53,1
	1_ml	7,9	1,11	239,7	0,30	156,4	0,51	79,4
	1_mr	9,5	1,11	248,0	0,35	173,3	0,55	95,2
	1_r	9,4	1,11	264,4	0,32	173,7	0,54	94,4
	2_l	10,8	1,12	216,7	0,44	154,8	0,70	107,6
	2_ml	8,7	1,11	185,3	0,42	127,9	0,68	87,2
	2_mr	8,3	1,11	181,2	0,41	122,7	0,68	83,3
	2_r	8,7	1,11	182,3	0,43	122,2	0,72	87,4
	3_l	9,6	1,09	229,8	0,38	172,3	0,56	96,0
	3_ml	12,4	1,10	211,6	0,53	168,2	0,73	123,6
	3_mr	13,1	1,11	218,0	0,54	170,4	0,77	130,5
	3_r	14,0	1,11	238,8	0,53	181,8	0,77	140,2
	4_l	12,7	1,08	255,1	0,46	183,2	0,70	127,4
	4_ml	14,8	1,07	238,8	0,58	197,5	0,75	147,6
	4_mr	15,6	1,06	249,1	0,59	208,2	0,75	156,4
	4_r	12,8	1,04	220,7	0,56	174,6	0,73	128,2
09.11.2018	1_l	11,4	1,09	253,8	0,41	191,0	0,60	113,7
	1_ml	16,4	1,08	234,6	0,65	213,6	0,77	164,3
	1_mr	16,1	1,07	228,2	0,66	200,2	0,80	160,7
	1_r	18,0	1,08	264,3	0,63	227,1	0,79	180,1
	2_l	16,4	1,14	250,6	0,58	216,4	0,76	164,2
	2_ml	14,5	1,11	228,5	0,57	186,1	0,78	144,7
	2_mr	15,2	1,11	245,2	0,56	198,5	0,77	152,3
	2_r	15,6	1,10	253,5	0,56	207,9	0,75	156,2
	3_l	16,3	1,13	241,0	0,60	208,4	0,78	163,2
	3_ml	14,8	1,11	232,6	0,57	188,9	0,78	148,1
	3_mr	13,9	1,11	234,9	0,54	183,5	0,76	139,4
	3_r	12,8	1,11	236,7	0,49	172,7	0,74	128,3
	4_l	16,9	1,13	249,7	0,60	216,7	0,78	168,6
	4_ml	16,0	1,12	236,8	0,60	195,2	0,82	160,1
	4_mr	14,4	1,11	238,7	0,54	190,4	0,76	144,1
	4_r	13,9	1,11	247,4	0,50	196,6	0,70	138,5

16.11.2018	1_l	12,6	1,15	242,8	0,45	196,1	0,64	125,8
	1_ml	13,7	1,15	234,8	0,51	184,3	0,74	137,2
	1_mr	14,3	1,14	236,1	0,53	196,7	0,73	142,9
	1_r	14,2	1,14	244,0	0,51	192,0	0,74	142,4
	2_l	14,3	1,14	236,8	0,53	198,3	0,72	142,6
	2_ml	14,0	1,13	208,6	0,59	175,5	0,80	139,6
	2_mr	14,3	1,12	224,1	0,57	179,7	0,80	143,2
	2_r	13,1	1,12	226,6	0,52	175,2	0,75	130,7
	3_l	10,8	1,12	201,4	0,48	156,0	0,69	107,7
	3_ml	12,3	1,12	212,4	0,52	159,3	0,77	122,8
	3_mr	13,0	1,13	221,1	0,52	167,1	0,78	129,8
	3_r	13,8	1,13	243,9	0,50	175,7	0,79	138,1
	4_l	9,9	1,11	226,6	0,39	162,9	0,60	98,5
	4_ml	12,5	1,13	207,6	0,53	160,5	0,78	125,1
	4_mr	13,0	1,13	210,6	0,55	169,0	0,77	130,3
	4_r	13,2	1,14	223,3	0,52	169,2	0,78	131,8
20.11.2018	1_l	9,7	1,15	232,4	0,36	171,8	0,56	96,7
	1_ml	11,2	1,15	215,0	0,46	169,4	0,66	112,4
	1_mr	12,9	1,14	234,0	0,48	187,0	0,69	128,7
	1_r	13,5	1,14	262,2	0,45	196,5	0,69	135,3
	2_l	11,6	1,15	233,6	0,43	185,6	0,62	115,6
	2_ml	12,3	1,11	230,4	0,48	179,6	0,68	122,8
	2_mr	14,4	1,14	243,4	0,52	191,8	0,75	144,1
	2_r	14,2	1,14	257,3	0,48	203,8	0,69	141,6
	3_l	13,2	1,15	244,8	0,47	192,9	0,68	131,5
	3_ml	14,8	1,14	238,3	0,54	195,9	0,75	147,6
	3_mr	16,2	1,14	246,7	0,58	204,8	0,79	162,2
	3_r	16,4	1,14	259,6	0,55	215,9	0,76	163,8
	4_l	11,5	1,13	265,6	0,38	168,7	0,68	115,4
	4_ml	14,7	1,12	243,4	0,54	198,4	0,74	147,5
	4_mr	15,8	1,13	253,5	0,56	212,7	0,74	158,4
	4_r	16,1	1,12	266,7	0,54	220,9	0,73	160,7

	Batches	Substrates	Cells
Nr. of	5	20	80

	Efficiency [%]	V_{OC} [V]	J_{SC} [A/m^2]	FF	J_{WP} [A/m2]	V_{WP} [V]	MPP [W/m^2]
Average	**12,7**	**1,11**	**230,0**	**0,49**	**176,3**	**0,72**	**127,1**
Sandard deviation	**2,91**	**0,02**	**24,93**	**0,09**	**31,80**	**0,07**	**29,10**
Best Cell	**18,0**	**1,08**	**264,3**	**0,63**	**227,1**	**0,79**	**180,1**

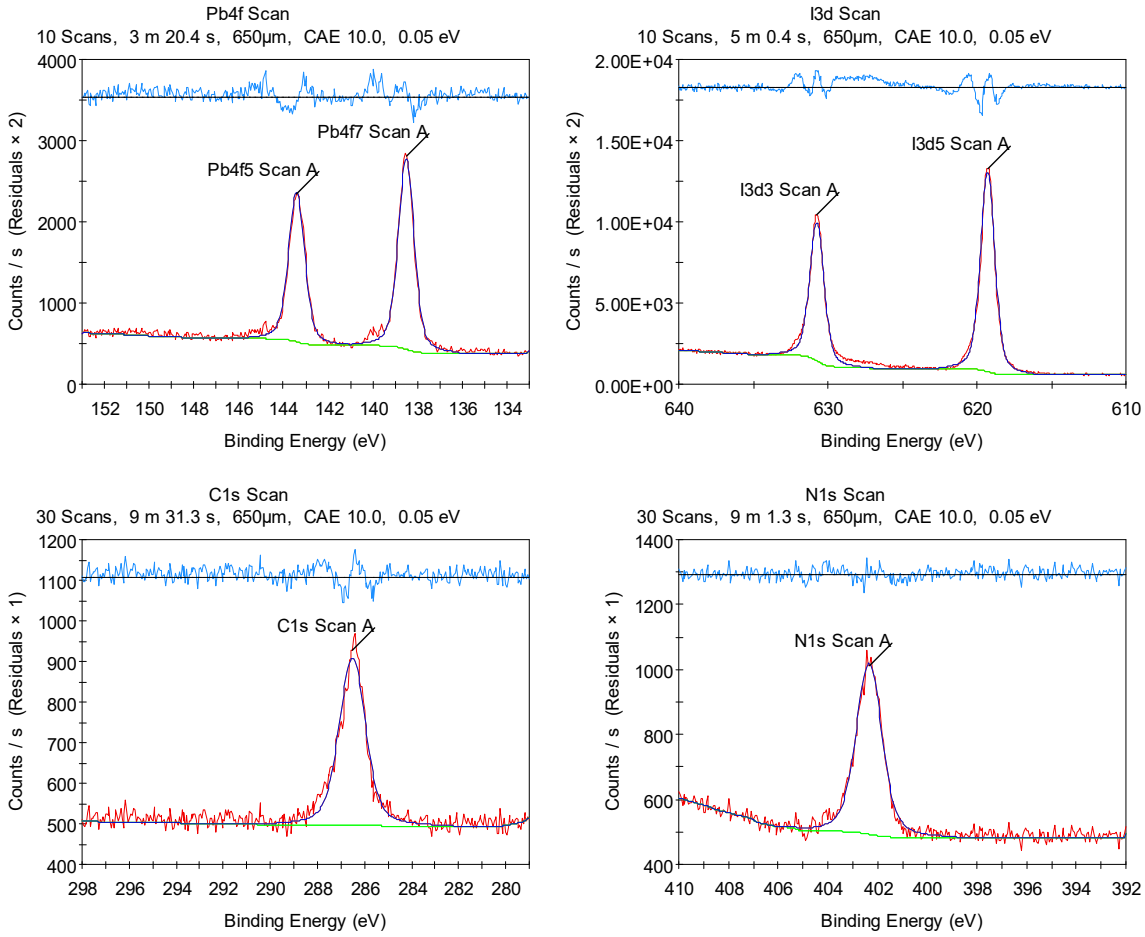

Figure 9.1 XPS measurements of a MAPI flash evaporated sample at 60% source power, equivalent to 250°C, with peak fits for the respective elements. **The XPS energy position has not been calibrated and values can be shifted by as much as 1 eV**

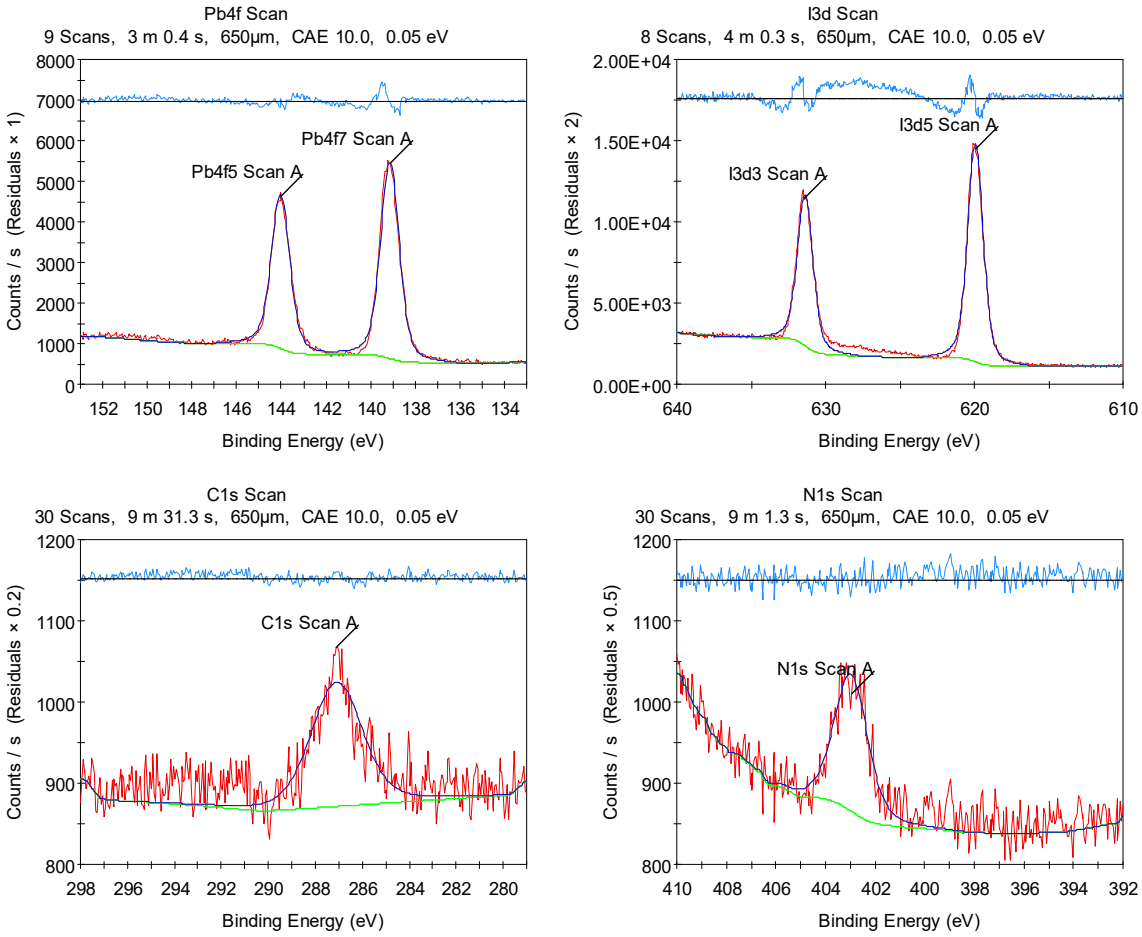

Figure 9.2 XPS measurements of a MAPI flash evaporated sample at 65% source power, equivalent to 285°C, with peak fits for the respective elements. **The XPS energy position has not been calibrated and values can be shifted by as much as 1 eV**

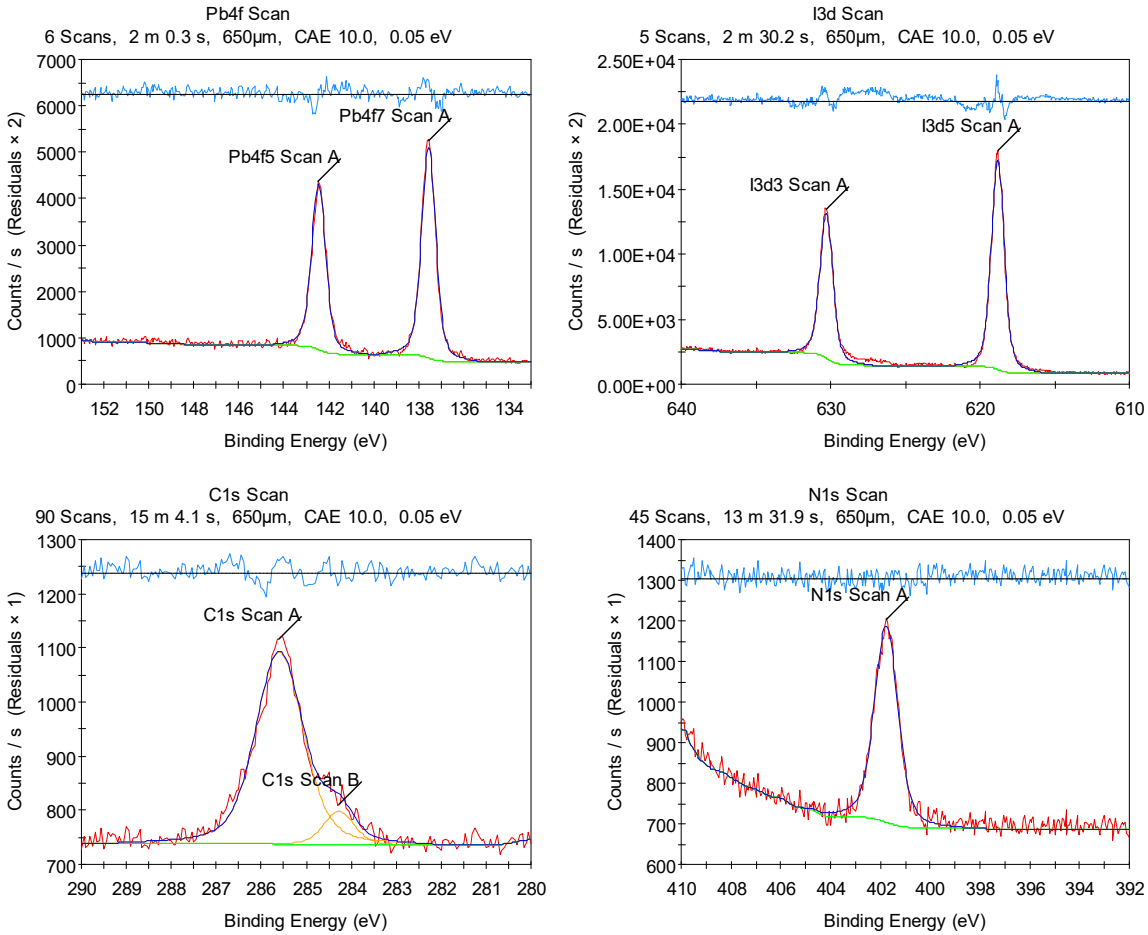

Figure 9.3 XPS measurements of a second MAPI flash evaporated sample at 65% source power, equivalent to 285°C, with peak fits for the respective elements. **The XPS energy position has not been calibrated and values can be shifted by as much as 1 eV**

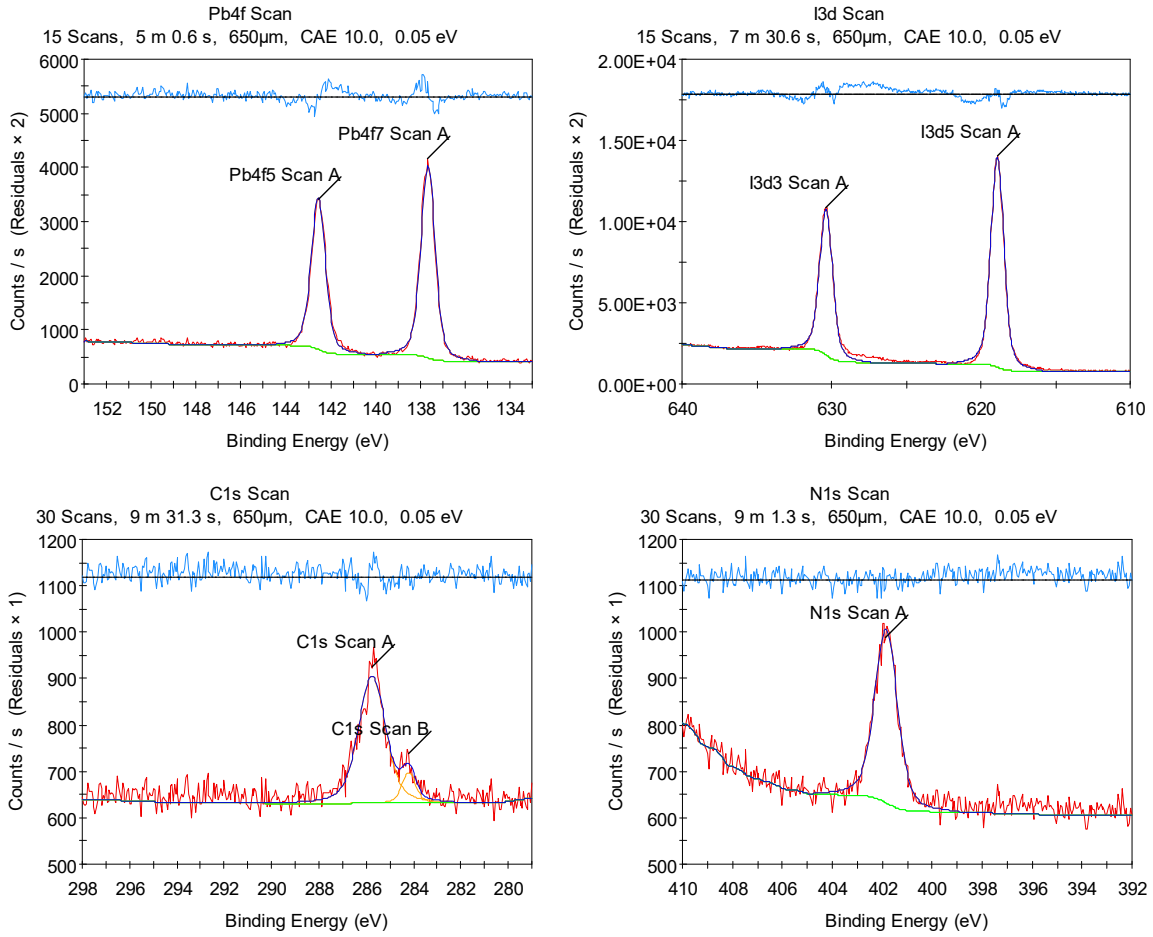

Figure 9.4 XPS measurements of a MAPI flash evaporated sample at 67,5% source power, equivalent to 300°C, with peak fits for the respective elements. **The XPS energy position has not been calibrated and values can be shifted by as much as 1 eV**

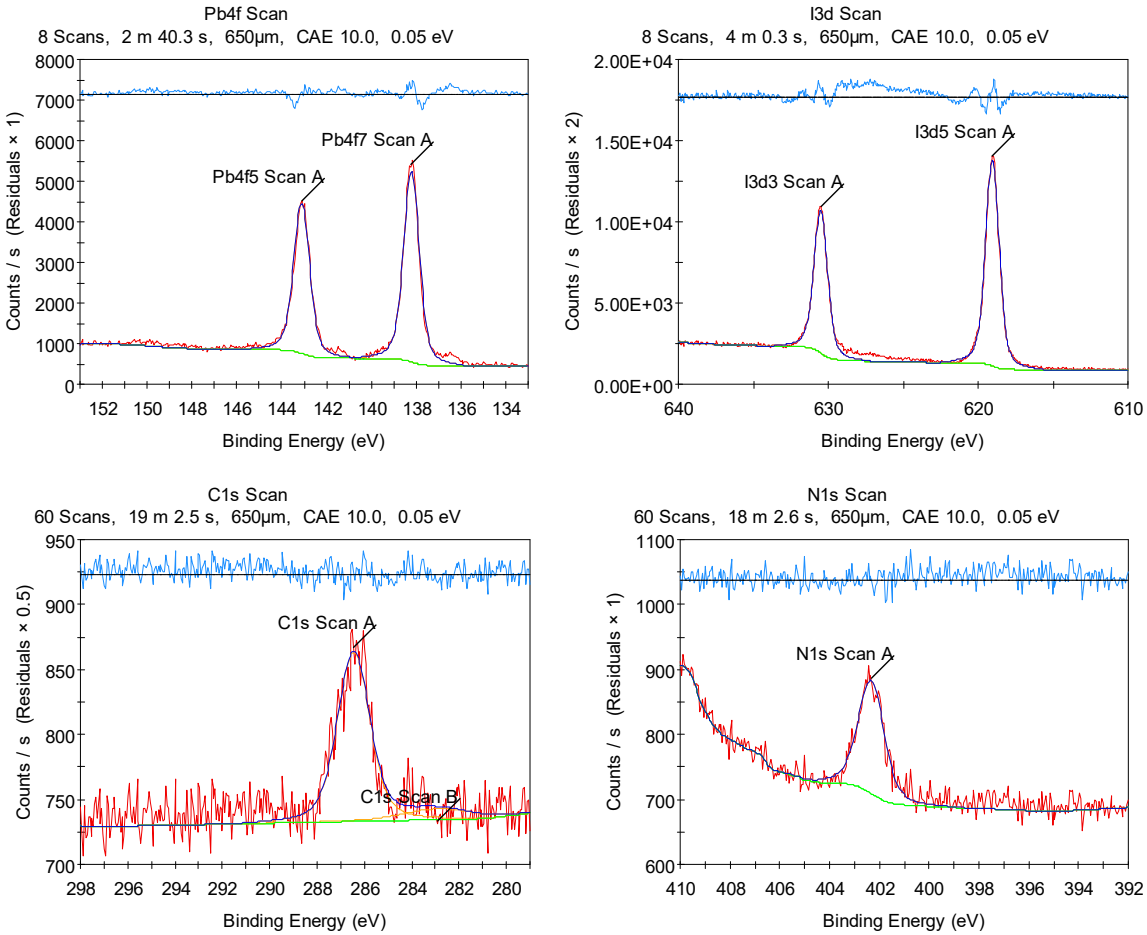

Figure 9.5 XPS measurements of a MAPI flash evaporated sample at 70% source power, equivalent to 325°C, with peak fits for the respective elements. **The XPS energy position has not been calibrated and values can be shifted by as much as 1 eV**

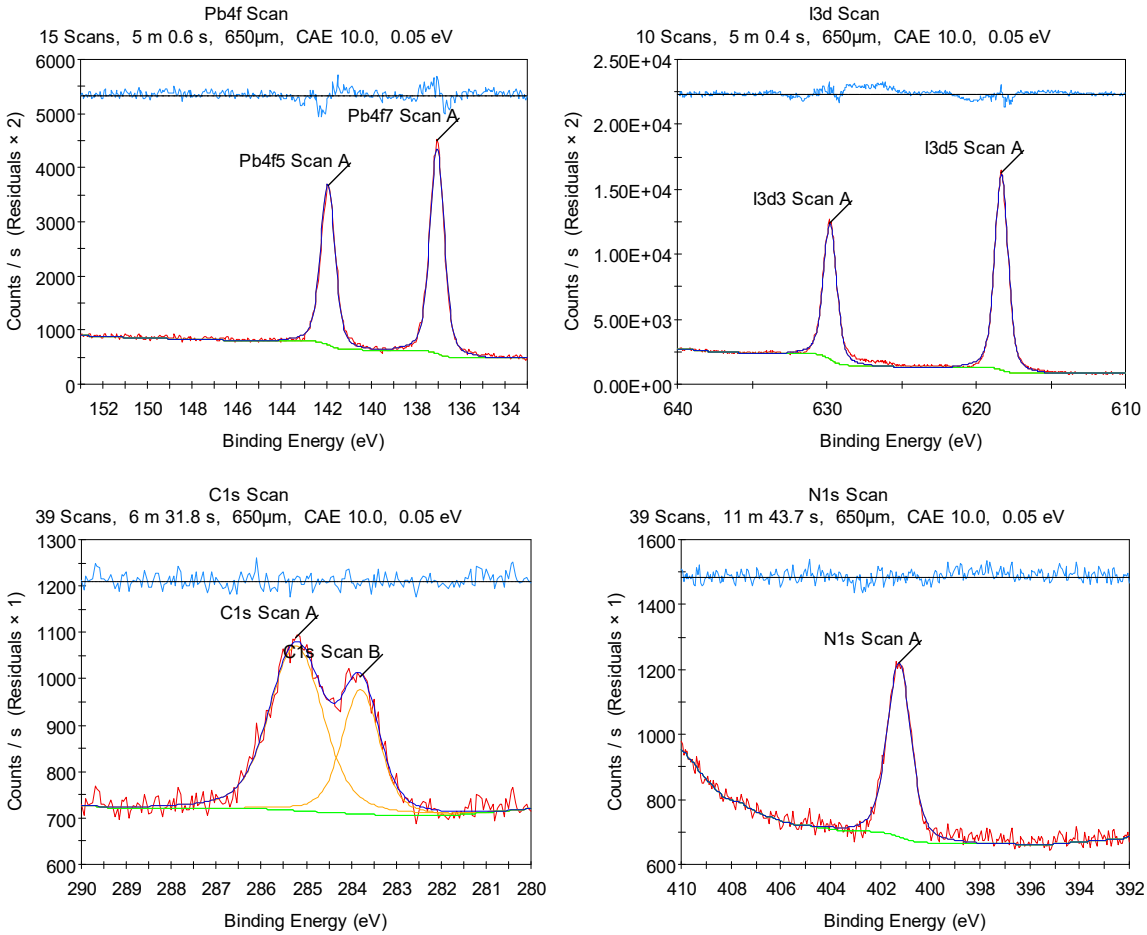

Figure 9.6 XPS measurements of a MAPI flash evaporated sample at 75% source power, equivalent to 365°C, with peak fits for the respective elements. **The XPS energy position has not been calibrated and values can be shifted by as much as 1 eV**

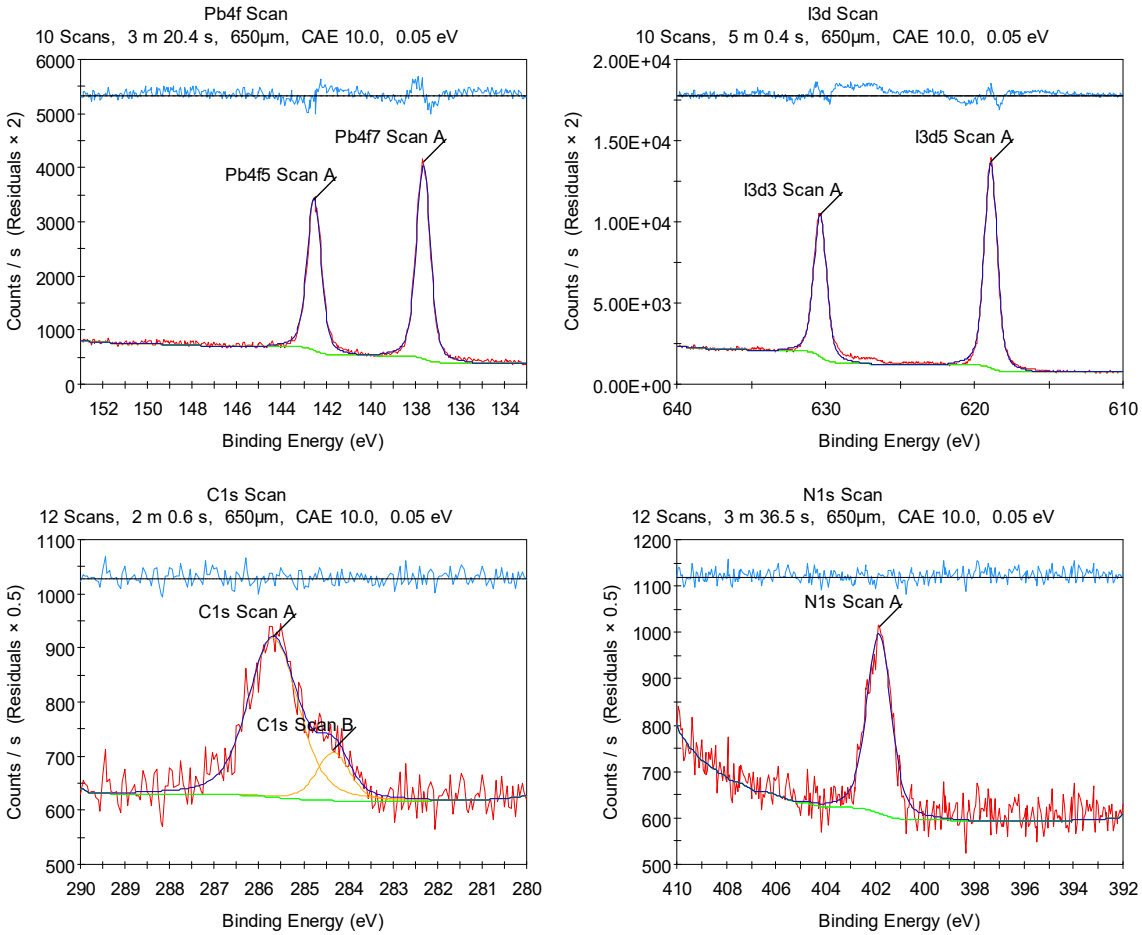

Figure 9.7 XPS measurements of a MAPI flash evaporated sample at 85% source power, equivalent to 430°C, with peak fits for the respective elements. **The XPS energy position has not been calibrated and values can be shifted by as much as 1 eV**

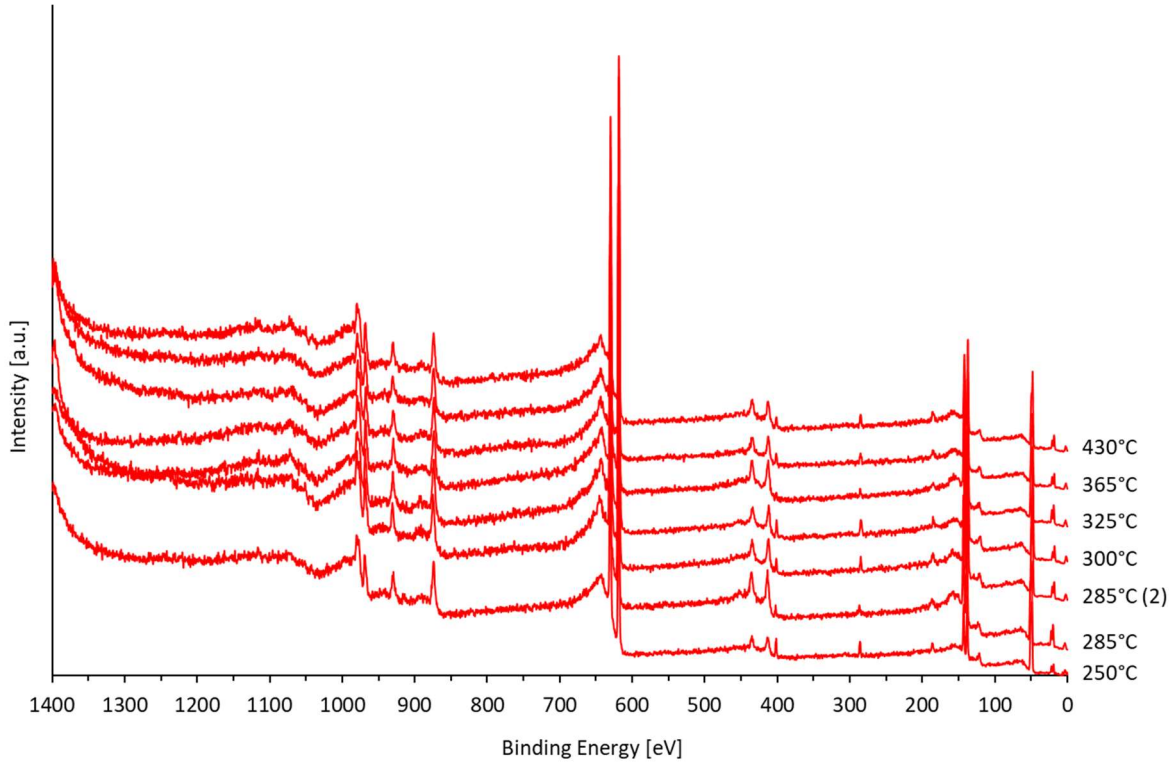

Figure 9.8 XPS survey measurements of MAPI flash evaporated films. **The XPS energy position has not been calibrated and values can be shifted by as much as 1 eV**

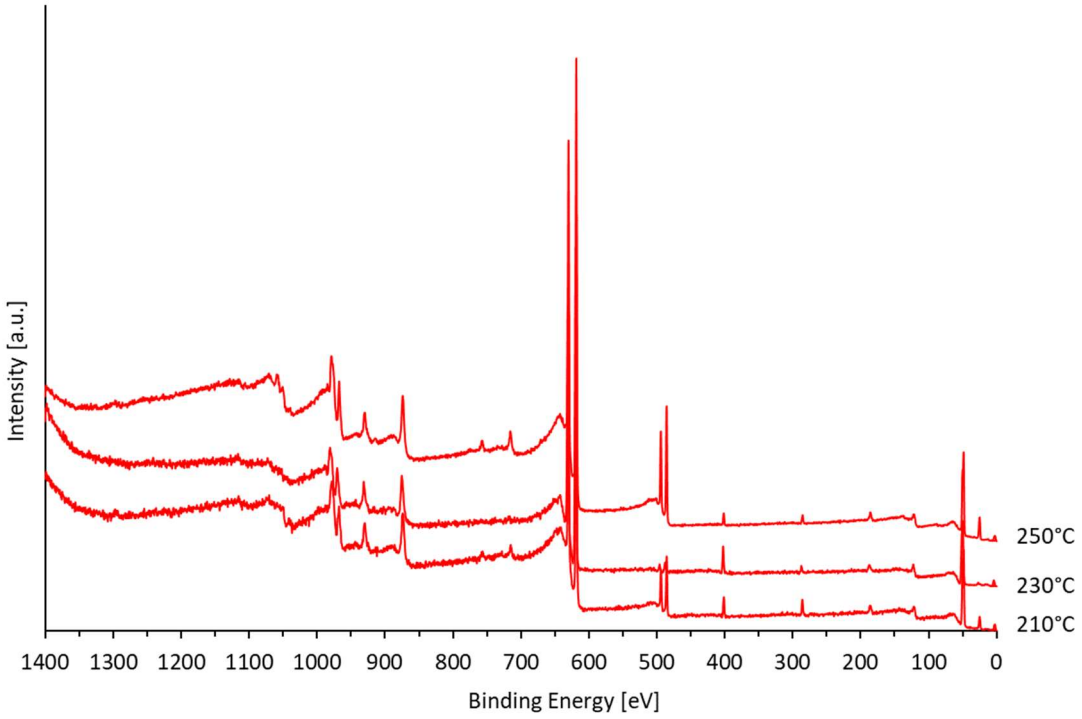

Figure 9.9 XPS survey measurements of MASI flash evaporated films. **The XPS energy position has not been calibrated and values can be shifted by as much as 1 eV**

Table 9.4 Properties and amounts of precursors to produce the hydrogen lead halide compounds: $HPbI_3$, $HPbI_2Br$, $HPbIBr_2$ and $HPbBr_3$

	c [wt%]		ro [g/mL]		M [g/mol]	m [g]	n [mol]	Solution		n [mol]	m [g]		m [g]	V [mL]
HI (aq.)	0,57	HI (aq.)	1,7	PbI2	461,01	1	2,169E-03	1	HI	3,254E-03	0,416	HI (aq.)	0,730	0,429
HBr (aq.)	0,47	HBr (aq.)	1,49	PbBr2	367,01	1	2,725E-03	2	HBr	3,254E-03	0,263	HBr (aq.)	0,560	0,376
				HBr	80,91			3	HI	4,087E-03	0,523	HI (aq.)	0,917	0,540
				HI	127,91			4	HBr	4,087E-03	0,331	HBr (aq.)	0,704	0,472

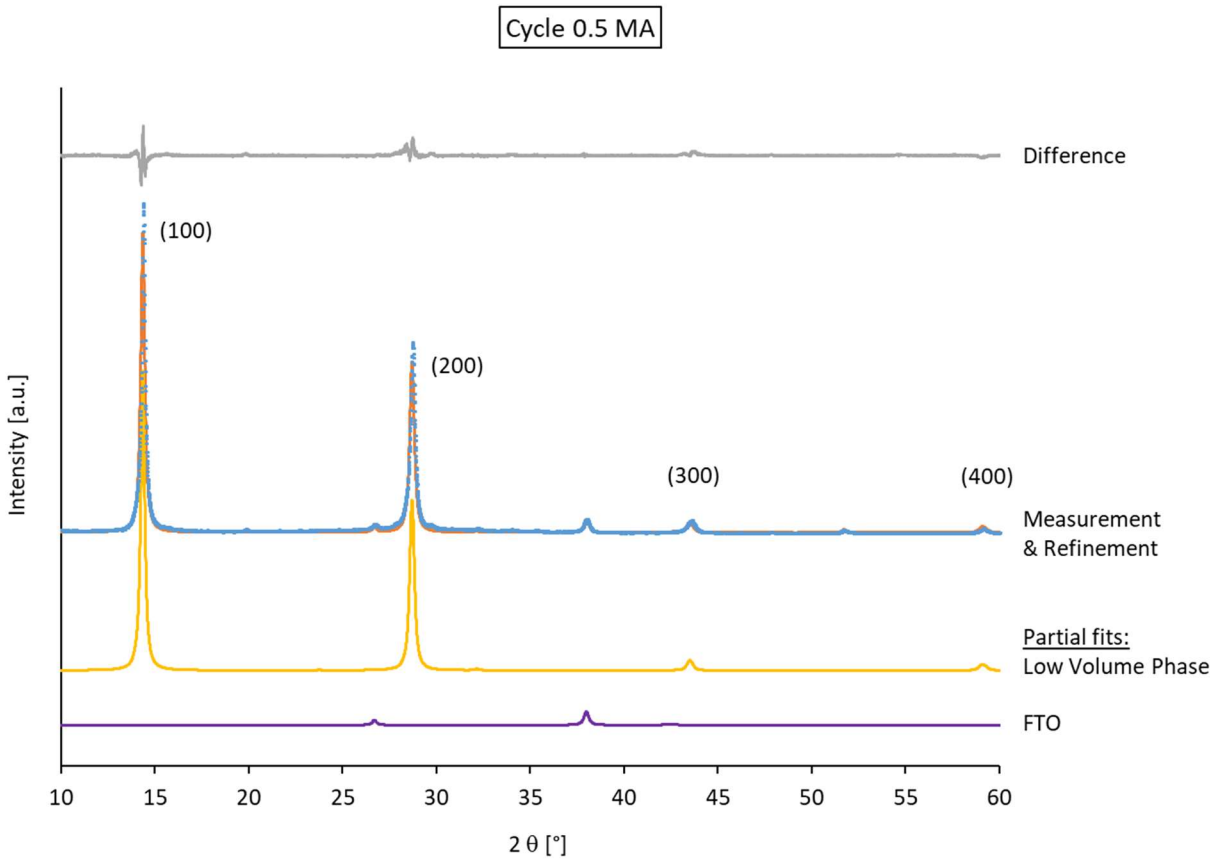

Figure 9.10 XRD pattern and refinements of the 0.5 MA substrate from the MA and HI gas CVD process

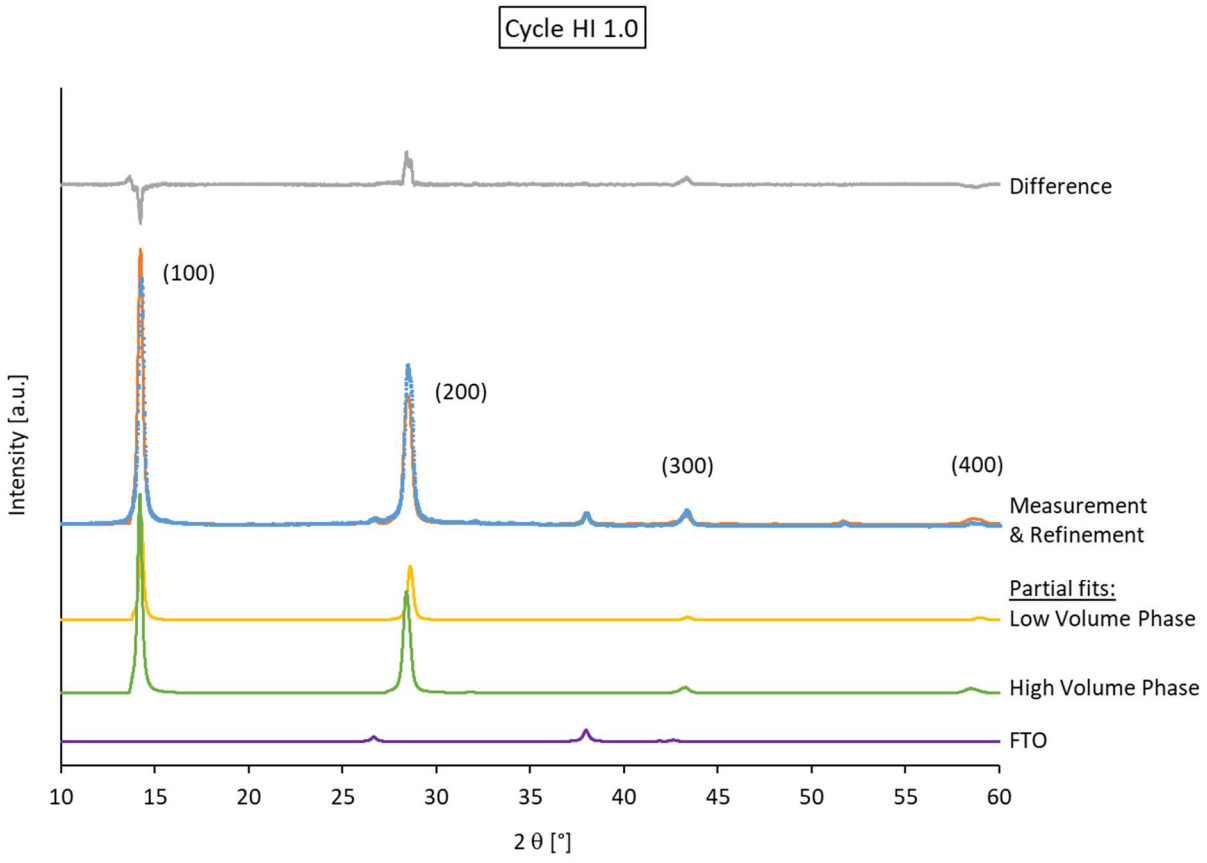

Figure 9.11 XRD pattern and refinements of the 1.0 HI substrate from the MA and HI gas CVD process, made without using the drying agent in the HI gas production

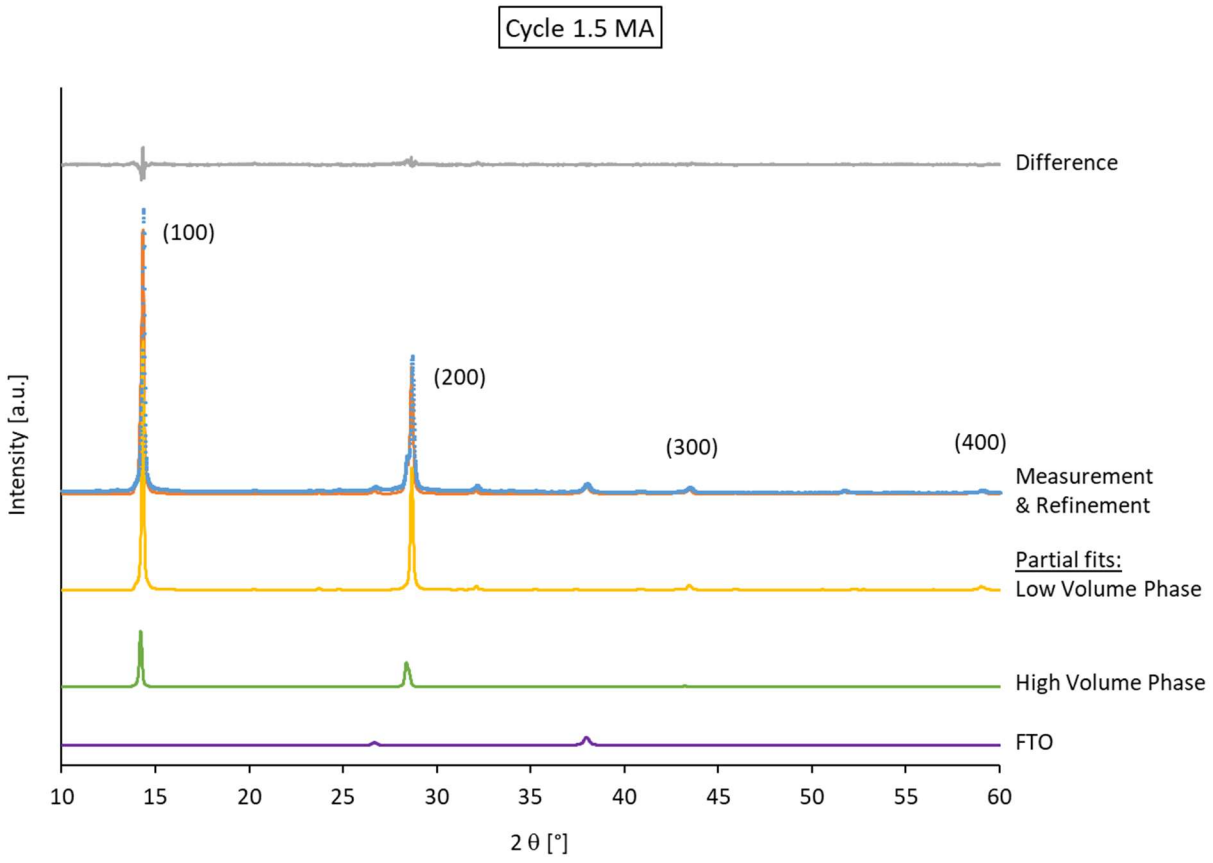

Figure 9.12 XRD pattern and refinements of the 1.5 MA substrate from the MA and HI gas CVD process, made without using the drying agent in the HI gas production

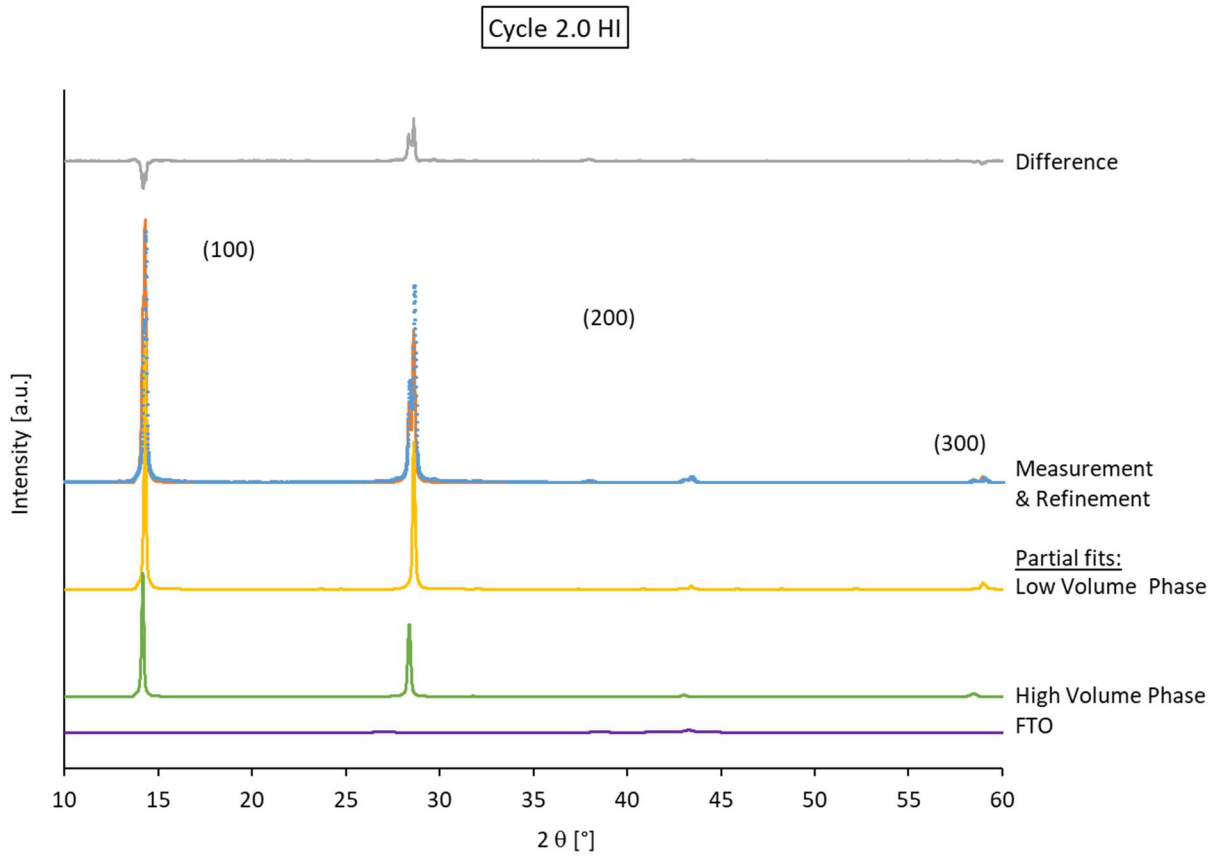

Figure 9.13 XRD pattern and refinements of the 2.0 HI substrate from the MA and HI gas CVD process, made without using the drying agent in the HI gas production

Table 9.5 XPS measurements of foils of the pure elements Au, Ag and Cu, measured with the ThermoFisher Scientific ESCALAB 250X with a Mg K_α source, for the calibration of the binding energy (B.E.), with real B.E. target values and their difference

Metal	Measured [eV]	Target [eV]	Diff [eV]
Au4f 7/2	84,00	84,00	0,00
Ag3d 5/2	368,22	368,30	0,08
Cu2p 3/2	932,44	932,70	0,27

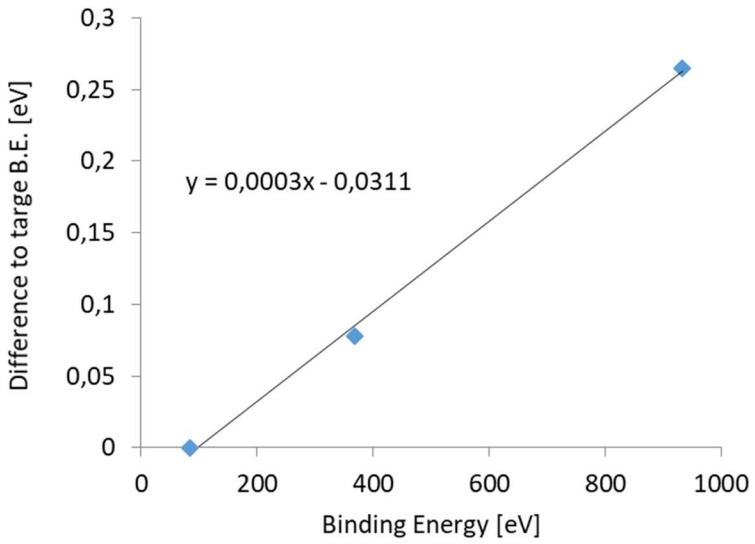

Figure 9.14 Difference values between measurements and target values of the elements Au, Ag and Cu from Table 9.5, used for the calibration of the binding energies for the XPS spectrometer

Table 9.6 Correction factors (Shift) for the binding energy calibration of the elements contained in the cycled CVD experiments, calculated from the formula in Figure 9.14

Element	Measured [eV]	m	b	Shift [eV]	New [eV]
I3d 5/2	630,92	0,0003	0,0311	0,16	631,08
C1s	286,70	0,0003	0,0311	0,05	286,75
N1s	402,60	0,0003	0,0311	0,09	402,69
O1s	529,86	0,0003	0,0311	0,13	529,99
Pb4f 7/2	138,71	0,0003	0,0311	0,01	138,72

Table 9.7 Background data for the fitted curves of the XP(S) spectra for the 0.5 MA sample, made by the MA and HI gas CVD method

0.5 MA	Start BE [eV]	Peak BE [eV]	End BE [eV]	Height [cps]	FWHM [eV]	Area CPS [eV]	Atomic %
C1s - CH_3I	298.00	285.35	279.10	409.47	1.30	625.77	6.40
C1s - MA	298.00	285.10	279.10	95.00	1.35	138.60	1.42
C1s - MAOH	298.00	285.40	279.10	76.18	1.78	147.34	1.51
C1s - other	298.00	286.80	279.10	344.75	2.12	857.47	8.77
I3d - PbI_2	640.10	619.59	610.20	45586.34	1.31	64511.36	36.19
I3d - Species A	640.10	622.23	610.20	1468.46	1.28	2204.38	1.24
I3d - Species B	640.10	618.18	610.20	3673.65	1.13	4860.19	2.73
I3d - Species C	640.10	620.75	610.20	2361.42	1.07	2974.10	1.67
N1s - MA	410.05	397.79	392.15	136.70	1.62	239.70	1.41
N1s - MAOH	410.05	400.24	392.15	245.00	0.97	257.32	1.51
O1s - MAOH	545.10	531.10	525.20	210.43	1.82	414.72	1.55
O1s - $Pb(OH)_2$	545.10	532.30	525.20	655.16	2.17	1543.28	5.76
O1s - PbO	545.10	529.98	525.20	230.00	1.19	295.72	1.10
O1s - other	545.10	530.00	525.20	681.71	1.26	1007.24	3.76
Pb4f - $Pb(OH)_2$	152.95	138.70	133.05	2900.00	1.17	3674.81	2.88
Pb4f - PbI_2	152.95	138.72	133.05	20950.00	1.06	24120.33	18.93
Pb4f - PbO	152.95	137.76	133.05	1885.00	0.69	1407.26	1.10
Pb4f - Pb^0	152.95	137.30	133.05	614.25	0.66	476.24	0.37
Pb4f - Pb_xO_y	152.95	138.79	133.05	1010.54	1.03	1216.81	0.95
Pb4f - Pb_xO_y	152.95	139.69	133.05	756.74	1.10	976.68	0.77

Table 9.8 Background data for the fitted curves of the XP(S) spectra for the 1.0 HI sample, made by the MA and HI gas CVD method

1.0 HI	Start BE [eV]	Peak BE [eV]	End BE [eV]	Height [cps]	FWHM [eV]	Area CPS [eV]	Atomic %
C1s - MA	298.00	285.00	279.10	226.00	1.11	271.17	3.22
C1s - MAPI	298.00	286.45	279.10	352.00	1.41	539.67	6.41
C1s - MAI	298.00	287.00	279.10	131.10	1.48	210.11	2.50
C1s - other	298.00	286.91	279.10	398.04	1.51	650.06	7.73
N1s - MA	410.05	398.00	392.15	245.07	1.72	456.55	3.11
N1s - MAPI	410.05	402.65	392.15	589.79	1.47	936.72	6.39
N1s - MAI	410.05	402.45	392.15	203.46	1.69	372.62	2.54
Pb4f - MAPI	152.95	138.60	133.05	5016.32	1.29	7016.50	6.40
Pb4f - PbI_2	152.95	138.65	133.05	6186.88	0.96	6441.76	5.87
Pb4f - Pb^0	152.95	137.30	133.05	595.82	0.71	456.56	0.42
I3d - MAI	640.10	619.03	610.20	5000.00	0.72	3888.26	2.53
I3d - MAPI	640.10	619.63	610.20	26220.51	1.04	29531.39	19.25
I3d - PbI_2	640.10	619.61	610.20	13500.00	1.23	18005.53	11.74
I3d - Species A	640.10	620.68	610.20	5316.85	1.18	6771.66	4.42
I3d - Species B	640.10	618.29	610.20	4595.57	1.42	7059.30	4.60
I3d - Species C	640.10	622.27	610.20	2154.31	1.15	2696.31	1.76
I3d - I_2	640.10	619.60	610.20	11786.83	1.33	17034.57	11.10

Table 9.9 Background data for the fitted curves of the XP(S) spectra for the 1.5 MA sample, made by the MA and HI gas CVD method

1.5 MA	Start BE [eV]	Peak BE [eV]	End BE [eV]	Height [cps]	FWHM [eV]	Area CPS [eV]	Atomic %
C - CH3I	298.00	285.35	279.10	293.54	1.35	463.79	4.97
C1s - MA	298.00	285.11	279.10	99.20	1.35	144.71	1.55
C1s - MAOH	298.00	285.40	279.10	125.00	1.94	263.05	2.82
C1s - other	298.00	286.65	279.10	459.42	2.70	1344.42	14.42
I3d - PbI_2	640.15	619.62	610.15	38622.66	1.22	55280.68	32.51
I3d - Species A	640.15	618.49	610.15	2590.18	1.30	3951.21	2.32
I3d - Species B	640.15	622.36	610.15	562.46	1.31	864.33	0.51
I3d - Species C	640.15	620.59	610.15	2238.47	1.30	3414.70	2.01
N1s - MA	410.05	397.92	392.15	218.97	1.06	252.20	1.55
N1s - MAOH	410.05	400.29	392.15	270.00	1.57	458.16	2.82
O1s - MAOH	545.10	531.10	525.20	366.00	1.82	720.78	2.82
O1s - $Pb(OH)_2$	545.10	532.30	525.20	334.40	2.15	778.04	3.04
O1s - PbO	545.10	529.98	525.20	168.50	1.18	215.96	0.84
O1s - other	545.10	530.07	525.20	954.64	1.12	1250.28	4.89
Pb4f - $Pb(OH)_2$	152.95	138.70	133.05	1388.00	1.23	1848.95	1.52
Pb4f - PbI_2	152.95	138.72	133.05	17253.00	1.06	19775.14	16.27
Pb4f - PbO	152.95	137.76	133.05	1275.00	0.74	1025.48	0.84
Pb4f - Pb^0	152.95	137.30	133.05	545.33	0.66	422.19	0.35
Pb4f - Pb_xO_y	152.95	138.87	133.05	3274.04	1.25	4783.70	3.94

Table 9.10 Background data for the fitted curves of the XP(S) spectra for the 2.0 HI sample, made by the MA and HI gas CVD method

2.0 HI	Start BE [eV]	Peak BE [eV]	End BE [eV]	Height [cps]	FWHM [eV]	Area CPS [eV]	Atomic %
C1s - MA	292.00	285.10	279.10	253.99	1.11	304.35	3.24
C1s - MAPI	292.00	286.50	279.10	854.82	1.24	1146.63	12.19
C1s - MAI	292.00	287.00	279.10	123.50	1.48	198.18	2.11
C1s - other	292.00	287.44	279.10	168.53	1.29	234.75	2.50
N1s - MA	406.05	398.10	392.15	284.00	1.72	529.70	3.23
N1s - MAPI	406.05	402.65	392.15	1200.00	1.53	1992.58	12.17
N - MAI	406.05	402.45	392.15	170.92	1.86	345.03	2.11
Pb - MAPI	147.95	138.62	133.05	12800.00	1.09	15069.29	12.29
Pb4f - Pb^0	147.95	137.30	133.05	668.97	0.71	515.82	0.42
I3d - MAI	640.10	618.85	610.20	4380.00	0.76	3623.91	2.11
I3d - MAPI	640.10	619.63	610.20	50000.00	1.14	61833.41	36.06
I3d - Species A	640.10	620.82	610.20	5182.61	1.17	6588.26	3.84
I3d - Species B	640.10	618.15	610.20	4350.53	2.24	10556.02	6.15
I3d - Species C	640.10	622.27	610.20	2154.31	1.15	2693.72	1.57

Table 9.11 Background data for the fitted curves of the XP(S) spectra for the 2.5 MA sample, made by the MA and HI gas CVD method

2.5 MA	Start BE [eV]	Peak BE [eV]	End BE [eV]	Height [cps]	FWHM [eV]	Area CPS [eV]	Atomic %
C1s - CH_3I	298.00	285.35	279.10	150.89	1.81	320.86	2.28
C1s - MA	298.00	285.05	279.10	218.00	1.08	253.97	1.81
C1s - MAI	298.00	287.00	279.10	119.00	1.48	190.95	1.36
C1s - MAPI	298.00	286.50	279.10	360.00	1.41	551.42	3.93
C1s - other	298.00	286.57	279.10	195.57	1.22	279.33	1.99
I3d - MAI	640.10	618.98	610.20	3390.00	0.95	3476.57	1.36
I3d - MAPI	640.10	619.65	610.20	24346.30	1.14	30188.55	11.79
I3d - I_2	640.10	619.55	610.20	6765.55	1.28	10156.11	3.97
I3d - Species A	640.10	620.84	610.20	3400.88	1.22	4866.59	1.90
I3d - Species B	640.10	622.37	610.20	1375.31	1.28	2064.55	0.81
I3d - Species C	640.10	618.12	610.20	2662.04	1.28	3996.12	1.56
N1s - MA	410.05	398.10	392.15	237.48	1.72	442.93	1.81
N1s - MAI	410.05	402.45	392.15	180.71	1.69	331.40	1.35
N1s - MAPI	410.05	402.65	392.15	608.57	1.45	957.40	3.91
O1s - $Pb(OH)_2$	546.10	532.30	526.20	381.49	2.17	898.36	17.22
O1s - other	546.10	530.22	526.20	998.32	1.66	1937.61	37.06
Pb4f - MAPI	152.95	138.62	133.05	5750.00	1.06	7152.14	3.91
Pb4f - $Pb(OH)_2$	152.95	138.70	133.05	2529.05	1.17	3214.99	1.76
Pb4f - Pb^0	152.95	137.30	133.05	204.16	0.64	140.41	0.24

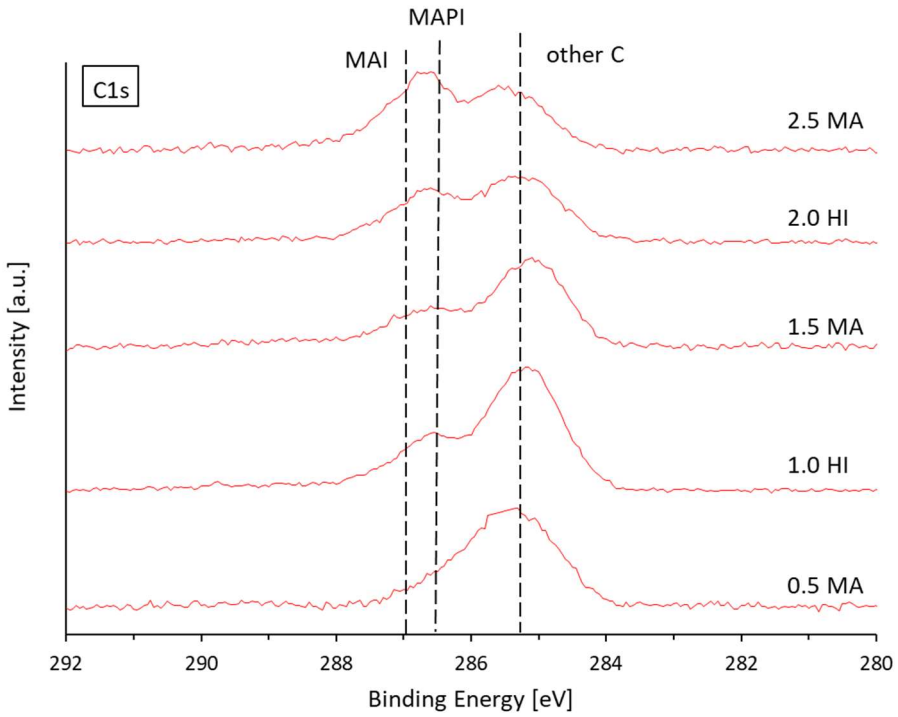

Figure 9.15 C1s XPS measurements of samples from the MA and HI gas CVD process, which were made without a drying agent in the HI production step

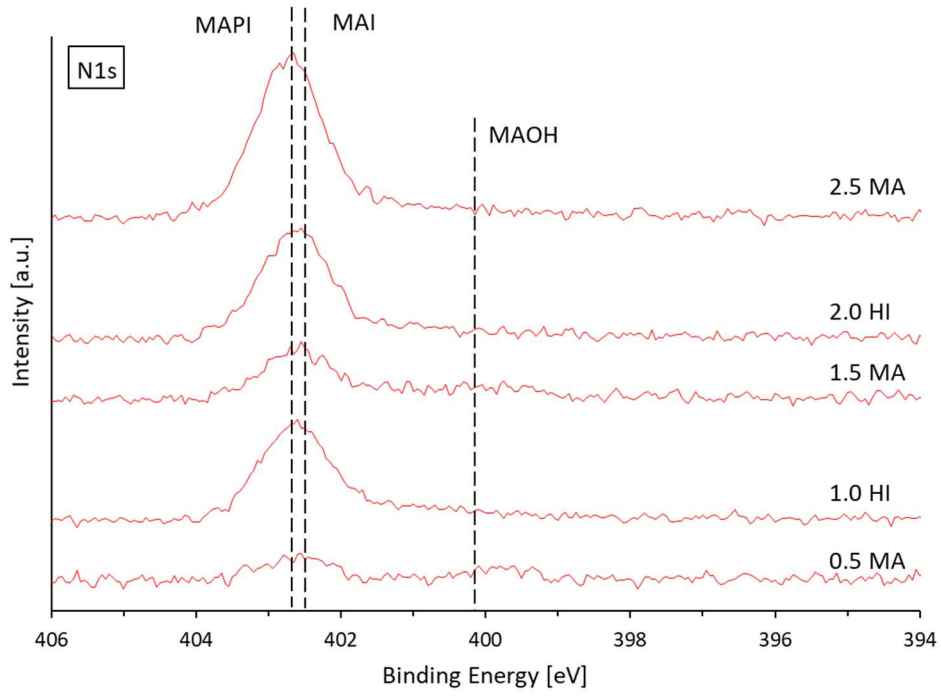

Figure 9.16 N1s XPS measurements of samples from the MA and HI gas CVD process, which were made without a drying agent in the HI production step

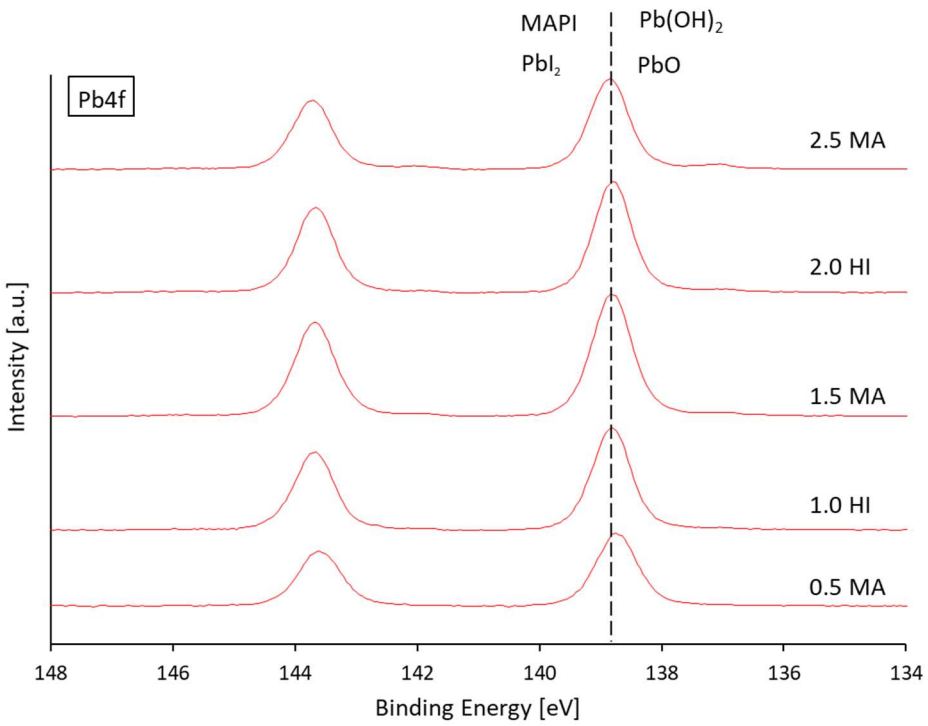

Figure 9.17 Pb4f XPS measurements of samples from the MA and HI gas CVD process, which were made without a drying agent in the HI production step

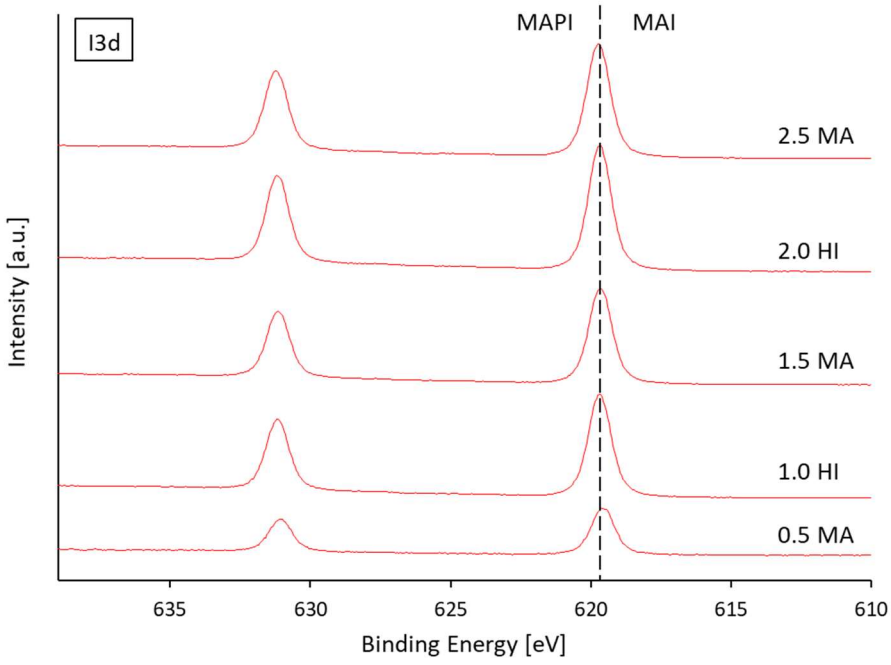

Figure 9.18 I3d XPS measurements of samples from the MA and HI gas CVD process, which were made without a drying agent in the HI production step

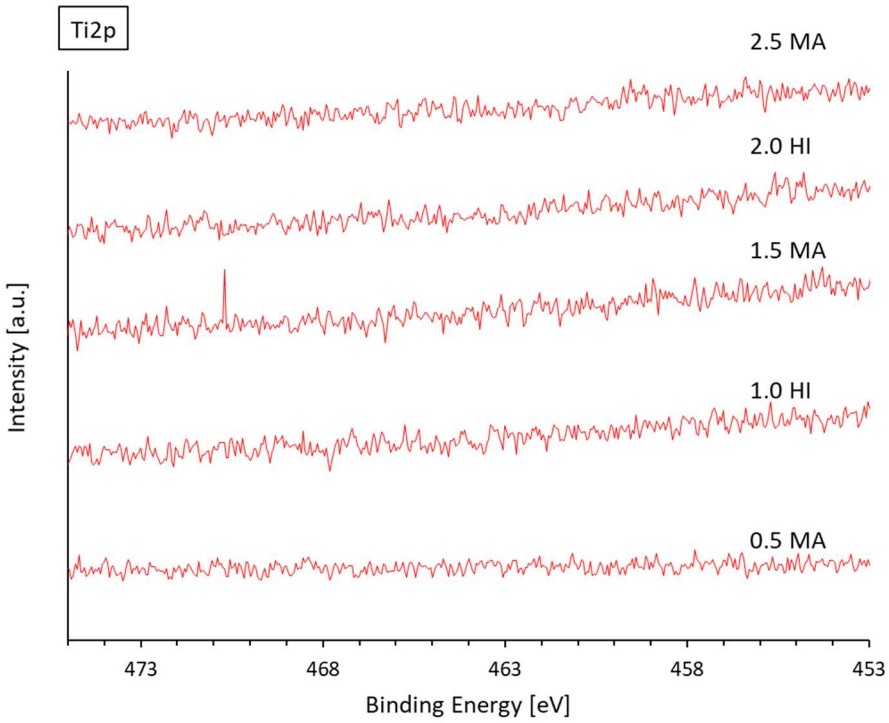

Figure 9.19 Ti2p XPS measurements of samples from the MA and HI gas CVD process, that were made without a drying agent in the HI production step

Publications, student theses and conference contributions

Publications

Publications as first author:

1. Mortan, C.; Hellmann, T.; Clemens, O.; Mayer, T.; Jaegermann, W. Preparation of Methylammonium Tin Iodide (CH3NH3SnI3) Perovskite Thin Films via Flash Evaporation. *Phys Status Solidi A* **2019,** *216* (18)
2. Mortan, C.; Hellmann, T.; Buchhorn, M.; d'Eril Melzi, M.; Clemens, O.; Mayer, T.; Jaegermann, W., Preparation of methylammonium lead iodide (CH3NH3PbI3) thin film perovskite solar cells by chemical vapor deposition using methylamine gas (CH3NH2) and hydrogen iodide gas. **2020,** *Energy Sci Eng*.; 8: 3165– 3173

Publication as contributing author:

3. Hellmann, T.; Wussler, M.; Das, C.; Dachauer, R.; El-Helaly, I.; Mortan, C.; Mayer, T.; Jaegermann, W. The difference in electronic structure of MAPI and MASI perovskites and its effect on the interface alignment to the HTMs spiro-MeOTAD and CuI. *J Mater Chem C* **2019,** *7* (18), 5324.
4. **In preparation:** S. Weyand, K. Kawajiri, C. Mortan, T. Mayer, W. Jaegermann, L. Schebek. Perovskite solar cells: A climate-friendly emerging energy technology? Systematic upscaling approach from lab to fab for Life Cycle Assessment of emerging functional material-based technologies

Student theses

Supervision of an advanced research lab:

1. Marco d'Eril Melzi; Quadruple Cation (MA+ FA+ Rb+ Cs+) and Double Anion (I- Br-) Perovskite Solar Cells – Optimizing Stability and Reproducibility; TU Darmstadt, Surface Science, **2019**

Supervision of master theses:

1. Moritz Buchhorn; Chemische Gasphasenabscheidung als Depositionsmethode zur Darstellung von Dünnschicht-Perowskitsolarzellen; TU Darmstadt, Surface Science, **2018**
2. Marco d'Eril Melzi; Chemical Vapor Deposition as a Method for the Preparation of Thin Film Perovskite Solar Cells; TU Darmstadt, Surface Science, **2019**

Conference contributions

Oral presentations

1. Perovskite Solar Cells: from Lead (Pb) to Tin (Sn) – Flash Evaporation, ABXPV Conference, Valencia, **2017**
2. Perovskite Solar Cells – An Upscalable CVD Process – XPS Analysis of the Sequential Reaction Mechanism, EMRS Conference, Warsaw, **2019**

Poster presentations

1. Perovskite Solar Cell Devices – Flash Evaporation, EMRS Conference, Warsaw, **2017**
2. Perovskite Solar Cell Devices – Flash Evaporation, PSCO Conference, Oxford, **2017**
3. Perovskite Solar Cells – An Upscalable CVD Process – XPS Analysis of the Sequential Reaction Mechanism, MRS Conference, Phoenix, **2019**

Acknowledgements

Completing a PhD is most of all a learning experience. It teaches resilience, perseverance and is overall character building. An important lesson in practical science and engineering that I internalized through countless experiments is the feed-back loop of hypothesizing, making a prediction, running experiments, observing, concluding and returning to hypothesizing, improving the initial theory.

First and foremost, I would like to thank both Prof. Wolfram Jaegermann and Dr. Thomas Mayer equally for their support and supervision provided at all times during my PhD work within the Surface Science group. Prof. Jaegermann, as an experienced doctor father, provided me with general goals and great ideas, still leaving plentiful freedom for self-development. Dr. Thomas Mayer as my direct supervisor always had an open door for fruitful scientific and practical discussions when experiments and their outcome were questionable. I learned a great deal about science, engineering and high quality leadership from both of you.

I would like to thank Dr. Tanja Drobek, the manager of the Graduate School Energy Science and Engineering (GSC ESE) at the TU Darmstadt, from which I received my scholarship, for the outstanding organization within the graduate school and the very interesting talks.

Many thanks to Prof. Barbara Albert for her kindness in providing an assessment of this dissertation.

A big thanks to our secretaries Marga Lang (Surface Science), Heide Rinnert and Vera Becker (GSC ESE) who always helped with their expertise on organizational issues.

I would also like to thank Prof. Oliver Clemens for the many discussions and expertise on XRD data and for the cooperation with our publications.

Many thanks to our technician Kerstin Lakus-Wollny who was there in the good and bad times during my stay and who helped with her many years of experience.

I would also like to thank all my colleagues within the Solar Cells group for all the fun times outside of the labs, but also for all the serious moments of struggle when the next device seemed to break, as soon as the previous one has been repaired, Dr. Eric Mankel, Dr. Chittaranjan Das, Michael Wußler, Tim-Dominik Hellmann, Moritz Buchhorn, Marco d'Eril Melzi, Dr. Ralph Dachhauer, Dr. Carolin Wittich, Maximilan Stöhr, Nils Schäfer, Christian Hoyer, Ian Coates, Waqas Zia, Islam Elhelaly and Chandra Prabowo.

Many thanks to the group of nano materials for the help with most of the XRD measurements Manuel Donzelli, Aamir Iqbal Waidha, Mohammad Ali Nowroozi and Kerstin Wissel.

I would also like to thank all the assistant scientist for their help with our experiments in the labs, Akash, Mutahir, Narges, Baris, Hamza, Ali, Deepthi and many thanks to all other awesome members of the Surface Science group, the Material Science Department and those of the Energy Science and Engineering group!

I am also grateful for the employees of the mechanical and electrical workshop of the Materials Science department, especially the head mechanical engineer Jochen Rank and the head electrical engineer Michael Weber who both helped immensely in completing this work, with their invaluable knowledge and skills.

Last, but not least, I would like to thank my Garage friends and also my family, especially my mom, Dipl.-Ing. Daniela Mortan and my dad, Dipl.-Ing. Liviu Mortan for their continuous support and kindness.

Résumé

Education:

06/2016 – 11/2019: Doctorate in the Material Science department, Surface Science group: *Thin Film Perovskite Solar Cells – Fabrication via Spin Coating, Flash Evaporation and Chemical Vapor Deposition (CVD);* Scholarship from the Graduate School of Excellence Energy Science and Engineering (DFG project) at the Technical University of Darmstadt

10/2013 – 03/2016: M.Sc. Energy Science and Engineering, Technical University of Darmstadt; Master Thesis in the department for Surface Science: *Wet Chemical Preparation and Analysis of Thin Film Perovskite Solar Cells (2015)*

10/2008 – 02/2013: B.Sc. Chemistry, University of Stuttgart; Bachelor Thesis in the department of Physical Chemistry: *Photoisomerization of rod-shaped azo compounds in ionic liquid crystals* (2012)

9/2004 – 06/2008: Abitur, Werner-Siemens-Schule Stuttgart, Profile: Information Technology

09/2000 – 07/2004: Mittlere Reife, Realschule Weil der Stadt, Germany

09/1998 – 06/2000: Iosif Vulcan Gymnasium in Oradea, Romania

Work Experience:

06/2014 - present: Independent contractor as a Search Engine Evaluator (SEE) at Appen Ltd.

Extracurricular Activities:

11/2018 – 11/2019: Representative member of the joint committee for the Master Course Energy Science and Engineering at the Technical University of Darmstadt

05/2018 – 09/2019: Member of the PhD Committee at the Darmstadt Graduate School of Excellence Energy Science and Engineering

05/2018 – 09/2019: Member of the Equal Opportunity Commission of the Darmstadt Graduate School of Excellence Energy Science and Engineering